UNIVERSITY OF CALIFORNIA

Los Angeles

Economic Model Predictive Control: Handling Preventive Actuator and Sensor Maintenance and Application to Transport-Reaction Processes

A dissertation submitted in partial satisfaction of the
requirements for the degree Doctor of Philosophy
in Chemical Engineering

by

Liangfeng Lao

2015

ABSTRACT OF THE DISSERTATION

Economic Model Predictive Control: Handling Preventive Actuator and Sensor Maintenance and Application to Transport-Reaction Processes

by

Liangfeng Lao

Doctor of Philosophy in Chemical Engineering

University of California, Los Angeles, 2015

Professor Panagiotis D. Christofides, Chair

In chemical process industries, maintenance costs may comprise of up to $20-30\%$ of the operating budget, and therefore, improving maintenance practices can significantly impact plant economics and reduce production losses. Developing so-called "Smart" preventive maintenance policies/systems of key manufacturing components, especially those that may cause process upsets, losses and downtime, is therefore an important task. A high percentage of the day-to-day preventive maintenance tasks in the chemical process industry deals with control actuators and measurement sensors employed by process control systems. Motivated by these considerations, the first part of this dissertation focuses on the development of methods for integrating the on-line preventive maintenance of actuators and sensors with advanced process control system design. To accomplish these preventive maintenance tasks, economic model predictive control (EMPC), that optimizes economic process performance over an operating horizon by employing a dynamic process model to predict the evolution of the process, is employed to maintain stable operation of

a process while dictating an economically optimal operating policy with respect to varying numbers of control actuators and measurement sensors. Novel EMPC schemes are developed that explicitly account for scheduled preventive control actuator/sensor maintenance programs, process economics and feedback control. In the second part of this dissertation, EMPC of transport-reaction processes is considered for the first time. Compared with lumped-parameter processes, no work has been done on the problem of designing EMPC for transport-reaction processes modeled by partial differential equations (PDEs). The thesis proposes EMPC schemes those are formulated on the basis of suitable reduced-order models to ensure input and state constraint satisfaction and economics optimization for both parabolic and hyperbolic PDEs. Finally, the thesis concludes with the presentation of multiscale, computational fluid dynamics modeling framework for an industrial-level steam methane reforming unit.

The dissertation of Liangfeng Lao is approved.

Tsu-Chin Tsao

Dante Simonetti

James F. Davis

Panagiotis D. Christofides, Committee Chair

University of California, Los Angeles

2015

Contents

List of Figures

ACKNOWLEDGEMENTS

I would first like to express my gratitude to my advisor, Professor Panagiotis D. Christofides, for his nonstop support throughout my doctoral work. I feel very fortunate I contacted Professor Christofides after being accepted at UCLA. He was very direct which fit well with my personality and I could see the great opportunity I would have if I were to join his laboratory. After my initial contact with Professor Christofides, he told me my background would fit well with his research project. Overall, I could not have asked for a better advisor during my graduate studies. I would like to thank Professor James F. Davis, Professor Dante Simonetti, and Professor Tsu-Chin Tsao for agreeing to serve on my doctoral committee.

I would like to thank Matthew James Ellis for being an excellent colleague who worked closely with me on many of our group projects. Our teamwork combined our strengths, thereby accelerating our research progress. Furthermore, I would like to thank Andres Aguirre and Anh Tran for being excellent colleagues who worked closely with me on the steam methane modeling project. Also, a special thanks, in particular, to Helen Durand and Andres Aguirre for their comments in proofreading my dissertation. I would like to thank all of my lab mates during my graduate career. In particular: Dr. Xianzhong Chen who started me on model predictive control; Drs. David Ernesto Chilin, Jianqiao Huang and Mohsen Heidarinejad who were all great graduate student advisors to me and showed me what to expect as a graduate student; Dawson Tu who worked with me on economic model predictive control; Larry Gao, Michael Nayhouse, Joseph Sang-II Kwon, Anas Wael Alanqar, Fahad Albalawi and Marquis Grant Crose who were great lab mates in addition to being close friends throughout my time at UCLA.

I was also fortunate to meet and get to know a number of people outside of my research group during my time at UCLA which made the experience much more enjoyable. I would like to thank Prakashan Korambath from the Institute for Digital Research and Education

in UCLA for his help on the cluster computation for my CFD model and Kwamina Bedu-Amissah from Praxair Inc. for his information on steam methane modeling from the point of view of industrial design and operation.

Financial support from the Department of Energy (DOE) and the National Science Foundation (NSF) is gratefully acknowledged and my work could not have been done without them. Additionally, the Graduate Fellowship and Dissertation Year Fellowship of UCLA Graduate Division, were also a great help in allowing me freedom in my graduate studies.

Finally, and most importantly, I would like to thank my wife Lin Zhao. Her support, encouragement, quiet patience and unwavering love were undeniably the bedrock upon which my Ph.D. life has been built. Her tolerance of my occasional vulgar moods is a testament in itself of her unyielding devotion and love. Her support and encouragement throughout my PhD study were extremely important to me. I thank my parents, for their faith in me and allowing me to be as ambitious as I wanted. It was under their watchful eye that I gained so much drive and an ability to tackle challenges head on. Their upbringing started me on a path to success that I am extremely grateful to have had.

Chapter 2 is a version of: L. Lao, M. Ellis, and P. D. Christofides. Smart Manufacturing: Handling Preventive Actuator Maintenance and Economics using Model Predictive Control. *AIChE J.*, 60:2179-2196, 2014.

Chapter 3 is a version of: L. Lao, M. Ellis, and P. D. Christofides. Real-Time Preventive Sensor Maintenance Using Robust Moving Horizon Estimation and Economic Model Predictive Control. *AIChE J.*, 2015, in press.

Chapter 4 is a version of: L. Lao, M. Ellis, and P. D. Christofides. Proactive Fault-Tolerant Model Predictive Control. *AIChE J.*, 59:2810-2820, 2013.

Chapter 5 is a version of: L. Lao, M. Ellis, and P. D. Christofides. Economic Model Predictive Control of Transport-Reaction Processes. *Industrial & Engineering Chemical*

Research, 53:7382-7396, 2014.

Chapter 6 is a version of: L. Lao, M. Ellis, and P. D. Christofides. Economic Model Predictive Control of Parabolic PDE Systems: Addressing State Estimation and Computational Efficiency. *Journal of Process Control*, 24:448-462, 2014.

Chapter 7 is a version of: L. Lao, M. Ellis, and P. D. Christofides. Handling State Constraints and Economics in Feedback Control of Transport-Reaction Processes. *Journal of Process Control*, 32:98-108, 2015.

Chapter 8 is a version of: L. Lao, M. Ellis, and P. D. Christofides. Economic Model Predictive Control of a Hyperbolic PDE System. *Proceedings of the 53rd Conference on Decision and Control*, 563-570, Los Angeles, CA, 2014.

VITA

2007–2011	Bachelor of Science, Chemical Engineering Department of Chemical Engineering Tsinghua University
2008–2011	Bachelor of Arts, Ecnomics School of Economic and Management Tsinghua University
2011	Graduation Distinction Tsinghua University
2011–2015	Graduate Student Researcher / Teaching Assistant Department of Chemical and Biomolecular Engineering University of California, Los Angeles
2015	Dissertation Year Fellowship Teaching Assistant Fellow Department of Chemical and Biomolecular Engineering University of California, Los Angeles

PUBLICATIONS

1. L. Lao, M. Ellis, and P. D. Christofides, "Real-Time Preventive Sensor Maintenance Using Robust Moving Horizon Estimation and Economic Model Predictive Control," *AIChE Journal*, 2015, in press.

2. L. Lao, M. Ellis, and P. D. Christofides, "Handling State Constraints and Economics in Feedback Control of Transport-Reaction Processes," *Journal of Process Control*, 2015, **32**, 98-108.

3. L. Lao, M. Ellis, and P. D. Christofides, "Economic Model Predictive Control of Parabolic PDE Systems: Addressing State Estimation and Computational Efficiency," *Journal of Process Control*, 2014, **24**, 448-462.

4. L. Lao, M. Ellis, and P. D. Christofides, "Economic Model Predictive Control of Transport-Reaction Processes," *Industrial & Engineering Chemical Research*, 2014, **53**, 7382-7396.

5. L. Lao, M. Ellis, and P. D. Christofides, "Smart Manufacturing: Handling Preventive Actuator Maintenance and Economics using Model Predictive Control," *AIChE Journal*, 2014, **60**, 2179-2196.

6. L. Lao, M. Ellis, and P. D. Christofides, "Proactive Fault-Tolerant Model Predictive Control," *AIChE Journal*, 2013, **59**, 2810-2820.

Chapter 1

Introduction

1.1 Economic Model Predictive Control

A recent theoretical development within the process control community is the establishment of a theoretical basis for economic model predictive control (EMPC), an optimization-based control methodology with a structure based on that of traditional tracking model predictive control (MPC) but with a cost function that represents the process economics. EMPC optimizes economic process performance over an operating horizon by employing a dynamic process model to predict the evolution of the process.[4,5,34,45,60,65,71,72,106,118] Thus, the control actions computed by EMPC will, ideally, force the process operation to remain economically optimal throughout time.

Some of the recent developments on EMPC include: a reformulation of EMPC based on a Lyapunove-based controller design with two switching operation modes,[65] proof of asymptotic stability of EMPC formulated without terminal constraints,[60] proposition of an EMPC scheme with a self-tuning terminal cost,[106] an EMPC formulation that can account for explicitly time-varying parameters in the cost function,[45] asymptotic average performance bounds for EMPC using a self-tuning terminal cost or a generalized terminal region

constraint,[107] performance and stability analysis for EMPC without terminal costs or constraints,[61] the use of event-triggering to initiate EMPC evaluations and reduce computation requirements,[143] an output feedback EMPC scheme with robust moving horizon estimation,[49] and a fast EMPC scheme by employing nonlinear programming sensitivities[77] (see, also, the review[48] for more recent results on EMPC).

1.2 Preventive Maintenance in Chemical Industries

Smart Manufacturing has been deemed by many manufacturing experts as the next frontier of manufacturing that will revolutionize future manufacturing.[16,22,28,32,124] Objectives put forth by the proponents of Smart Manufacturing can be summarized as the design, development, and deployment of integrated systems to achieve a significant step-change in overall manufacturing intelligence.[22,32] One example of the challenge problems next-generation manufacturing faces is being able to successfully manage the trade-off between sustainability and profitability.[124] In the current manufacturing paradigm, many individual components or phases of the manufacturing process are optimized and/or operate independently of other components (e.g., planning/scheduling, control, plant-wide optimization, etc.) and thus, the aforementioned challenge problem cannot be handled in the context of traditional manufacturing paradigms. One of the key components of Smart Manufacturing is to unite individual components into a completely integrated platform.[32] The results of making these interconnections have the potential to transform operations from a reactive or corrective environment to a proactive or preventive setting yielding major economic benefit.[16] Identifying the interconnections between components and systems has been the subject of recent research.

Specifically, in the context of process operations, maintenance programs and policies are a vital part of maintaining operations, reliability, and safety of manufacturing processes

(e.g., Refs[12,92]). Maintenance tasks can be divided into two main categories: (1) corrective and (2) preventive.[137] Corrective maintenance deals with repairing or replacing a failed component of the process; while, preventive maintenance consists of tasks or measures taken to prevent component failure. The scope and scale of the latter maintenance program varies in the process industries. At one end of the scale, scheduled preventive maintenance may only consist of a spreadsheet containing a schedule and historical log of the preventive maintenance tasks which has been compiled from past experience. Another simple approach to preventive maintenance could be to utilize existing process identification tools or alarms used to assess safety and operability performance of processes. For example, preventive maintenance action may be taken when tools identify near-misses which are considered to be precursors to abnormal events.[111] On the other hand, more complex, model-based and optimization-based approaches to preventive maintenance have been explored (e.g., Refs[12,19,20,132,137]). In fact, extensive literature exists on the mathematical theory of reliability which is a key metric in most complex preventive maintenance programs.[12] Examples of optimization-based approaches to preventive maintenance include: developing a framework for preventive maintenance optimization to solve the so-called opportunistic maintenance problem by combining Monte Carlo simulation with a genetic algorithm,[132] integrating statistical process control techniques with optimization of preventive maintenance policies which was demonstrated to yield a reduction in operation costs over only using a control chart or preventive maintenance policy,[19] determining the optimal maintenance policy by constructing an optimization problem which includes maximizing the expected revenue minus the maintenance costs subject to a (steady-state) process model and maintenance model,[137] and developing an integrated model to coordinate maintenance planning and production scheduling.[20]

Preventive maintenance is of interest in the context of the Smart Manufacturing given the direct connection between the objectives of the two. Furthermore, maintenance costs

can be significant. In the context of the literature on maintenance policies, an often cited statistic on maintenance costs is that it may comprise of up to 20-30% of the operating budget of a chemical plant,[120] and therefore, improving maintenance practices can impact maintenance costs and production losses.[132] Developing so-called "Smart" maintenance policies/systems through unifying manufacturing components especially those that reduce process upset, loss, and downtime like preventive maintenance programs is an important task given the possibility of significant cost-savings.

A high percentage of the small-scale, day-to-day preventive maintenance tasks for the chemical process industry is for process control systems (e.g., actuators, sensors, etc.).[132] In the context of process operation, sensor and actuator maintenance programs and policies can greatly impact the process reliability, manufacturing safety and process economic performance. Among modern maintenance programs for process manufacturing, preventive maintenance of sensors and actuators in real-time can significantly mitigate the damage from production losses, process upsets and downtime based on specific routine regulations.[55] To accomplish these preventive maintenance tasks, the ability of a control system to maintain stable operation of the process while dictating an economically optimal operating policy with respect to the available control actuators and process sensors is desirable and can be considered within the scope of the Smart Manufacturing paradigm.

In terms of control actuators, potential defects, excess wear and refurbishment becomes a priority to routinely conduct preventive maintenance on the control actuators of the process in an attempt to avoid/prevent a process upset caused by a failed or unreliable actuator.[132] Preventive maintenance on control actuators in the context of control system design can achieve these objectives by taking adequate control measures to minimize the negative impact of pre-arranged control actuator maintenance on process operation.[16] It accounts for a future potential fault on the actuator before it happens and sets up the reconfiguration of the control system to avoid the production loss due to the potential fault and ensure a

smooth transition to the post-fault control system. Ideally, process operators would like to maintain process operation during any maintenance task to prevent production losses as long as operators are able to sustain safe process operation with fewer control actuators. It is also highly desirable to operate the process in an economically optimal fashion by accounting for the process economics and the fact that fewer actuators are available.[120] Therefore, the preventive maintenance on actuators requires that the control system be able to adjust to a change in the number of manipulated inputs that it controls. Also, from the viewpoint of closed-loop stability, once the actuator number changes in the actuator preventive maintenance program, the available control energy changes which may lead to a change in the region of stable operation. Consequently, the change in the number of actuators requires a change in the region of operation as actuators are taken off-line/brought back on-line, which poses unique theoretical and implementation challenges.

On the other hand, sensor preventive maintenance programs are also very important in the chemical processing industry,[56] e.g., sensors working under severe conditions need to be frequently replaced since they may not withstand their working environment and consequently result in inaccurate readings.[30] From a maintenance logistics point of view, sensors present a challenge because they are widely dispersed throughout a manufacturing plant. During a maintenance procedure when no redundant sensors are available, sensor replacement will directly result in sensor data losses which may cause significant process performance degradation under continuous operation. For example, when conducting the maintenance of some important sensors, vital machinery may be affected and bring process operation to a halt which makes large production losses unavoidable. Consequently, control system designs accounting for sensor data losses have received a lot of attention lately.[81,101,105,121] More specifically, in,[101] a sensor reconfiguration-based method was proposed through characterizing stability regions for different control configurations utilizing different numbers of sensors to ensure stability after a sensor is taken off-line. In,[105]

a Lyapunov-based model predictive control (LMPC) system was designed to explicitly account for sensor data losses and implement the last computed optimal input trajectory (when sensor measurements are available for the last time) when sensor data is not available. However, in the context of smart manufacturing, integrating preventive sensor maintenance and process economic optimization becomes an important problem to avoid unnecessary plant shutdown.[28,32]

Up to this point, however, little work has been done on preventive maintenance practice in the context of chemical process control, despite recent calls for moving into this direction.[16] To complete the preventive maintenance tasks on sensors and actuators in real-time, it is necessary to design a control system that can simultaneously compute economically optimal control actions for a process and maintain process closed-loop stability even as the number of sensors or actuator is varied. Considering all of the above requirements and objectives, EMPC is one natural approach to accomplish these tasks. EMPC was first presented as a control methodology to overcome some of the challenges faced with integrating real-time optimization (RTO) and regulatory control, but a consequence of the unique formulation of EMPC (i.e., control methodology that accounts directly for the process economics) is that it can be integrated into other systems as part of the Smart Manufacturing paradigm (e.g., preventive maintenance programs). However, EMPC cannot be applied directly because the optimization problem dimensionality, cost function, and constraints change as a result of the changing number of control inputs (i.e., actuators) and state inputs (i.e., state measurements).

1.3 Control of Transport-Reaction Processes

Transport-reaction processes are characterized by significant spatial variations and nonlinearities due to the underlying diffusion and convection phenomena and complex reaction

mechanisms, respectively. Currently, the approach followed for the solution of the control problem of transport-reaction processes is essentially determined by the well-known classification of partial differential equations (PDEs) into hyperbolic, parabolic, or elliptic.[128] Specifically, processes whose convective mechanisms dominate over diffusive ones can be adequately described by systems of quasi-linear hyperbolic PDEs. However, the diffusive phenomena also play a prominent role in the dynamic models of several industrially-important transport-reaction processes, e.g., tubular, fluidized bed and packed-bed reactors and should be accounted for. These processes are typically modeled by quasi-linear parabolic PDEs whose spatial differential operators can be characterized by a spectrum that can be partitioned into a finite (possibly unstable) slow part and an infinite dimensional stable fast complement.[31]

The development of computationally efficient control methods for PDEs has been a major research topic in the past 30 years (e.g., Ref[25]). The design of feedback control systems for PDEs is usually achieved on the basis of finite-dimensional systems (i.e., sets of ordinary differential equations (ODEs) in time) obtained by applying a variety of spatial discretization and/or order reduction methods to the PDEs. The traditional approach to the control of quasi-linear parabolic PDEs involves the application of eigenfunction expansion techniques to the PDEs to derive systems of finite-dimensional ordinary differential equations (ODEs) that accurately describe the dynamics of the dominant (slow) modes of the PDEs. In detail, the solution of the original PDEs is initially expanded as the sum of an infinite series of the eigenfunctions of the spatial differential operator with time-varying coefficients. This expansion is used to derive an infinite set of ODEs for the coefficients of the expansion. Then, a finite-dimensional ODE model is derived by discarding an infinite set of equations. The finite-dimensional ODE model is subsequently used as the basis for the synthesis of finite-dimensional controllers (e.g., Refs[9,23,119]). A potential drawback of this approach is that the number of modes that should be retained to derive an ODE system

which yields the desired degree of approximation may be very large. To overcome these controller synthesis and implementation problems, research efforts focused on taking advantage of the concept of inertial manifolds (IM) (e.g., Ref[133]) and approximate inertial manifolds (AIMs) (e.g., Refs[27,53,54]) for the construction of low-order ODE systems of desired accuracy. Based on this, significant work over the last twenty years has focused on the synthesis of low-order controllers for quasi-linear parabolic PDEs on the basis of low-order nonlinear ODE models derived through a combination of Galerkin's method (using analytical or empirical basis functions) with the concept of approximate inertial manifolds (e.g., Refs[8,27,44] and the book[25] for results and references in this area).

In terms of the basis functions used in Galerkin's method for model reduction of parabolic PDEs, analytical eigenfunctions is the most common type which can be obtained by solving the eigenvalue/eigenfunctions problem of the parabolic operator in the original PDEs. However, the solution of the eigenvalue/eigenfunctions problem of the parabolic operator is not guaranteed due to various boundary conditions of the PDEs. Considering this possible limitation for using analytical basis functions and to improve the ROM accuracy, empirical eigenfunctions as the basis functions for the Galerkin's method is another option. The empirical eigenfunctions may be constructed by applying Karhunen-Loève (K-L) expansion (e.g., Refs[69,127]). By collecting an ensemble of the system solution data from process historical data or simulation data, the K-L expansion method considers the presence of the dominant spatial patterns in the solution of the parabolic PDEs and results in a more comprehensive and accurate ROM than a ROM based on analytical basis functions. This data-based construction of the basis functions for order reduction to systems of PDEs has been widely adopted in the recent years in the context of model-based control problems for parabolic PDEs (e.g., Refs[6,8,11,113,134,136]). However, to achieve high accuracy of the ROM derived from the empirical eigenfunctions of the original system of PDEs, the POD method usually needs a large ensemble of solution data (snapshots) to contain as much local

and global process dynamics as possible. Constructing such a large ensemble of snapshots becomes a significant challenge from a practical point of view; because currently, there is no general way to realize a representative ensemble. Based on this consideration, an adaptive proper orthogonal decomposition (APOD) methodology was proposed to recursively update the ensemble of snapshots and compute on-line the new empirical eigenfunctions in the on-line closed-loop operation of PDEs (e.g., Refs[115,116,126,136]). While the APOD methodology of[136] and[115] demonstrated its ability to capture the dominant process dynamics by a relatively small number of snapshots which reduces the overall computational burden, these works did not address the issue of computational efficiency with respect to optimal control action calculation and input and state constraint handling. Moreover, the ROM accuracy is limited by the number of the empirical eigenfunctions adopted for the ROM; in practice, when a process faces state constraints, the accuracy of the ROM based on a limited number of eigenfunctions may not be able to allow the controller to avoid a state constraint violation.

However, for hyperbolic PDEs (e.g., convection-reaction processes where the convective phenomena dominate over diffusive ones), it is common that the eigenvalues of the spatial differential operator cluster along vertical or nearly vertical asymptotes in the complex plane, and thus, many modes are required to construct finite-dimensional models of desired accuracy.[25] Considering this, Galerkin's method would be computationally expensive for this case compared to finite-difference method utilizing a sufficient large number of discretization points.[51] The orthogonal collocation method is another weighted residual method which has also been used for the control of hyperbolic PDEs.[73] The orthogonal collocation method is based on the collocation points chosen as roots of a series of specific orthogonal polynomial functions. Although the collocation method is easy to apply, its accuracy can be promised only if the collocation points are judiciously chosen which has been a general difficulty for its wide application.[52] With respect to controller design

for systems of hyperbolic PDE , many researchers have proposed various control methods (e.g., Refs[3,21,64,103,104]), and several works (e.g., Refs[39,40,57,73,123]) have been done on the application of (tracking) MPC to chemical processes modeled by hyperbolic PDEs.

Specifically, MPC is a popular control method for handling constraints (both on manipulated inputs and state variables) within an optimal control setting. In the past ten years, significant work has been done on the application of MPC to distributed parameter systems. Contributions include analyzing the predictive control problem on the basis of the infinite-dimensional system using control Lyapunov functionals,[76] the use of finite difference method to derive approximate ODE models for MPC design,[42] the methodology of model predictive control design for highly dissipative PDEs,[36] and the application of MPC to a catalytic reverse flow reactor (RFR).[41] Furthermore, computationally efficient predictive control algorithms for nonlinear parabolic and hyperbolic PDEs with state and control constraints have been proposed in.[37–39]

EMPC has been extensively studied recently in the context of finite dimensional systems (e.g., Refs[24,34,65,67,68] for results and references in this area). Most of the research in the area of EMPC, however, has focused on lumped-parameter processes modeled by ODE systems. Compared with lumped-parameter systems, no work has been done on the problem of designing EMPC for distributed parameter systems modeled by PDEs for both hyperbolic and parabolic PDEs. Moreover, operation of transport-reaction processes typically requires that the state of the closed-loop system be maintained within certain bounds to achieve acceptable performance like requiring the temperature of a tubular reactor not to exceed a certain limit, and is also limited by the finite capacity of control actuators and constraints on reactant availability. Therefore, EMPC of distributed parameter systems modeled by PDEs is an important theoretical problem with practical importance.

1.4 Dissertation Objectives and Structure

Motivated by the above considerations, this dissertation focuses on the development of methods for integrating on-line preventive maintenance of actuators and sensors with EMPC system design and the application of EMPC to transport-reaction processes modeled as either parabolic PDEs or hyperbolic PDEs. Lyapunov-based economic model predictive control (LEMPC) methods that can maintain stability while also, dictating an economically optimal dynamic operating policy and dealing with preventive maintenance of actuators and sensors are proposed. A proactive fault-tolerant model predictive controller (MPC) designed via Lyapunov-based techniques for nonlinear systems capable of taking proactive measures to minimize the effect of a future control actuator fault is also formulated. EMPC formulations with various reduced-order models for transport-reaction processes modeled by parabolic PDEs are also proposed and are evaluated with respect to computational efficiency, model accuracy and process economic performance. The dissertation has the following structure:

Chapter 2 focuses on the development of a Lyapunov-based economic model predictive control (LEMPC) method that can maintain stability while also dictating an economically optimal dynamic operating policy with a changing number of manipulated inputs as a result of control actuators being taken off-line for preventive maintenance or placed back on-line after the maintenance work has been completed. To deal with the closed-loop stability challenge, a novel integration of EMPC with preventive maintenance is proposed. The stability for a LEMPC scheme capable of handling these objectives is formulated and proved. The proposed LEMPC is applied to a process network used for the alkylation of benzene to demonstrate that the LEMPC is able to maintain stability of the process, perform successful reconfiguration of the control system accounting for a variable number of manipulated inputs, and operate the process in an economically-optimal fashion.

Chapter 3 presents a control system scheme of handling scheduled preventive sensor maintenance via the EMPC system design. A RMHE scheme is developed that accommodates a varying number of sensors to continuously supply accurate state estimates to an EMPC system. In detail, the overall scheme integrates the real-time preventive sensor maintenance, process economics optimization and control system reconfiguration. The LEMPC combined with RMHE is proved to be stabilizing under certain observability and stabilizability assumptions. Then, a chemical process example utilizing the proposed RMHE-based LEMPC is presented for which the controller maintains the process stability, accomplishes control system reconfiguration under a changing number of on-line sensors, and achieves minimal economic performance degradation by adjusting the optimization problem as the number of on-line sensors changes.

Chapter 4 proposes a proactive fault-tolerant MPC designed via Lyapunov-based techniques for nonlinear systems capable of taking proactive measures to minimize the effect of a future known control actuator fault. This approach to proactive fault-tolerant control combines the unique stability and robustness properties of LMPC as well as explicitly accounting for future known control actuator faults in the formulation of the MPC. These theoretical results are applied to a chemical process example, and different case studies with various types of actuator faults were simulated to demonstrate that the proposed proactive fault-tolerant model predictive control method can achieve practical stability after a control actuator fault.

Chapter 5 focuses on the development of EMPC systems for transport-reaction processes that are described by nonlinear parabolic PDEs. Through the application of Galerkin's method, finite-dimensional ordinary differential equation models are first derived that capture the dominant dynamics of the parabolic PDEs. The reduced-order models are then used to formulate finite-dimensional EMPC systems of varying dimension depending on the type of state constraints imposed. The EMPC systems are applied to a non-isothermal

tubular reactor, described by two nonlinear parabolic PDEs, where a second-order chemical reaction takes place. A state constraint that bounds the reactor temperature as well as an input constraint that bounds the available reactant material over a fixed period of operation are considered in the formulations of the EMPC systems which use the average reaction rate along the length of the reactor as the economic cost function. Closed-loop simulations are conducted where a low-order EMPC system and a high-order EMPC system are separately applied to a high-order discretization of the reactor PDEs model, and they demonstrate that the EMPC systems operate the process in a time-varying fashion to improve the economic cost over steady-state operation and meet input and state constraints.

Chapter 6 focuses on the formulation and comparison of several EMPC systems with different reduced order models to a non-isothermal tubular reactor where a second-order chemical reaction takes place. First, an output feedback EMPC formulation is presented. Second, a reduced-order model (ROM) of the PDEs is constructed on the basis of historical data-based empirical eigenfunctions by applying Karhunen-Loève expansion to formulate a computationally efficient EMPC system. Several EMPC systems each using a different ROM (i.e., different number of modes and derived from either using analytical sinusoidal/cosinusoidal eigenfunctions or empirical eigenfunctions) are applied to the non-isothermal tubular reactor example. The model accuracy, computational time and closed-loop economic performance of the closed-loop tubular reactor under the different EMPC systems is compared and discussed.

Chapter 7 focuses on the development of an EMPC scheme with model reduction technology and a standard discretization method to deal with state estimation accuracy and computational efficiency. First, the APOD method is applied to systems of parabolic PDEs by considering process control system computational efficiency and some specific constraints imposed on the process (i.e., state and input constraints), and then a novel EMPC design integrating APOD method with a high-order finite-difference method is proposed

to improve the EMPC scheme's performance on dealing with hard state constraint over the traditional EMPC scheme with APOD method only. The proposed EMPC method is applied to a non-isothermal tubular reactor where a second-order chemical reaction takes place and the computational efficiency, state and input constraint satisfaction, and closed-loop economic performance are evaluated.

Chapter 8 focuses on the development of both state and output feedback EMPC systems that account for both manipulated input and state constraints for first-order hyperbolic PDEs. When measurements of the state variables are available only at a finite number of spatial positions, a pole placement-based state observer technique is adopted to get estimates of the full spatial state profile. The EMPC system is applied to a non-isothermal plug flow reactor whose first-principles model consists of two quasi-linear first-order hyperbolic PDEs. EMPC systems utilizing different numbers of output measurement points and different prediction horizons are applied to this plug flow reactor process. Various results of state estimation accuracy, process economic performance, and computational efficiency are presented and compared.

Chapter 9 focuses on the development of a CFD model of an industrial level reformer including both furnace and process sides. Firstly, the CAD geometry of the objective industrial level reformer is designed. Then, to develop the full-size CFD model of the reformer, a single reforming tube CFD model is developed to simulate the steam methane reforming reactions within porous media. Secondly, we construct a small-scale reformer model with all key characteristics of the full-size reformer and then develop its CFD model considering both the combustion in the furnace side and the reforming reactions in the process side as designed in the single reforming tube CFD model. Finally, the successful CFD modeling development method of the small-scale reformer model is applied to the full-size reformer. For the CFD simulation, ANSYS ICEM-CFD is adopted as the mesh generation platform, and ANSYS Fluent is used as the CFD simulation platform.

Finally, Chapter 10 summarizes the contributions of this dissertation.

Chapter 2

Smart Manufacturing: Handling Preventive Actuator Maintenance and Economics using Model Predictive Control

2.1 Introduction

This chapter addresses the task of accounting for scheduled actuator maintenance via the control system design. Specifically, the focus of this chapter is to develop a Lyapunov-based economic model predictive control (LEMPC) method that can maintain stability while also dictating an economically optimal dynamic operating policy with a changing number of manipulated inputs as a result of control actuators being taken off-line for preventive maintenance or placed back on-line after the maintenance work has been completed. To deal with the closed-loop stability challenge, a novel integration of EMPC with preventive maintenance is proposed. The stability for a LEMPC scheme capable of han-

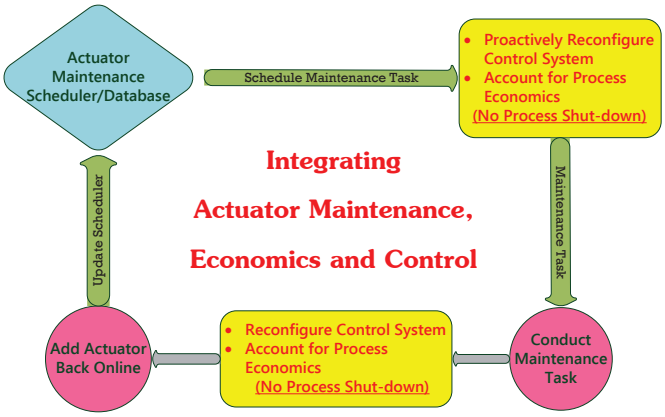

Figure 2.1: Integrated approach to preventive control actuator maintenance, process control, and real-time economic process performance optimization.

dling these objectives is formulated and proved. The proposed LEMPC is applied to a process network used for the alkylation of benzene to demonstrate that the LEMPC is able to maintain stability of the process, perform successful reconfiguration of the control system accounting for a variable number of manipulated inputs, and operate the process in an economically-optimal fashion.

2.2 Preliminaries

2.2.1 Notation

The following notation will be used in this work. The operator $|\cdot|$ denotes the Euclidean norm of a vector. A continuous function $\alpha : [0,a)$ is said to belong to class $\mathscr{K}$ if it is strictly increasing and is equal to zero when evaluated at zero (i.e., $\alpha(0) = 0$). A level set (level surface) of a scalar function $V : \mathbb{R}^n \to \mathbb{R}$ is denoted as $\Omega_r := \{x \in \mathbb{R}^n : V(x) \leq r\}$. The symbol $\setminus$ denotes the standard relative complement, that is, the relative complement of A with respect to B is denoted as $B \setminus A = \{x \in B : x \notin A\}$. The symbol diag$(v)$ denotes a

diagonal matrix with diagonal elements equal to the elements of the vector v.

2.2.2 Class of Nonlinear Process Systems

In the present work, the class of nonlinear process systems considered for the design of an economic model predictive control scheme for handling preventive maintenance of the j-th control actuator are of the form:

$$\dot{x}(t) = f(x(t), u(t), w(t)) \tag{2.1}$$

where $x \in \mathbb{R}^n$ is the state vector, $u \in \mathbb{R}^m$ is the input vector, and $w \in \mathbb{R}^l$ is the disturbance vector. The amount of available control energy is bounded in a convex set. A scheduler or decision-maker schedules a preventive maintenance task on the j-th actuator that effectively takes the j-th actuator off-line at t_r. In other words, the set of available control actions with all actuators on-line is given by

$$U_0 = \{u \in \mathbb{R}^m : |u_i| \leq u_i^{\max}, i = 1, \ldots, m\}$$

for $t \in [t_0, t_r)$. After the j-th actuator is taken off-line at t_r, the set becomes

$$U_j = \left\{u \in \mathbb{R}^m : |u_i| \leq u_i^{\max}, i = 1, \ldots, j-1, j+1, \ldots, m, u_j = 0\right\}$$

until the maintenance task is completed, and the j-th actuator is brought back on-line at t_r'. The vector function f is assumed to be a locally Lipschitz vector function of its arguments. The disturbance vector is considered to be bounded in a set, i.e.,:

$$W = \left\{w \in \mathbb{R}^l : |w| \leq \theta\right\}.$$

The state vector of the continuous-time system of Eq. 2.1 is assumed to be measured at sampling instances: $t_k = t_0 + k\Delta$, $k = 0, 1, \ldots$ where Δ is the sampling period.

With respect to the system of Eq. 2.1, a time-invariant cost function that describes the real-time process economics is assumed to be available of the form $l_e(x,u)$. The economically optimal steady-state for the system with respect to the economic cost for the system with all available actuators on-line is denoted as $i = 0$ and for the system with the j-th actuator off-line is denoted as $i = j$ and are defined as

$$x_{s,i}^* = \underset{x_s \in X_s}{\arg\max} \left\{ l_e(x_s, u_s) \,:\, f(x_s, u_s, 0) = 0, u_s \in U_i \right\}, \quad i = 0, j \tag{2.2}$$

where the set X_s is the set of admissible steady-states.

2.2.3 Stabilizability Assumption

Additional assumptions must be placed on the system of Eq. 2.1 to guarantee that the closed-loop system can be stabilizable with all available control actuators and with $m-1$ control actuators (i.e., the j-th actuator is off-line). Specifically, the existence of two explicit Lyapunov-based controllers $h_i(\bar{x}_i)$ for $i = 0, j$ that render the steady-state $x_{s,i}^*$ of the nominal system of Eq. 2.1 asymptotically stable under continuous implementation is assumed. The notation $\bar{x}_i$ is the deviation of the state from the corresponding steady-state (i.e., $\bar{x}_i = x - x_{s,i}^*$). Using converse theorems,[79,97] the existence of Lyapunov functions $V_i(\bar{x}_i)$ for $i = 0, j$ for the closed-loop system with all m actuators and with $m-1$ actuators, respectively, follows from the stabilizability assumption. The closed-loop Lyapunov functions under the Lyapunov-based controllers satisfy the following conditions:

$$\alpha_{1,i}(|\bar{x}_i|) \leq V_i(\bar{x}_i) \leq \alpha_{2,i}(|\bar{x}_i|), \tag{2.3a}$$

$$\frac{\partial V_i(\bar{x}_i)}{\partial x} f(\bar{x}_i + x^*_{s,i}, h_i(\bar{x}_i), w) \leq -\alpha_{3,i}(|\bar{x}_i|)\,, \tag{2.3b}$$

$$\left| \frac{\partial V(\bar{x}_i)}{\partial x} \right| \leq \alpha_{4,i}(|\bar{x}_i|)\,, \tag{2.3c}$$

$$h_i(\bar{x}_i) \in U_i,\ i = 0,\ j \tag{2.3d}$$

for $\bar{x}_i \in D_i$ where D_i is an open neighborhood of the origin for $i = 0,\ j$. This assumption is similar to assuming that the pair (A, B) is stabilizable for linear systems. The stability regions $\Omega_{\rho_i} \subseteq D_i$ for $i = 0,\ j$ can be estimated for the closed-loop system of Eq. 2.1 under the explicit stabilizing controllers $h_0(x - x^*_{s,0})$ and $h_j(x - x^*_{s,j})$ by taking these regions to be a level set of the Lyapunov function where the Lyapunov function is decreasing along the closed-loop state trajectory. Since Ω_{ρ_i} is taken to be a level set of V_i, it is a compact (closed and bounded) set. For the remainder of this work, a state x is said to be contained in the set Ω_{ρ_i} if the deviation state ($\bar{x}_i = x - x^*_{s,i}$) is contained in Ω_{ρ_i}. A variety of control laws have been developed using Lyapunov techniques for various classes of nonlinear systems (see Refs[29,82] and the references therein).

Additionally, certain conditions must be satisfied to ensure that it is possible to force the closed-loop state from any point in the stability region Ω_{ρ_0} to the stability region Ω_{ρ_j} in preparation for taking the j-th control actuator off-line for maintenance. These conditions must also ensure that it is possible to force the closed-loop state back to the stability region Ω_{ρ_0} from any point in Ω_{ρ_j} after the maintenance task is completed and the j-th actuator is ready to be placed back on-line. To establish these conditions, the closed-loop properties of the Lyapunov-based controllers applied in a sample-and-hold fashion to the system of Eq. 2.1 are presented below.

First, some basic properties of the closed-loop system are needed. By the Lipschitz property of the vector field f, the continuous differentiability property of the Lyapunov function, and the compactness of Ω_{ρ_i}, there exists positive constants $L_{x,i}$, $L_{w,i}$, $L'_{x,i}$, and $L'_{w,i}$

for $i = 0$, j such that the following inequalities hold:

$$\left|f(x,u,w) - f(x',u,0)\right| \leq L_{x,i}\left|x - x'\right| + L_{w,i}\left|w\right| \tag{2.4}$$

$$\left|\frac{\partial V_i}{\partial x} f(x,u,w) - \frac{\partial V_i}{\partial x} f(x',u,0)\right| \leq L'_{x,i}\left|x - x'\right| + L'_{w,i}\left|w\right| \tag{2.5}$$

for all $(x - x^*_{s,i})$, $(x' - x^*_{s,i}) \in \Omega_{\rho_i}$, $u \in U_i$, $w \in W$ for $i = 0$, j. By continuity, the bound on the inputs and the aforementioned Lipschitz properties, a positive constant M_i can be found to bound the vector field:

$$\left|f(x,u,w)\right| \leq M_i \tag{2.6}$$

that holds for all $(x - x^*_{s,i}) \in \Omega_{\rho_i}$, $u \in U_i$, $w \in W$ for $i = 0$, j.

The main stability result of applying a Lyapunov-based controller in a sample-and-hold fashion in the presence of disturbances is provided below without proof for the sake of brevity. The interested reader is referred to Ref[105] for a complete discussion and proof of the main result on the Lyapunov-based controller. The following proposition establishes practical stability of the Lyapunov-based controller when applied to the system of Eq. 2.1.

Proposition 2.1 (c.f. Ref[105]) *Consider the closed-loop system of Eq. 2.1 under the controller $h(\bar{x}_i)$ that satisfies the conditions of Eq. 2.3 when the controller $h(\bar{x}_i)$ is implemented in a sample-and-hold fashion with sampling period $\Delta > 0$. Let $\Delta > 0$, $\rho_i > \rho_{s,i} > 0$, $\rho_{\min,i} \leq \rho_i$ and $\varepsilon_{s,i} > 0$ satisfy*

$$-\alpha_{3,i}(\alpha_{2,i}^{-1}(\rho_{s,i})) + L'_{x,i} M_i \Delta + L'_{w,i}\theta \leq -\varepsilon_{s,i}/\Delta \tag{2.7}$$

for each $i = 0$, j. Then, the Lyapunov function $V_i(x - x^*_{s,i})$ will decrease over the sampling period Δ:

$$V(x(t_{k+1}) - x^*_{s,i}) \leq V(x(t_k) - x^*_{s,i}) - \varepsilon_{s,i} \tag{2.8}$$

for any $(x(t_k) - x^*_{s,i}) \in \Omega_{\rho_i} \setminus \Omega_{\rho_{s,i}}$. *Furthermore, if* $(x(t_0) - x^*_{s,i}) \in \Omega_{\rho_i}$, *then* $(x(t) - x^*_{s,i})$ *is ultimately bounded in* $\Omega_{\rho_{\min,i}}$ *where*

$$\rho_{\min,i} = \max_{\tau \in [t, t+\Delta)} \left\{ V_i(x(\tau) - x^*_{s,i}) \, : \, V_i(x(t) - x^*_{s,i}) \leq \rho_{s,i} \right\} \tag{2.9}$$

Under the Lyapunov-based controller, the closed-loop system will converge to a neighborhood of the steady-state for a sufficiently small sampling period and bound on the disturbance. Applying Eq. 2.8 recursively, one can show that the state converges to $\Omega_{\rho_{s,i}}$ in a finite number of sampling periods. Once the state converges to $\Omega_{\rho_{s,i}}$, it is maintained in $\Omega_{\rho_{\min,i}}$ as a result of the definition of $\Omega_{\rho_{\min,i}}$ (Eq. 2.9). This implies that one can find a sufficiently long (finite-time) horizon such that the closed-loop state will converge to $\Omega_{\rho_{\min,i}}$ by the end of the horizon for any initial state $(x(t_0) - x^*_{s,i}) \in \Omega_{\rho_i}$. With the stability properties of the Lyapunov-based controllers, conditions are imposed on $x^*_{s,j}$ which will be used in the design of an economic model predictive controller for handling actuator maintenance and is stated in the following assumption. Assumption 2.1 can be satisfied by imposing appropriate constraints in the steady-state optimization problem constructed to solve for $x^*_{s,j}$.

Assumption 2.1 *The steady-state* $x^*_{s,j}$ *is chosen so there exists a region* $\Omega_{\rho^*_j}$ *with* $\rho^*_j \geq \rho_{\min,j}$ *such that* $\Omega_{\rho^*_j} \subseteq \Omega_{\rho_0}$. *Furthermore, the stability region* Ω_{ρ_j} *contains a region* $\Omega_{\rho^*_0}$ *where* $\rho^*_0 \geq \rho_{\min,0}$.

Applying the results of Proposition 2.1 and the conditions of Assumption 2.1, a sufficiently long operating horizon denoted as $t_{N^*_0}$ can be found such that the closed-loop state can be forced to Ω_{ρ_j} starting from any initial state in Ω_{ρ_0} because the closed-loop state can be forced into $\Omega_{\rho^*_0} \subseteq \Omega_{\rho_j}$ in a finite number of sampling periods. Similar arguments can be applied to define a sufficiently long horizon $t_{N^*_j}$, such that any initial state in the stability region Ω_{ρ_j} can be forced into the stability region Ω_{ρ_0} by the end of the horizon. Thus, an

operating horizon t_{N^*} defined as

$$N^* = \max\left\{N_0^*, N_j^*\right\} \tag{2.10}$$

can be found which is a horizon that guarantees that the closed-loop state under the Lyapunov-based controller $h_0(x - x_{s,0}^*)$ implemented in a sample-and-hold fashion satisfies $(x(t_{N^*}) - x_{s,j}^*) \in \Omega_{\rho_j}$ for any state starting $(x(t_0) - x_{s,0}^*) \in \Omega_{\rho_0}$, and for all initial states $(x(t_0) - x_{s,j}^*) \in \Omega_{\rho_j}$, the closed-loop state under the Lyapunov-based controller $h_j(x - x_{s,j}^*)$ implemented in a sample-and-hold fashion satisfies $(x(t_{N^*}) - x_{s,j}^*) \in \Omega_{\rho_0}$.

Remark 2.1 *The main idea of accounting for control actuator maintenance in the control system is to maintain operation of the process while an actuator is taken off-line to be repaired or replaced. To accomplish this, the control system must be able to first force the process into a region where the* $m-1$ *remaining actuators can maintain stability of the system and is robust to the influence of disturbances and uncertainty. The next priority would be to operate the process in an economically optimal way with the* $m-1$ *available actuators. Assumption 2.1, while it may restrict the feasible set of the admissible steady-states for computing the economically optimal steady-state with* $m-1$ *actuators, reflects this hierarchical level of objectives of the control system. Instead of imposing Assumption 2.1, one could assume the existence of an input trajectory that can force the closed-loop state from the stability region* Ω_{ρ_0} *to the stability region* Ω_{ρ_j} *and then, force the state back to* Ω_{ρ_0} *after the maintenance is completed. However, this assumption is difficult, in general, to verify.*

2.2.4 Lyapunov-based Economic Model Predictive Control

Utilizing the properties presented above, a Lyapunov-based EMPC (LEMPC) inspired by the results in Ref[65] will be used to design an EMPC scheme that explicitly accounts for control actuator maintenance. A brief review of the formulation of LEMPC is provided below. LEMPC is characterized by the following optimization problem:

$$\max_{u\in S(\Delta)} \quad \int_{t_k}^{t_{k+N}} l_e(\tilde{x}(\tau),u(\tau))\,d\tau \tag{2.11a}$$

$$\text{s.t.} \quad \dot{\tilde{x}}(t) = f(\tilde{x}(t),u(t),0) \tag{2.11b}$$

$$\tilde{x}(t_k) = x(t_k) \tag{2.11c}$$

$$u(t) \in U, \forall t \in [t_k,t_{k+N}) \tag{2.11d}$$

$$V(\tilde{x}(t)) \leq \tilde{\rho}, \forall t \in [t_k,t_{k+N}) \quad \text{if } V(x(t_k)) < \tilde{\rho} \tag{2.11e}$$

$$\frac{\partial V}{\partial x} f(x(t_k),u(t_k),0) \leq \frac{\partial V}{\partial x} f(x(t_k),h(x(t_k)),0), \quad \text{if } V(x(t_k)) \geq \tilde{\rho} \tag{2.11f}$$

where the decision variable of the optimization problem is the piecewise constant input trajectory over the finite-time prediction horizon t_k to t_{k+N}. Within this context, the economic cost function, which describes the process economics, is optimized over the finite prediction horizon, $S(\Delta)$ denotes the family of piecewise constant functions and $\tilde{x}$ denotes the predicted state trajectory of the system with the input trajectory computed by the LEMPC.

To predict the state trajectory under the computed input trajectory, the nominal dynamic model of the process system is used (Eq. 2.11b) with an initial condition provided by a measurement of the current state (Eq. 2.11c). The constraint of Eq. 2.11d is the bound on the available control actuation. The remaining two Lyapunov-based constraints are used to

ensure that the closed-loop state is always maintained in the stability region Ω_ρ and defines a two mode control strategy. Mode 1 operation of the LEMPC is active (i.e., the constraint of Eq. 2.11e is imposed on the optimization problem) when the current state is within $\Omega_{\tilde{\rho}}$ where $\Omega_{\tilde{\rho}}$ is a subset of the stability region Ω_ρ. The size of $\Omega_{\tilde{\rho}}$ is a function of the stability properties of the system. Under mode 1 operation of the LEMPC, the LEMPC allows for dynamic operation to optimize the economic cost function while maintaining the predicted evolution in $\Omega_{\tilde{\rho}}$. If the current state $x(t_k) \in \Omega_\rho \setminus \Omega_{\tilde{\rho}}$, mode 2 is active (i.e., the constraint of Eq. 2.11f is imposed). Under mode 2 operation of the LEMPC, the LEMPC optimizes the input trajectory with respect to the economic cost while enforcing that the computed control action decreases the Lyapunov function by at least the rate given by the Lyapunov-based controller for the first sampling period of the prediction horizon. With the two Lyapunov-based constraints, stability under LEMPC is defined as maintaining the closed-loop state in the stability region Ω_ρ (i.e., the set Ω_ρ is an invariant set for the closed-loop system under LEMPC) and is guaranteed for any initial state $x(t_0) \in \Omega_\rho$ (see Ref[65] for details on this point).

Remark 2.2 *Without loss of generality, the origin of the unforced system (i.e., $f(0,0,0) = 0$) is assumed to be the equilibrium of the model of Eq. 2.11b and thus, the Lyapunov-based constraints are formulated with a Lyapunov function with respect to the origin. The origin is typically also taken to be the economically optimal steady-state. Specifically, in conventional MPC schemes and in EMPC formulated with a terminal constraint, the target state or set-point that is used in these MPC schemes is usually the economically optimal steady-state. In LEMPC, the Lyapunov-based constraints of Eqs. 11e and 11f do not necessarily need to be formulated with the economically optimal steady-state since the LEMPC may enforce a dynamic operating policy that is better than operating at the economically optimal steady-state. Therefore, the Lyapunov-based constraints could be formulated with a Lya-*

punov function for some other steady-state. This steady-state can be chosen, for instance, as a steady-state that yields a large estimate of the stability region. This steady-state can be chosen, for instance, as the steady-state that yields a large estimate of the stability region or a steady-state whose corresponding stability region is a region in state-space where process constraints (e.g., input and state constraints) are satisfied. Throughout the theoretical developments of an LEMPC scheme for handling control actuator maintenance, the economically optimal steady-states (i.e., $x^*_{s,0}$ when all m actuators are available and $x^*_{s,j}$ when $m-1$ actuators are available) will be used for the sake of consistency between LEMPC and EMPC formulated with a terminal constraint where the terminal constraint is typically taken to be the economically optimal steady-state.[5]

2.3 Proposed Lyapunov-based Economic Model Predictive Control Scheme for Handling Actuator Maintenance

In this section, the design of the LEMPC for explicitly handling control actuator maintenance is presented. First, the implementation strategy and formulation of the proposed LEMPC is provided. Subsequently, the main theoretical contribution of this work is given.

2.3.1 Implementation and Formulation

The implementation strategy is similar to the implementation strategy of LEMPC[65] that does not handle actuator maintenance. The main difference in the implementation strategy occurs during the period of time where the LEMPC proactively transitions from the control configuration with all available m actuators to the control configuration with $m-1$ actuators before the j-th actuator is taken off-line and vice versa when the actuator is brought back on-line after the maintenance task is completed. Much like Ref,[65] subsets of the sta-

bility region whereby dynamic operation is allowed are defined to make the sets Ω_{ρ_0} and Ω_{ρ_j} invariant in the presence of disturbances and uncertainties. The two sets are denoted $\Omega_{\tilde{\rho}_0} \subset \Omega_{\rho_0}$ and $\Omega_{\tilde{\rho}_j} \subset \Omega_{\rho_j}$ and are explicitly characterized in the "Closed-loop Stability Analysis" subsection below. The main advantage of using EMPC (LEMPC) over other stabilizing controllers is to take advantage of the unique ability of EMPC to optimize dynamic operation (inherently transient) with respect to the process economics during the transition to the new control configuration.

The actuator is to be taken off-line at t_r which has been scheduled by a maintenance scheduler. The actuator will be put back on-line at t_r' after the maintenance task has been completed and the actuator is ready to be put back on-line. Prior to t_r and t_r', it is desirable from a stability point-of-view to transition to the next control configuration (i.e., m available actuators to $m-1$ actuators and vice versa). To do this, the stability region of the next control configuration is used in the formulation of the LEMPC. More specifically, the state must converge to the set Ω_{ρ_j} by t_r and be maintained in Ω_{ρ_j} for $t \in [t_r, t_r')$. Similarly, the state must converge to the set Ω_{ρ_0} by t_r'.

To accomplish the above control objectives, the proposed LEMPC scheme for handling control actuator maintenance (i.e., taking the j-th control actuator off-line at t_r) is as follows

$$\max_{u\in S(\Delta)} \quad \int_{t_k}^{t_{k+N}} l_e(\tilde{x}(\tau),u(\tau))\,d\tau \tag{2.12a}$$

$$\text{s.t.} \quad \dot{\tilde{x}}(t) = f(\tilde{x}(t),u(t),0),\ \tilde{x}(t_k) = x(t_k) \tag{2.12b}$$

$$u(t) \in U_0, \forall\, t \in [t_k, t_r) \tag{2.12c}$$

$$u(t) \in U_j, \forall\, t \in [t_r, t_{k+N}) \tag{2.12d}$$

$$V_0(\tilde{x}(t) - x^*_{s,0}) \leq \tilde{\rho}_0, \forall\, t \in [t_k, t_{k+N})$$
$$\text{if } V_0(x(t_k) - x^*_{s,0}) < \tilde{\rho}_0 \text{ and } t_r \notin [t_k, t_{k+N}) \tag{2.12e}$$

$$\frac{\partial V_0}{\partial x} f(x(t_k),u(t_k),0) \leq \frac{\partial V_0}{\partial x} f(x(t_k), h_0(x(t_k) - x^*_{s,0}),0),$$
$$\text{if } \left(V_0(x(t_k) - x^*_{s,0}) \geq \tilde{\rho}_0 \text{ and } t_r \notin [t_k, t_{k+N})\right)$$
$$\text{or } \left(V_j(x(t_k) - x^*_{s,j}) \geq \rho_j \text{ and } t_r \in [t_k, t_{k+N})\right) \tag{2.12f}$$

where the notation is similar to that of the LEMPC of Eq. 2.11. When $t_r \notin [t_k, t_{k+N})$, the Lyapunov-based constraints that define mode 1 and mode 2 operation of the LEMPC are identical to the constraints used in the LEMPC of Eq. 2.11. If the time the actuator is taken off-line is within the prediction horizon (i.e., $t_r \in [t_k, t_{k+N})$) and the current state is outside Ω_{ρ_j}, the mode 2 constraint is active to force the closed-loop state closer to $\Omega_{\rho^*_0} \subseteq \Omega_{\rho_j}$. Once the state converges to the region Ω_{ρ_j}, the Lyapunov-based constraints of the LEMPC

switches to

$$\max_{u\in S(\Delta)} \quad \int_{t_k}^{t_{k+N}} l_e(\tilde{x}(\tau),u(\tau))\,d\tau \tag{2.13a}$$

$$\text{s.t.} \quad \dot{\tilde{x}}(t) = f(\tilde{x}(t),u(t),0),\ \tilde{x}(t_k) = x(t_k) \tag{2.13b}$$

$$u(t) \in U_0, \forall t \in [t_k,t_r) \tag{2.13c}$$

$$u(t) \in U_j, \forall t \in [t_r,t_{k+N}) \tag{2.13d}$$

$$V_j(\tilde{x}(t)-x^*_{s,j}) \leq \tilde{\rho}_j, \forall t \in [t_k,t_{k+N}) \quad \text{if } V_j(x(t_k)-x^*_{s,j}) < \tilde{\rho}_j \tag{2.13e}$$

$$\frac{\partial V_j}{\partial x} f(x(t_k),u(t_k),0) \leq \frac{\partial V_j}{\partial x} f(x(t_k),h_j(x(t_k)-x^*_{s,j}),0), \quad \text{if } V_j(x(t_k)-x^*_{s,j}) \geq \tilde{\rho}_j \tag{2.13f}$$

based on the Lyapunov function and the Lyapunov-based controller with $m-1$ control actuators. However, the LEMPC can utilize all m actuators until t_r when the j-th actuator is taken off-line. In this fashion, the actuator maintenance is proactively accounted for via the control system. Owing to the fact that the control configuration is switching from m available actuators to $m-1$ available actuators, the LEMPC of Eq. 2.13 will be feasible if the closed-loop state converges to the region Ω_{ρ_j} before t_r because a solution with $u_j(t) = 0$ for $t \in [t_k,t_r)$ is a feasible solution to the optimization problem (this point will be discussed further in the "Closed-loop Stability Analysis" subsection below).

Once the actuator is ready to be brought back on-line, the state must converge to the set Ω_{ρ_0} by t_r'. The LEMPC for this case is similar to Eq. 2.12 until the closed-loop state converges to Ω_{ρ_0} when the LEMPC switches to a formulation similar to Eq. 2.13. The formulations for each of these phases of operation are the same as Eqs. 2.12-2.13 except for the following notation modifications: $0 \to j$, $j \to 0$, and $t_r \to t_r'$. Another difference in the implementation strategy when switching from $m-1$ available actuators to m available

actuators is that after the closed-loop state has converged to Ω_{ρ_0} no guarantee can be made that $m-1$ actuators can maintain the closed-loop state in Ω_{ρ_0}. However, this presents little practical complications as the time t_r' most likely can be treated as a soft constraint. In other words, t_r' can be treated as the time the closed-loop state converges to Ω_{ρ_0} because the transition from $m-1$ actuators to m actuators will likely only be activated after the maintenance task has been successfully completed. If the time t_r' is a hard constraint, one could force the LEMPC to operate in mode 2 (based on the Lyapunov function and Lyapunov-based controller for $m-1$ actuators) to enforce the system to converge to $\Omega_{\rho_j^*} \subseteq \Omega_{\rho_0}$ and maintain it there until t_r' when the actuator is ready to be brought back on-line.

The proposed LEMPC scheme for handling scheduled control actuator maintenance (consisting of switching constraints) is implemented in a receding horizon fashion. The optimal solution, obtained at each sampling period, to the optimization problem (either Eq. 2.12 or Eq. 2.13 depending on the phase of operation) is denoted as $u^*(t)$ which is defined for $t \in [t_k, t_{k+N})$. The LEMPC sends the control action computed for the first sampling period to the actuators to be implemented in a sample-and-hold fashion which is denoted as $u^*(t_k)$.

A summary of the implementation strategy for the transition from m to $m-1$ actuators is provided below:

1. At the current sampling instance t_k, the LEMPC receives a state measurement $x(t_k)$.

2. If $t_{k+N} < t_r$, go to Step 2.1. If $t_r \in [t_k, t_{k+N})$ and $(x(t_k) - x_{s,j}^*) \notin \Omega_{\rho_j}$, go to Step 2.2. Else, go to Step 2.3.

   2.1 If $(x(t_k) - x_{s,0}^*) \in \Omega_{\tilde{\rho}_0}$, the LEMPC (Eq. 2.12) operates in mode 1. Else, the LEMPC (Eq. 2.12) operates in mode 2. Go to Step 3.

   2.2 The LEMPC (Eq. 2.12) operates in mode 2 to enforce convergence to Ω_{ρ_j}. Go to Step 3.

2.3 If $(x(t_k) - x^*_{s,j}) \in \Omega_{\tilde{\rho}_j}$, the LEMPC (Eq. 2.13) operates in mode 1. Else, the LEMPC (Eq. 2.13) operates in mode 2. Go to Step 3.

3. The LEMPC computes its optimal input trajectory over the horizon $t \in [t_k, t_{k+N})$.

4. The LEMPC sends the optimal control action, $u^*(t_k)$ over the first sampling period ($t \in [t_k, t_{k+1})$) to the control actuators to be implemented in a sample-and-hold fashion.

5. Go to Step 1 ($k \leftarrow k+1$).

The implementation strategy for the transition from $m-1$ to m actuators is the same with the following notation changes: $0 \rightarrow j$, $j \rightarrow 0$, and $t_r \rightarrow t'_r$ and the control configuration switches from $m-1$ to m available actuators once the closed-loop state converges to Ω_{ρ_0}.

Remark 2.3 *An issue that is not within the scope of the present work is developing an EMPC scheme that accounts for an explicitly time-varying economic cost. With traditional real-time optimization (RTO) and MPC frameworks, the economically optimal steady-state is re-computed as the process economics are updated in such a case . This will lead to different regions of operation and updated stability regions in the case of LEMPC. The interested reader is referred to Ref[45] for further details on constructing a larger estimate of the stability region and explicitly handling the time-dependent economic parameters in the cost function. For the case when the estimate of the stability region is large as is often times the case when the steady-state is open-loop asymptotically stable, it may be sufficient in terms of achievable closed-loop performance to use the stability region Ω_ρ corresponding to one particular steady-state in the formulation of the LEMPC when the economic cost parameters change with time.*

2.3.2 Closed-loop Stability Analysis

In this subsection, sufficient conditions are presented such that the closed-loop state remains bounded in Ω_{ρ_0} and Ω_{ρ_j} depending on the control configuration. Previously established results of Ref[105] are first presented for completeness of presentation. The interested reader is referred to these works for the details of these results.

Two propositions that have been previously established in Ref[105] are presented. The first proposition bounds the difference between the nominal closed-loop trajectory ($w(t) \equiv 0$) and the actual closed-loop trajectory over one sampling period; while, the second proposition bounds the difference between the Lyapunov function values of two states in Ω_{ρ_i} for $i = 1, j$.

Proposition 2.2 *(c.f. Ref[105]) Consider the systems*

$$\begin{aligned} \dot{\hat{x}}(t) &= f(\hat{x}(t), u(t), 0), \\ \dot{x}(t) &= f(x(t), u(t), w(t)) \end{aligned} \tag{2.14}$$

for any initial states $(\hat{x}(t_0) - x^*_{s,i}) = (x(t_0) - x^*_{s,i}) \in \Omega_{\rho_i}$ *and* $u(t) \in U_i$ *for* $i = 0, j$. *There exists two class* $\mathscr{K}$ *functions* $\gamma_{e,i}(\cdot)$ *such that*

$$|\hat{x}(t+\Delta) - x(t+\Delta)| \leq \gamma_{e,i}(\Delta), \tag{2.15}$$

for all $(\hat{x}(t+\Delta) - x^*_{s,i})$, $(x(t+\Delta) - x^*_{s,i}) \in \Omega_{\rho_i}$ *and all* $w(t) \in W$ *with*

$$\gamma_{e,i}(\Delta) = \frac{L_{w,i}\theta}{L_{x,i}} \left(e^{L_{x,i}\Delta} - 1 \right) \tag{2.16}$$

for $i = 0, j$.

Proposition 2.3 *(c.f. Ref[105]) Consider the Lyapunov function* $V_i(\cdot)$ *of the system of Eq. 2.1*

(with $u \in U_i$). There exists quadratic functions $\alpha_{V,i}(\cdot)$ such that

$$V_i(x - x^*_{s,i}) \leq V_i(\hat{x} - x^*_{s,i}) + \alpha_{V,i}(|x - \hat{x}|) \tag{2.17}$$

for all $(x - x^*_{s,i})$, $(\hat{x} - x^*_{s,i}) \in \Omega_{\rho_i}$ with

$$\alpha_{V,i}(s) = \alpha_{4,i}(\alpha^{-1}_{1,i}(\rho))s + M_{V,i}s^2 \tag{2.18}$$

where $M_{V,i}$ is a positive constant for $i = 0,\ j$.

The following theorem provides sufficient conditions for closed-loop stability in the sense of boundedness of the closed-loop state in a compact set.

Theorem 2.1 *Consider the system of Eq. 2.1 in closed-loop under the proposed LEMPC design (Eqs. 2.12-2.13) based on a controllers $h_0(x - x^*_{s,0})$ and $h_j(x - x^*_{s,j})$ that satisfies the conditions of Eq. 2.3 for $i = 0,\ j$. Let the conditions of Assumption 2.1 hold and let $\varepsilon_{w,i} > 0$, $\Delta > 0$, $\rho_i > \tilde{\rho}_i \geq \rho_{s,i} > 0$ satisfy*

$$\tilde{\rho}_i \leq \rho_i - \alpha_{V,i}(\gamma_{e,i}(\Delta)) \tag{2.19}$$

and

$$-\alpha_{3,i}(\alpha^{-1}_{2,i}(\rho_{s,i})) + L'_{x,i}M_i\Delta + L'_{w,i}\theta \leq -\varepsilon_{w,i}/\Delta \tag{2.20}$$

for $i = 0,\ j$ where $M_{V,i}$ is positive constant. If $(x(t_0) - x^*_{s,0}) \in \Omega_{\rho_0}$, $t_N \leq t_r$, $t_r + t_N < t'_r$, and $N \geq N^* > 0$, then, the closed-loop state is bounded in $\Omega_{\rho_0} \cup \Omega_{\rho_j}$ for $t \geq t_0$.

Proof 2.1 *The proof consists of two main parts. First, the feasibility of the LEMPC is demonstrated for all times. Second, the main stability result (i.e., boundedness of the closed-loop state in $\Omega_{\rho_0} \cup \Omega_{\rho_j}$) is proven which is broken up into multiple subparts. The*

proof proceeds on the basis of the transition from m to $m-1$ actuators (i.e., the j-th actuator is taken off-line at t_r). Similar arguments can be made to prove similar results for the transition from $m-1$ to m actuators.

Part 1. When $t_r \notin [t_k, t_{k+N})$, the Lyapunov-based constraints of the LEMPC follow the formulation for the first phase of operation (Eq. 2.12). Under this phase, feasibility for any initial state $(x(t_k) - x^*_{s,0}) \in \Omega_{\rho_0}$ is guaranteed because the input trajectory obtained from the Lyapunov-based controller ($u(t_i) = h_0(\tilde{x}(t_i) - x^*_{s,0})$ for $i = k, k+1, \ldots, k+N$) is a feasible solution to the optimization problem for both mode 1 or mode 2 operation of the LEMPC as it satisfies the input and Lyapunov-based constraints. When $t_r \in [t_k, t_{k+N})$ and $(x(t_k) - x^*_{s,j}) \notin \Omega_{\rho_j}$, the LEMPC with the constraints of Eq. 2.12 operates in mode 2. Again, the input trajectory obtained from the Lyapunov-based controller ($u(t_i) = h_0(\tilde{x}(t_i) - x^*_{s,0})$ for $i = k, k+1, \ldots, k+N$) is a feasible solution to the optimization problem as it satisfies the constraints. Lastly, if the state converges to Ω_{ρ_j} by t_r, then feasibility of the optimization problem (Eq. 2.13) is guaranteed because the input trajectory obtained from the Lyapunov-based controller for the control configuration with the $m-1$ actuators ($u(t_i) = h_j(\tilde{x}(t_i) - x^*_{s,j})$ for $i = k, k+1, \ldots, k+N$) is a feasible solution. Feasibility of the proposed LEMPC scheme for handling scheduled actuator maintenance hinges on boundedness inside Ω_{ρ_0} before the j-th actuator is taken off-line and convergence of the closed-loop state to Ω_{ρ_j} by at least the time t_r which is proven below.

The basic idea of feasibility of the proposed LEMPC scheme is displayed in Fig. 2.2. Starting from x_1, one feasible input trajectory that will force the closed-loop state trajectory by t_r is the input trajectory obtained by the Lyapunov-based controller. The closed-loop state under the Lyapunov-based control input trajectory is the dashed gray line in Fig. 2.2. However, the LEMPC forces the state to follow a trajectory (solid gray line) different because it accounts for both the process economics and the need to force the closed-loop state to Ω_{ρ_j}. A similar situation is observed in the illustration for the case when the control

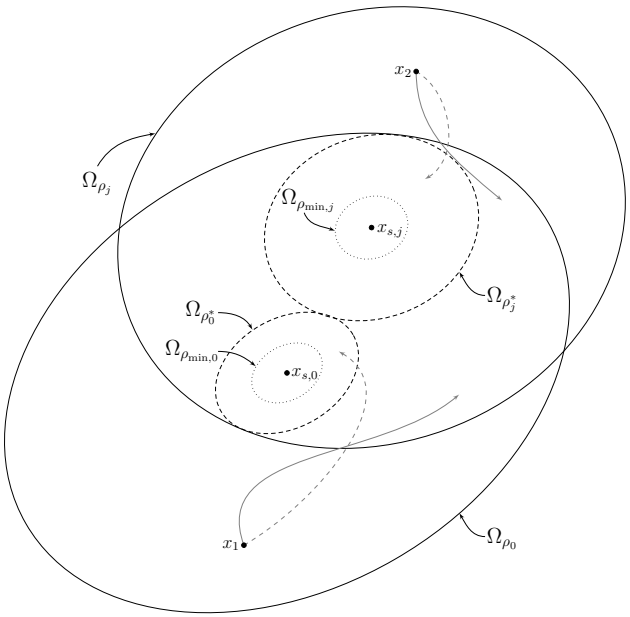

Figure 2.2: Illustration of the feasibility of the proposed LEMPC scheme for handling scheduled actuator maintenance.

configurations changes from $m-1$ to m actuators (starting from x_2 in Fig. 2.2).

Part 2.1. The proof proceeds by exploring the stability properties of mode 1 operation of the LEMPC (Eq. 2.12) which occurs when $t_r \notin [t_k, t_{k+N})$ and $(x(t_k) - x^*_{s,0}) \in \Omega_{\tilde{\rho}_0}$. If $(x(t_k) - x^*_{s,0}) \in \Omega_{\tilde{\rho}_0}$, then the predicted state at the next sampling period $(\tilde{x}(t_{k+1}) - x^*_{s,0}) \in \Omega_{\tilde{\rho}_0}$ as a consequence of the constraint of Eq. 2.12e. By Propositions 2.2-2.3, the following bound on the Lyapunov function can be written:

$$V_0(x(t_{k+1}) - x^*_{s,0}) \leq V_0(\tilde{x}(t_{k+1}) - x^*_{s,0}) + \alpha_{V,0}(\gamma_{E,0}(\Delta)) \tag{2.21}$$

Since $V(\tilde{x}(t_{k+1}) - x^*_{s,0}) \leq \tilde{\rho}_0$ and if $\tilde{\rho}_0$ is chosen sufficiently small such that the condition of Eq. 2.19 is satisfied for $i = 0$, then $V_0(x(t_{k+1}) - x^*_{s,0}) \leq \rho_0$ or $(x(t_{k+1}) - x_{s,0}) \in \Omega_{\rho_0}$.

Part 2.2. If $(x(t_k) - x_{s,0}) \in \Omega_{\rho_0} \setminus \Omega_{\tilde{\rho}_0}$ or $t_r \in [t_k, t_{k+N})$ and $(x(t_k) - x_{s,j}) \in \Omega_{\rho_j}$, the

LEMPC operates in mode 2 (Eq. 2.12) and computes a control action that satisfies:

$$\frac{\partial V_0}{\partial x} f(x(t_k), u^*(t_k), 0) \leq \frac{\partial V_0}{\partial x} f(x(t_k), h_0(x(t_k) - x^*_{s,0}), 0) \tag{2.22}$$

The time derivative of the Lyapunov function along the state trajectory for $\tau \in [t_k, t_{k+1})$ *is*

$$\dot{V}_0(x(\tau) - x^*_{s,0}) = \frac{\partial V_0}{\partial x} f(x(\tau), u^*(t_k), w(\tau)) \tag{2.23}$$

Adding and subtracting $\dot{V}_0(x(t_k) - x^*_{s,0})$ *to and from the derivative of the Lyapunov function (Eq. 2.23) and accounting for Eq. 2.3b, the time derivative of the Lyapunov function can be upper bounded over the sampling period:*

$$\begin{aligned} \dot{V}_0(x(\tau) - x^*_{s,0}) \leq & -\alpha_{3,0}(|x(t_k) - x^*_{s,0}|) + \frac{\partial V_0}{\partial x} f(x(\tau), u^*(t_k), w(\tau)) \\ & - \frac{\partial V_0}{\partial x} f(x(t_k), u^*(t_k), 0) \end{aligned} \tag{2.24}$$

for $\tau \in [t_k, t_{k+1})$. *Utilizing the Lipschitz property of Eq. 2.5 and the bound on the disturbance, the derivative of the Lyapunov function becomes:*

$$\dot{V}_0(x(\tau) - x^*_{s,0}) \leq -\alpha_{3,0}(|x(t_k) - x^*_{s,0}|) + L'_{x,0} |x(\tau) - x(t_k)| + L'_{w,0} \theta \tag{2.25}$$

Taking into account $|f(x,u,w)| \leq M_0$ *and continuity of* $x(t)$, $|x(\tau) - x(t_k)|$ *can be bounded for* $\tau \in [t_k, t_{k+1})$ *by*

$$|x(\tau) - x(t_k)| \leq M_0 \Delta \tag{2.26}$$

Since $(x(t_k) - x^*_{s,0}) \in \Omega_{\rho_0} \setminus \Omega_{\tilde{\rho}_0}$ *and if* $\tilde{\rho}_0 \geq \rho_{s,0}$, *the following bound on the deviation of the*

actual state and the steady-state can be derived from Eq. 2.3a:

$$|x(t_k) - x^*_{s,0}| \geq \alpha^{-1}_{2,0}(\rho_{s,0}) \tag{2.27}$$

Combining Eqs 2.26-2.27 with Eq. 2.25, the result is

$$\dot{V}_0(x(\tau) - x^*_{s,0}) \leq -\alpha_{3,0}(\alpha^{-1}_{2,0}(\rho_{s,0})) + L'_{x,0}M_0\Delta + L'_{w,0}\theta \tag{2.28}$$

for $\tau \in [t_k, t_{k+1})$. If the condition of Eq. 2.20 holds for $i = 0$, then the Lyapunov function is decreasing along the state trajectory over the sampling period:

$$\dot{V}_0(x(\tau) - x^*_{s,0}) \leq -\varepsilon_{w,0}/\Delta, \quad \forall\, \tau \in [t_k, t_{k+1}) \tag{2.29}$$

Integrating the above bound, it is shown that

$$V_0(x(t_{k+1}) - x^*_{s,0}) \leq V_0(x(t_k) - x^*_{s,0}) - \varepsilon_{w,0} \tag{2.30}$$

for all $(x(t_k) - x^*_{s,0}) \in \Omega_{\rho_0} \setminus \Omega_{\tilde{\rho}_0}$. Using the result of Eq. 2.30 recursively, the state converges to $\Omega_{\tilde{\rho}_0}$ without leaving Ω_{ρ_0} in a finite number of sampling periods.

Part 2.3. If $t_r \in [t_k, t_{k+N})$ and $(x(t_k) - x_{s,j}) \notin \Omega_{\rho_j}$, the LEMPC operates in mode 2 for any initial state $(x(t_k) - x^*_{s,0}) \notin \Omega_{\rho_j}$. Applying the result of Eq. 2.30 recursively, if the prediction horizon is chosen such that $N \geq N^*$, and if $t_N \leq t_r$ (i.e., $t_N = t_0 + N\Delta$), then the state will converge to the set Ω_{ρ_j} by at least t_r. This statement holds because recursively enforcing the constraint of Eq. 2.12f on the computed control action will lead to successive decrease in the Lyapunov function value over each sampling period (Eq. 2.30) until the state converges to $\Omega_{\rho_{\min,0}} \subseteq \Omega_{\rho_j}$ (if the conditions of Assumption 2.1 hold).

Part 2.4 Once the state converges to the Ω_{ρ_j}, the Lyapunov-based constraints switch to

the form of Eq. 2.13. Applying similar steps as Part 2.1 and Part 2.2, one can show that the closed-loop is maintained in Ω_{ρ_j} if the conditions of Eqs. 2.19-2.20 hold for $i = j$. Also, the arguments can be repeated for the case when the control configuration switches from $m-1$ to m actuators. Therefore, the closed-loop state is maintained in $\Omega_{\rho_0} \cup \Omega_{\rho_j}$ over the length of operation.

Remark 2.4 *The closed-loop stability properties presented here depend on a sufficiently long prediction horizon to ensure that it is feasible to force the closed-loop state to the stability region of the next control configuration by the time the control configuration changes (i.e., the number of available actuators changes). This may lead to a computationally challenging problem to be solved on-line (i.e., possibly non-convex, nonlinear optimization problem to be solved over a long horizon). To alleviate the computational burden, one could impose additional constraints on the computation of the optimal steady-state $x^*_{s,j}$ such that it is chosen to be close to $x^*_{s,0}$ so that large overlap exists between the two stability regions. If this is not desirable to impose such additional constraints in the computation of $x^*_{s,j}$ from a closed-loop performance perspective, one could employ, for instance, a two-layer LEMPC architecture like the one presented in Ref[46] to ease the computational burden.*

Remark 2.5 *The closed-loop results can be extended to the case with multiple actuators taken off-line by making similar assumptions about the control configuration resulting after multiple actuators are taken off-line.*

Remark 2.6 *If it is desirable to enforce convergence to the optimal steady-state, one can impose the Lyapunov-based constraints of either Eq. 2.12f or Eq. 2.13f depending on the phase of operation (i.e., the number of control actuators on-line) to enforce convergence to the optimal steady-state. Within this context, the provable stability is practical stability of the optimal steady-state; please refer to Ref[65] for complete details on this point.*

Remark 2.7 *Potentially, one could extend EMPC formulated with a terminal constraint to handle actuator maintenance. Before the actuator is taken off-line, the terminal constraint would be the optimal steady-state $x_{s,0}$. After the actuator is taken off-line, the terminal constraint would be the optimal steady-state $x_{s,j}$ for the control system with only $m-1$ available actuators. When the time the actuator is taken off-line is within the prediction horizon of the EMPC, the terminal constraint of the EMPC would switch from $x_{s,0}$ to $x_{s,j}$. The resulting controller would have a similar closed-loop stability property (boundedness of the closed-loop state) assuming recursive feasibility of the EMPC could be guaranteed and the stability region of the EMPC would be the feasible region of the controller. To accomplish recursive feasibility in the presence of bounded disturbances (like we consider in the present work), modifications to the EMPC may be needed (e.g., use of a terminal region constraint instead of a terminal constraint, add a terminal cost, etc.). Assuming these modifications can be made to guarantee recursive feasibility, one must carefully consider recursive feasibility during the transition between the two control configurations. The feasible region of EMPC formulated with a terminal constraint is difficult to explicitly characterize especially for processes with many states and inputs such as the example considered in the present work. Also, the feasible region depends on the prediction horizon. Therefore, it is difficult to guarantee that for any initial state starting in the feasible region of the first controller configuration, the state can be forced to the feasible region of the second configuration. With the proposed LEMPC, an explicit characterization of the stability region (feasible region) can be completed and it does not depend on the prediction horizon length.*

2.4 Application to the Alkylation of Benzene Process

The proposed LEMPC for handling actuator maintenance is applied to a chemical process network example. Specifically, a process network of industrial importance used to produce ethylbenzene through the alkylation of benzene is considered. Ethylbenzene is an important chemical for the chemical process industries because it is an intermediate chemical in the production of polystyrene and other styrene-based plastics. The process flow and first-principles model of the alkylation of benzene process was first presented in Ref[96] which was adapted from Refs.[58,91,112,142]

2.4.1 Description of the Alkylation of Benzene Process

A process flow diagram of the alkylation of benzene process is displayed in Fig. 2.3. In Fig. 2.3, the notation F_i corresponds to the volumetric flow rate of the i-th stream and the other notation will be introduced below. The process consists of five vessels: four continuously stirred tank reactors (CSTRs) and one flash tank separator (SEP-1). Benzene and ethylene, which are denoted as component A and B, respectively, are fed to CSTR-1; while, CSTR-2 and CSTR-3 are only fed with a fresh ethylene feedstock. Within CSTR-1, CSTR-2 and CSTR-3, benzene reacts with ethylene to form the desired product, ethylbenzene, which is denoted as component C. Ethylbenzene can subsequently undergo further alkylation to form a byproduct 1,3-diethylbenzene (component D). The outlet stream of the three reactors (F_7) is fed to a flash separator to separate the desired product contained in the liquid bottoms of the separator and recover unreacted product. The overhead vapor stream containing mostly unreacted benzene of the separator is condensed and split. A portion of the condensed overhead stream is recycled back to CSTR-1. The remainder is send to CSTR-4. Within CSTR-4, a catalyzed transalkylation reaction occurs where 1,3-diethylbenzene reacts with benzene to produce ethylbenzene. Further alkylation of ethyl-

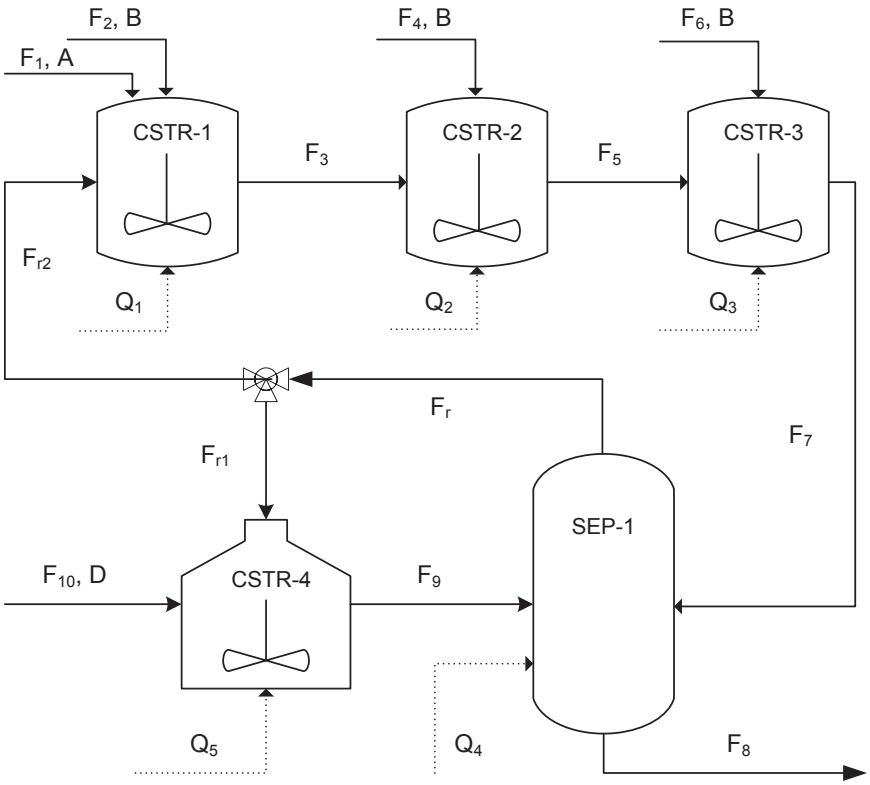

Figure 2.3: Process flow diagram of alkylation of benzene.

benzene to 1,3-diethylbenzene also occurs in CSTR-4. To simply the notation, the index $j = 1, 2, 3$ is used to denote CSTR-1, CSTR-2, and CSTR-3, respectively, $j = 4$ denotes SEP-1, and $j = 5$ denotes CSTR-4.

The three reactions described above are considered to be the dominant reactions of the

benzene alkylation process network and are summarized below:

$$A + B \rightarrow C, \qquad \Delta H_{R1} = -1.5 \times 10^5, \text{ J/mol} \tag{R1}$$

$$B + C \rightarrow D, \qquad \Delta H_{R2} = -1.1 \times 10^5, \text{ J/mol} \tag{R2}$$

$$A + D \rightarrow C, \qquad \Delta H_{R3} = 4.1 \times 10^5, \text{ J/mol} \tag{R3}$$

where R1 and R2 are exothermic and take place in CSTR-1, CSTR-2, and CSTR-3; while, R2 and R3 (R3 is endothermic) take place in CSTR-4. The rate expression of each reaction is given by:

$$r_1 = 0.084 e^{-9502/RT} C_A^{0.32} C_B^{1.5} \tag{2.31}$$

$$r_2 = \frac{0.085 e^{-20640/RT} C_B^{2.5} C_C^{0.5}}{\left(1 + 0.015 e^{-3933/RT} C_D\right)} \tag{2.32}$$

$$r_3 = \frac{237.8 e^{-61280/RT} C_A^{1.0218} C_D}{1 + 0.490 e^{-50870/RT} C_A} \tag{2.33}$$

where C_i is the concentration of component i ($i = A, B, C, D$), R is the gas constant, and T is the absolute temperature in Kelvin.

Applying the modeling assumptions detailed in Ref,[96] a first-principles model can be constructed describing the dynamic behavior of the process network which includes 25 states (e.g., temperatures and component concentrations). Owing to the complex reaction mechanisms (Eqs. 2.31-2.33) and the recycle streams, the resulting system of coupled ordinary differential equations (ODEs) is a nonlinear system of the form of Eq. 2.1. Eight manipulated inputs are considered for the process network which include the heat rate supplied and/or removed to each of the vessels and the inlet flow volumetric rates of the ethylene feedstock to CSTR-1, CSTR-2, and CSTR-3. The states and inputs of the process and the notation used to denote them are summarized in Table 2.1. The available control

Table 2.1: Process state and input variables.

$C_{A1}, C_{B1}, C_{C1}, C_{D1}$	Concentrations of A, B, C, D in CSTR-1
$C_{A2}, C_{B2}, C_{C2}, C_{D2}$	Concentrations of A, B, C, D in CSTR-2
$C_{A3}, C_{B3}, C_{C3}, C_{D3}$	Concentrations of A, B, C, D in CSTR-3
$C_{A4}, C_{B4}, C_{C4}, C_{D4}$	Concentrations of A, B, C, D in SEP-1
$C_{A5}, C_{B5}, C_{C5}, C_{D5}$	Concentrations of A, B, C, D in CSTR-4
T_1, T_2, T_3, T_4, T_5	Temperatures in each vessel
F_2, F_4, F_6	Ethylene feedstock flow rates
Q_1, Q_2, Q_3, Q_4, Q_5	External heat supply/removal to each vessel

energy is $Q_i \in [-7.2, -0.8] \times 10^6$ J/s for $i = 1, 2, 3$, $Q_i \in [1.6, 14.4] \times 10^6$ J/s for $i = 4, 5$, and $F_i \in [2.0, 18.0] \times 10^{-4}$ m^3/s for $i = 2, 4, 6$.

2.4.2 Control Objectives and Process Economics

For the benzene alkylation process, we assume that it is a priority to routinely conduct preventive maintenance on the control actuators of the process in an attempt to avoid/prevent a process upset caused by a failed or unreliable actuator. Ideally, process operators would like to maintain process operation during any maintenance task to prevent production loss as long as operators are able to sustain safe process operation with fewer control actuators. The next objective would be to operate the process network in an economically optimal fashion by accounting for the process economics and the fact that fewer actuators are available. These operating objectives are considered to be control objectives in addition to traditional control objectives (i.e., maintain process stability, robustness to disturbances, etc.).

For the process network, the process economics are assumed to be adequately described by the summation of four terms:

$$l_e(x,u) = L_1 + L_2 + L_3 + L_4 \tag{2.34}$$

where $L_1 = A_1(r_{1,1}+r_{1,2}+r_{1,3})/(r_{2,1}+r_{2,2}+r_{2,3})$ is the weighted instantaneous selectivity of reaction R1 over reaction R2 in CSTR-1, CSTR-2, and CSTR-3 (the notation $r_{i,j}$ denotes the i-th reaction rate in the j-th vessel), $L_2 = A_2 r_{3,4}$ is the weighted production rate of C through R3 in CSTR-4, $L_3 = A_3 F_8 C_{C4}$ is the weighted (instantaneous) molar flow rate of the desired product out of the separator, and L_4 is given by the following expression:

$$L_4 = A_4 \sum_{i=1}^{3} Q_i - A_5 \sum_{i=4}^{5} Q_i \tag{2.35}$$

which penalizes energy consumption and removal from the process network. The coefficients A_k, $k = 1, 2, 3, 4, 5$ are positive weighing factors with the following values: $A_1 = 1.00$, $A_2 = 1.50$, $A_3 = 0.50$, $A_4 = 1.25 \times 10^{-6}$, and $A_5 = 2.00 \times 10^{-6}$. The reason for the difference between the weight values A_4 and A_5 is associated with the difference in cost of removing heat from a vessel and cost of supplying heat to a vessel.

Additionally, the amount of ethylene that may be fed to each CSTR over the operating horizon t_f is constrained to be equal to an average amount:

$$\frac{1}{t_f}\int_{t_0}^{t_0+t_f} F_i(\tau) C_{Bi0}\, d\tau = F_{\text{avg},i} C_{Bi0}, \quad i = 2, 4, 6 \tag{2.36}$$

where C_{Bi0} denotes the concentration of ethylene in the i-th stream ($i = 2, 4, 6$) and $F_{\text{avg},i}$ is the average flow rate amount of the i-th stream. In the example below, $F_{\text{avg},i}$ is taken to be a steady-state flow rate. The three economics-oriented constraints formed from Eq. 2.36 allow for the LEMPC to distribute ethylene in a non-uniform fashion (with respect to time) to each reactor if it is economically desirable. However, the LEMPC must compute an input profile that uses the same amount of ethylene as the amount used when ethylene is distributed (fed) uniformly with time.

2.4.3 Lyapunov-based EMPC Design

A control scheme that can achieve the control objectives outlined above is the proposed LEMPC for handling preventive maintenance of control actuators for the benzene alkylation process network. In this subsection, the design of the LEMPC is detailed and subsequently, applied to the benzene alkylation process network. The benzene alkylation process network is an input-affine nonlinear system, that is the vector field f of Eq. 2.1 has a specific form:

$$f(\bar{x}(t),u(t),0) = \bar{f}(\bar{x}(t)) + \sum_{j=1}^{8} \bar{g}_i(\bar{x}(t))u_i(t) \tag{2.37}$$

where $\bar{f} : \mathbb{R}^{25} \to \mathbb{R}^{25}$ and $\bar{g}_i : \mathbb{R}^{25} \to \mathbb{R}^{25}$ for $i = 1, \ldots, 8$. For simplicity of presentation, we assume that after converting the system of Eq. 2.37 into appropriate deviation variables, the origin is the steady-state of Eq. 2.37 and we drop the $\bar{\cdot}$ notation for the remainder. To design a Lyapunov-based controller for the process network, the input vector is partitioned on the basis of the input type: $u = [u_h \, u_f]^T$ where u_h denotes a vector with the heat rate inputs (Q_i, $i = 1, 2, 3, 4, 5$) and u_f denotes a vector with the flow rate inputs (F_i, $i = 2, 4, 6$). The reason for partitioning the input vector in this fashion is because the heat rate inputs are considered to have the most influence on maintaining process stability and the flow rates are essentially additional degrees of freedom that can be used to optimize the process economics and/or be used to compensate for fewer on-line actuators. The Lyapunov-based controller designed to asymptotically stabilize the origin of the nonlinear system is designed element-wise to reflect the difference in responsibilities of the heat rate inputs and the flow rate inputs. For the heat rate inputs, the following feedback control law[129] is used:

$$h_{hi}(x) = \begin{cases} -\frac{L_f V + \sqrt{(L_f V)^2 + (L_{g_i} V)^4}}{(L_{g_i} V)^2} L_{g_i} V & \text{if } L_{g_i} V \neq 0 \\ 0 & \text{if } L_{g_i} V = 0 \end{cases} \tag{2.38}$$

Table 2.2: Steady-state input values for the benzene alkylation process network.

Q_{1s}, Q_{2s}, Q_{3s}	-4.0×10^6 J/s
Q_{4s}, Q_{5s}	8.0×10^6 J/s
F_{2s}, F_{4s}, F_{6s}	1.0×10^{-3} m^3/s

for $i = 1, \ldots, 5$ where $L_f V = \frac{\partial V}{\partial x} f(x)$ and $L_{g_i} V = \frac{\partial V}{\partial x} g_i(x)$ denote the Lie derivatives of V with respect to the vector fields f and g_i, respectively. For the flow rate inputs, the Lyapunov-based controller elements are $h_f(x) = [0\,0\,0]^T$. Thus, the resulting Lyapunov-based controller is $h(x) = [h_h^T(x)\ h_f^T(x)]^T$.

To characterize the stability region $\Omega_{\tilde{\rho}_0}$, a steady-state is iteratively selected so that it is within the acceptable operating range and its corresponding stability region is a region in state-space where state and input constraints are satisfied. The steady-state denoted as $x_{s,0}$ that satisfies these conditions corresponds to the steady-state input values contained in Table 2.2. Upon converting to appropriate deviation variables, $x_{s,0}$ is taken to be the origin in the deviation state-space coordinates. A quadratic Lyapunov function (i.e., $V(x) = x^T P x$ where P is a positive definite matrix) is considered with

$$P = \text{diag}([1\ 10\ 1\ 1\ 100\ 1\ 10\ 1\ 1\ 100\ 1\ 10\ 1\ 1\ 100\ 1\ 10\ 1\ 1\ 100\ 1\ 10\ 1\ 1\ 100])$$

which has been selected such that the closed-loop alkylation benzene process network under the Lyapunov-based controller $h(x)$ gives a desirable closed-loop response with respect to traditional control objectives (i.e., speed of response, fewer oscillations, etc.). Given that the steady-state $x_{s,0}$ is open-loop asymptotically stable, the stability region $\Omega_{\tilde{\rho}_0}$ is estimated to be a large region in state-space with $\tilde{\rho}_0 = 1.0 \times 10^8$.

Nominal operation ($w(t) \equiv 0$) of the benzene alkylation process is considered below for the case studies. Therefore, only mode 1 operation of the LEMPC is used, and the Lyapunov-based constraint of the LEMPC is formulated on the basis of the steady-state

Table 2.3: Optimal steady-state input values with respect to the economic cost function of Eq. 2.34.

Q_{1s}^*	-8.0×10^5 J/s	Q_{5s}^*	9.4×10^6 J/s
Q_{2s}^*	-8.1×10^5 J/s	F_{2s}^*	5.5×10^{-4} m^3/s
Q_{3s}^*	-8.0×10^5 J/s	F_{4s}^*	3.2×10^{-4} m^3/s
Q_{4s}^*	3.1×10^6 J/s	F_{6s}^*	2.6×10^{-4} m^3/s

$x_{s,0}$. The sampling time of the LEMPC is chosen to be $\Delta = 20$ s and the operating period that the material constraint of Eq. 2.36 is enforced is $t_f = 1800$ s $= 30$ min. To solve the optimization problem of the LEMPC at each sampling period, Ipopt[139] is employed.

Before we proceed with applying the LEMPC to demonstrate its capability of handling actuator maintenance, we apply it to the process network to show its applicability on closed-loop economic performance improvement over operating the process network at the economically optimal steady-state. Specifically, the steady-state optimization problem is solved using the steady-state model. The steady-state optimization problem is given by:

$$\max_{x_s,u_s} \quad l_e(x_s,u_s) \tag{2.39a}$$

$$\text{s.t.} \quad f(x_s)+\sum_{j=1}^{8} g_i(x_s)u_s = 0 \tag{2.39b}$$

$$u_s \in U_0 \tag{2.39c}$$

$$x_s \in X_s \tag{2.39d}$$

$$V(x_s) \leq \tilde{\rho}_0 \tag{2.39e}$$

where $l_e(x_s,u_s)$ is the economic cost function of Eq. 2.34 and $f(x_s,u_s,0)=0$ is the steady state process model for the benzene alkylation process network. The optimal steady-state, denoted as $x_{s,0}^*$ corresponds to the steady-state input $u_{s,0}^*$ given in Table 2.3.

In the optimization problem of Eq. 2.39, the constraint of Eq. 2.39c is the available control energy with all available actuators on-line. The constraint of Eq. 2.39d enforces that

the computed optimal steady-state be in the set of admissible steady-states and is defined through five temperature constraints:

$$\left|T_{js} - T_{js,0}\right| \leq 0.1 T_{js,0} \tag{2.40}$$

for $j = 1, \ldots, 5$ where T_{js} is the steady-state temperature of the j-th vessel (i.e., a decision variable of Eq. 2.39) and $T_{js,0}$ is the steady-state temperature of the j-th vessel corresponding to the steady-state $x_{s,0}$. Lastly, the constraint of Eq. 2.39e is a Lyapunov-based constraint to ensure the optimal steady-state is contained in the stability region $\Omega_{\tilde{\rho}_0}$. Given that $\Omega_{\tilde{\rho}_0}$ is a large region in state space that satisfies process constraints, this region will be used in the LEMPC formulation. For a fair comparison between the closed-loop performance under LEMPC and steady-state operation, the optimal steady-state must be a reachable steady-state when the LEMPC is operated in LEMPC mode 1. The Lyapunov-based constraint of the LEMPC (Eq. 2.11e) that enforces the predicted state be inside of $\Omega_{\tilde{\rho}_0}$, which is formulated with the steady-state $x_{s,0}$ (i.e., not necessarily the optimal steady-state), must therefore contain the optimal steady-state $x^*_{s,0}$.

We compare the closed-loop performance of the benzene alkylation process under LEMPC (mode 1 operation of the LEMPC only) and steady-state operation over one period of operation (operating window of 30 min). The material constraint of Eq. 2.36 is added to formulation of the LEMPC of Eq. 2.11 and the optimal flow rates are used as $F_{\text{avg},i}$ (i.e., $F_{\text{avg},i} = F^*_{is}$ for $i = 2, 4, 6$). The benzene alkylation process is initialized at the economically optimal steady-state $x^*_{s,0}$. For the case of steady-state operation, the total economic cost is computed by maintaining operation at the steady-state over the period of operation considered. The total economic cost is defined as

$$J = \int_0^{t_f} l_e(x(\tau), u(\tau))\, d\tau \tag{2.41}$$

where $l_e(\cdot,\cdot)$ is the economic cost function of the benzene alkylation process of Eq. 2.34. The following prediction horizons of the LEMPC were considered: $N = 2,4,6,8,10$.

Figs. 2.4-2.5 display the temperature, heat rate, and flow rate profiles of the closed-loop benzene alkylation process under LEMPC with a prediction horizon of $N = 2$ and $N = 6$, respectively. For the cases with $N > 6$, no significant performance improvement was observed with respect to the total economic cost of Eq. 2.41 over the case with $N = 6$. With $N = 2$, LEMPC operates the process network in a cyclic operating pattern (Fig. 2.4) and exhibits three phases of operation over the operating window which is observed in the temperature profiles of Fig. 2.4a. The first phase from approximately $t = 0$ to $t = 80$ s is caused by the effect of initial condition; the second phase from approximately $t = 80$ s to $t = 1400$ s is a cyclic operating pattern; the last phase results from the material constraint since it needs to be satisfied over the operating window (refer to Fig. 2.4c). With $N = 6$ (Fig. 2.5), a similar, albeit chaotic-like, behavior is observed. The chaotic-type operation is mainly associated with the computed input profiles Q_4 and Q_5 which could be due to the interaction between the two inputs (i.e., different Q_4 and Q_5 combinations yield similar economic cost values) and/or the cost is not particularly sensitive to these inputs. However, it is important to point out that the operation pattern enforced by the computed input profile of the LEMPC is not truly chaotic since repeated simulations with $N = 6$ yielded the same closed-loop profiles.

For the benzene alkylation process under the LEMPC with $N = 2$, the total economic cost is 12.01% over steady-state operation; while, the total economic cost is 15.92% greater under the LEMPC with $N = 6$ compared to steady-state. From this analysis, non-uniform (with respect to time) distribution of ethylene to the benzene alkylation process network yields greater total economic cost than uniform in time distribution of ethylene to the process network. Even though the benzene alkylation process is operated in a chaotic-like dynamic operating pattern, $N = 6$ was selected as the appropriate prediction horizon of the

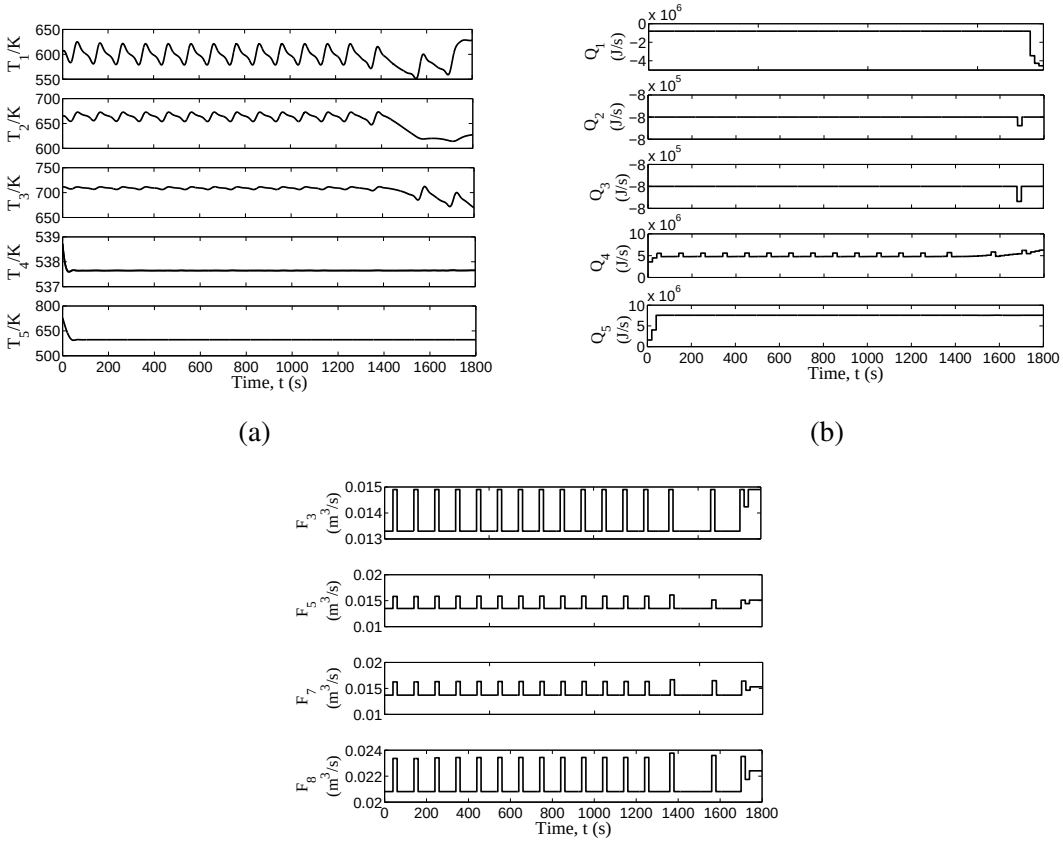

(a) (b)

(c)

Figure 2.4: Closed-loop (a) temperature, (b) heat rate, and (c) flow rate profiles under LEMPC with $N = 2$.

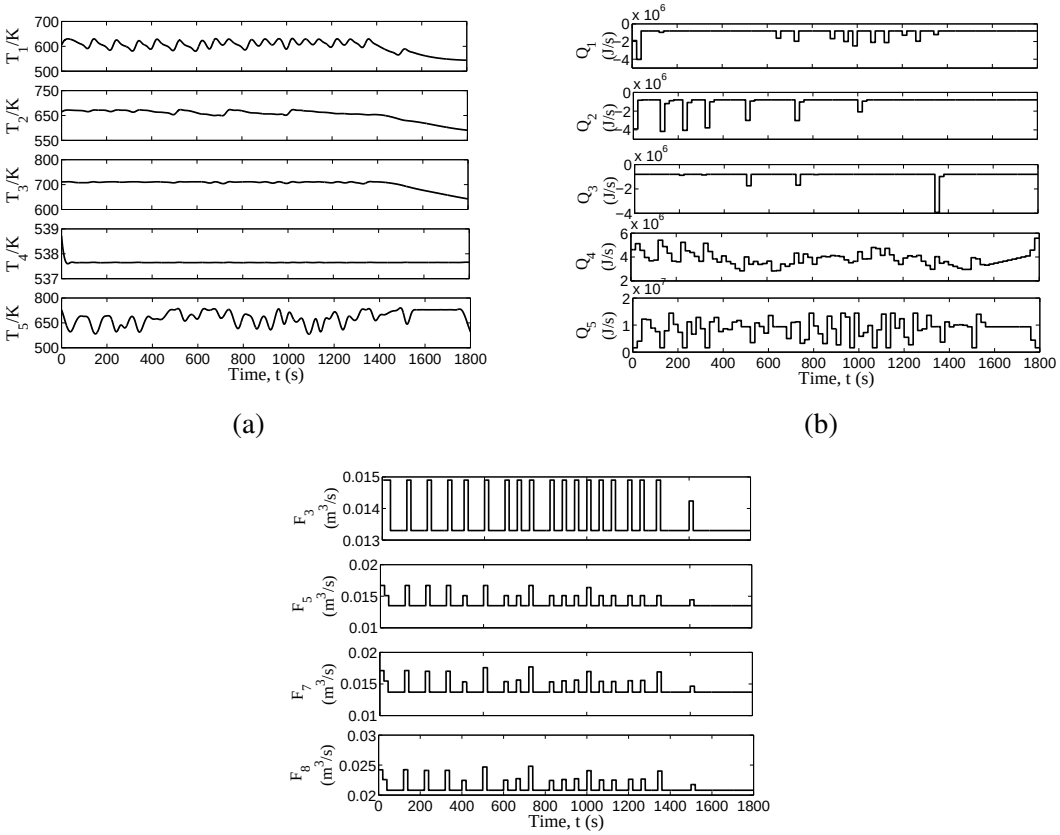

Figure 2.5: Closed-loop (a) temperature, (b) heat rate, and (c) flow rate profiles under LEMPC with $N = 6$.

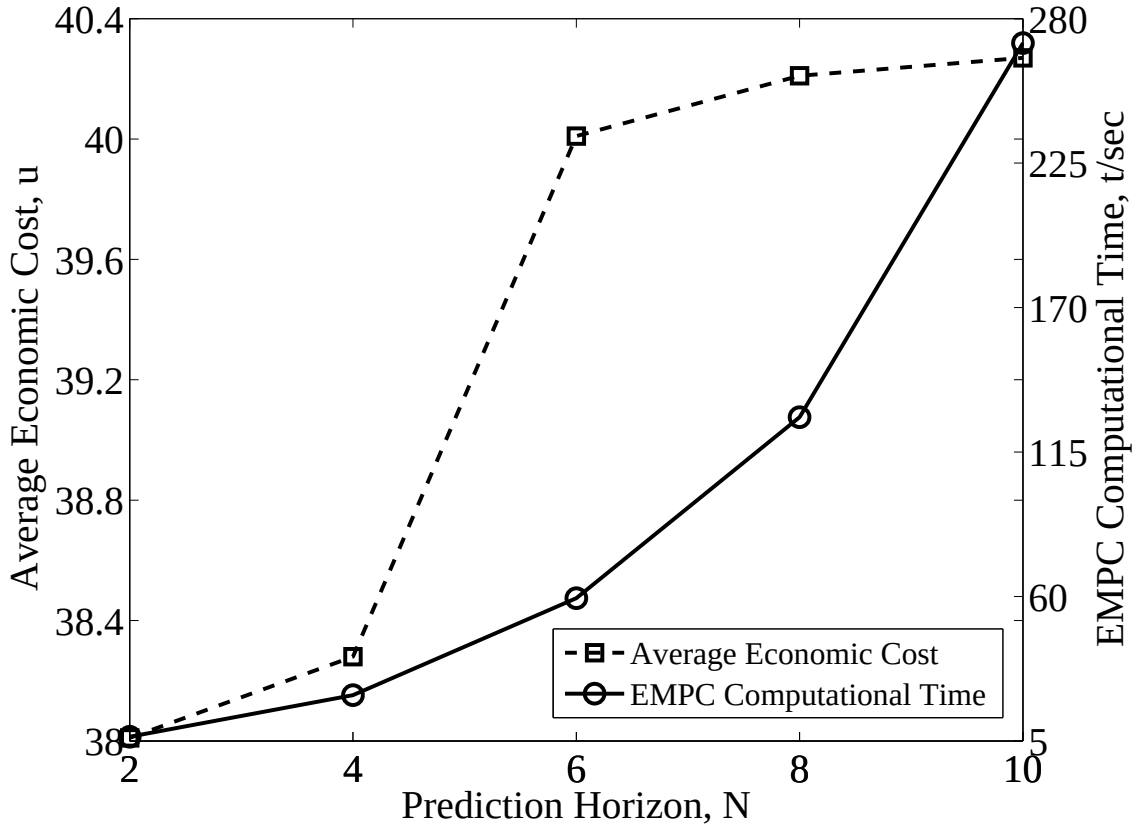

Figure 2.6: Average economic cost and EMPC computational time under different prediction horizons.

LEMPC to use in the case studies considered below.

Furthermore, we compared the impact of the prediction horizon on the economic performance and the computational efficiency for $N = 2,4,6,8,10$ in Fig. 2.6. Since no significant benefit on economic performance was observed for $N = 8$ and $N = 10$ while the computational burden increases a lot, using $N = 6$ is desirable from the trade-off between the computational efficiency and economic performance optimization.

Remark 2.8 *If one deemed the operating pattern enforced by the LEMPC with $N = 6$ is undesirable, one could potentially add penalty terms in the cost function of the LEMPC penalizing the rate of change of the inputs (i.e., add a quadratic term of the form $(u(t_{k+1}) -$*

Table 2.4: Optimal steady-state input values with respect to the economic cost function of Eq. 2.34 with the Q_4 actuator taken off-line.

Q_{1s}^*	-6.4×10^5 J/s	Q_{5s}^*	6.7×10^6 J/s
Q_{2s}^*	-12.3×10^5 J/s	F_{2s}^*	3.1×10^{-4} m^3/s
Q_{3s}^*	-8.0×10^5 J/s	F_{4s}^*	6.8×10^{-4} m^3/s
Q_{4s}^*	8.0×10^6 J/s	F_{6s}^*	4.5×10^{-4} m^3/s

$u(t_k))^T R_c(u(t_{k+1}) - u(t_k))$ *to the cost where* R_c *is a positive definite matrix) so that the LEMPC computes a smoother input profile.*

2.4.4 LEMPC for Handling Actuator Maintenance

We apply the proposed LEMPC (Eqs. 2.12-2.13) to the benzene alkylation process network. The ethylene material constraint (Eq. 2.36) is added as a constraint in the LEMPC of Eq. 2.11 based on the optimal flow rates $F_{\text{avg},i} = F_{is}^*$ for $i = 2, 4, 6$ which are given in Table 2.3. For the following case studies, we consider preventive maintenance in the actuator supplying heat to the separator. We assume that the Q_4 actuator loses its ability to change and becomes fixed at its steady-state value ($Q_{4s} = 8.0 \times 10^6$ J/s). To motivate the practical scenario for this, the heat supplied to the separator could be provided through a steam jacket and the maintenance is scheduled for the flow control valve that controls the steam pressure. To perform the maintenance task, we assume that another (uncontrolled) steam line can provide steam to the jacket at a constant rate. As a consequence, the steady-state when all available actuators are on-line and when the Q_4 actuator is taken off-line are the same. Furthermore, for stability and constraint satisfaction reasons mentioned above, the steady-state and level set value used in the formulation of the mode 1 Lyapunov-based constraint of the LEMPC are $x_{s,0}$ (i.e., the one corresponding to the steady-state input values contained in Table 2.2) and $\tilde{\rho}_0 = 1.0 \times 10^8$, respectively.

Case I: Prediction Horizon Effect on Process Stability

We apply different values of the prediction horizon, N, i.e., $N = 2, 4, 6$ to the proposed LEMPC mode 1 of Eqs. 2.12-2.13 to see the effect of the prediction horizon length on the process stability performance. The Lyapunov function values of these simulations are demonstrated in Fig.2.7. As we mentioned in Section 2.3.2, a sufficiently long prediction horizon is needed to ensure that it is feasible to force the closed-loop state to the stability region of the next control configuration by the time the control configuration changes. From Fig.2.7, we can see a LEMPC mode 1 of Eqs. 2.12-2.13 with prediction horizon, $N = 2$ fails to decrease its Lyapunov function value below $\tilde{\rho}_{1,j}$ by the time the j-th actuator is removed at $t_r = 400$ *sec* (we only plot the Lyapunov function trajectory by the time, t_r since the following trajectory is meaningless) which means it can't drag the system into the stability region of the new economically optimal steady state, $x_{s1,j}$; for a LEMPC mode 1 of Eqs. 2.12-2.13 with prediction horizon, $N = 4$, it successfully drives the process into the stability region of $x_{s1,j}$ by the time $t_r = 400$ *sec* as shown in Fig.2.7; however, in the end of this operation period, its Lyapunov function value violates the Lyapunov function level, $\tilde{\rho}_{1,j}$ since the reactant material integral constraints on u_{f1}, u_{f2} and u_{f3} narrows the optimal manipulated input scope of the proposed LEMPC of Eqs. 2.12-2.13 and consequently affect the state trajectories to be deviated more far away from $x_{s1,j}$ which increases the Lyapunov function value; if we increase the prediction horizon to be $N = 6$, the simulation results as shown in Fig.2.7 demonstrate that LEMPC mode 1 of Eqs. 2.12-2.13 with this length of prediction horizon can avoid both of the above infeasibility problems in the situation of LEMPC with $N = 2$ and LEMPC with $N = 4$. Based on the above results, we can see a sufficiently long prediction horizon is required to ensure the process stability by the time of control system reconfiguring and also avoid infeasibility in the end of operation period when the control energy is constrained. Therefore, using $N = 6$ is not only desirable from

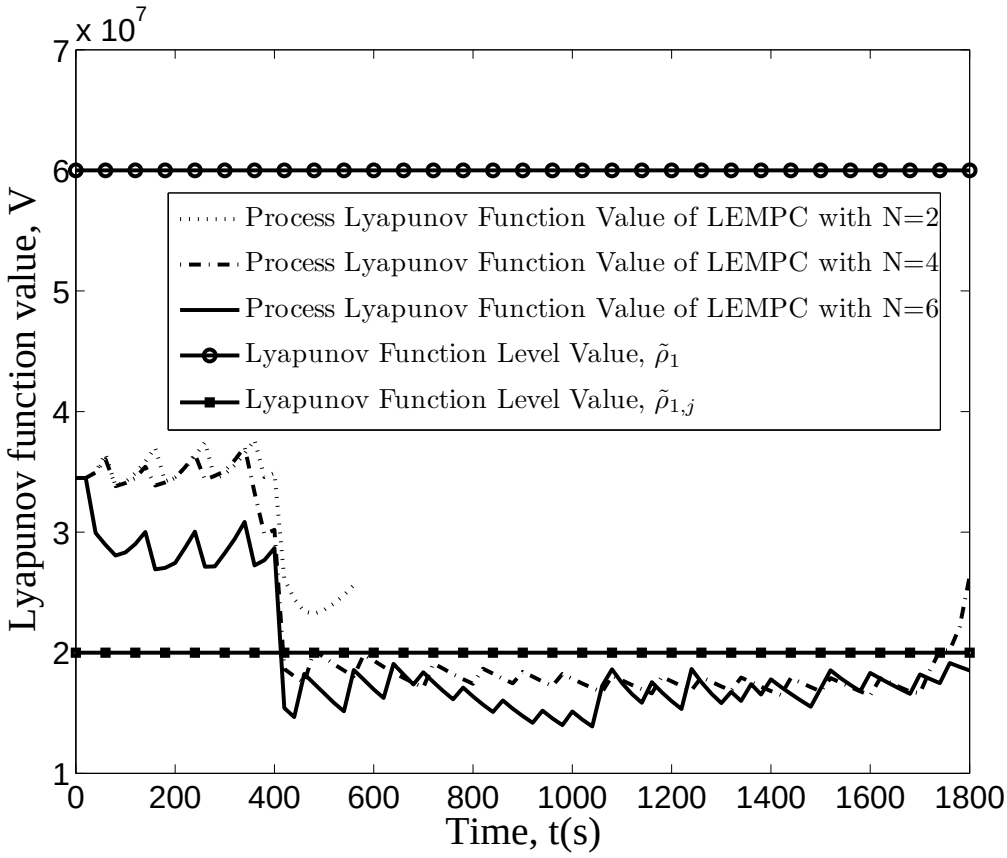

Figure 2.7: Prediction horizon's impact on process stability.

the perspective of computational efficiency and process performance, but also necessary from the point of process stability.

Case II: Actuator Taken Off-line for Preventive Maintenance

In the first case, we consider a preventive maintenance task will be completed on the actuator that manipulates the amount of heat supplied to the separator Q_4. The actuator is scheduled to be shut-down at $t_r = 400$ s for a preventive maintenance task to be completed on it. The closed-loop temperature and input profiles are given in Fig. 2.8. To demonstrate the benefit of integrating actuator maintenance, process economics, and process control in a unified system, we compare the closed-loop behavior of the benzene alkylation process

under the proposed LEMPC (Eqs. 2.12-2.13) with two other cases under different LEMPC formulations. In the first case, denoted as LEMPC-A, the LEMPC uses the input constraint with all available control actuators on-line until the sampling period $t_r = 400$ s where the input constraint switches to the remaining available actuators. For this case, LEMPC-A cannot proactively prepare for when the Q_4 actuator will be taken off-line since LEMPC-A does not account for the control system change until after the actuator is taken off-line. However, it is unlikely that current control systems even have the ability to easily change from m to $m-1$ actuators. Therefore, a second case, denoted as LEMPC-B, was considered where the LEMPC continues to compute control actions for all the inputs even after the Q_4 actuator is taken off-line. This second case may be considered as the worst case scenario. The closed-loop profiles of the process network under LEMPC-A are also shown in Fig. 2.8 as the dashed profiles. The most noticeable difference between the two profiles is that the temperature for CSTR-4 (T_5) under the proposed LEMPC is less than that the one under LEMPC-A when Q_4 is taken off-line. Comparing the total economic cost of the three scenarios, the total economic cost under the proposed LEMPC is 2.17% higher than that of the process under LEMPC-A; the total economic cost under the proposed LEMPC is 5.38% greater than that under LEMPC-B.

To demonstrate that the LEMPC can maintain stability of the process regardless of the time the actuator is taken off-line (i.e., the choice of t_r is arbitrary), we perform another simulation where the Q_4 actuator is taken off-line at $t_r = 1400$ s. The closed-loop profiles of this case are shown in Fig. 2.9. The LEMPC is able to maintain boundedness of the closed-loop state as observed from the temperature profile of Fig. 2.9a.

Remark 2.9 *The concepts presented in the present work could be extended to distributed MPC although a rigorous theoretical treatment and presentation of proposed distributed MPC algorithms for handling actuator maintenance are outside the scope of the present*

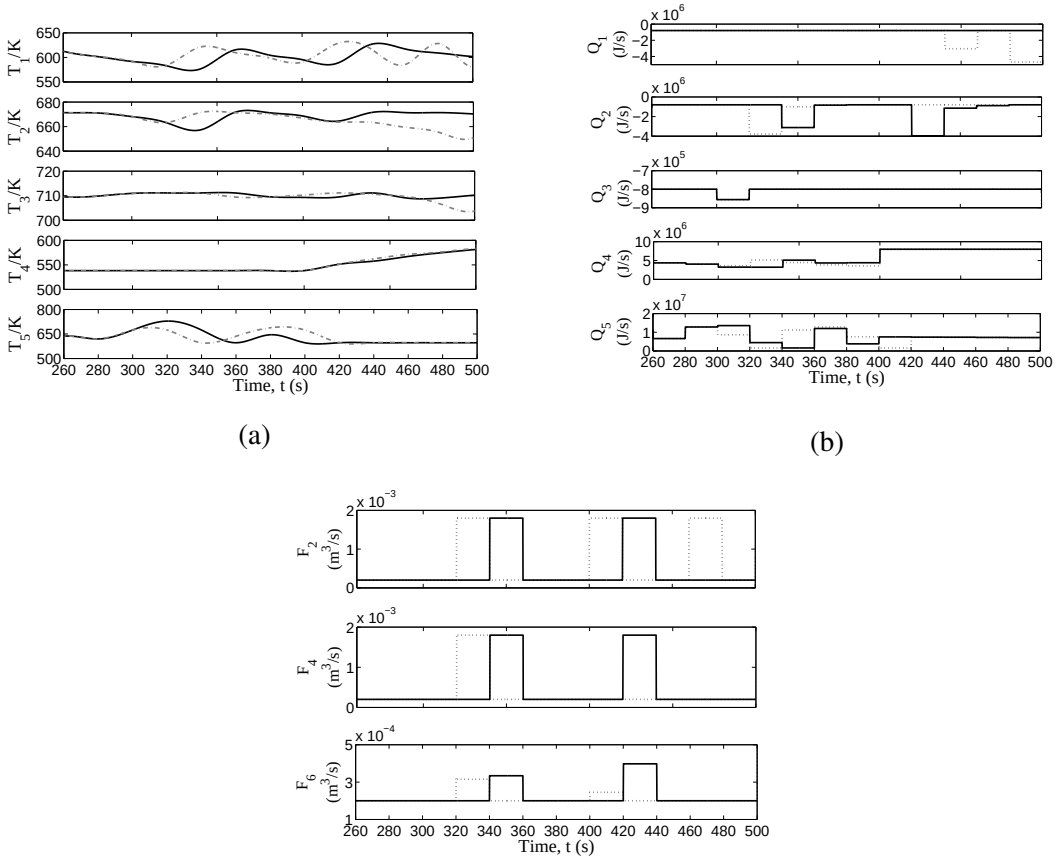

Figure 2.8: Closed-loop (a) temperature, (b) heat rate, and (c) flow rate profiles under the proposed LEMPC for handling actuator maintenance (solid line) and under LEMPC-A (dashed line). The Q_4 actuator is taken off-line at $t_r = 400$ s.

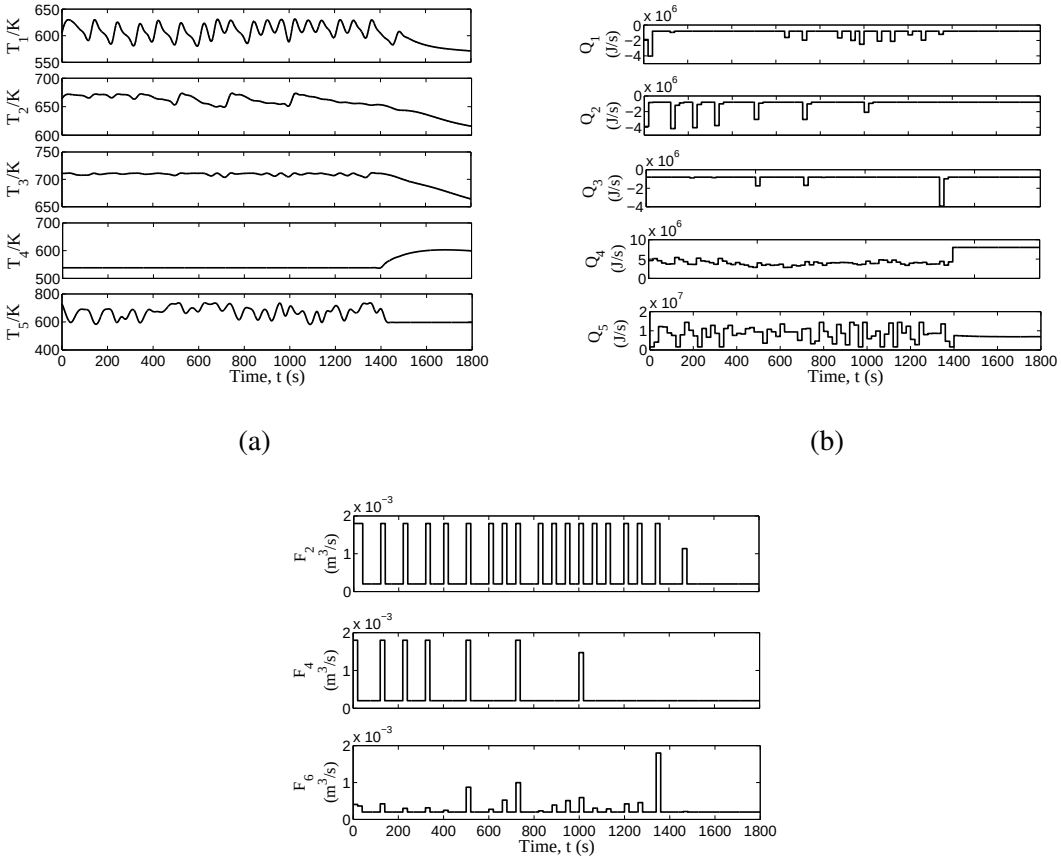

(a) (b)

(c)

Figure 2.9: Closed-loop (a) temperature, (b) heat rate, and (c) flow rate profiles under the proposed LEMPC (Eqs. 2.12-2.13 with mode 1 only). The Q_4 actuator is taken off-line at $t_r = 1400$ s.

work. It is important to point out that for the present chemical process example, the simulations were carried out on a desktop PC and the computational time required for the computation of the control action by the centralized LEMPC was within the sampling time thereby ensuring that this controller can be implemented in real-time, so for this specific example, a distributed MPC strategy may not be needed.

Remark 2.10 *Integrating scheduling and control is an important research topic especially in the context of Smart manufacturing albeit outside the scope of the present work. Furthermore, integrating scheduling and control is more complex than rational extensions to existing optimal control problems (e.g., model predictive control (MPC) or economic MPC) owing to the fact that there may be discrete variables in the scheduling optimal control problem making the resulting optimal control problem which integrates scheduling and control a mix-integer nonlinear program (MINLP) and in general, the control horizon (i.e., the prediction horizon of MPC) is shorter than the scheduling horizon.*

Case III: Actuator Briefly Taken Off-line for Inspection

Another important part of scheduled preventive maintenance is routine inspection of operating equipment. For this case, we consider that the Q_4 actuator is briefly taken off-line for a routine inspection. The time the actuator is taken off-line is $t_r = 400$ s and after the inspection is completed, the actuator is brought back on-line at $t_r' = 1200$ s. The temperature and input profiles of this closed-loop simulation are displayed in Fig. 2.10. Again, stability throughout the simulation is maintained under the LEMPC.

Remark 2.11 *Regarding potential delay in the actuator replacement, by the time the actuator is taken off-line, the closed-loop state is forced to a region in state-space where stability (i.e., boundedness of the closed-loop state) can be maintained thereafter, so regardless of the time the actuator is brought back on-line closed-loop stability will be maintained.*

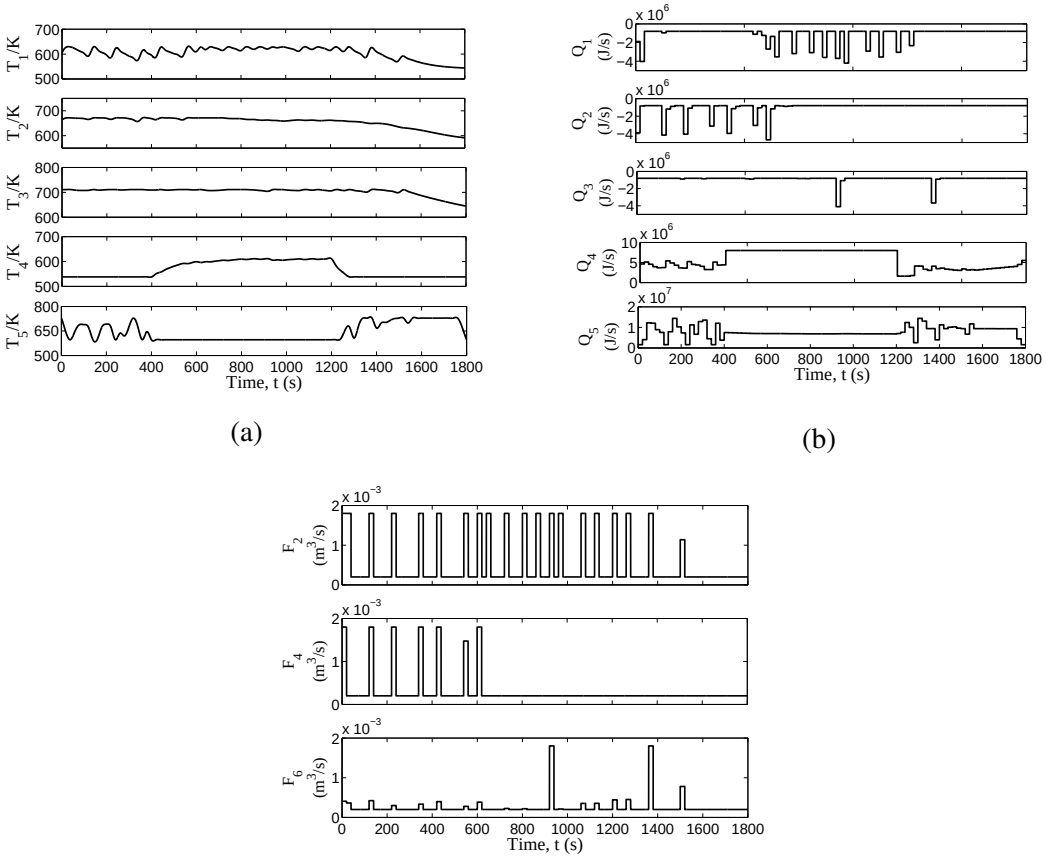

Figure 2.10: Closed-loop (a) temperature, (b) heat rate, and (c) flow rate profiles under the proposed LEMPC (Eqs. 2.12-2.13 with mode 1 only). The Q_4 actuator is briefly taken off-line for inspection from $t_r = 400$ s to $t_r' = 1200$ s.

Case IV: Multiple Actuators Taken Off-line for Inspection

The ability to maintain stability after multiple actuators are taken off-line is more of a concern with the controllability of the system. For this case, we consider that the Q_4 actuator is taken off-line for a routine inspection between $t_{r1} = 400\ s$ and $t'_{r1} = 800\ s$; and the Q_5 actuator is taken off-line for a routine inspection just after the Q_4 actuator is brought back on-line at $t_{r2} = t'_{r1} = 800\ s$ and be available again at $t'_{r2} = 1200\ s$ after its repair. The temperature and input profiles of this closed-loop simulation are displayed in Fig. 2.11. Stability of the closed-loop system was maintained throughout.

Remark 2.12 *Within the context of hybrid or switched systems minimum dwell time is important as sufficiently fast switching between modes of operation may cause the closed-loop system to become unstable. Within the context of the present work, the issue of stability after taking an actuator off-line has more to do with the controllability of the system and not the time the actuators are taken off-line. In other words, before any actuator is taken off-line, the closed-loop state trajectory is forced to a set in state-space where stability (i.e., boundedness of the closed-loop state) can be maintained with the remaining actuators which is imposed through the constraints of the proposed LEMPC. If the closed-loop state cannot be forced to this region in state-space with the available control energy or if no such region exist (i.e., when multiple actuators are off-line), one may adopt a maintenance policy where only one actuator can be taken off-line for maintenance at a time. One would expect that this type of maintenance policy would not pose many practical restrictions considering the limited availability of resources to accomplish these maintenance tasks such as maintenance personnel.*

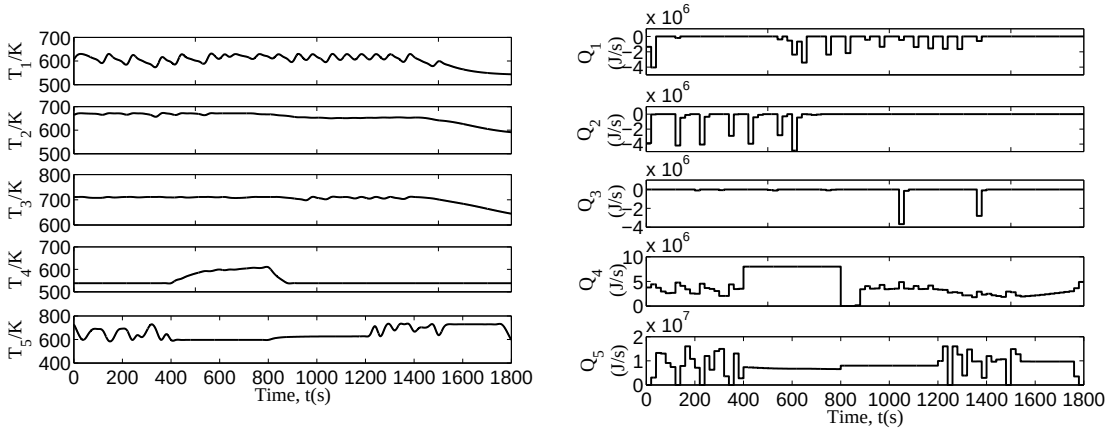

(a) (b)

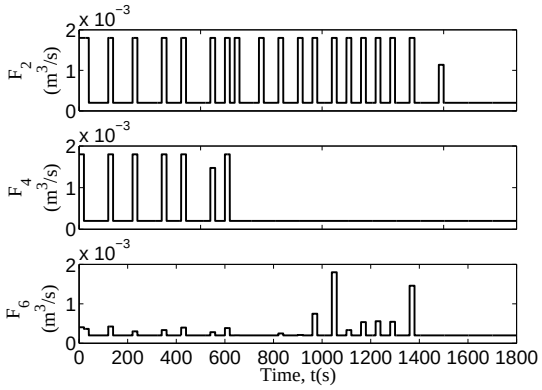

(c)

Figure 2.11: Closed-loop (a) temperature, (b) heat rate, and (c) flow rate profiles under the proposed LEMPC (Eqs. 2.12-2.13 with mode 1 only). The Q_4 actuator is briefly taken off-line for inspection from $t_{r1} = 400$ s to $t'_{r1} = 800$ s and the Q_5 actuator is briefly taken off-line for inspection from $t_{r2} = 800$ s to $t'_{r2} = 1200$ s.

Case V: Actuators Inspection Under Time-Varying Economic Cost

In industry, the per unit heat supply/removal cost changes frequently which may result from electricity price fluctuation caused by changes in electric power demand. Based on this consideration, for this case, we conduct a more realistic case where the process goes through a $24-hour$ periodic operation considering the time-varying per unit heat supply cost (i.e., time-varying economic cost function). Following the realistic electricity price trend in a single day,[130] we assume the parameter, A_5 increases 3.33% per half an hour for the first 12 hours and then decreases 3.33% per half an hour for the second 12 hours. We still set the length of each operation period to be $t_f = 1800\ s = 30\ min$. We assume the Q_4 actuator is taken off-line for a routine inspection between $t_r = 11.5\ hr$ and $t_r' = 12.0\ hr$. The temperature and input profiles of this closed-loop simulation are displayed in Fig. 2.12. Stability of the closed-loop system was still maintained throughout and the time-varying economic cost functions brings a dynamic operation for the process.

2.5 Conclusions

This work focused on the development of a Lyapunov-based economic model predictive controller (LEMPC) to integrate preventive maintenance of control actuators, process economic performance, and process control. During a scheduled preventive maintenance task on the j-th control actuator, the actuator is effectively taken off-line. In general, the steady-state with all available control actuators and with actuators taken off-line to perform a scheduled preventive maintenance task may be different (i.e., the former may not even be a steady-state of the latter scenario). To address this point, the proposed LEMPC was designed to ensure that the closed-loop state will be forced from the stability region of the steady-state of all m actuators to the stability region with $m-1$ actuators on-line before the

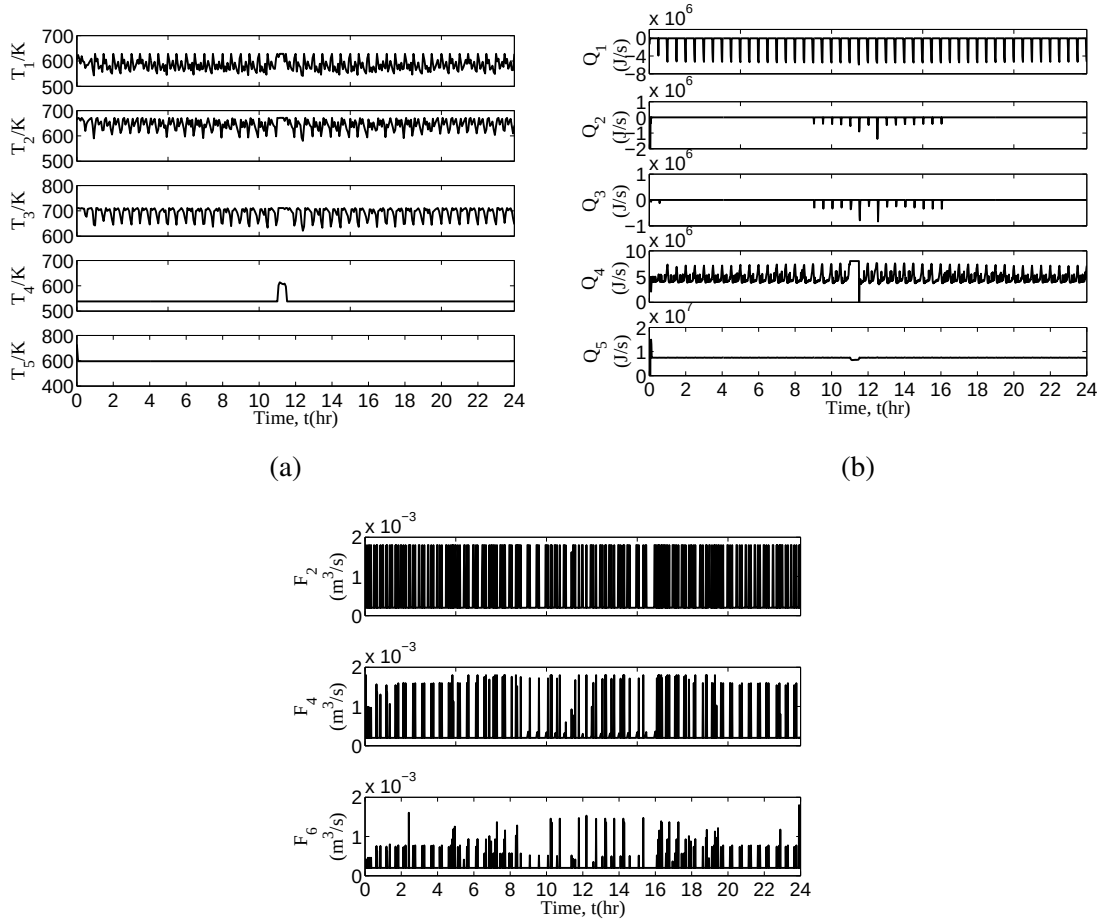

Figure 2.12: Closed-loop (a) temperature, (b) heat rate, and (c) flow rate profiles under the proposed LEMPC (Eqs. 2.12-2.13 with mode 1 only under time-varying economic cost function). The Q_4 actuator is briefly taken off-line for inspection from $t_{r1} = 11.5$ hr to $t'_{r1} = 12.0$ hr.

j-th control actuator was taken off-line. Closed-loop stability in the sense of boundedness of the closed-loop state was proved. The LEMPC capable of handling preventive maintenance was applied to a benzene alkylation process which yielded improved closed-loop economic performance over steady-state operation and demonstrated its ability to handle changing number of on-line actuators.

Chapter 3

Real-Time Preventive Sensor Maintenance Using Robust Moving Horizon Estimation and Economic Model Predictive Control

3.1 Introduction

This chapter presents the EMPC system design handling scheduled preventive sensor maintenance. A RMHE scheme is developed that accommodates a varying number of sensors to continuously supply accurate state estimates to an EMPC system. Fig. 3.1 illustrates the overall scheme integrating the real-time preventive sensor maintenance, process economics optimization and control system reconfiguration. The Lyapunov-based EMPC (LEMPC) combined with RMHE is proved to be stabilizing under certain observability and stabilizability assumptions. Then, a chemical process example utilizing the proposed RMHE-based LEMPC is presented for which the controller maintains the process stability, accom-

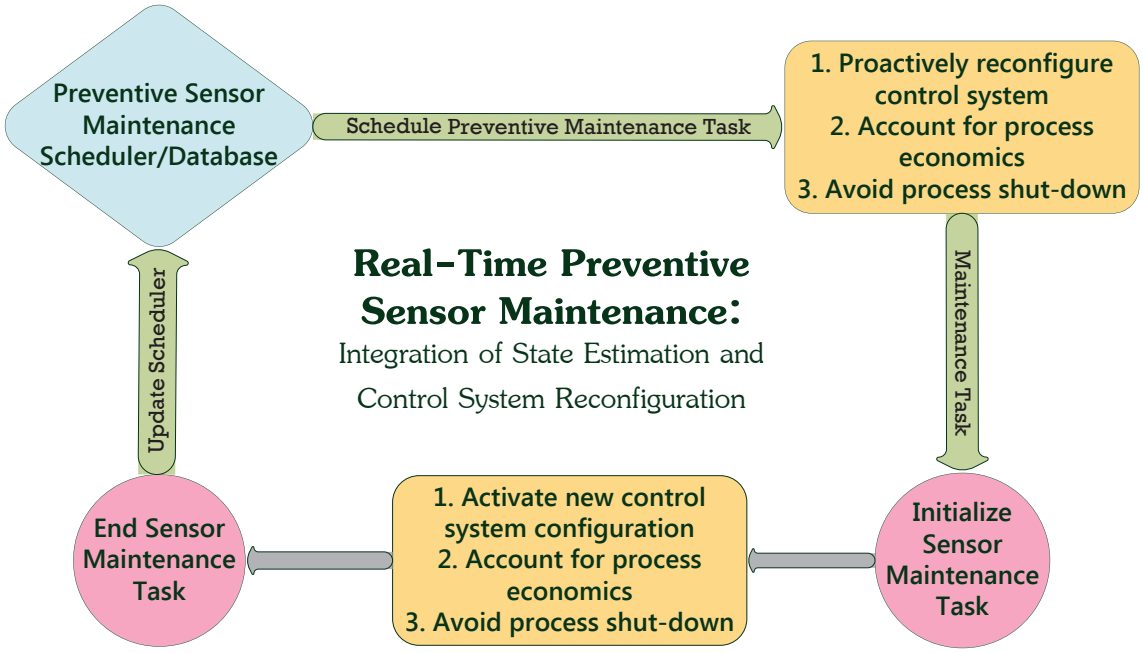

Figure 3.1: Logic sequence for real-time preventive sensor maintenance, incorporating maintenance events, economic optimization, and process control.

plishes control system reconfiguration under a changing number of on-line sensors, and achieves minimal economic performance degradation by adjusting the optimization problem as the number of on-line sensors changes. These results are mainly based on Ref.[88]

3.2 Preliminaries

3.2.1 Notation

The Euclidean norm of a vector is denoted by $|\cdot|$, and the notation $|\cdot|_Q$ denotes the weighted Euclidean norm with weighting matrix Q. A scalar-valued function $V : \mathbb{R}^n \to \mathbb{R}$ is positive definite if it evaluates to a positive scalar for all vectors $x \in \mathbb{R}^n$ in its domain except that $V(0) = 0$. The level set of a positive definite scalar-valued function is denoted $\Omega_r := \{x : V(x) \leq r\}$. A continuous, strictly increasing function $\alpha : [0,a) \to [0,\infty)$ with $\alpha(0) = 0$

is said to be a class $\mathscr{K}$ function. The relative complement of A with respect to B is denoted as $B \setminus A := \{x \in B : x \notin A\}$. diag$(v)$ signifies a diagonal matrix with the elements of the vector v on the diagonal. The sequence $\{t_{k\geq 0}\}$ denotes a synchronous partitioning of $\mathbb{R}_+$ where $t_k := k\Delta$ for $k = 0,\ 1,\ \ldots$ and $\Delta > 0$ is the sampling period.

3.2.2 Class of Nonlinear Process Systems

The control methodology that accounts for preventive sensor maintenance, as presented in this work, is developed for nonlinear systems of the following form:

$$\begin{aligned} \dot{x}(t) &= f(x(t)) + g(x(t))u(t) + l(x(t))w(t) \\ y(t) &= h(x(t)) + v(t) \end{aligned} \tag{3.1}$$

where the vector of states is $x \in \mathbb{R}^n$, the vector of manipulated inputs is $u \in \mathbb{R}^m$, the vector of disturbances is $w \in \mathbb{R}^l$, the vector of measured outputs is $y \in \mathbb{R}^q$, the vector of measurement noise is $v \in \mathbb{R}^q$, and f, g, l and h are sufficiently smooth vector or matrix functions of their arguments. Without loss of generality, we assume that $f(0) = 0$ (the origin is assumed to be the equilibrium of the unforced system) and the initial time $t_0 = 0$. It is assumed that the bounds on the available control energy restrict its allowable values to a convex set:

$$\mathbb{U} = \left\{ u \in \mathbb{R}^m : u_i^{\min} \leq u_i \leq u_i^{\max},\ i = 1, \ldots, m \right\}. \tag{3.2}$$

The disturbance and measurement noise vectors are also assumed to be bounded:

$$W = \left\{ w \in \mathbb{R}^l : |w| \leq \theta_w \right\} \tag{3.3}$$

$$V = \left\{ v \in \mathbb{R}^q : |v| \leq \theta_v \right\} \tag{3.4}$$

where θ_w and θ_v are positive constants that bound the disturbance and measurement noise vectors, respectively. The output measurement vector y of the system is assumed to be continuously available. It is assumed that the instantaneous value of the real-time process economics of the system of Eq. 3.1 can be modeled with a time-invariant, scalar-valued cost function $L_e(x,u)$.

The real-time preventive sensor maintenance schedule is defined as the change of the sensor group used in the EMPC system in real-time from the i-th sensor group with q_i number of sensors functioning well to the j-th sensor group with q_j number of sensors functioning well. This change in the number of on-line sensors occurs at the time $t = t_m$ determined by a scheduler or decision-maker, at which time one or more sensors are taken off-line for preventive maintenance. As a result, the measurement vector changes from $y_i(t) = h_i(x(t)) + v_i(t) \in \mathbb{R}^{q_i}$ to $y_j(t) = h_j(x(t)) + v_j(t) \in \mathbb{R}^{q_j}$ (q_i and q_j are less than or equal to q). The state estimation structure will change to the j-th group of sensors ($y_j(t)$) from the original i-th group of sensors ($y_i(t)$).

3.2.3 Stabilizability Assumption under State Feedback Control

A state feedback controller $u = k(x)$ that can asymptotically (and locally exponentially) stabilize the origin of the system of Eq. 3.1 when no disturbances are applied (the nominal closed-loop system, with $w(t) \equiv 0$) is assumed to exist. It is further assumed that this controller $k(x)$ meets all input constraints ($k(x) \in \mathbb{U}$) for all the initial states inside a given compact set containing the origin. These assumptions ensure the existence of class $\mathcal{K}$ functions $\alpha_i(\cdot)$, $i = 1,2,3,4$ and of a continuously differentiable Lyapunov function $V(x)$

for the closed-loop nominal system under the feedback control law $k(x)$ that satisfy:[29,79,94]

$$\begin{aligned} \alpha_1(|x|) \leq V(x) \leq \alpha_2(|x|) \\ \frac{\partial V(x)}{\partial x}(f(x)+g(x)k(x)) \leq -\alpha_3(|x|) \\ \left|\frac{\partial V(x)}{\partial x}\right| \leq \alpha_4(|x|) \end{aligned} \tag{3.5}$$

These inequalities hold for all $x \in \mathbb{D} \subseteq \mathbb{R}^n$ where $\mathbb{D}$ is an open neighborhood of the origin. The region of attraction of the nominal closed-loop system under the controller $k(x)$ is estimated as a level set of a Lyapunov function $V(x)$ for this closed-loop system ($\Omega_\rho \subseteq \mathbb{D}$) and is termed the "stability region."

3.2.4 Lyapunov-based Economic Model Predictive Control

This section describes the mathematical formulation of Lyapunov-based economic model predictive control (LEMPC),[65] a control strategy that will be used in this work to develop the structure and stability properties of a controller that can account for real-time preventive sensor maintenance. LEMPC is an optimization-based control methodology that calculates

an input trajectory based on the following optimization problem:

$$\max_{u\in S(\Delta)} \quad \int_{t_k}^{t_{k+N}} L_e(\tilde{x}(\tau),u(\tau))\,d\tau \tag{3.6a}$$

$$\text{s.t.} \quad \dot{\tilde{x}}(t) = f(\tilde{x}(t)) + g(\tilde{x}(t))u(t) \tag{3.6b}$$

$$\tilde{x}(t_k) = x(t_k) \tag{3.6c}$$

$$u(t) \in \mathbb{U}, \forall t \in [t_k, t_{k+N}) \tag{3.6d}$$

$$V(\tilde{x}(t)) \leq \rho_e, \forall t \in [t_k, t_{k+N})$$

$$\text{if } V(x(t_k)) \leq \rho_e \tag{3.6e}$$

$$\frac{\partial V}{\partial x}(f(x(t_k)) + g(x(t_k))u(t_k)) \leq \frac{\partial V}{\partial x}(f(x(t_k)) + g(x(t_k))k(x(t_k))),$$

$$\text{if } V(x(t_k)) > \rho_e \tag{3.6f}$$

The LEMPC maximizes the economics-based objective function in Eq. 3.6a to find the optimal value of the input u within the set $S(\Delta)$, which denotes the set of all piecewise constant input trajectories with period Δ. The input u must be maintained in the set of allowable inputs $\mathbb{U}$ per Eq. 3.6d, and also must cause the predicted state trajectory $\tilde{x}$ (from Eq. 3.6b) to satisfy the stability constraints of Eqs. 3.6e and 3.6f. Eqs. 3.6e and 3.6f define two modes of operation of the LEMPC, depending on the measured value $x(t_k)$ (Eq. 3.6c) of the actual process system state at time t_k, the time at the beginning of a sampling period Δ. The first mode (mode 1) maintains the state within the level set Ω_{ρ_e} of the Lyapunov function V, where $\Omega_{\rho_e} \subset \Omega_\rho$. The set Ω_{ρ_e} is a region within which, if the process state at the beginning of a sampling period is within Ω_{ρ_e}, the process state at the end of the sampling period will still be within Ω_ρ even if bounded process noise is present. If the process state is not in Ω_{ρ_e} at the beginning of a sampling period, the constraint of Eq. 3.6f, which represents mode 2, is activated. This constraint forces the time derivative of the Lyapunov function V along the trajectories of the nominal closed-loop system under LEMPC at the

time t_k to decrease by at least as much as the time derivative of the Lyapunov function along the trajectories of the closed-loop system under the controller $k(x)$ at time t_k. The constraint of Eq. 3.6f is guaranteed to drive the closed-loop system state under LEMPC from $\Omega_\rho \backslash \Omega_{\rho_e}$ into Ω_{ρ_e} in finite time.

LEMPC is a receding-horizon strategy, which means that it receives a measurement of the process state x at the current time t_k, solves the optimization problem of Eq. 3.6 for the trajectory of u throughout the (finite) N sampling periods in the prediction horizon, and then only implements $u^*(t_k)$, the value of u for the first sampling period (sample-and-hold implementation). At the beginning of the next sampling period, the LEMPC receives a new state measurement and is re-solved. The two-mode LEMPC design maintains stability of the closed-loop system in the sense that the state trajectories are always within Ω_ρ for any initial condition within this stability region.[65]

3.2.5 Observability Assumption

For both the i-th and j-th state estimation structures, it is assumed that there exists a deterministic observer that takes the following general form (to facilitate the presentation, the subscript i/j is used to denote that an observer, which is required to satisfy specific assumptions given below, is defined for both the i-th and the j-th groups of sensors):

$$\dot{z}_{i/j}(t) = F_{i/j}(\varepsilon_{i/j}, z_{i/j}, y_{i/j}) \tag{3.7}$$

where $z_{i/j}(t)$ are the observer states which are estimates of the actual system states, $y_{i/j}$ is the output measurement vector and $\varepsilon_{i/j}$ are positive parameters. When the state feedback controller $u = k(x)$ uses state estimates from the observers, it becomes an output feedback controller: $\dot{z}_{i/j} = F(\varepsilon_{i/j}, z_{i/j}, y_{i/j})$, $u = k(z_{i/j})$. The following assumptions are made:

Assumption 3.1 (c.f.[49])

(1) there exist positive constants θ_w^*, $\theta_{vi/j}^*$ *such that for each pair* $\{\theta_w, \theta_{vi/j}\}$ *with* $\theta_w \leq \theta_w^*$, $\theta_{vi/j} \leq \theta_{vi/j}^*$, *there exist* $0 < \rho_{1i/j} < \rho$, $e_{m0i/j} > 0$, $\varepsilon_{Li/j}^* > 0$, $\varepsilon_{Ui/j}^* > 0$ *such that if* $x(0) \in \Omega_{\rho_{1i/j}}$, $|z_{i/j}(0) - x(0)| \leq e_{m0i/j}$ *and* $\varepsilon_{i/j} \in (\varepsilon_{Li/j}^*, \varepsilon_{Ui/j}^*)$, *the trajectories of the closed-loop system are bounded in* Ω_ρ *for all* $t \geq 0$*;*

(2) and there exists $e_{mi/j}^* > 0$ *such that for each* $e_{mi/j} \geq e_{mi/j}^*$, *there exists* $t_{bi/j}(\varepsilon_{i/j})$ *such that* $|z_{i/j}(t) - x(t)| \leq e_{mi/j}$ *for all* $t \geq t_{bi/j}(\varepsilon_{i/j})$.

An example of an observer for which these assumptions hold is a high-gain observer.[2] To increase the speed of estimation error convergence, the observer parameter $\varepsilon_{i/j}$ should be chosen as small as possible; however, when the parameter $\varepsilon_{i/j}$ is too small (i.e., the observer gain is too large), it will make the observer state estimate very sensitive to measurement noise. Thus, the observer parameter $\varepsilon_{i/j}$ must be picked to be small enough so that the estimation error is reduced as quickly as possible, but not so small that the state estimates are corrupted by the noise. In the remainder of this work, the estimate given by the observer $F_{i/j}$ will be denoted as $z_{i/j}$.

Remark 3.1 *Assumption 3.1 defines a state region (i.e.,* $\Omega_{\rho_{1i/j}}$*) from which the closed-loop system will be bounded in the stability region* Ω_ρ *for all initial conditions in* $\Omega_{\rho_{1i/j}}$ *and a required time length (i.e.,* $t_{bi/j}$*) which the observer needs to converge the state estimates to the actual process state values.*

3.3 State Estimation with Varying Number of Sensors

In this section, to compute the state estimates for both the *i*-th and *j*-th state estimation structures, the robust moving horizon estimation (RMHE) method is adopted with a deterministic observer used to calculate a confidence region. One of the deterministic observer

designs is the high-gain observer formulation for multiple-input multiple-output systems.[80] For the sake of brevity, only the RMHE formulation is provided below.

3.3.1 Robust Moving Horizon Estimation

To achieve considerable convergence speed of the state observer while significantly reducing its sensitivity to measurement noise, a robust moving horizon estimation (RMHE) scheme[95] is adopted with the following formulation:

$$\min_{\tilde{X}(t_k)} \sum_{i=k-N_e}^{k-1} |w(t_i)|^2_{Q^{-1}} + \sum_{i=k-N_e}^{k} |v(t_i)|^2_{R^{-1}} + V_T(t_{k-N_e}) \tag{3.8a}$$

$$\text{s.t. } \dot{\tilde{x}}(t) = f(\tilde{x}(t)) + g(\tilde{x}(t))u(t) + l(\tilde{x}(t))w(t), \tag{3.8b}$$

$$v(t) = y(t) - h(\tilde{x}(t)), \forall t \in [t_{k-N_e}, t_k], \tag{3.8c}$$

$$w(t) \in \mathbb{W},\ v(t) \in \mathbb{V},\ \tilde{x}(t) \in \Omega_\rho \tag{3.8d}$$

$$\dot{z} = F(\varepsilon, z, y) \tag{3.8e}$$

$$z(t_{k-1}) = \hat{x}^*_{RMHE}(t_{k-1}) \tag{3.8f}$$

$$|\tilde{x}(t_k) - z(t_k)| \leq \kappa |y(t_k) - h(z(t_k))| \tag{3.8g}$$

$$\tilde{X}(t_k) := \tilde{x}(t_{k-N_e}), \ldots, \tilde{x}(t_k) \tag{3.8h}$$

where N_e is the estimation horizon, κ is a positive adjustable parameter, Q is the covariance matrix for w, and R is the covariance matrix for v. The function $V_T(t_{k-N_e})$ is an arrival cost, which is a function that contains information on past process states, $\tilde{x}$ is the prediction of state x which follows the dynamic model in Eq. 3.8b, $y(t_k)$ is the vector of measured outputs at time t_k, and $z(t_k)$ is the estimate of the process states from the deterministic state observer of Eq. 3.8e at time t_k based on continuous measurement of the output vector $y(t)$. The value of the observer state at t_{k-1} is initialized with the optimal estimate of the state

$\hat{x}^*_{RMHE}(t_{k-1})$ from the RMHE at time t_{k-1} (Eq. 3.8f). This RMHE scheme is implemented with a finite horizon by approximating $w(t)$ and $v(t)$ as piecewise constant functions with sampling period Δ.

The RMHE is evaluated at time instants $\{t_{k\geq 0}\}$. It explicitly uses distribution/boundedness information on w, v, and x by considering that the most recent N_e measurements and past measurements are accounted for in the arrival cost $V_T(t_{k-N_e})$. The RMHE scheme optimizes the state estimate within a confidence region by maintaining the difference between the predicted and observer states within the region specified by Eq. 3.8g. In this way, the RMHE inherits the robustness properties of the deterministic observer and gives estimates with bounded errors. The solution to the optimization problem gives the optimal estimate of the current state which is denoted by:

$$\hat{x}^*_{RMHE}(t_k) = \tilde{x}^*(t_k) \tag{3.9}$$

3.4 Preventive Sensor Maintenance via RMHE-based LEMPC

We assume that the process operates under the RMHE-based LEMPC system with q_i sensors on-line (i-th state estimation structure); at t_m, one or more sensors are taken off-line for preventive maintenance and subsequently, the RMHE-based LEMPC system with q_j sensors (j-th state estimation structure) is used. We note that the case that the sensors are brought back on-line could also be handled within this framework. In this section, the details are provided for the RMHE-based LEMPC design that facilitates preventive sensor maintenance, and in addition, stability of the process of Eq. 3.1 in closed-loop with such a controller is proved under the assumptions to be given below.

3.4.1 RMHE-based LEMPC Design

As a result of the considered bounded process noise and uncertainties in the state estimation, subsets of the stability region Ω_ρ will be used to bound the process states in the design of the RMHE-based LEMPC. Specifically, the sets are defined as follows: $\Omega_{\rho_{ei}}$ is the subset of Ω_ρ for the state estimation based on the i-th group of sensors and $\Omega_{\rho_{ej}}$ is the subset of Ω_ρ under the state estimation based on the j-th group of sensors. To deal with the process uncertainty and measurement noise when the sensor state estimation structure changes from the i-th group of sensors to the j-th group of sensors, we need to ensure that the process state is driven into the new operation region $\Omega_{\rho_{ej}}$ by the time the available sensor group changes at $t = t_m$. Specifically, the RMHE-based LEMPC drives the process state into the suitable operation region $\Omega_{\rho_{ej}}$ by the time the q_j sensors are used to determine the measurement $y_j(t)$. Once the j-th group of sensors is active, the RMHE method based on the new observer denoted as F_j using the j-th group of sensors and the corresponding new state measurement vector, $y_j(t)$, is used to provide the optimal state estimate $\hat{x}^*_{RMHE}(t_k)$ to the RMHE-based LEMPC. To facilitate practical implementation, we assume that $t_{bi/j}$ is an integer multiple of the sampling time, Δ, and $t_m \geq t_{bi/j}$ so that the process state estimation can converge before the available number of sensors changes.

The proposed RMHE-based LEMPC scheme can incorporate these issues that arise

from real-time preventive sensor maintenance by solving the following

$$\max_{u\in S(\Delta)} \quad \int_{t_k}^{t_{k+N}} L_e(\tilde{x}(\tau),u(\tau))\,d\tau \tag{3.10a}$$

$$\text{s.t.} \quad \dot{\tilde{x}}(t) = f(\tilde{x}(t)) + g(\tilde{x}(t))u(t), \tag{3.10b}$$

$$\tilde{x}(t_k) = \begin{cases} z_i(t_k), & \text{if } t_k < t_{bi} \\ \hat{x}^*_{RMHEi}(t_k), & \text{if } t_{bi} \le t_k < t_m \end{cases} \tag{3.10c}$$

$$u(t) \in \mathbb{U},\ \forall t \in [t_k, t_{k+N}) \tag{3.10d}$$

$$V(\tilde{x}(t)) \le \rho_{ei},\ \forall t \in [t_k, t_{k+N}) \quad \text{if } V(\hat{x}(t_k)) \le \rho_{ei} \text{ and } t_k < t_m - t_s \tag{3.10e}$$

$$\frac{\partial V}{\partial x}(f(\hat{x}(t_k)) + g(\hat{x}(t_k))u(t_k)) \le \frac{\partial V}{\partial x}(f(\hat{x}(t_k)) + g(\hat{x}(t_k))k(\hat{x}(t_k))), \quad \text{if } V(\hat{x}(t_k)) > \rho_{ei} \text{ or } t_k \ge t_m - t_s \tag{3.10f}$$

where the notation follows that in Eq. 3.6. When $t < t_{bi}$, state estimates, $z_i(t)$, are provided by an observer denoted as F_i using the i-th group of sensors. When $t_{bi} \le t < t_m$, the robust moving horizon estimation based on the observer F_i is utilized to provide the state estimate, which is denoted $\hat{x}^*_{RMHEi}(t)$, to the RMHE-based LEMPC. After t_m, the RMHE-based LEMPC problem is defined similarly to Eq. 3.10 and is based on the observer F_j (i.e., for $t \in [t_m, t_m + t_{bj})$, the state estimate is provided by the observer F_j and for $t \ge t_m + t_{bj}$, the state estimate is provided by the RMHE based on the observer F_j).

The mode 1 and mode 2 Lyapunov-based constraints of Eq. 3.6 are modified for the RMHE-based LEMPC strategy to account for the changing number of sensors. The mode 2 constraint of the RMHE-based LEMPC is triggered not only if the state is outside $\Omega_{\rho_{ei}}$, but also when the time is between $t_m - t_s$ and t_m. This adjustment to the constraints is made for stability reasons which are explained further in the "Stability Analysis" subsection

below (i.e., $t_s > 0$ is selected such that the RMHE-based LEMPC operates in mode 2 for sufficiently long to ensure closed-loop stability after t_m).

Remark 3.2 *The objective of this work is to propose a control framework that integrates process economic optimization, process control, and preventive sensor maintenance. Because EMPC is a control scheme that integrates economic optimization within the context of feedback control, it has been chosen for use as the controller for this work. Also, it is important to point out that EMPC may be considered a more general form of model predictive control (MPC) than tracking MPC, which uses a positive definite cost function with respect to a pre-specified reference trajectory or set-point. While other MPC schemes may be considered in place of EMPC for preventive sensor maintenance, the specific EMPC scheme considered (Lyapunov-based EMPC) may dictate a time-varying operating policy along with allowing for closed-loop stability guarantees. Furthermore, as the available number of sensors that are on-line changes, the state estimation problem must change to account for the varying number of measurements, which is not an issue of whether EMPC or MPC is used, but rather, an issue of the estimation scheme design to account for a varying number of measurements.*

Remark 3.3 *While the integration of scheduling and control has become a popular research topic in the process control community, it is not immediately clear what, if any, benefit would be achieved by integrating scheduling of sensor maintenance tasks into the proposed control framework because it is likely that the use of a scheduler or another decision-maker would be used in determining which sensor needs to be taken off-line for maintenance to minimize the impact of process performance degradation. The scheduler may be based on the life-cycle data of sensors, the observability of the process which has one or more sensors under maintenance and the priority of different sensors. Nevertheless, closed-loop simulations like the type performed in the example section may help to develop*

a plan/schedule for sensor maintenance based on stability and economics concerns.

3.4.2 Implementation Strategy

The implementation strategy of the preventive sensor maintenance method is illustrated by Fig. 3.2. Specifically, the control system initially uses the i-th group of sensors where q_i ($q_i < n$) outputs are continuously measured to compose the measurement vector, y_i. A state estimation method is utilized to obtain the state estimate based on these q_i sensor measurements by either observer F_i or robust moving horizon estimation. Initially, the RMHE is not utilized until the state estimation error converges to a small value based on the observability assumption (i.e., up to $t = t_{bi}$ only the observer is utilized to provide state estimates to the RMHE-based LEMPC for the optimal input trajectory calculation). Then, starting from $t = t_{bi}$, the RMHE-based LEMPC takes advantage of the state estimate from the RMHE to compute the optimal input trajectories. At the same time, since the optimal state estimate from RMHE is expected to be more accurate after $t = t_{bi}$, the current state of the observer F_i is reset to be the optimal state estimate from RMHE at every sampling period. A similar RMHE implementation holds using F_j after the sensor group changes at t_m.

LEMPC is the proposed control framework for this preventive sensor maintenance problem because of its ability to economically optimize the process even while switching constraints as the on-line sensor groups are varied. The RMHE-based LEMPC is a receding horizon control strategy like the LEMPC of Eq. 3.6. The following algorithm describes the logic for the implementation of the RMHE-based LEMPC, including the change in the state estimation structure:

1. Initialize the observer F_i with $z_i(0)$ and implement the observer F_i continuously based on the continuous output measurement $y_i(t)$.

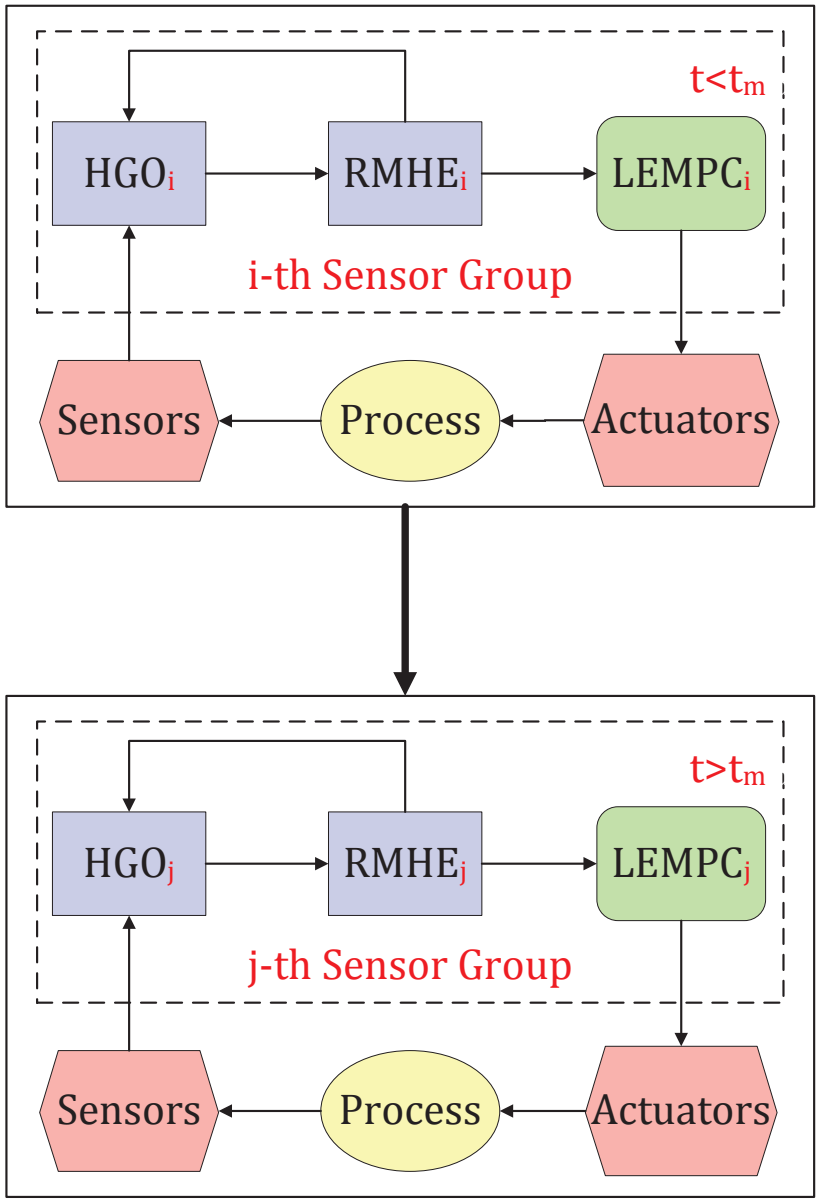

Figure 3.2: RMHE-based LEMPC system reconfiguration diagram for real-time preventive sensor maintenance (LEMPC$_i$ denotes the LEMPC scheme with the i-th sensor group based on the state estimates from the RMHE denoted as RMHE$_i$ and the HGO denoted as HGO$_i$; the same holds for LEMPC$_j$ but with i replaced by j).

2. At the current sampling instance t_k, if $t_k < t_{bi}$ or $t_k \in [t_m, t_m + t_{bj})$, go to Step 2.1; else if $t_k \in [t_{bi}, t_m)$ or $t_k \geq t_m + t_{bj}$, go to Step 2.2.

   2.1 The RMHE-based LEMPC receives the state estimate from the deterministic observer of Eq. 3.7; then go to Step 3.

   2.2 Based on the state estimate provided by the state observer of Eq. 3.7 and the output measurements at the current and previous sampling instants, the RMHE of Eq. 3.8 calculates the optimal state estimate $\hat{x}^*_{RMHE}(t_k)$ which is sent to the RMHE-based LEMPC; then go to Step 3.

3. If $x(t_k) \notin \Omega_{\rho_{ei}}$ and $t_k \in [0, t_m - t_s)$, or if $x(t_k) \notin \Omega_{\rho_{ej}}$ and $t_k \geq t_m$, or if $t_k \in [t_m - t_s, t_m)$, go to Step 3.1. Else, go to Step 3.2.

   3.1 The RMHE-based LEMPC operates in mode 2. Go to Step 4.

   3.2 The RMHE-based LEMPC operates in mode 1. Go to Step 4.

4. The RMHE-based LEMPC calculates N vectors of control actions, one for each sampling period in the prediction horizon $t \in [t_k, t_{k+N})$, and sends the control action $u^*(t_k)$ to the actuators for sample-and-hold implementation for one sampling period ($t \in [t_k, t_{k+1})$).

5. Go to Step 2 ($k \leftarrow k+1$).

Remark 3.4 *Variations of the maintenance schedule outside of the schedule considered in the paper can be handled by the proposed RMHE-based LEMPC scheme and are a conceptually straightforward extension of the present work. For example, a sensor maintenance schedule where some sensors are taken off-line at time t_m, but only a few are brought back on-line at a later time can be handled. For simplicity of presentation and notation, we have only presented the most (conceptually) challenging case where sensors are taken off-line*

at a time for preventive sensor maintenance. Nevertheless, all of the arguments could be repeated to handle the case where (some) sensors are being brought on-line through re-defining the notation (e.g., t_m now becomes the time at which the sensors are being brought back on-line). From a stability and observability perspective, the stabilizability and observability assumptions must be satisfied for the new sensor group, which may require the design of an additional deterministic observer and RMHE scheme for this sensor group.

Remark 3.5 *From a practical perspective, when sensors are being brought back on-line or taken off-line and the estimation problem changes, the estimation error may be sufficiently small such that one may use the RMHE to provide state estimates to the LEMPC starting at t_m (i.e., applying the deterministic observer from t_m to $t_m + t_{bj}$ may not be required). This is the case in the chemical process example presented in this work.*

Remark 3.6 *For output feedback-based control of nonlinear systems, typically what is required to prove closed-loop stability is that the estimation error converges sufficiently fast relative to the time-scale of the process dynamics (i.e., there is a time-scale separation between the estimation error dynamics and the process dynamics). This means that it takes very little time for the estimation error to converge. Therefore, there is little, if not no, limitation to conducting sensor maintenance after the state estimation problem has converged. For the case that a sensor is taken off-line before the estimation error has converged, one may simply disregard the measurements of the sensor(s) that will be taken off-line and formulate the estimation problem at $t = 0$ utilizing the measurements of sensors that will remain on-line. Moreover, for the proposed RMHE-based LEMPC scheme to work in either case (whether the sensor is taken off-line before the estimation error converges or the sensor is taken off-line after the state estimator has converged), the same assumptions need to be satisfied. We note that when the state estimation problem converges, it converges to a neighborhood of the actual state value (i.e., the estimated state never becomes identically*

equal to the actual state).

3.4.3 Stability Analysis

This section addresses the stability of the system of Eq. 3.1 when controlled by the RMHE-based LEMPC of Eq. 3.10. We first present several propositions and then summarize the main results in a theorem. Proposition 3.1 characterizes the continuity property of the Lyapunov function V. Proposition 3.2 characterizes the effects of bounded state estimation error and process noise. The proofs of these statements can be found in the sources referenced for each.

Proposition 3.1 (c.f.[102,105]) *Consider the Lyapunov function $V(\cdot)$. There exists a quadratic function $f_V(\cdot)$ such that*

$$V(x) \leq V(\hat{x}) + f_V(|x-\hat{x}|) \tag{3.11}$$

for all $x, \hat{x} \in \Omega_\rho$ with

$$f_V(s) = \alpha_4(\alpha_1^{-1}(\rho))s + M_v s^2 \tag{3.12}$$

where M_v is a positive constant.

Proposition 3.2 (c.f.[49]) *Consider the systems*

$$\begin{aligned} \dot{x}_a(t) &= f(x_a) + g(x_a)u(t) + l(x_a)w(t) \\ \dot{x}_b(t) &= f(x_b) + g(x_b)u(t) \end{aligned} \tag{3.13}$$

with initial states $|x_a(0) - x_b(0)| \leq \delta_{xi/j}$. There exists a function $f_W(\cdot,\cdot)$ such that

$$|x_a(t) - x_b(t)| \leq f_W(\delta_{xi/j}, t) \tag{3.14}$$

for all $x_a(t), x_b(t) \in \Omega_\rho$ *and* $u \in \mathbb{U}$, $w \in \mathbb{W}$ *with:*

$$f_W(s,\tau) := \left(s + \frac{M_l \theta_w}{L_f + L_g u^{\max}} \right) e^{(L_f + L_g u^{\max})\tau} - \frac{M_l \theta_w}{L_f + L_g u^{\max}} \tag{3.15}$$

where L_f, L_g, M_l *are positive constants associated with functions* f, g, l.

If the system is initialized using either the i-th sensor group or j-th sensor group and the sensor group does not change on-line throughout the length of operation, then closed-loop stability follows if certain conditions hold.[49] The following result provides sufficient conditions such that the closed-loop state under the RMHE-based LEMPC of Eq. 3.10 will be bounded in Ω_ρ for the case that the available sensors do not change on-line.

Proposition 3.3 ([49]) *Consider the system of Eq. 3.1 in closed-loop under the RMHE-based LEMPC of Eq. 3.10 based on an observer satisfying Assumption 3.1 (formulated for either the i-th sensor group or the j-th sensor group) and a controller that renders the origin of the closed-loop system asymptotically (and locally exponentially) stable under state feedback and continuous implementation. Let* $\theta_w \leq \theta_w^*$, $\theta_{vi/j} \leq \theta_{vi/j}^*$, $\varepsilon_{i/j} \in (\varepsilon_{Li/j}^*, \varepsilon_{Ui/j}^*)$ *and* $|z_{i/j}(0) - x(0)| \leq e_{m0i/j}$. *Also, let* $\varepsilon_w > 0$, $\Delta > 0$ *and* $\rho > \rho_{1i/j} > \rho_{ei/j} > \rho_{\min,i/j} > \rho_{si/j} > 0$ *and* $\kappa_{i/j} \geq 0$ *satisfy the following conditions:*

$$\rho_{ei/j} \leq \rho - \max\{f_V(f_W(\delta_{xi/j}, \Delta)) + f_V(\delta_{xi/j}), M t_{bi/j} \alpha_4(\alpha_1^{-1}(\rho))\}, \tag{3.16}$$

$$-\alpha_3(\alpha_2^{-1}(\rho_{si/j})) + \left(L_V^f + L_V^g u^{\max} \right)(M\Delta + \delta_{xi/j}) + M_V^l \theta_w \leq -\varepsilon_w/\Delta \tag{3.17}$$

where $\delta_{xi/j} = (\kappa_{i/j} L_{hi/j} + 1) e_{mi/j} + \kappa_{i/j} \theta_{vi/j}$, $L_{hi/j}$, L_V^f, L_V^g *are Lipschitz constants associated with* $h_{i/j}$, $\frac{\partial V}{\partial x} f$, *and* $\frac{\partial V}{\partial x} g$, *respectively,* M *is a constant that bounds the time derivative of* x *(i.e.,* $|\dot{x}| \leq M$*) and* M_V^l *is a constant that bounds* $\left| \frac{\partial V}{\partial x} l \right|$ *for* $x \in \Omega_\rho$. *Then, if* $x(0) \in \Omega_{\rho_{ei/j}}$, *then* $x(t) \in \Omega_\rho$ *for all* $t \geq 0$. *Moreover, if after some time, the RMHE-based LEMPC oper-*

ates in mode 2 only then the state is ultimately bounded in $\Omega_{\rho_{\min,i/j}}$.

To cope with the changing number of sensors at t_m, the state needs to be forced to a compact set containing the origin (i.e., $\Omega_{\rho_{ej}}$) in preparation for the switch from sensor group i to sensor group j. This is addressed by enforcing the mode 2 constraint in the RMHE-based LEMPC of Eq. 3.10 from $t_m - t_s$ to t_m. If $x(t_m) \in \Omega_{\rho_{ej}}$, we can apply the results of Proposition 3.3 and thus, guarantee that the closed-loop state is bounded in Ω_ρ. This result is stated in the following theorem.

Theorem 3.1 *Let* $\rho_{\min,i} \leq \rho_{ej}$ ($\Omega_{\rho_{\min,i}} \subseteq \Omega_{\rho_{ej}}$), $e_{mi} \leq e_{m0j}$, *and the assumptions of Proposition 3.3 be satisfied for the i-th and j-th sensor groups. If* $t_s > 0$ *is sufficiently large and* $x(0) \in \Omega_{\rho_{ei}}$, *then the closed-loop state under the RMHE-based LEMPC of Eq. 3.10 is bounded in* Ω_ρ *for* $t \geq 0$.

Proof 3.1 *It is necessary to show that the estimation error is less than* e_{m0j} *at* t_m *and that the RMHE-based LEMPC drives the state of the closed-loop system into* $\Omega_{\rho_{ej}}$ *by* t_m. *If both of these can be shown, Proposition 3.3 states that the closed-loop trajectory for* $t > t_m$ *will remain bounded in* Ω_ρ.

After t_{bi} *(i.e., after the deterministic observer* F_i *has converged), the estimation error is bounded by* e_{mi} *owing to the properties of the deterministic observer (Assumption 3.1). If the deterministic observer* F_j *is initialized at* t_m *with the state estimate computed by the RMHE for the i-th sensor group at* t_m, *then the initial error when* F_j *takes over at* t_m *is bounded by* $|z(t_m) - x(t_m)| \leq e_{mi} \leq e_{m0j}$ *if* $e_{mi} \leq e_{m0j}$. *Thus, the estimation error is less than* e_{m0j} *at* t_m.

It is possible for the RMHE-based LEMPC with mode 2 operation only, in a finite but sufficiently long time interval, to drive the state from any initial condition in Ω_ρ *into* $\Omega_{\rho_{\min,i}}$ *and maintain the state within that set (i.e.,* $\Omega_{\rho_{\min,i}}$ *is forward invariant under the*

RMHE-based LEMPC). This follows from the fact that the state is ultimately bounded in $\Omega_{\rho_{\min,i}}$ *(Proposition 3.3) if the RMHE-based LEMPC operates exclusively in mode 2 and no changes are made to the sensors throughout the length of operation (see, also, the proof of [49, Theorem 1] for a complete proof of this fact). If* $\rho_{\min,i} \leq \rho_{ej}$*, then there exists* $N^* \in \mathbb{I}_+$ *such that under the RMHE-based LEMPC of Eq. 3.10 operating under mode 2 only* $x(N^*\Delta) \in \Omega_{\rho_{\min,i}} \subseteq \Omega_{\rho_{ej}}$ *for all* $x(0) \in \Omega_{\rho_{ei}}$*. If* $t_s \geq N^*\Delta$*, then* $x(t_m) \in \Omega_{\rho_{\min,i}} \subseteq \Omega_{\rho_{ej}}$ *under the RMHE-based LEMPC of Eq. 3.10. From Proposition 3.3, boundedness of the closed-loop state in* Ω_ρ *under the RMHE-based LEMPC when the available sensors change at* t_m *follows.*

Remark 3.7 *In terms of the relationship between* $t_{bi/j}$ *and* $N_e\Delta$*, we note here that when* $t \geq t_{bi/j}$*, the RMHE is activated and its horizon length is chosen as* $min\{\frac{t_{bi/j}}{\Delta}, N_e\}$ *considering the assumption that* $t_{bi/j}$ *is a integer multiple of* Δ*. Based on this choice, after the RMHE is activated (i.e.,* $t \geq t_{bi/j}$*) it is possible for the process to have a time-varying horizon length for several sampling times if* $t_{bi/j} \leq N_e\Delta$*.*

3.5 Application to a Chemical Process Network

3.5.1 Description of the Chemical Process Network

The chemical process network from[47] is used to illustrate the design of the proposed RMHE-based LEMPC and its usefulness when sensor preventive maintenance is scheduled. The process consists of three vessels: two continuously stirred tank reactors (CSTRs) in series, and a flash tank that receives the effluent from the second CSTR. The process is depicted by the process flow diagram of Fig. 3.3. A second-order reaction with rate r occurs in the CSTRs:

$$A \xrightarrow{r} B$$

Both CSTRs (CSTR-1 and CSTR-2) receive fresh feeds of the reactant A in an inert solvent C at flow rates F_{10} and F_{20} with concentrations C_{A10} and C_{A20}, respectively. In addition, to recover unreacted A, CSTR-1 receives recycled condensed vapor at flow rate F_r from the flash tank (SEP). The desired product B is obtained from the liquid that exits the flash tank. The temperature in the vessels is adjusted by controlling the heating/cooling rate $Q_j,\ j = 1,2,3$ to each of the vessels. It is assumed that the heat of reaction and heat capacity are constant in the temperature range considered and that the liquid has constant density such that all three vessels have static holdup. In the separator, the reaction rate of the reaction $A \xrightarrow{r} B$ is negligible. Material and energy balances were used to derive the following dynamic equations for the system:

$$\frac{dT_1}{dt} = \frac{F_{10}}{V_1}(T_{10} - T_1) + \frac{F_r}{V_1}(T_3 - T_1) + \frac{-\Delta H}{\rho C_p} k e^{\frac{-E}{RT_1}} C_{A1}^2 + \frac{Q_1}{\rho C_p V_1} \tag{3.18a}$$

$$\frac{dC_{A1}}{dt} = \frac{F_{10}}{V_1}(C_{A10} - C_{A1}) + \frac{F_r}{V_1}(C_{Ar} - C_{A1}) - k e^{\frac{-E}{RT_1}} C_{A1}^2 \tag{3.18b}$$

$$\frac{dC_{B1}}{dt} = \frac{-F_{10}}{V_1} C_{B1} + \frac{F_r}{V_1}(C_{Br} - C_{B1}) + k e^{\frac{-E}{RT_1}} C_{A1}^2 \tag{3.18c}$$

$$\frac{dT_2}{dt} = \frac{F_1}{V_2}(T_1 - T_2) + \frac{F_{20}}{V_2}(T_{20} - T_2) + \frac{-\Delta H}{\rho C_p} k e^{\frac{-E}{RT_2}} C_{A2}^2 + \frac{Q_2}{\rho C_p V_2} \tag{3.18d}$$

$$\frac{dC_{A2}}{dt} = \frac{F_1}{V_2}(C_{A1} - C_{A2}) + \frac{F_{20}}{V_2}(C_{A20} - C_{A2}) - k e^{\frac{-E}{RT_2}} C_{A2}^2 \tag{3.18e}$$

$$\frac{dC_{B2}}{dt} = \frac{F_1}{V_2}(C_{B1} - C_{B2}) - \frac{F_{20}}{V_2} C_{B2} + k e^{\frac{-E}{RT_2}} C_{A2}^2 \tag{3.18f}$$

$$\frac{dT_3}{dt} = \frac{F_2}{V_3}(T_2 - T_3) - \frac{\Delta H_{vap} F_{rm}}{\rho C_p V_3} + \frac{Q_3}{\rho C_p V_3} \tag{3.18g}$$

$$\frac{dC_{A3}}{dt} = \frac{F_2}{V_3}(C_{A2} - C_{A3}) - \frac{F_r}{V_3}(C_{Ar} - C_{A3}) \tag{3.18h}$$

$$\frac{dC_{B3}}{dt} = \frac{F_2}{V_3}(C_{B2} - C_{B3}) - \frac{F_r}{V_3}(C_{Br} - C_{B3}) \tag{3.18i}$$

where the temperatures of vessels $j = 1,2,3$, corresponding to CSTR-1, CSTR-2, and SEP, respectively, are denoted as T_j, C_{Aj} and C_{Bj} are the concentrations of species A and B in

Table 3.1: Description of process parameters and their values for the reactor and separator process network.[47]

Parameter/Value	Description
$F_{10} = 5.0\ m^3/h$	Flow rate of CSTR-1 inlet
$F_{20} = 5.0\ m^3/h$	Flow rate of CSTR-2 inlet
$F_r = 2.0\ m^3/h$	Recycle flow rate of SEP
$T_{10} = 300\ K$	Temperature of F_{10}
$T_{20} = 300\ K$	Temperature of F_{20}
$V_1 = 5.0\ m^3$	Volume of CSTR-1
$V_2 = 5.0\ m^3$	Volume of CSTR-2
$V_3 = 3.0\ m^3$	Volume of SEP
$k = 1.9 \times 10^9\ m^3/(kmol\ h)$	Pre-exponential factor
$E = 7.1 \times 10^4\ kJ/kmol$	Activation energy
$\Delta H = -7.8 \times 10^3\ kJ/kmol$	Heat of reaction
$\Delta H_{vap} = 4.02 \times 10^4\ kJ/kmol$	Heat of vaporization
$C_p = 0.231\ kJ/(kg\ K)$	Heat capacity
$R = 8.314\ kJ/(kmol\ K)$	Gas constant
$\rho = 1000\ kg/m^3$	Liquid solution density
$\alpha_A = 3.0$	Relative volatility of A
$\alpha_B = 0.8$	Relative volatility of B
$\alpha_C = 1.0$	Relative volatility of C
$M_A = 18\ kg/kmol$	Molecular weight of A
$M_B = 18\ kg/kmol$	Molecular weight of B
$M_C = 40\ kg/kmol$	Molecular weight of C

vessel j, and the molar flow rate of the recycle stream is F_r. The parameter notation and values are given in Table 3.1. The flow rates F_1, F_2, and F_3 are the outlet flow rates from CSTR-1, CSTR-2, and SEP, respectively, and their values can be obtained by setting the sums of the flow rates into each vessel equal to the sums of the flow rates out of each vessel because of the constant fluid density assumption used with the mass balances.

It is assumed that approximating the relative volatilities of A, B, and C as constants results in a sufficiently accurate model for this process. Under that assumption, the flash

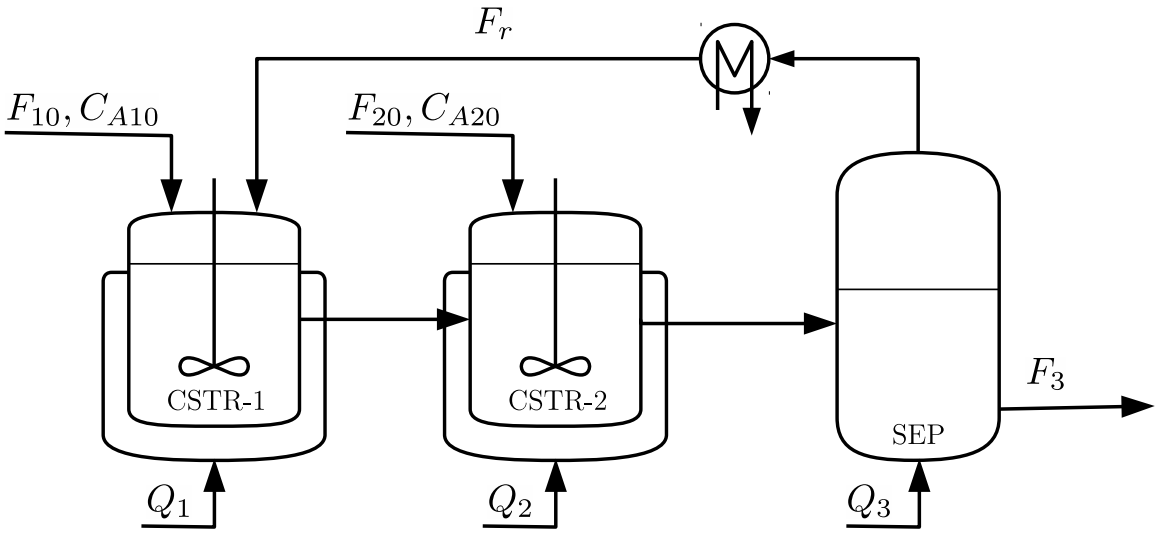

Figure 3.3: Process flow diagram of the CSTR-CSTR-Separator process network from.[47]

separator overhead composition can be described using algebraic equations:

$$C_{C3} = (\rho - C_{A3}M_A - C_{B3}M_B)/M_C \tag{3.19a}$$

$$C_{ir} = \frac{\alpha_i \rho C_{i3}}{\alpha_A C_{A3} M_A + \alpha_B C_{B3} M_B + \alpha_C C_{C3} M_C},\ i = A,\ B,\ C \tag{3.19b}$$

$$F_{rm} = F_r(C_{Ar} + C_{Br} + C_{Cr}) \tag{3.19c}$$

where α_i and C_{ir} are the relative volatility and the overhead vapor concentration of each species, respectively. F_{rm} is the molar flow rate of the recycle stream.

3.5.2 Control Objectives and Process Economics

The five manipulated inputs for the process are the heat rates Q_j to vessels $j = 1, 2, 3$ and the concentrations C_{A10} and C_{A20} of A in the fresh feeds to CSTR-1 and CSTR-2,

respectively. These inputs are bounded as follows:

$$\left|Q_j\right| \leq 1.0 \times 10^5 \, kJ/h, \;\; j = 1, 2 \tag{3.20a}$$

$$2.2 \times 10^6 \leq Q_3 \leq 2.6 \times 10^6 \, kJ/h \tag{3.20b}$$

$$0.5 \leq C_{Aj0} \leq 7.5 \, kmol/m^3, \;\; j = 1, 2 \tag{3.20c}$$

where the input vector has the form $u = [Q_1 \, Q_2 \, Q_3 \, C_{A10} \, C_{A20}]^T = [u_1 \, u_2 \, u_3 \, u_4 \, u_5]^T$. In addition to the input constraints, state constraints are imposed on the operating temperature of the two CSTRs and of the separator of the form:

$$370 \leq T_j \leq 395 \; K, \;\; j = 1, 2 \; , \tag{3.21a}$$

$$380 \leq T_3 \leq 400 \; K \; . \tag{3.21b}$$

The control objective is to maximize the revenue per unit cost under the proposed RMHE-based LEMPC while accounting for preventive sensor maintenance. The process economic objective function chosen to accomplish this goal is:

$$L(x,u) = \frac{P_p C_{B3}}{P_h(|Q_1| + |Q_2| + |Q_3|) + P_m(F_{10} C_{A10} + F_{20} C_{A20})} \tag{3.22}$$

where the unit price of product is $P_p = 10$, the unit price of reactant material is $P_m = 2$, and the unit price of heat supply/removal is $P_h = 1.0 \times 10^{-4}$. The same pricing is taken to apply for both heating and cooling, but this assumption does not limit the essence of the results of this study and can be readily relaxed.

The economically optimal steady-state is determined so that its stability region can be used in the RMHE-based LEMPC. The economically optimal steady-state is determined

by solving:

$$\max_{x_s,u_s} \quad L(x_s,u_s) \tag{3.23a}$$

$$\text{s.t.} \quad f(x_s)+g(x_s)u_s=0 \tag{3.23b}$$

$$u_s \in \mathbb{U} \tag{3.23c}$$

$$x_s \in \mathbb{X} \tag{3.23d}$$

where $L(x_s,u_s)$ is the revenue per unit cost that will be used as the RMHE-based LEMPC objective (Eq. 3.22). The algebraic equation in Eq. 3.23b provides the steady-state solutions to the nominal input-affine dynamic system of Eq. 3.18, and the constraints in Eqs. 3.23c-3.23d correspond to the input constraints of Eq. 3.20 and the state constraints of Eq. 3.21, respectively. The solution to this steady-state optimization problem is x_s^*, which satisfies Eq. 3.23b when paired with u_s^*:

$$\begin{aligned} x_s^* &= \begin{bmatrix} T_{1s}^* & C_{A1s}^* & C_{B1s}^* & T_{2s}^* & C_{A2s}^* & C_{B2s}^* & T_{3s}^* & C_{A3s}^* & C_{B3s}^* \end{bmatrix}^T \\ &= \begin{bmatrix} 395 & 2.32 & 2.17 & 395 & 2.75 & 2.15 & 380 & 1.88 & 2.31 \end{bmatrix}^T, \\ u_s^* &= \begin{bmatrix} Q_{1s}^* & Q_{2s}^* & Q_{3s}^* & C_{A10s}^* & C_{A20s}^* \end{bmatrix}^T \\ &= \begin{bmatrix} -3.25\times10^3 & -1.08\times10^3 & 2.2\times10^6 & 0.5 & 0.5 \end{bmatrix}^T. \end{aligned} \tag{3.24}$$

The units for each variable in the optimal steady-state vector x_s^* and optimal steady-state input vector u_s^* are the same as for the corresponding variables in Table 3.1. The steady-state of Eq. 3.24 is open-loop unstable.

It is assumed that the sensors in this chemical process example undergo routine sensor preventive maintenance to prevent the potentially large economic losses that could occur

due to the consequences of sensor failure, such as product contamination or plant shut-down. Thus, we assume that the given process can be safely operated with the remaining sensors when the maintenance procedures considered in this example are performed (the process can continue to be safely operated even as certain sensors are taken off-line).

The process is outfitted with sensors that provide measurements of C_{A3}, C_{B1}, C_{B2}, C_{B3}, T_1, T_2 and T_3. A state estimation method is applied to the process to compute state estimates of C_{A1} and C_{A2}. There is a scheduled maintenance task on the sensor that measures C_{A3} at $t_m = 0.3\ h$ (i.e., for $t \geq t_m$, the control system will not receive any measurements from the sensor of C_{A3} any longer). The sensors that provide the measurements of C_{B1}, C_{B2}, C_{B3}, T_1, T_2 and T_3 will continue to be available to the control system and the states C_{A1}, C_{A2} and C_{A3} need to be estimated. Thus, the first sensor group consists of all the available sensors and the second sensor group consists of all the available sensors except the sensor that measures C_{A3}.

3.5.3 Deterministic Observer and RMHE Design

Here, we use a high-gain observer (HGO) as the deterministic observer in the RMHE design. We note that the HGO changes after the preventive sensor maintenance is conducted at t_m. We will use HGO-1 and HGO-2 to denote the high-gain observers formulated for the first and second sensor groups, respectively. The design of HGO-2 (see[80]) is provided here, and the design of HGO-1 follows from the design of HGO-2. The measurement vector after the C_{A3} sensor is taken off-line at t_m is defined as $y = [h_1(x)\ h_2(x)\ h_3(x)\ h_4(x)\ h_5(x)\ h_6(x)] = [T_1\ C_{B1}\ T_2\ C_{B2}\ T_3\ C_{B3}]$. To obtain the state estimates, a high-gain observer is formulated as

follows:

$$\frac{d\bar{z}_1}{dt} = \frac{\alpha_1}{\varepsilon}(y_1 - \bar{z}_1) \tag{3.25a}$$
$$\frac{d\bar{z}_2}{dt} = \frac{\alpha_2}{\varepsilon}(y_2 - \bar{z}_2) + \bar{z}_3 \tag{3.25b}$$
$$\frac{d\bar{z}_3}{dt} = \frac{\alpha_3}{\varepsilon^2}(y_2 - \bar{z}_2) \tag{3.25c}$$
$$\frac{d\bar{z}_4}{dt} = \frac{\alpha_4}{\varepsilon}(y_3 - \bar{z}_4) \tag{3.25d}$$
$$\frac{d\bar{z}_5}{dt} = \frac{\alpha_5}{\varepsilon}(y_4 - \bar{z}_5) + \bar{z}_6 \tag{3.25e}$$
$$\frac{d\bar{z}_6}{dt} = \frac{\alpha_6}{\varepsilon^2}(y_4 - \bar{z}_5) \tag{3.25f}$$
$$\frac{d\bar{z}_7}{dt} = \frac{\alpha_7}{\varepsilon}(y_5 - \bar{z}_7) \tag{3.25g}$$
$$\frac{d\bar{z}_8}{dt} = \frac{\alpha_8}{\varepsilon}(y_5 - \bar{z}_8) + \bar{z}_9 \tag{3.25h}$$
$$\frac{d\bar{z}_9}{dt} = \frac{\alpha_9}{\varepsilon^2}(y_6 - \bar{z}_8) \tag{3.25i}$$

where the observer states are defined as

$$\bar{z} = T(x) = [T_1\ C_{B1}\ \dot{C}_{B1}\ T_2\ C_{B2}\ \dot{C}_{B2}\ T_3\ C_{B3}\ \dot{C}_{B3}]^T$$

and the mapping $T : \mathbb{R}^n \to \mathbb{R}^n$ is an appropriately chosen invertible coordinate change. The design parameters of HGO-2 are ε, which is a small positive design parameter, and $\alpha = [\alpha_1\ \cdots\ \alpha_9]^T$. Based on the mapping $\bar{z} = T(x)$ of Eq. 3.25, the estimated state, $z = [z_1\ \cdots\ z_9]^T$, is derived as $z = T^{-1}(sat(\bar{z}))$ where $sat(\cdot)$ is a saturation function of the form:

$$sat(\bar{z}_i) := \begin{cases} \bar{z}_{i,m}, & \bar{z}_i \geq \bar{z}_{i,m} \\ \bar{z}_i, & -\bar{z}_{i,m} \leq \bar{z}_i \leq \bar{z}_{i,m} \\ -\bar{z}_{i,m}, & \bar{z}_i \leq -\bar{z}_{i,m} \end{cases} \tag{3.26}$$

where $\bar{z}_{i,m}$ ($i = 1,\ldots,9$) is the saturation limit of the transformed state $\bar{z}_i$. The saturation function is used to prevent the peaking phenomena.

The following design parameters for the HGOs and for the RMHE scheme of Eq. 3.8 were used in all case studies below. It was verified through extensive closed-loop simulations that these parameters achieved good estimation performance. The parameters of HGO-1 were chosen to be

$$[\alpha_1\ \alpha_2\ \alpha_3\ \alpha_4\ \alpha_5\ \alpha_6] = [2\ \ 15\ \ 10^{-2}\ \ 2\ \ 15\ \ 10^{-2}] \tag{3.27}$$

and $\varepsilon = 0.01$, and for HGO-2 :

$$[\alpha_1\ \alpha_2\ \alpha_3\ \alpha_4\ \alpha_5\ \alpha_6\ \alpha_7\ \alpha_8\ \alpha_9] = [1\ \ 10\ \ 10^{-2}\ \ 1\ \ 10\ \ 10^{-2}\ \ 1\ \ 10\ \ 10^{-2}] \tag{3.28}$$

and $\varepsilon = 0.01$. The design parameters of the RMHE of Eq. 3.8 were chosen as $\kappa = 0.4$ and $N_e = 8$. The estimation horizon was chosen so that acceptable estimation performance was achieved without the use of an arrival cost. In the subsequent sections, we use RMHE-1 to denote the RMHE designed based on HGO-1 and RMHE-2 to denote the RMHE designed based on HGO-2.

3.5.4 RMHE-based LEMPC Design Handling Real-Time Preventive Sensor Maintenance

A Lyapunov-based controller is designed for the process that can asymptotically stabilize the economically optimal steady-state. It will be used to define the Lyapunov-based constraints of the RMHE-based LEMPC. The heat rate inputs Q_1, Q_2, and Q_3 have a larger impact on closed-loop stability of this process system than the concentration inputs C_{A10} and C_{A20}. For this reason, the inputs in vector u_q ($u_q = [Q_1\ Q_2\ Q_3]^T$) are used to stabi-

lize the closed-loop system, while the inputs in vector u_c ($u_c = [C_{A10}\, C_{A20}]^T$) are primarily used to attain better economic performance of the closed-loop process and $u = [u_q^T\ u_c^T]^T$. The Lyapunov-based controller will be designed using different control laws for the heat rates and for the inlet concentrations. The heat rate inputs are controlled per the following feedback control law:[129]

$$k_{qi}(x) = \begin{cases} -\frac{L_f V + \sqrt{(L_f V)^2 + (L_{g_i} V)^4}}{(L_{g_i} V)^2} L_{g_i} V & \text{if } L_{g_i} V \neq 0 \\ 0 & \text{if } L_{g_i} V = 0 \end{cases} \tag{3.29}$$

for $i = 1,\ 2,\ 3$ where g_i denotes the i-th column of g and $L_f V = (\partial V/\partial x) f(x)$ and $L_{g_i} V = (\partial V/\partial x) g_i(x)$ denote the Lie derivatives of V with respect to the vector fields f and g_i, respectively. The elements of u_c per the Lyapunov-based strategy are $k_c(x) = [0.5\ 0.5]^T$. The full Lyapunov-based control law for all five inputs is $k(x) = [k_q^T(x)\ k_c^T(x)]^T$.

A quadratic function (i.e., $V(x) = (x - x_s^*)^T P (x - x_s^*)$) was chosen for the Lyapunov function of the process under the controller $k(x)$, and extensive closed-loop simulations under this controller facilitated the choice of the matrix P and an estimate of the stability region of the process under the $k(x)$ control law. The stability region estimate was made by choosing the largest level set of V within which $\dot{V} < 0$ along the trajectories of the closed-loop system. The positive definite matrix P is given by:

$$P = \text{diag}([10^{-3}\ \ 1.5\ \ 0.5\ \ 10^{-3}\ \ 1.5\ \ 0.5\ \ 10^{-3}\ \ 1.5\ \ 0.5]) \tag{3.30}$$

The stability region is estimated to be the level set Ω_ρ with $\rho = 12.4$. The subsets of the stability region Ω_ρ are estimated to be level sets: $\Omega_{\rho_{e1}}$ with $\rho_{e1} = 10$ and $\Omega_{\rho_{e2}}$ with $\rho_{e2} = 8$.

To deal with the scheduled preventive maintenance on the sensor of C_{A3} at $t_m = 0.3\ h$, the proposed RMHE-based LEMPC of Eq. 3.10 for this chemical process network has the

following form:

$$\max_{u \in S(\Delta)} \quad \int_{t_k}^{t_{k+8}} L(\tilde{x}(\tau), u(\tau))\, d\tau \tag{3.31a}$$

$$\text{s.t.} \quad \dot{\tilde{x}}(t) = f(\tilde{x}(t)) + g(\tilde{x}(t))u(t), \tag{3.31b}$$

$$\tilde{x}(t_k) = \begin{cases} \hat{x}_{HGO-1}(t_k), & \text{if } t_k < t_{b1} = 0.08 \\ \hat{x}^*_{RMHE-1}(t_k), & \text{if } 0.08 \leq t_k < 0.30 \end{cases} \tag{3.31c}$$

$$u(t) \in \mathbb{U},\ \forall t \in [t_k, t_{k+8}) \tag{3.31d}$$

$$\tilde{x}(t) \in \mathbb{X}, \forall t \in [t_k, t_{k+8}) \tag{3.31e}$$

$$V(\tilde{x}(t)) \leq 10, \forall t \in [t_k, t_{k+8})$$

$$\text{if } V(\hat{x}(t_k)) \leq 10 \text{ and } t_m \notin [t_k, t_{k+8}) \tag{3.31f}$$

$$\frac{\partial V}{\partial x}(f(\hat{x}(t_k)) + g(\hat{x}(t_k))u(t_k)) \leq \frac{\partial V}{\partial x}(f(\hat{x}(t_k)) + g(\hat{x}(t_k))k(\hat{x}(t_k))),$$

$$\text{if } (V(\hat{x}(t_k)) > 10 \text{ and } t_m \notin [t_k, t_{k+8}))$$

$$\text{or } (t_m \in [t_k, t_{k+8})) \tag{3.31g}$$

which is used for $t \in [0, t_m)$ and

$$\max_{u \in S(\Delta)} \quad \int_{t_k}^{t_{k+8}} L(\tilde{x}(\tau), u(\tau))\, d\tau \tag{3.32a}$$

$$\text{s.t.} \quad \dot{\tilde{x}}(t) = f(\tilde{x}(t)) + g(\tilde{x}(t))u(t), \tag{3.32b}$$

$$\tilde{x}(t_k) = \hat{x}^*_{RMHE-2}(t_k), \text{ if } t_k \geq 0.30 \tag{3.32c}$$

$$u(t) \in \mathbb{U}, \ \forall t \in [t_k, t_{k+8}) \tag{3.32d}$$

$$\tilde{x}(t) \in \mathbb{X}, \forall t \in [t_k, t_{k+8}) \tag{3.32e}$$

$$V(\tilde{x}(t)) \leq 8, \forall t \in [t_k, t_{k+8}) \quad \text{if } V(\hat{x}(t_k)) \leq 8 \tag{3.32f}$$

$$\frac{\partial V}{\partial x}(f(\hat{x}(t_k)) + g(\hat{x}(t_k))u(t_k)) \leq \frac{\partial V}{\partial x}(f(\hat{x}(t_k)) + g(\hat{x}(t_k))k(\hat{x}(t_k))), \quad \text{if } V(\hat{x}(t_k)) > 8 \tag{3.32g}$$

which is used for $t \geq t_m$. For this example, t_{b1} is estimated to be 0.08 h. Considering that this means $t_{b1} = N_e\Delta$ for this specific case, HGO-1 is utilized to provide the state estimates of C_{A1} and C_{A2} during the first N_e sampling times. For $t \geq 0.08$ h, RMHE-1 is activated to provide the estimates of C_{A1} and C_{A2} until $t_m = 0.3$ h. After $t_m = 0.3$ h, RMHE-2 is utilized to provide state estimates of not only C_{A1} and C_{A2} but also C_{A3} as well. RMHE-2 is immediately used at t_m to provide the state estimate to the LEMPC of Eq. 3.32 because the state estimation error is small at $t = t_m$, which was verified through simulations (i.e., applying HGO-2 from t_m to $t_m + t_{b2}$ to ensure the convergence of the estimation error to a small value was not needed for this particular example).

The sampling time used for the RMHE-based LEMPC is $\Delta = 0.01$ h and the prediction horizon used is $N = 8$. The optimization software Ipopt[139] was used to find a local solution to the RMHE-based LEMPC optimization problem. The simulations were carried out using the Java programming language in a Intel® i7, 3.40 GHz processor running a Windows 7

Professional system.

3.5.5 Case Studies

As we discussed in the introduction of this work, routine sensor replacement is necessary to avoid potential sensor failure which may bring production loss to the process. We now compare four case studies which a process operation manager may evaluate when weighing the risks, costs, and benefits of conducting a sensor maintenance procedure:

I. Process operation without preventive sensor maintenance on the sensor of C_{A3}.

II. Process operation with preventive sensor maintenance on the sensor of C_{A3} at $t_m = 0.3\ h$.

III. Process operation subject to faulty sensor readings of C_{A3} after $t_f = 0.5\ h$.

IV. Process operation with preventive maintenance of the sensor of C_{A3} at $t_m = 0.3\ h$ followed by preventive maintenance of the actuator of C_{A20} at $t_a = 0.6\ h$.

In these four case studies, the RMHE-based LEMPC formulation of Eqs. 3.31-3.32 is applied to the process of Eq. 3.18. The state estimation accuracy between the high-gain observer and the robust moving horizon estimation method is compared, and the RMHE-based LEMPC's ability to handle the preventive sensor maintenance task is demonstrated in all four cases; the process economic performance degradation is also evaluated for different cases under the preventive sensor maintenance.

To model the process and measurement noise, bounded Gaussian white noise is added to the process state and measurement values, respectively, with a zero mean and standard deviation $\sigma_{w,C_A} = \sigma_{w,C_B} = 0.05$, $\sigma_{w,T} = 5.0$, $\sigma_{v,C_A} = \sigma_{v,C_B} = 0.03$ and $\sigma_{v,T} = 5.0$, and subject to the bounds $\theta_{w,C_A} = \theta_{w,C_B} = 0.1\ kmol/m^3$, $\theta_{w,T} = 10.0\ K$, $\theta_{v,C_A} = \theta_{v,C_B} = 0.05\ kmol/m^3$

and $\theta_{v,T} = 5.0\,K$. For each case study, the same realization of the noise was used to compare the various control strategies.

Case I: RMHE vs HGO - No Preventive Sensor Maintenance

In the first case, we compare the state estimation performance between the RMHE method (Eq. 3.8) and the HGO method (HGO-1) for the process network of Eq. 3.18. For this case, no preventive sensor maintenance is completed. The RMHE method consists of the output feedback RMHE-based LEMPC of Eq. 3.31 with $t_m \to \infty$, while the HGO method consists of the output feedback RMHE-based LEMPC of Eq. 3.31 with $t_m \to \infty$ and $t_{b1} \to \infty$ (i.e., HGO-1 provides the state estimate to the LEMPC for all time).

HGO-1 for both the RMHE and HGO methods is initialized such that initially there is non-zero estimation error (i.e., it is initialized with an initial condition not equal to the actual state value). The estimated state and closed-loop state profiles under the HGO and RMHE methods are shown in Figs. 3.4-3.5. From Fig. 3.4, the HGO initially computes a state estimate close to the actual values of C_{A1} and C_{A2}. After RMHE-1 is activated at 0.08 h in the RMHE method (Fig. 3.4a), it computes state estimates of C_{A1} and C_{A2} very close to the actual state values throughout the length of operation.

When comparing the estimated state profiles of C_{A3}, C_B, and T, the HGO is more sensitive to the measurement noise (e.g., compare Fig. 3.5a with Fig. 3.5b). Thus, the RMHE method provides better state estimation performance and robustness to measurement noise when compared with the HGO method. In addition, the closed-loop economic performance under the RMHE method is 14.8% greater than that under steady-state operation for the one hour operation period.

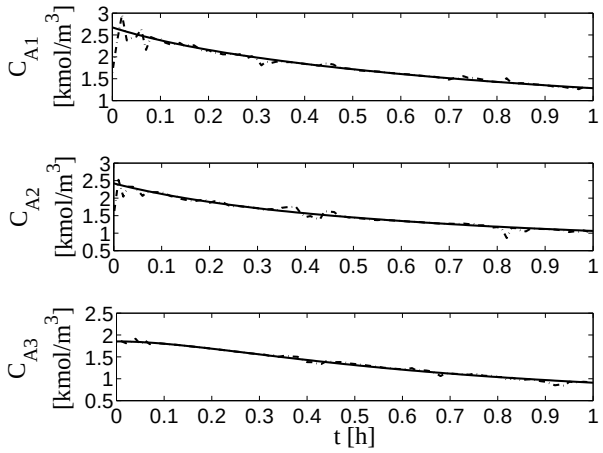

(a)

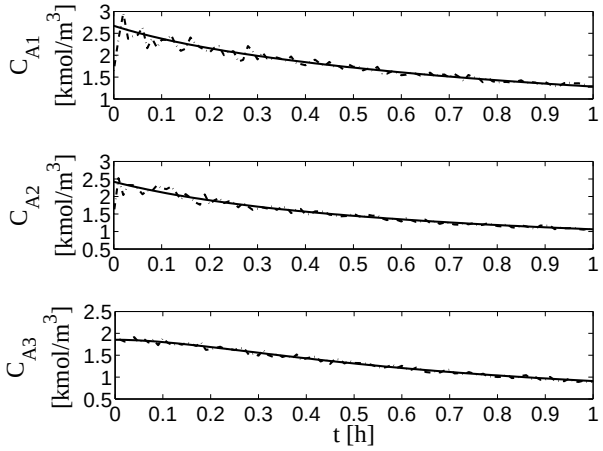

(b)

Figure 3.4: The estimated reactant concentration profiles (dashed lines) compared to the closed-loop reactant concentration profiles (solid lines) of the process network of Eq. 3.18 under (a) the RMHE-based output feedback LEMPC and (b) the HGO-based output feedback LEMPC for Case I (no sensor maintenance).

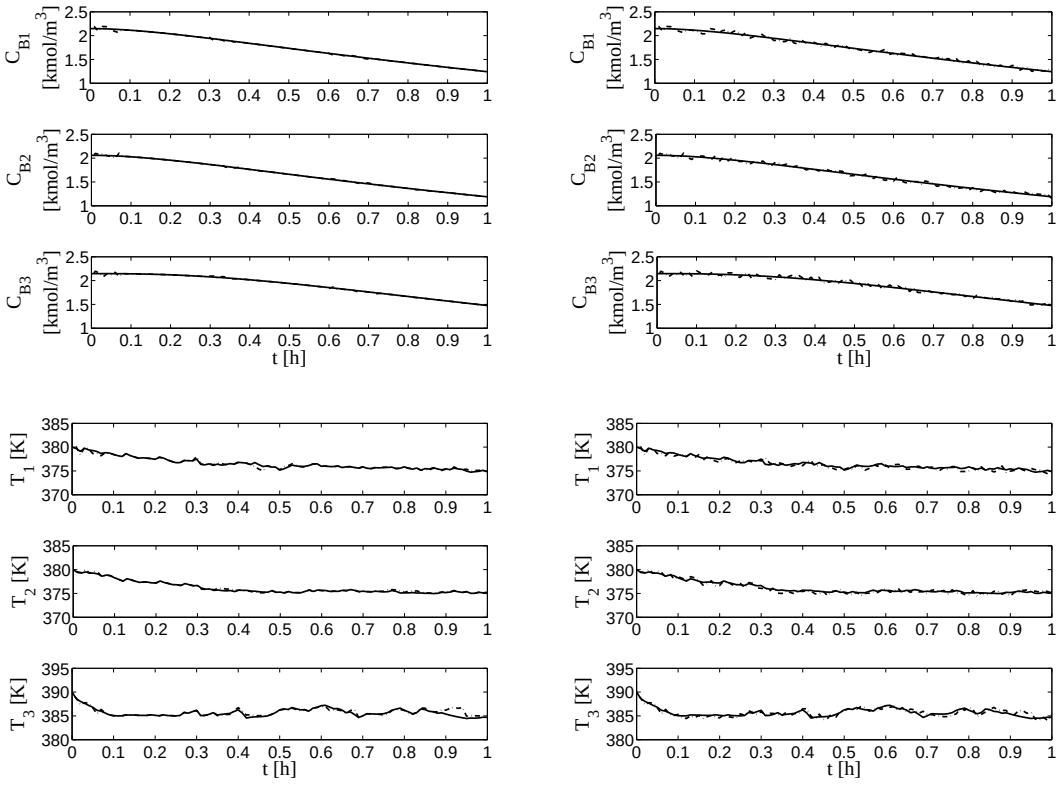

Figure 3.5: The estimated product concentration and temperature profiles (dashed lines) compared to the closed-loop product concentration and temperature profiles (solid lines) of the process network of Eq. 3.18 under (a) the RMHE-based output feedback LEMPC and (b) the HGO-based output feedback LEMPC for Case I (no sensor maintenance).

Case II: RMHE vs HGO - Preventive Sensor Maintenance

In this case study, we consider that preventive sensor maintenance on the sensor of C_{A3} will be conducted as scheduled at $t_m = 0.3\ h$. Again, we compare the RMHE method with the HGO method, but here the RMHE method is applied according to the output feedback RMHE-based LEMPC strategy of Eqs. 3.31-3.32, and the HGO method is applied using HGO-1 and HGO-2 to provide state estimates to the output feedback-based LEMPC schemes of Eqs. 3.31-3.32 before and after t_m, respectively.

We compare the estimated state profiles from the RMHE and HGO methods with the actual closed-loop state profiles in Figs. 3.6-3.7. From Fig. 3.6a, we can see that the estimated C_{A3} trajectory from the RMHE method is nearly overlapping with the actual state trajectories after the C_{A3} sensor is taken off-line at $t_m = 0.3\ h$. However, the state estimate for C_{A3} from the HGO method significantly deviates from the actual state profile as shown by Fig. 3.6b. From Fig. 3.6b, the state estimates of C_{A1} and C_{A2} from the HGO are also affected by its sensitivity to the measurement noise and the removal of the measurement of C_{A3}. Fig. 3.7 displays the T and C_B profiles of the process under the RMHE and HGO methods. The inaccurate estimation of C_{A3} from the HGO decreases the estimation accuracy of the estimated profiles of C_B and T as shown in Figs. 3.7a-3.7b. These results demonstrate the advantage of the RMHE method for state estimation when the measurements are corrupted by noise since it provides accurate state estimates within a small neighborhood of the actual process states. They also show that the proposed RMHE-based LEMPC is able to smoothly deal with the preventive sensor maintenance task without leading to poor performance and process shut-down.

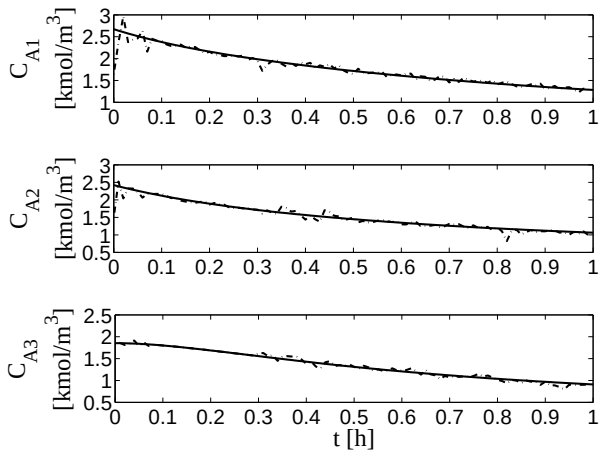

(a)

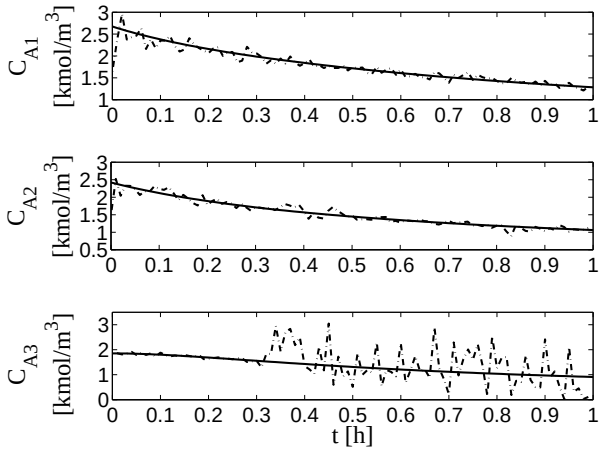

(b)

Figure 3.6: The estimated reactant concentration profiles (dashed lines) compared to the closed-loop reactant concentration profiles (solid lines) of the process network of Eq. 3.18 under (a) the RMHE-based output feedback LEMPC and (b) the HGO-based output feedback LEMPC for Case II where preventive maintenance is conducted on the C_{A3} sensor making it unavailable at 0.3 h.

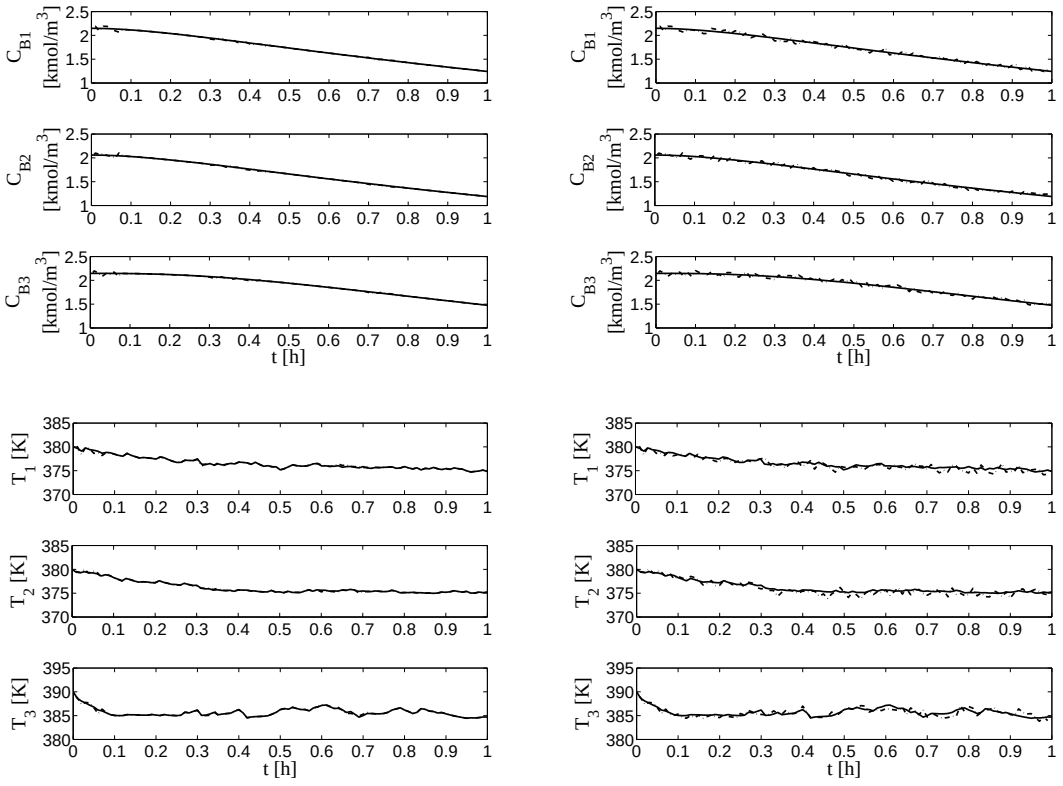

Figure 3.7: The estimated product concentration and temperature profiles (dashed lines) compared to the closed-loop product concentration and temperature profiles (solid lines) of the process network of Eq. 3.18 under (a) the RMHE-based output feedback LEMPC and (b) the HGO-based output feedback LEMPC for Case II where preventive maintenance is conducted on the C_{A3} sensor making it unavailable at 0.3 h.

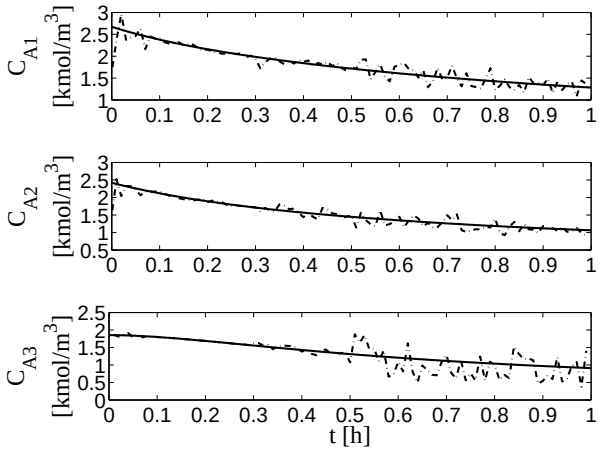

Figure 3.8: The estimated reactant concentration profiles (dashed lines) compared to the closed-loop reactant concentration profiles (solid lines) of the process network of Eq. 3.18 under the RMHE-based output feedback LEMPC for Case III where no preventive maintenance is completed on the C_{A3} sensor and the sensor provides faulty readings at 0.5 h.

Case III: RMHE vs Faulty Sensor Readings

The state profiles of the third case are shown in Figs. 3.8-3.9. The third case with the faulty sensor illustrates the consequences of not performing sensor maintenance and then having a sensor fault. It is developed by using the output feedback RMHE-based LEMPC of Eq. 3.31, except that this LEMPC is used for all times and it does not account for the faulty sensor readings.

To model the faulty sensor, random noise is added to the process measurements starting at time t_f.

From Fig. 3.8, the faulty reading from the sensor of C_{A3} causes large deviations of the estimated states from the actual closed-loop states.

The different estimated state values, which are provided to the RMHE-based LEMPC system of Eqs. 3.31-3.32, result in a different computed input trajectory for Case III than for Cases I and II as shown in Fig. 3.9. Specifically, the input profiles from the process with preventive maintenance on the sensor of C_{A3} are close to those from the process with-

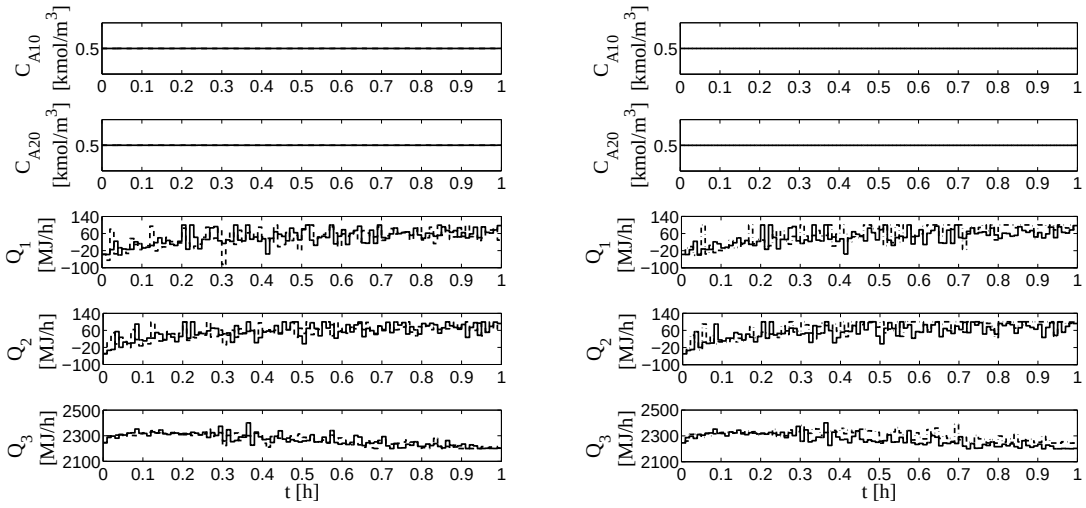

Figure 3.9: Manipulated input profiles from the RMHE-based LEMPC of Eqs. 3.31-3.32 when sensor maintenance is completed on the C_{A3} sensor at 0.3 h (dashed lines in (a)), when the C_{A3} sensor provides faulty readings of C_{A3} after 0.5 h (dashed lines in (b)). For a comparison, the manipulated input profiles from the RMHE-based LEMPC when the sensor of C_{A3} is available and functioning well for all times are given as the solid lines.

out preventive sensor maintenance on the sensor of C_{A3} due to the accurate state estimate of C_{A3}, while for the process with a faulty sensor reading of C_{A3}, the controller requires increased energy consumption than that actually required due to the inaccurate state estimates.

In terms of the economic cost of Eq. 3.22, the average revenue per unit cost over the one hour operation period for the process with faulty sensor readings decreases 5.18 % when compared with the process using state feedback without sensor maintenance and with fully functional sensors. However, the process economic performance degradation for the process conducting the preventive sensor maintenance work based on the proposed output feedback RMHE-based LEMPC is only 1.27 % due to the accurate state estimates provided by the RMHE method and the control system reconfiguration of the LEMPC scheme of Eqs. 3.31-3.32 when t approaches t_m. In particular, the RMHE-based LEMPC

takes full advantage of the estimation performance from the RMHE method.

Remark 3.8 *Sensor faults can come in a variety of forms. For the purposes of the Case III comparison made in this paper, the sensor fault type simulated demonstrates that sensor faults can be more costly than removing a sensor for preventive maintenance using the proposed control strategy. If the faulty sensors have more severe problems, such as constant or drifting signals, the process economic performance degradation will likely be much larger than that demonstrated in Case III.*

Case IV: Integrating Actuator and Sensor Maintenance

The chemical processing industry is concerned not only with maintenance of sensors, but also with preventive maintenance of actuators. It is possible to consider the situation that the maintenance work for the sensor and actuator is scheduled in sequence. To address this problem, we apply a LEMPC scheme handling preventive maintenance on both sensors and actuators to the chemical process network based on the LEMPC design handling preventive actuator maintenance[86] and the LEMPC handling the preventive sensor maintenance of Eqs. 3.31-3.32.

In this case, the preventive sensor maintenance on C_{A3} is scheduled at $t_m = 0.3\ h$, and we assume the actuator of C_{A20} is taken off-line at $t_a = 0.6\ h$ when it is no longer available to the LEMPC. In Fig. 3.10, closed-loop state and estimated state profiles under the RMHE-based LEMPC are compared. From Fig. 3.10, we can see that the proposed RMHE-based LEMPC still provides accurate state estimates even after the actuator of C_{A20} is taken off-line (i.e., control system reconfiguration caused by the loss of the actuator of C_{A20}). Based on the manipulated input profiles shown in Fig. 3.11, the manipulated input value of C_{A20} is set to be 0 when its actuator is taken off-line for maintenance at $t_a = 0.6\ h$. The process economic performance following Eq. 3.22 decreases 2.63% compared to the situation shown in Case

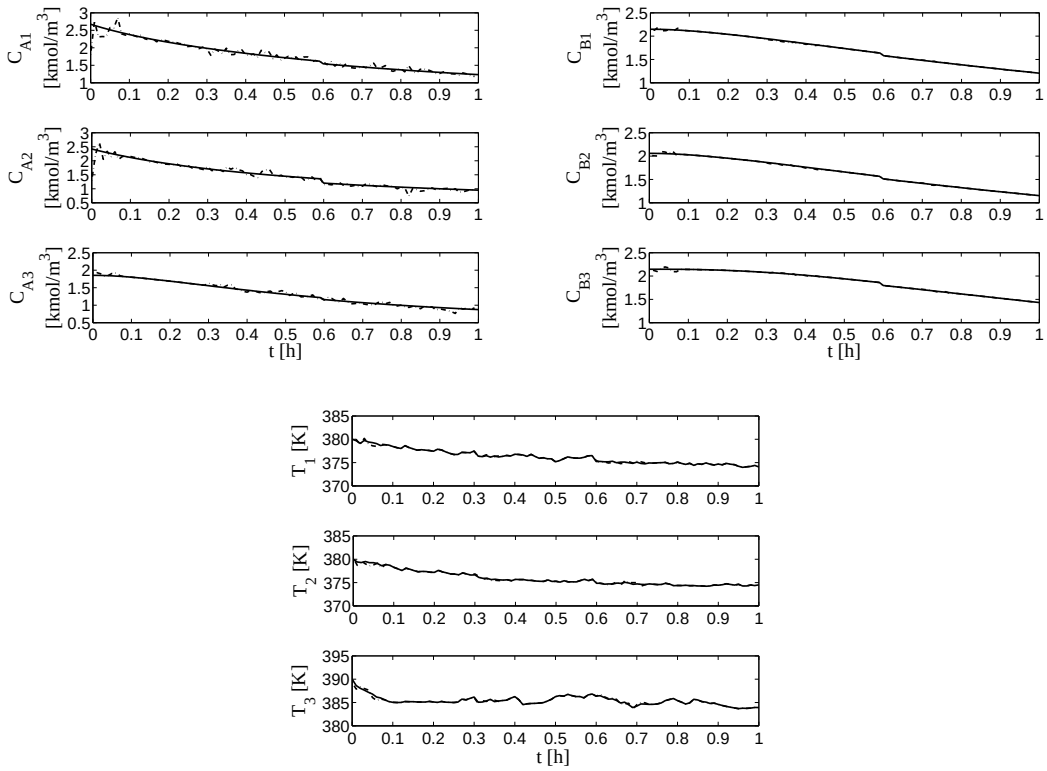

Figure 3.10: The closed-loop state (solid lines) and estimated state (dashed) profiles for the process network of Eq. 3.18 under the RMHE-based LEMPC for handling sensor and actuator maintenance where the sensor of C_{A3} is unavailable after $t_m = 0.3$ h and actuator of C_{A20} is unavailable after $t_a = 0.6$ h.

II where the actuator maintenance is not conducted over this one hour operation but sensor maintenance is performed. This Case IV simulation run demonstrates that the integration of the method proposed in the present manuscript and the results of[86] produces a control scheme capable of handling both sensor and actuator maintenance in a single framework.

3.6 Conclusions

This paper establishes a novel robust moving horizon estimation scheme that accommodates a varying number of sensors to continuously supply accurate state estimates to a LEMPC system. It was shown that the proposed RMHE-based LEMPC scheme can main-

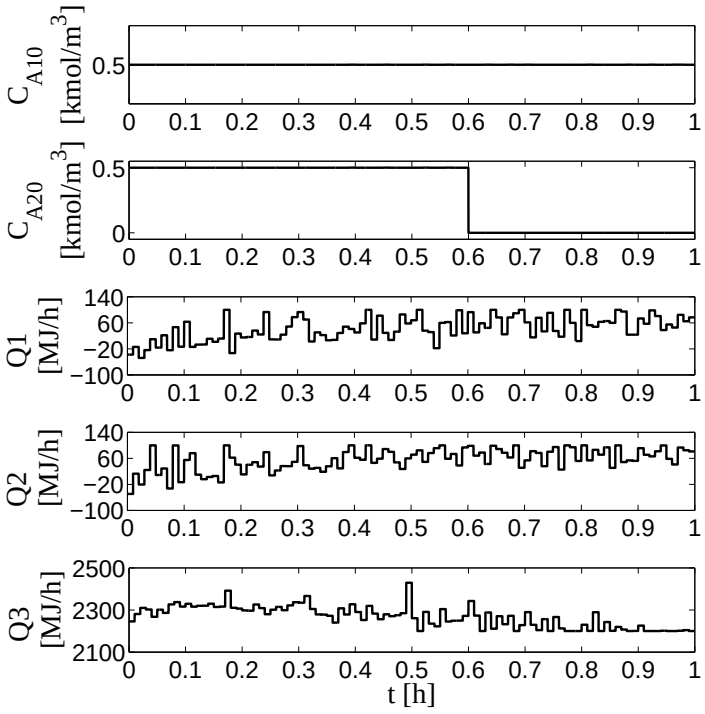

Figure 3.11: Manipulated input profiles with the sensor of C_{A3} unavailable after $t_m = 0.3\ h$ and the actuator of C_{A20} unavailable after $t_a = 0.6\ h$ under the RMHE-based LEMPC for handling both sensor and actuator preventive maintenance.

tain process closed-loop stability under standard observability and stabilizability assumptions. Then, the proposed RMHE-based LEMPC was applied to a chemical process; the simulation results exhibited its ability to accomplish control system reconfiguration under a changing number of on-line sensors and to achieve minimal economic performance degradation by operating the process in an economically optimal fashion, while preserving closed-loop stability.

Chapter 4

Proactive Fault-Tolerant Model Predictive Control

4.1 Introduction

This chapter presents the formulation of a proactive fault-tolerant model predictive controller (MPC) designed via Lyapunov-based techniques for nonlinear systems capable of taking proactive measures to minimize the effect of a future known control actuator fault. This approach to proactive fault-tolerant control combines the unique stability and robustness properties of Lyapunov-based MPC (LMPC) as well as explicitly accounting for future known control actuator faults in the formulation of the MPC. We apply our theoretical results to a chemical process example, and different case studies with various types of actuator faults were simulated to demonstrate that the proposed proactive fault-tolerant model predictive control method can achieve practical stability after a control actuator fault.

4.2 Preliminaries

4.2.1 Notation

The operator $|\cdot|$ is used to denote the Euclidean norm of a vector and $|\cdot|_Q$ denotes the square of the weighted Euclidean norm of a vector (i.e., $|\cdot|_Q = x^T Q x$). A continuous function $\alpha : [0,a) \to [0,\infty)$ belongs to class $\mathscr{K}$ functions if it is strictly increasing and satisfies $\alpha(0) = 0$. We use Ω_ρ to denote the level set $\Omega_\rho := \{x \in \mathbf{R}^{n_x} \,|\, V(x) \leq \rho\}$. The symbol $\mathrm{diag}(v)$ denotes a square diagonal matrix with diagonal elements equal to the vector v.

4.2.2 Class of Nonlinear Systems

In this work, we consider a class of input-affine nonlinear systems described by the following state-space model

$$\dot{x}(t) = f(x(t)) + G_1(x(t))(u(t) + \tilde{u}(t)) + G_2(x(t))w(t) \tag{4.1}$$

where $x(t) \in \mathbf{R}^n$ is the state vector, $u(t) \in \mathbf{R}^m$ is the manipulated input vector, $\tilde{u}(t) \in \mathbf{R}^m$ is the control actuator fault vector, and $w(t) \in W \subset \mathbf{R}^w$ is the disturbance vector that is bounded by $|w(t)| \leq w_p$. We consider that $u + \tilde{u}$ is bounded in a nonempty convex set $U \subseteq \mathbf{R}^m$ defined as $U := \{u \in \mathbf{R}^m \,|\, |u_i + \tilde{u}_i| \leq u_i^{\max}, i = 1,\ldots,m\}$. We assume that $f : \mathbf{R}^n \to \mathbf{R}^n$, $G_1 : \mathbf{R}^n \to \mathbf{R}^n \times \mathbf{R}^m$ and $G_2 : \mathbf{R}^n \to \mathbf{R}^n \times \mathbf{R}^w$, are locally Lipschitz vector and matrix functions, respectively. We use $j = 0$ to denote the fault-free system and $j = 1,\ldots,m$ to denote the system with a fault in the jth control actuator.

We assume that the nominal system of Eq. 4.1 ($\tilde{u} \equiv 0$) has an equilibrium point at the origin. We also assume that the state x of the system is sampled synchronously and continuously and the time instants where the state measurements become available is indicated by the time sequence $\{t_{k\geq 0}\}$ with $t_k = t_0 + k\Delta$, $k = 0, 1, \ldots$ where t_0 is the initial time and Δ

is the sampling time.

4.2.3 Lyapunov-based Controller

We assume that there exists a Lyapunov-based controller $u(t) = h_0(x)$ which renders the origin of the fault-free closed-loop system asymptotically stable under continuous implementation. This assumption is essentially a stabilizability requirement for the system of Eq. 4.1. Furthermore, we assume after the jth control actuator fails that there exists another Lyapunov-based controller $u(t) = h_j(x)$ that renders the origin of the resulting faulty closed-loop system asymptotically stable. Using converse Lyapunov theorems,[79,97,100] this assumption implies that there exist functions $\alpha_{i,j}(\cdot)$, $i = 1,2,3,4$, $j = 0,1,2,\ldots,m$ of class $\mathscr{K}$ and continuous differentiable Lyapunov functions $V_j(x)$ for the closed-loop system that satisfy the following inequalities:

$$\alpha_{1,j}(|x|) \leq V_j(x) \leq \alpha_{2,j}(|x|) \tag{4.2}$$

$$\frac{\partial V_j(x)}{\partial x}(f(x) + G_1(x)h_j(x)) \leq -\alpha_{3,j}(|x|) \tag{4.3}$$

$$\left|\frac{\partial V_j(x)}{\partial x}\right| \leq \alpha_{4,j}(|x|) \tag{4.4}$$

$$h_j(x) \in U_j \tag{4.5}$$

for all $x \in D \subseteq \mathbf{R}^n$ where D is an open neighborhood of the origin. We denote the region $\Omega_{\rho_j} \subseteq D$ as the stability region of the closed-loop system under the control $u = h_j(x)$. Note that explicit stabilizing control laws that provide explicitly defined stability regions Ω_{ρ_j} for the closed-loop system have been developed using Lyapunov techniques for input-affine nonlinear systems (see[29,82,93]).

We assume that after some known time t_f the jth control actuator fails. We note that

there exists a horizon $t_f - t_0$ sufficiently large such that the controller $h_0(x)$ can force the system into the stability region Ω_{ρ_j} by the time t_f starting from any initial state $x(t_0) \in \Omega_{\rho_0}$ (more precisely, it will drive the system to the intersection between Ω_{ρ_j} and Ω_{ρ_0}). We also assume that $V_0 = V_1 = \cdots = V_m = V$.

By continuity and the local Lipschitz property assumed for the vector fields, the manipulated input u is bounded in a convex set, and the continuous differentiable property of the Lyapunov function V, there exists positive constants M, L_x, and L_w such that

$$|f(x) + G_1(x)(u+\tilde{u}) + G_2(x)w| \leq M \tag{4.6}$$

$$\left| \frac{\partial V}{\partial x}\left(f(x) + G_1(x)(u+\tilde{u}) + G_2(x)w(t)\right) - \frac{\partial V}{\partial x}\left(f(x') + G_1(x')(u+\tilde{u})\right) \right| \leq L_x \left|x - x'\right| + L_w |w| \tag{4.7}$$

for all $x, x' \in \Omega_{\rho_j}$, $u + \tilde{u} \in U$, and $w \in W$.

Remark 4.1 *For input-affine nonlinear systems arising in the context of chemical process control applications, weighted Euclidean norm Lyapunov functions (i.e., $V(x) = x^T(t)Px(t)$) have been widely used (see[29] and the references therein). See the "Application to a chemical process example" section for an example.*

Remark 4.2 *The assumption that there exists a controller $h_j(x)$ that stabilizes the faulty system is a necessary requirement. Typically, this can be accomplished in chemical process control in one of two ways: (1) the principle of redundancy is used in fault-tolerant systems to ensure stability after a fault (i.e., if a control actuator fails, there is another actuator that can be used to maintain stability), and (2) many chemical processes are designed to be open-loop asymptotically stable so the failure of a control actuator does not affect the stability of the closed-loop system.*

Remark 4.3 *We note that there is no guarantee that the stability region Ω_{ρ_j} of the faulty system is a subset of the fault-free stability region Ω_{ρ_0} because the controllers $h_0(x)$ and $h_j(x)$ can be different. We do know that the two regions intersect in a neighborhood of the origin and it is this intersection that we use in our design of the proactive fault-tolerant controller.*

4.3 Proactive Fault-Tolerant MPC

In this section, we introduce the proposed proactive fault-tolerant Lyapunov-based model predictive controller and prove practical stability of the closed-loop system of Eq. 4.1 with the proactive fault-tolerant LMPC.

4.3.1 Implementation Strategy

The implementation strategy of the proposed proactive fault-tolerant LMPC is represented by Fig. 4.1. Specifically, from t_0 to t_f, the LMPC with sampling period Δ and prediction horizon N starts from an initial condition in the stability region Ω_{ρ_0} and recomputes optimal control actions at every sampling period by solving an on-line optimization problem while accounting for the actuator fault that occurs at t_f. It does so by working to drive the system into the stability region Ω_{ρ_j} by the time t_f (the time of the fault). After the fault renders the jth actuator inactive, the proactive fault-tolerant LMPC drives the system to the origin using its available (remaining) $m-1$ actuators. The implementation strategy steps of the proposed proactive fault-tolerant LMPC can be summarized as follows:

1. At t_k, the proactive fault-tolerant LMPC receives the process state from the sensors;

2. If $t_{k+1} < t_f$ (the time of the fault), go to Step 2.1; otherwise go to Step 2.2;

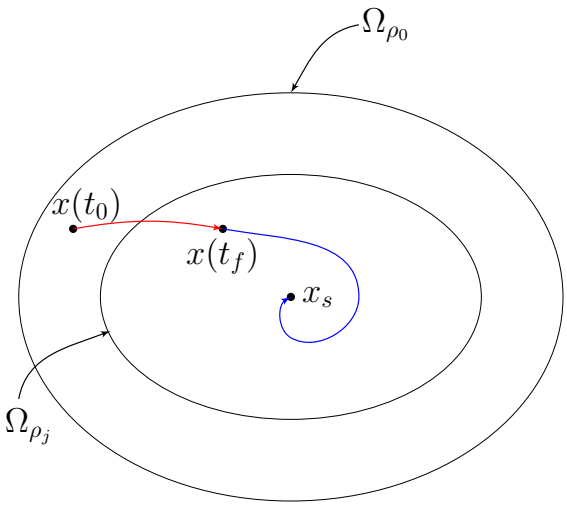

Figure 4.1: Conceptual diagram of the implementation strategy of proactive fault-tolerant LMPC. The proactive fault-tolerant LMPC works to drive the system into the stability region Ω_{ρ_j} by the time t_f and uses the remaining $m-1$ actuators to drive the system to the origin after the fault renders the jth actuator inactive.

2.1. Compute control actions that account for the fault at t_f and drive the system to the stability region Ω_{ρ_j} by t_f; go to Step 3;

2.2. Drive the system to the origin with the remaining $m-1$ control actuators; go to Step 3;

3. Go to Step 1, $t_k := t_{k+1}$.

By comparing the time of the fault with the next sampling time (t_{k+1}), the proactive fault-tolerant LMPC completes control system reconfiguration before the fault.

With this implementation strategy, we point out that the key difference between this proactive approach to dealing with actuator faults and traditional reactive fault tolerant control is that when there is a known fault it may be necessary to adjust the control energy to drive the system to the stability region Ω_{ρ_j} before the jth control actuator fails compared to a controller which does not account for an upcoming fault. This guarantees that the remaining $m-1$ control actuators can stabilize the system after the fault occurs. This

strategy differs from reactive fault tolerant control that cannot proactively drive the system to a region whereby stability is guaranteed after the jth actuator fails. After a fault occurs and has been identified with reactive fault-tolerant control, the closed-loop system may lose stabilizability of the origin with the remaining control actuators if the closed-loop state is outside the stability region Ω_{ρ_j}.

4.3.2 Formulation

We formulate an LMPC based on the conceptual framework proposed in[100,105] for use as a proactive fault-tolerant controller. The LMPC is based on the Lyapunov-based controllers $h_0(x)$ and $h_j(x)$ because the controllers are used to define a stability constraint for the LMPC which guarantees that the LMPC inherits the stability and robustness properties of the Lyapunov-based controllers. The proactive fault-tolerant LMPC is based on the following optimization problem:

$$\min_{u\in S(\Delta)} \int_{t_k}^{t_{k+N}} [|\tilde{x}(\tau)|_{Q_c} + |u(\tau)|_{R_c}] d\tau \tag{4.8a}$$

$$\text{s.t. } \dot{\tilde{x}}(t) = f(\tilde{x}(t)) + G_1(\tilde{x}(t))(u(t) + \tilde{u}(t)), \tag{4.8b}$$

$$u(t) \in U, \tag{4.8c}$$

$$\tilde{u}_j(t) = \begin{cases} 0, & \text{if } t < t_f, \\ -u_j(t), & \text{if } t \geq t_f, \end{cases} \tag{4.8d}$$

$$\tilde{x}(t_k) = x(t_k), \tag{4.8e}$$

$$\frac{\partial V}{\partial x}(f(x(t_k)) + G_1(x(t_k))u(t_k)) \leq \frac{\partial V}{\partial x}(f(x(t_k)) + G_1(x(t_k))h_0(x(t_k))), \quad \text{if } t_{k+1} < t_f, \tag{4.8f}$$

$$\frac{\partial V}{\partial x}(f(x(t_k)) + G_1(x(t_k))u(t_k)) \leq \frac{\partial V}{\partial x}(f(x(t_k)) + G_1(x(t_k))h_j(x(t_k))), \quad \text{if } t_{k+1} \geq t_f \tag{4.8g}$$

where $S(\Delta)$ is the family of piece-wise constant functions with sampling period Δ, N is the prediction horizon of the LMPC, $\tilde{u}(t)$ is the known actuator fault trajectory, $\tilde{x}(t)$ is the state trajectory predicted by the nominal model ($w(t) \equiv 0$) with manipulated input $u(t)$ computed by the LMPC. The optimal solution of the optimization problem of Eq. 4.8 is denoted by $u^*(t|t_k)$ and is defined for $t \in [t_k, t_{k+N})$.

In the optimization problem of Eq. 4.8, the first constraint of Eq. 4.8b is the nonlinear system of Eq. 4.1 used to predict the future evolution of the system. The constraint of Eq. 4.8c defines the control energy available to all manipulated inputs. The constraint of Eq. 4.8d is the complete fault of the jth control actuator that cause the actuator to be unusable for $t \geq t_f$. The constraint of Eq. 4.8e is the initial condition of the optimization problem. The constraints of Eq. 4.8f and 4.8g ensure that over the sampling period $t \in [t_k, t_k + \Delta)$ the LMPC computes a manipulated input that decreases the Lyapunov function by at least the rate achieved by the Lyapunov-based controllers $h_0(x)$ when $t_{k+1} < t_f$ and $h_j(x)$ when $t_{k+1} \geq t_f$ when the Lyapunov-based controllers are implemented in a sample-and-hold fashion. We note that in the optimization problem of Eq. 4.8 the time instance that is used to determine which Lyapunov-based constraint to use is t_{k+1} to account for a fault that may occur between two sampling times. In this manner, the controller is proactively regulating the closed-loop system trajectory.

4.3.3 Stability Analysis

In this section, we provide sufficient conditions whereby the proactive fault-tolerant controller of Eq. 4.8 guarantees practical stability of the closed-loop system. Theorem 1 below provides sufficient conditions such that the proactive fault-tolerant LMPC guarantees that the state of the closed-loop system is always bounded and is ultimately bounded in a small region containing the origin.

Theorem 4.1 *Consider the system in closed-loop under the proactive fault-tolerant LMPC design of Eq. 4.8 based on controllers $h_j(x)$, $j = 0, 1, \ldots, m$ that satisfies the conditions of Eqs. 4.2-4.5. Let $\Delta > 0$, $\varepsilon_0 > 0$, $\rho_0 > \rho_{s,0} > 0$, $\varepsilon_j > 0$, and $\rho_j > \rho_{s,j} > 0$ satisfy:*

$$-\alpha_{3,0}(\alpha_{2,0}^{-1}(\rho_{s,0})) + L_x M\Delta + L_w w_p \leq -\varepsilon_0/\Delta \tag{4.9}$$

$$-\alpha_{3,j}(\alpha_{2,j}^{-1}(\rho_{s,j})) + L_x M\Delta + L_w w_p \leq -\varepsilon_j/\Delta \tag{4.10}$$

If $x(t_0) \in \Omega_{\rho_0}$, $\rho_{\min} \leq \rho_j$ and $t_f - t_0$ is sufficiently large such that $x(t_f) \in \Omega_{\rho_j}$, then the state $x(t)$ of the closed-loop system is always bounded and is ultimately bounded in $\Omega_{\rho_{\min}}$ where $\rho_{\min} = \max\{V(x(t+\Delta)) : V(x(t)) \leq \rho_{s,j}\}$.

Proof 4.1 *The proof consists of three parts. We first prove that the optimization problem is feasible. Subsequently, we prove that, under the LMPC design, the closed-loop state of the system is always bounded and will converge to a small set containing the origin after a finite number of sampling periods. Finally, we prove that under the LMPC, the closed-loop state of the system is ultimately bounded in the set $\Omega_{\rho_{\min}}$.*

Part 1: When $x(t)$ is maintained in Ω_{ρ_0} for $t < t_f$ and in Ω_{ρ_j} for $t \geq t_f$ (which will be proved in Part 2), the feasibility of the LMPC follows because the input trajectory $u(t) = h_j(x(t_{k+q}))$, $\forall t \in [t_{k+q}, t_{k+q+1})$ with $q = 0, \ldots, N-1$ ($j = 0$ for $t < t_f$) is a feasible solution to the optimization problem since such trajectory satisfies the input constraint and the Lyapunov-based constraints. This is guaranteed by the closed-loop stability property of the Lyapunov-based controllers $h_0(x)$ and $h_j(x)$.

Part 2: We prove that if $x(t_k) \in \Omega_{\rho_0} \setminus \Omega_{\rho_{s,0}}$ and $t_{k+1} < t_f$, then $V(x(t_{k+1})) < V(x(t_k))$ and after a finite time, either the system will converge to the set $\Omega_{\rho_{s,0}}$ which is contained in the set Ω_{ρ_j} or it will converge to the set $\Omega_{\rho_0} \cup \Omega_{\rho_j}$ by t_f.

When $x(t_k) \in \Omega_{\rho_0} \setminus \Omega_{\rho_{s,0}}$ and $t_{k+1} < t_f$, from the last constraint of the LMPC of Eq. 4.8 and accounting for Eq. 4.3, the derivative of the Lyapunov function along the system

trajectory at t_k is

$$\frac{\partial V(x(t_k))}{\partial x}\left(f(x(t_k))+G_1(x(t_k))u^*(t_k)\right) \leq \frac{\partial V(x(t_k))}{\partial x}\left(f(x(t_k))+G_1(x(t_k))h_0(x(t_k))\right)$$
$$\leq -\alpha_{3,0}(|x(t_k)|) \tag{4.11}$$

The time derivative of the Lyapunov function along the computed optimal trajectories u^* for $\forall \tau \in [t_k, t_{k+1})$ can be written as follows

$$\dot{V}(x(\tau)) = \frac{\partial V(x(\tau))}{\partial x}(f(x(\tau))+G_1(x(\tau))u^*(t_k)+G_2(x(\tau))w(t)) \tag{4.12}$$

Adding and subtracting the term $\frac{\partial V(x(t_k))}{\partial x}\left(f(x(t_k))+G(x(t_k))u^*(t_k)\right)$ to/from the above equation and considering the bound of Eq. 4.11, we have

$$\dot{V}(x(\tau)) \leq -\alpha_{3,0}(|x(t_k)|) - \frac{\partial V}{\partial x}\left(f(x(t_k))+G_1(x(t_k))u^*(t_k)\right)$$
$$+\frac{\partial V}{\partial x}(f(x(\tau))+G_1(x(\tau))u^*(t_k)+G_2(x(\tau))w(\tau)) \tag{4.13}$$

From the Lipschitz property of Eq. 4.7 and accounting for the bounded disturbance, we can write

$$\dot{V}(x(\tau)) \leq -\alpha_{3,0}(|x(t_k)|) + L_x\,|x(\tau)-x(t_k)| + L_w w_p \tag{4.14}$$

Taking into account Eq. 4.6 and the continuity of $x(t)$, the following bound can be written for all $\tau \in [t_k, t_{k+1})$

$$|x(\tau)-x(t_k)| \leq M\Delta \tag{4.15}$$

Using the bound of Eq. 4.15 and since $x(t_k) \in \Omega_{\rho_0} \setminus \Omega_{\rho_{s,0}}$, the bound of Eq. 4.14 becomes

$$\dot{V}(x(\tau)) \leq -\alpha_{3,0}(\alpha_{2,0}^{-1}(\rho_{s,0})) + L_x M\Delta + L_w w_p \tag{4.16}$$

If the condition of Eq. 4.9 is satisfied, then there exists $\varepsilon_0 > 0$ such that the following inequality holds for $x(t_k) \in \Omega_{\rho_0} \setminus \Omega_{\rho_{s,0}}$

$$\dot{V}(x(t)) \leq -\varepsilon_0/\Delta, \forall t = [t_k, t_{k+1}) \tag{4.17}$$

Integrating this bound on $t \in [t_k, t_{k+1})$, we obtain that

$$\begin{aligned} V(x(t_{k+1})) &\leq V(x(t_k)) - \varepsilon_0 \\ V(x(t)) &\leq V(x(t_k)), \quad \forall t \in [t_k, t_{k+1}) \end{aligned} \tag{4.18}$$

for all $x(t_k) \in \Omega_{\rho_0} \setminus \Omega_{\rho_{s,0}}$. Using Eq. 4.18 recursively, it is proved that, if $x(t_k) \in \Omega_{\rho_0} \setminus \Omega_{\rho_{s,0}}$, the state converges to $\Omega_{\rho_{s,0}} \subset \Omega_{\rho_j}$ in a finite number of sampling times without leaving the stability region Ω_{ρ_0}.

The horizon $(t_f - t_0)$ is chosen to be sufficiently large such that starting from any $x(t_0) \in \Omega_{\rho_0}$, the state will be driven into the set Ω_{ρ_j} by t_f. Similar arguments as above can be used to show that after t_f, operation is always maintained in the set Ω_{ρ_j} and converges to the set $\Omega_{\rho_{s,j}} \subset \Omega_{\rho_j}$ after some finite number of sampling periods if the conditions of Eq. 4.10 are satisfied.

Part 3: We prove that if $x(t_k) \in \Omega_{\rho_j}$ for $t_k \geq t_f$, then the system state will ultimately be bounded in an invariant set $\Omega_{\rho_{\min}}$. From Part 2, we proved that if $x(t_0) \in \Omega_{\rho_0}$, the state converges to Ω_{ρ_j} before t_f and after a finite number of sampling times, the system will be driven to the set $\Omega_{\rho_{s,j}}$. Once the state converges to $\Omega_{\rho_{s,j}}$, it remains inside $\Omega_{\rho_{\min}}$ for all times. This statement holds because of the definition of $\rho_{\min}$. This proves that the closed-loop system state under the LMPC of Eq. 4.8 is ultimately bounded in $\Omega_{\rho_{\min}}$.

Remark 4.4 *We note that in many realistic actuator faults a fault is initially gradual meaning that the maximum available actuator output decreases slowly with time until the max-*

imum output begins to drastically decrease (sigmoid relationship). In this manner, the bounds on the available actuator output become time-dependent. This is a mild extension of what is covered in the stability proof. As long as the evolution of the constraint set is a known function of time a priori, the time-dependent bound may be used in the LMPC formulation. From a stability point of view, the goal of the proactive fault-tolerant controller is to drive the closed-loop system to the stability region without the faulty control actuator Ω_j *by the time the fault starts whether that fault is abrupt or gradual. If this is accomplished at the time of the fault, then we can guarantee closed-loop stability. This follows from a simple argument that if we can stabilize the system with* $m-1$ *actuators, we can also stabilize with* $m-1$ *plus the gradually decaying one. This remark refers to case B in our application of this theory to a chemical process, where this type of fault is implemented and handled.*

4.4 Application to a Chemical Process

Consider a three vessel, reactor-separator chemical process consisting of two CSTRs in series followed by a flash tank separator as shown in Fig. 4.2. Two parallel first-order reactions occur in each of the reactors that have the form:

$$A \xrightarrow{r_1} B$$

$$A \xrightarrow{r_2} C$$

Each reactor is supplied with a fresh stream of the reactant A contained in an inert solvent D. A recycle stream is used to recover unreacted A from the overhead vapor of the flash tank and feed it back to the first CSTR. Some of the overhead vapor from the flash tank is condensed, and the bottom product stream is removed. All three vessels are

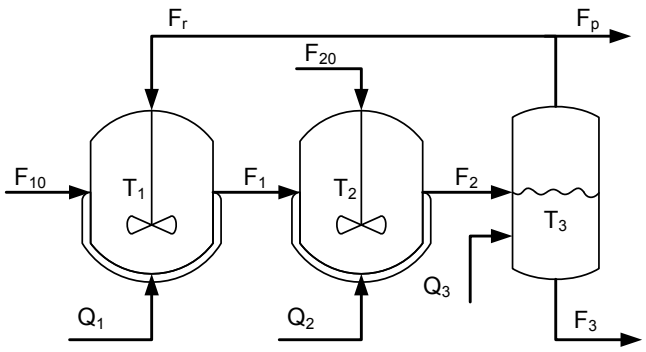

Figure 4.2: Process flow diagram of the reactor and separator chemical process.

assumed to have static holdup and are equipped with a jacket to supply/remove heat from the vessel. The dynamic equations describing the behavior of the system, obtained through material and energy balances under standard modeling assumptions, are given below:

$$\frac{dT_1}{dt} = \frac{F_{10}}{V_1}(T_{10} - T_1) + \frac{F_r}{V_1}(T_3 - T_1) + \frac{-\Delta H_1}{\rho C_p} k_1 e^{\frac{-E_1}{RT_1}} C_{A1} + \frac{-\Delta H_2}{\rho C_p} k_2 e^{\frac{-E_2}{RT_1}} C_{A1} + \frac{Q_1}{\rho C_p V_1} \tag{4.19}$$

$$\frac{dC_{A1}}{dt} = \frac{F_{10}}{V_1}(C_{A10} - C_{A1}) + \frac{F_r}{V_1}(C_{Ar} - C_{A1}) - k_1 e^{\frac{-E_1}{RT_1}} C_{A1} - k_2 e^{\frac{-E_2}{RT_1}} C_{A1} \tag{4.20}$$

$$\frac{dC_{B1}}{dt} = \frac{-F_{10}}{V_1} C_{B1} + \frac{F_r}{V_1}(C_{Br} - C_{B1}) + k_1 e^{\frac{-E_1}{RT_1}} C_{A1} \tag{4.21}$$

$$\frac{dC_{C1}}{dt} = \frac{-F_{10}}{V_1} C_{C1} + \frac{F_r}{V_1}(C_{Cr} - C_{C1}) + k_2 e^{\frac{-E_2}{RT_1}} C_{A1} \tag{4.22}$$

$$\frac{dT_2}{dt} = \frac{F_1}{V_2}(T_1 - T_2) + \frac{F_{20}}{V_2}(T_{20} - T_2) + \frac{-\Delta H_1}{\rho C_p} k_1 e^{\frac{-E_1}{RT_2}} C_{A2} + \frac{-\Delta H_2}{\rho C_p} k_2 e^{\frac{-E_2}{RT_2}} C_{A2} + \frac{Q_2}{\rho C_p V_2} \tag{4.23}$$

$$\frac{dC_{A2}}{dt} = \frac{F_1}{V_2}(C_{A1} - C_{A2}) + \frac{F_{20}}{V_2}(C_{A20} - C_{A2}) - k_1 e^{\frac{-E_1}{RT_2}} C_{A2} - k_2 e^{\frac{-E_2}{RT_2}} C_{A2} \tag{4.24}$$

$$\frac{dC_{B2}}{dt} = \frac{F_1}{V_2}(C_{B1} - C_{B2}) - \frac{F_{20}}{V_2} C_{B2} + k_1 e^{\frac{-E_1}{RT_2}} C_{A2} \tag{4.25}$$

$$\frac{dC_{C2}}{dt} = \frac{F_1}{V_2}(C_{C1} - C_{C2}) - \frac{F_{20}}{V_2} C_{C2} + k_2 e^{\frac{-E_2}{RT_2}} C_{A2} \tag{4.26}$$

$$\frac{dT_3}{dt} = \frac{F_2}{V_3}(T_2 - T_3) - \frac{H_{vap} F_{rm}}{\rho C_p V_3} + \frac{Q_3}{\rho C_p V_3} \tag{4.27}$$

$$\frac{dC_{A3}}{dt} = \frac{F_2}{V_3}(C_{A2} - C_{A3}) - \frac{F_r}{V_3}(C_{Ar} - C_{A3}) \tag{4.28}$$

$$\frac{dC_{B3}}{dt} = \frac{F_2}{V_3}(C_{B2} - C_{B3}) - \frac{F_r}{V_3}(C_{Br} - C_{B3}) \tag{4.29}$$

$$\frac{dC_{C3}}{dt} = \frac{F_2}{V_3}(C_{C2} - C_{C3}) - \frac{F_r}{V_3}(C_{Cr} - C_{C3}) \tag{4.30}$$

where the notation is defined in Table 4.1 and the process parameter values are given in Table 4.2.

To model the separator, we assume that the relative volatility of each species remains constant within the operating temperature range of the flash tank and that the amount of reacting material in the separator is negligible. The following algebraic equations model

Table 4.1: Notation used for the process parameters and variables

C_{Aj0}	Concentration of A in the feed stream to vessel j, $j = 1,2$
$C_{i,j}$	Concentration of species i, $i = A,B,C$ in vessel j, $j = 1,2,3$
$C_{i,r}$	Concentration of species i, $i = A,B,C$ in the recycle stream
T_{j0}	Temperature of the feed stream to vessel j, $j = 1,2$
T_j	Temperature in vessel j, $j = 1,2,3$
T_r	Temperature in the recycle stream
F_{j0}	Flow rate of the feed stream to vessel j, $j = 1,2$
F_j	Flow rates of the effluent stream from vessel j, $j = 1,2,3$
F_r	Flow rate of the recycle stream
F_p	Flow rate of the purge stream
V_j	Volumes of vessel j, $j = 1,2,3$
E_k	Activation energy of reaction k, $k = 1,2$
k_k	Pre-exponential factor of reaction k, $k = 1,2$
ΔH_k	Heat of reaction k, $k = 1,2$
H_{vap}	Heat of vaporization
α_i	Relative volatilities of species i, $i = A,B,C,D$
MW_j	Molecular weights of species i, $i = A,B,C,D$
C_p	Heat capacity
R	Gas constant

Table 4.2: Process parameter values.

$T_{10} = 300$, $T_{20} = 300$	K
$F_{10} = 5$, $F_r = 1.9$, $F_p = 0$	m^3/hr
$C_{A10} = 4$, $C_{A20} = 3$	$kmol/m^3$
$V_1 = 1.0$, $V_2 = 0.5$, $V_3 = 1.0$	m^3
$E_1 = 5 \times 10^4$, $E_2 = 5.5 \times 10^4$	$kJ/kmol$
$k_1 = 3 \times 10^6$, $k_2 = 3 \times 10^6$	$1/hr$
$\Delta H_1 = -5 \times 10^4$, $\Delta H_2 = -5.3 \times 10^4$	$kJ/kmol$
$H_{vap} = 5$	$kJ/kmol$
$C_p = 0.231$	$kJ/kg-K$
$R = 8.314$	$kJ/kmol-K$
$\rho = 1000$	kg/m^3
$\alpha_A = 2$, $\alpha_B = 1$, $\alpha_C = 1.5$, $\alpha_D = 3$	unitless
$MW_A = MW_B = MW_C = 50$, $MW_D = 18$	$kg/kmol$

the composition of the overhead stream of the separator:

$$C_{Ar} = \frac{\alpha_A C_{A3}}{K},\ C_{Br} = \frac{\alpha_B C_{B3}}{K},\ C_{Cr} = \frac{\alpha_C C_{C3}}{K} \tag{4.31}$$

$$K = \alpha_A C_{A3}\frac{MW_A}{\rho} + \alpha_B C_{B3}\frac{MW_B}{\rho} + \alpha_C C_{C3}\frac{MW_C}{\rho} + \alpha_D x_D \rho \tag{4.32}$$

$$\begin{aligned} F_{rm} = \frac{F_r}{MW_D}[\rho - C_{A3}MW_A - C_{B3}MW_B - C_{C3}MW_C \\ + (C_{A3} + C_{B3} + C_{C3})MW_D] \end{aligned} \tag{4.33}$$

where x_D is the mass fraction of the solvent in the flash tank liquid holdup and F_{rm} is the recycle molar flow rate.

The process has four manipulated input variables: the heat supplied/removed for each vessel and the inlet flow rate F_{20} to the second reactor. The available control energy is $|Q_i| \leq 3 \times 10^5\, kJ/hr$, $i = 1, 2, 3$ and $0 \leq F_{20} \leq 10\, m^3/hr$. The control objective we consider is to drive the system to the unstable steady-state:

$$\begin{aligned} x_s^T &= \begin{bmatrix} T_1 & C_{A1} & C_{B1} & C_{C1} & T_2 & C_{A2} & C_{B2} & C_{C2} & T_3 & C_{A3} & C_{B3} & C_{C3} \end{bmatrix} \\ &= \begin{bmatrix} 370 & 3.32 & 0.17 & 0.04 & 435 & 2.75 & 0.45 & 0.11 & 435 & 2.88 & 0.50 & 0.12 \end{bmatrix} \end{aligned}$$

while proactively accounting for an incipient fault under the various simulated control actuator faults.

To design the Lyapunov-based controller $h(x)$, we consider a quadratic Lyapunov function $V(x) = x^T P x$ with $P = \text{diag}([20\ 10^3\ 10^3\ 10^3\ 10\ 10^3\ 10^3\ 10^3\ 10\ 10^3\ 10^3\ 10^3])$ and design the controller $h(x)$ as three PI controllers with proportional gains $K_{p1} = 5000$, $K_{p2} = 7000$, $K_{p3} = 7000$ and integral time constants $\tau_{I1} = \tau_{I2} = \tau_{I3} = 10$ based on the devi-

ation of temperature measurements of T_1, T_2, and T_3 from their respective steady-state temperature values. The feed flow rate into the second reactor is set to be a constant $F_{20} = 5\ kmol/m^3$ in the controller $h(x)$. The auxiliary controller $h(x)$ is used in the design of a proactive fault-tolerant LMPC of Eq. 4.8 with weighting matrices chosen to be $Q_c = P$, $R = \text{diag}([5 \times 10^{-12}\ 5 \times 10^{-12}\ 5 \times 10^{-12}\ 100])$, prediction horizon $N = 6$, and sampling period $\Delta = 0.005\ hr = 18\ sec$.

We implement the proactive fault-tolerant LMPC on the reactor-separator chemical process of Eqs. 4.19 - 4.33. To compare the proactive fault-tolerant controller with the closed-loop system without proactive fault-tolerant control, we implement another LMPC that does not account for the fault. The reactor-separator system is initialized at the stable steady-state $T_1 = T_2 = T_3 = 301\ K$, $C_{A1} = 3.58$, $C_{A2} = 3.33$, $C_{A3} = 3.50$, $C_{B1} = C_{B2} = C_{B3} = 0$, and $C_{C1} = C_{C2} = C_{C3} = 0$. The simulations were carried out using Java programming language in a Intel® Core™ i7, 3.40 GHz computer. The optimization problems were solved using the open source interior point optimization software Ipopt.[139]

In terms of fault/failure, they can be classified by its degree and action time so we introduce different types of actuator faults in the system. In case study A, we conduct a simulation for a fault in Q_2, which is a complete fault in the corresponding actuator. To simulate a realistic gradual actuator fault, we model a fault in Q_2 as a logistic function in case B as well as introduce process noise into the system. In case C, we simulate process recovery from the faulty system back to the fault-free system with the proposed proactive fault-tolerant controller after the faulty actuator is repaired. The following case studies were completed to simulate these scenarios and demonstrate the practical stability of the closed-loop system of Eqs. 4.19 - 4.33 with the proposed proactive fault-tolerant LMPC.

4.4.1 Complete Fault on the Q_2 Actuator

We consider a fault in the heat supplied to/removed from CSTR2 that renders $Q_2 = 0$ for $t \geq 0.0545\ hr$. The results of two one-hour closed-loop simulations are shown in Fig. 4.3 and Fig. 4.4. Fig. 4.3 shows the closed-loop process evolution with LMPC but without accounting for the fault and Fig. 4.4 shows the closed-loop process evolution with the proposed proactive fault-tolerant LMPC. Fig. 4.5 shows a plot of the manipulated input trajectories for (a) the closed-loop process without accounting for the fault and (b) the closed-loop process with the proposed proactive fault-tolerant LMPC from $t = 0\ hr$ to $t = 0.3\ hr$ to better highlight the differences between the two types of controllers.

From Fig. 4.5, we observe that the proactive fault-tolerant LMPC feeds less cold reactant by reducing the inlet feed F_{20} into CSTR2 leading up to the fault compared to the closed-loop process without proactive fault-tolerant control. Before the fault, CSTR2 is rich with the reactant A and the temperature in the reactor is less than the desired set-point. Considering that the reaction is exothermic and the initial temperature of inlet feed F_{20}, T_{20} is colder relative to the desired temperature of CSTR2, the proactive fault-tolerant controller take advantages of the heat generated from the exothermic reaction to heat the contents of CSTR2. Furthermore, we see that the proactive fault-tolerant controller shuts off the manipulated input Q_2 at the sampling time before the fault occurs and uses only the feed flow F_{20} into CSTR2 to bring the temperature and species concentrations of CSTR2 close to the desired set-points with $Q_2 = 0$. From Figs. 4.3 and 4.4, the post-fault behavior of these two control strategies is observed. The closed-loop process without proactive fault-tolerant control settles on an offsetting steady-state; whereas, the closed-loop process with the proposed proactive fault-tolerant LMPC settles at the desired steady-state.

To check how our proactive fault-tolerant LMPC works, we compared the controller performance indices: the process control cost with the proposed proactive fault-tolerant

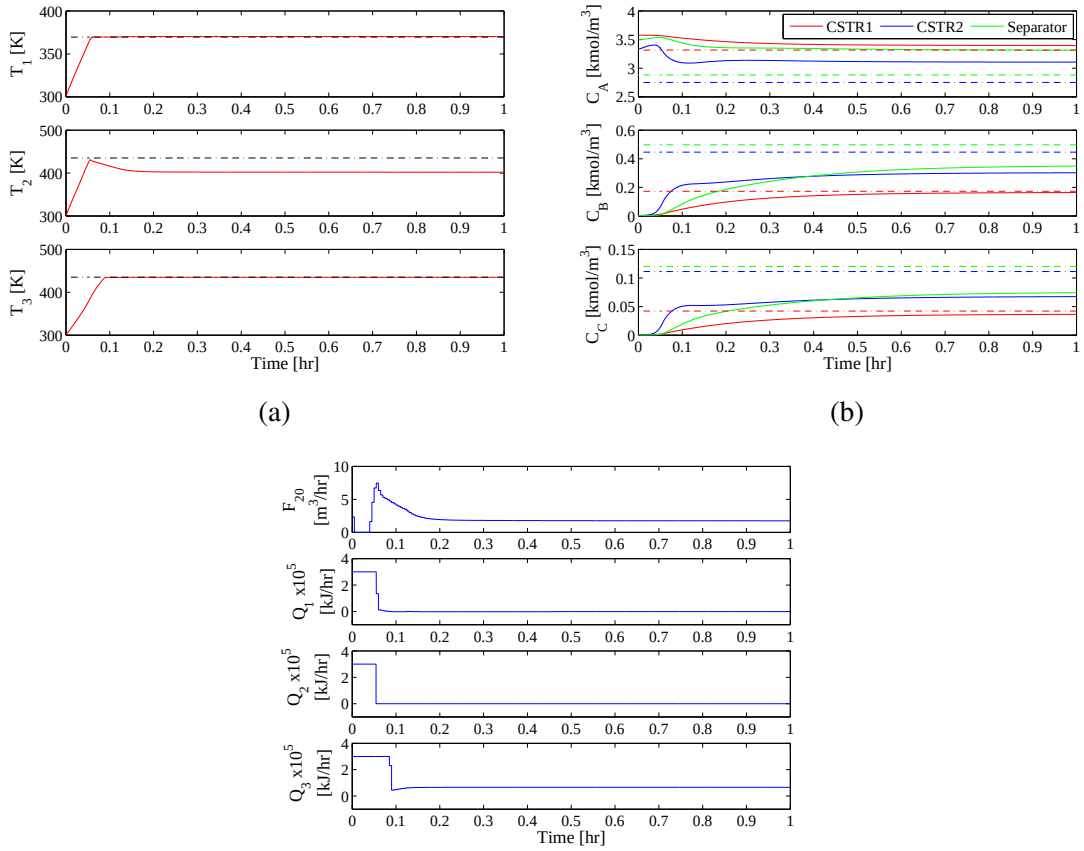

(a) (b)

(c)

Figure 4.3: The closed-loop process state and manipulated input trajectories (solid lines) and set-points (dashed lines): (a) vessel temperatures, (b) species concentrations, (c) manipulated inputs without proactive fault-tolerant control applied. The fault renders $Q_2(t) = 0$ for $t \geq 0.0545$ *hr*.

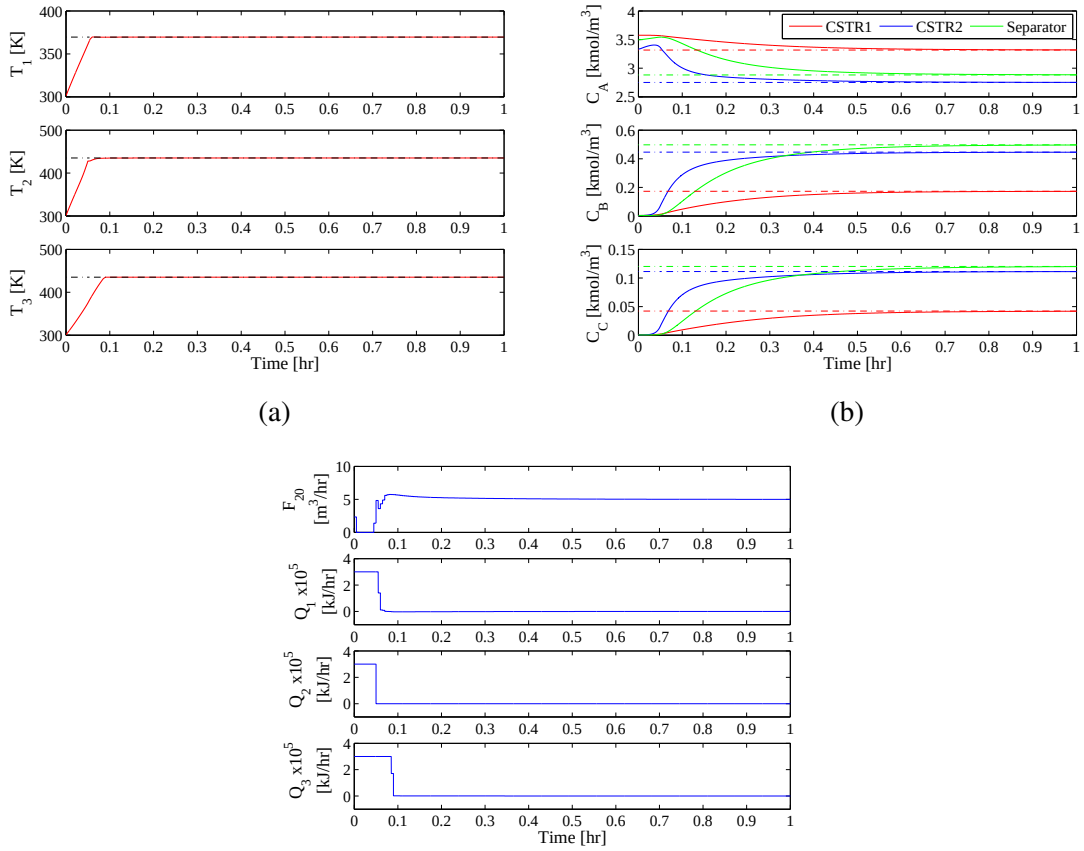

(a) (b)

(c)

Figure 4.4: The closed-loop process state and manipulated input trajectories (solid lines) and set-points (dashed lines): (a) vessel temperatures, (b) species concentrations, (c) manipulated inputs with proactive fault-tolerant control applied. The fault renders $Q_2(t) = 0$ for $t \geq 0.0545$ *hr*.

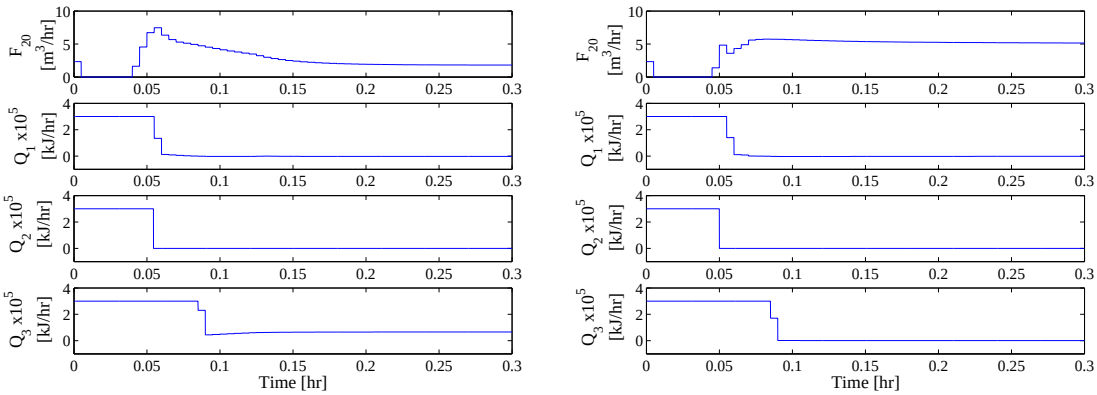

(a) (b)

Figure 4.5: The closed-loop input trajectories: (a) without proactive fault-tolerant control and (b) with the proposed proactive fault-tolerant LMPC. The fault renders $Q_2(t) = 0$ for $t \geq 0.0545$ *hr*.

LMPC is 2.35×10^4 which is much smaller than 1.99×10^5, that without accounting for the fault. The proposed proactive fault-tolerant LMPC take advantages of the known fault and adjust the control performance to adapt to the future fault.

4.4.2 Gradual Fault on the Q_2 Actuator with Bounded Process Noise

In certain cases, an actuator may fail gradually. Based on the empirical function of the reliability of process components, the maximum available output of the faulty actuator usually decreases exponentially on the basis of its original maximum available output.[43] Thus, in this case, we use a logistic function to represent the maximum available output of the faulty actuator for the heat input/removal to CSTR2. The logistic function has a general formula as follows:[138]

$$|U_{max}(t)| = \frac{a}{1+\exp\left(\frac{-(t-c)}{b}\right)} \left|U_{max,0}\right| \tag{4.34}$$

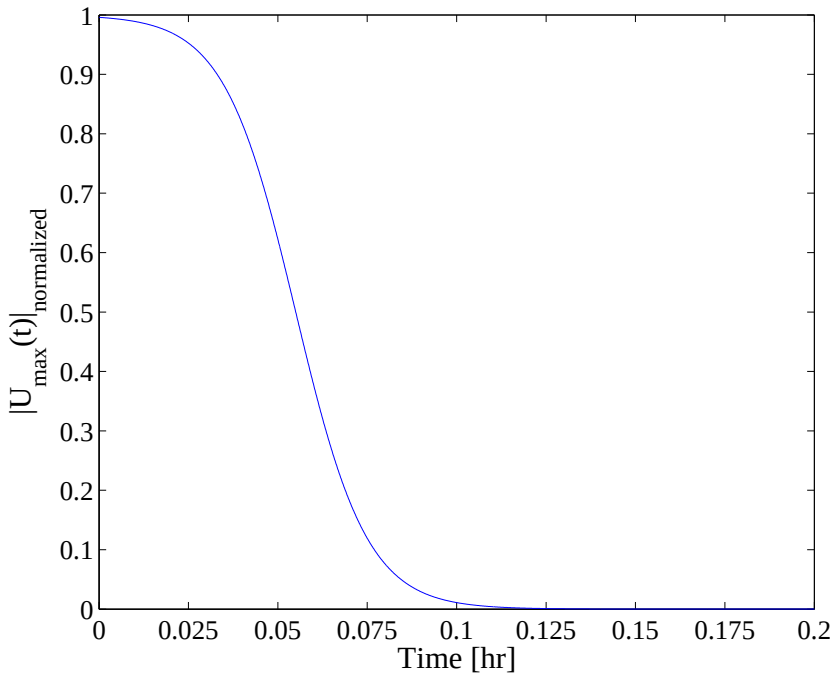

Figure 4.6: The plot of the logistic function for the normalized maximum output of the faulty actuator. At $t = 0.1\ hr$, the maximum output of the faulty actuator becomes very close to 0% of its fault-free output value.

where a, b and c are parameters, $|U_{max}(t)|$ is the maximum available control energy of the jth faulty control actuator, and $\left|U_{max,0}\right|$ is the maximum available output of the actuator under fault-free conditions. Fig. 4.6 shows a plot of the logistic function of Eq. 4.34 used to model a gradual fault in Q_2 with parameters: $a = 1$, $b = -0.01\ hr$ and $c = 0.055\ hr$. From the plot, we can observe that the maximum available output value decreases slowly at the beginning, but the derivative of this function decreases quickly which is characteristic of a realistic actuator fault. For this particular function, the maximum available output of the faulty actuator becomes very close to 0% of its fault-free output at $t = 0.1\ hr$.

Instead of switching the control problem from 4 control actuators to the 3 remaining control actuators at the beginning of the gradual fault, the proactive fault-tolerant LMPC accounts for the faulty actuator of Q_2 whose maximum available output decreases following

the above logistic function. In this case, the gradual fault begins at $t = 0.0545\ hr$ and the proactive fault-tolerant LMPC regards $t = 0.1545\ hr$ as the time to reconfigure the control system from 4 available control actuators to the 3 remaining control actuators. This time has been chosen as 0.1 *hr* after the beginning of the gradual fault because the maximum available output of the faulty actuator at this time is almost 0% of its fault-free output.

We also consider the effect of bounded process noise on the process. Process noise is added to each of the 12 states and modeled as bounded Gaussian white noise with 0 mean, unit variance, and bounds given by $w_p = [2\ 0.25\ 0.05\ 0.05\ 2\ 0.25\ 0.05\ 0.05\ 2\ 0.25\ 0.05\ 0.05]$. The results of two one-hour closed-loop simulations are shown in Fig. 4.7 and Fig. 4.8. Fig. 4.7 shows the closed-loop process evolution with LMPC, but without accounting for the fault and Fig. 4.8 shows the closed-loop process evolution with the proposed proactive fault-tolerant LMPC. Fig. 4.5b shows a plot of the manipulated input trajectories for (a) the closed-loop process without accounting for the fault and (b) the closed-loop process with the proposed proactive fault-tolerant LMPC from $t = 0\ hr$ to $t = 0.3\ hr$ to better highlight the differences between the two types of controllers. The maximum available control energy in the faulty actuator of Q_2 follows the logistic function of Eq. 4.34 with the parameters $a = 1$, $b = -0.01\ hr$ and $c = 0.055\ hr$. The gradual fault begins at $t = 0.0545\ hr$.

From Fig. 4.9b, we observe that the proactive fault-tolerant controller chooses a similar strategy as in case A. Specifically, by accounting for the gradual fault that limits the available maximum output of Q_2, the proactive fault-tolerant controller feeds less reactant material A into CSTR2 leading up to the fault and maintains the temperature T_2 at the desired steady-state as the maximum output of Q_2 decreases. The closed-loop process without proactive fault-tolerant control (Fig. 4.9a) feeds more feedstock into CSTR2 while demanding more heat removed to decrease the temperature T_2 to the desired steady-state after the fault. However, the fault has rendered the Q_2 actuator inactive and therefore, cannot remove heat from CSTR2. The effect of feeding more material without removing heat causes the

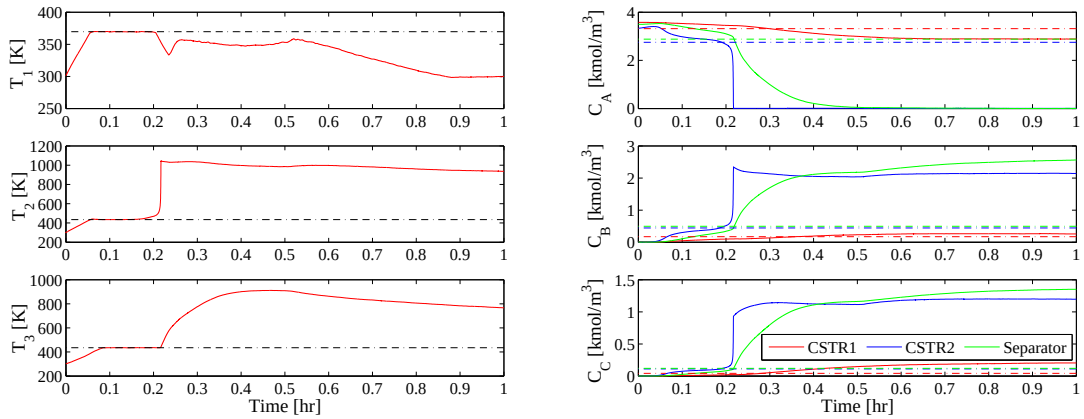

(a) (b)

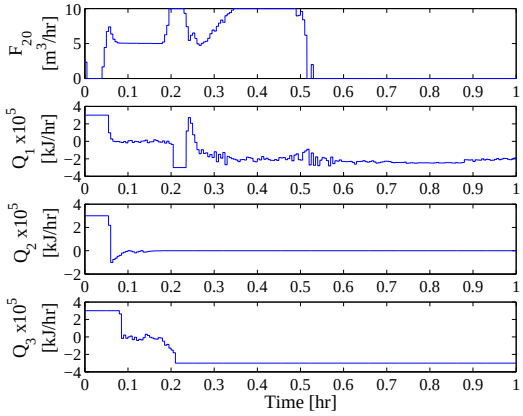

(c)

Figure 4.7: The closed-loop process state and manipulated input trajectories (solid lines) and set-points (dashed lines): (a) vessel temperatures, (b) species concentrations, (c) manipulated inputs without proactive fault-tolerant control applied. The maximum available control energy in the faulty actuator of Q_2 follows the logistic function; the gradual fault starts at $t = 0.0545\ hr$.

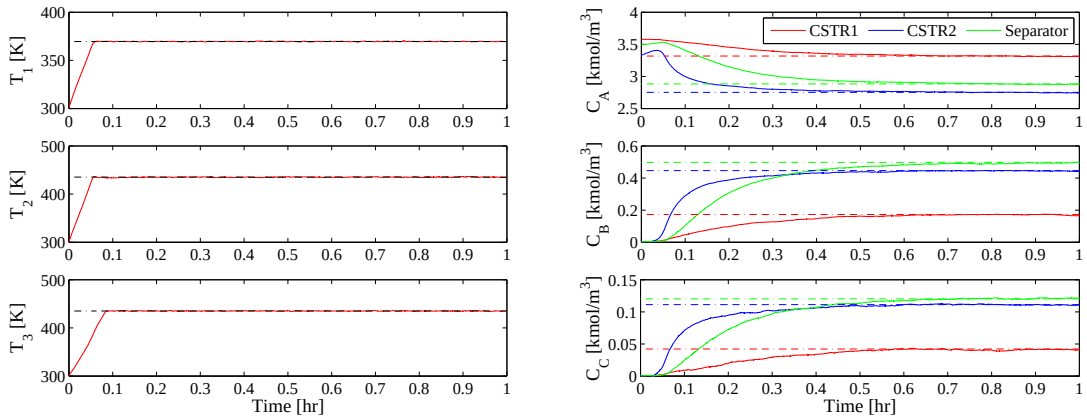

(a) (b)

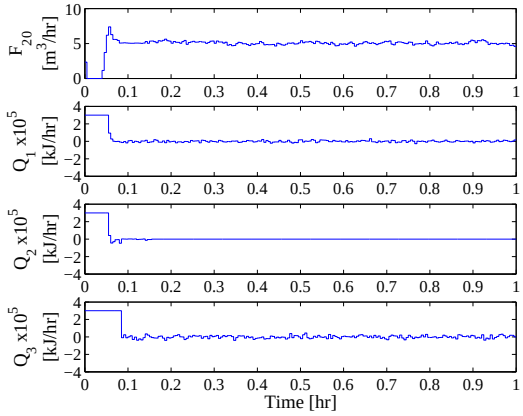

(c)

Figure 4.8: The closed-loop process state and manipulated input trajectories (solid lines) and set-points (dashed lines): (a) vessel temperatures, (b) species concentrations, (c) manipulated inputs with proactive fault-tolerant control applied. The maximum available control energy in the faulty actuator of Q_2 follows the logistic function; the gradual fault starts at $t = 0.0545$ *hr*.

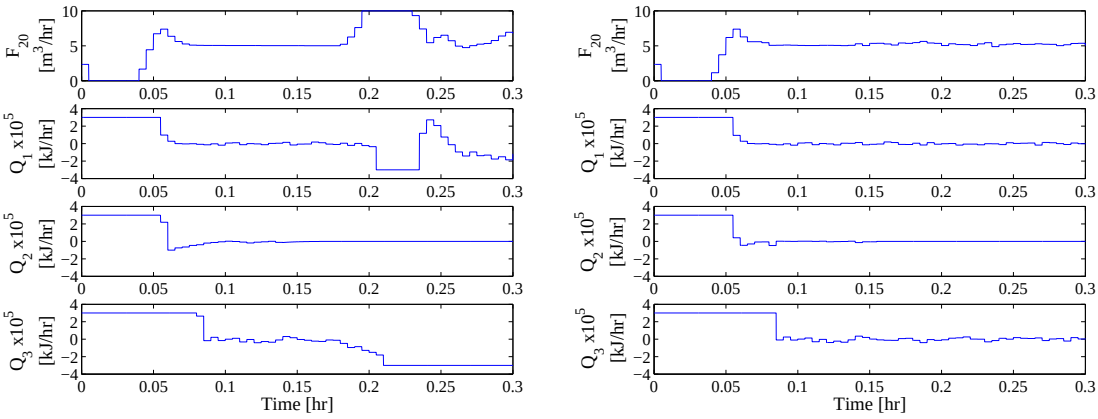

Figure 4.9: The closed-loop input trajectories: (a) without proactive fault-tolerant control and (b) with the proposed proactive fault-tolerant LMPC. The maximum available control energy in the faulty actuator of Q_2 follows the logistic function of Eq. 4.34 with parameters: $a = 1$, $b = -0.01$ hr and $c = 0.055$ hr; the gradual fault starts at $t = 0.0545$ hr.

reactions to runaway because the reactions are highly exothermic. The post-fault behavior of these two control strategies is observed in Fig. 4.7 and Fig. 4.8. The process under the proactive fault-tolerant controller brings the process states to the desired steady-state. The process without the proposed proactive LMPC settles on an offsetting steady-steady.

Also, we compared the controller performance indices: the process control cost with the proposed proactive fault-tolerant LMPC is 2.55×10^4 which is much smaller than 3.76×10^5, that without accounting for the gradual fault. The proposed proactive fault-tolerant LMPC take advantages of the known fault and adjust the control performance to adapt to the future fault.

4.4.3 Process Recovery from 3-input Control System to Fault-Free 4-input Control System

In this case, we demonstrate that with the proposed proactive LMPC we can successfully recover back to the full, fault-free system after an actuator fault has been rectified or re-

placed. Fig. 4.10 shows the closed-loop evolution of the process with the proactive fault tolerant controller with the same gradual fault in the Q_2 actuator as in case study B. We consider $t = 0.625\ hr$ is the time the faulty actuator has been fixed and added back. From Fig. 4.10, the controller is able to achieve practical stability both after the fault and after the faulty actuator has been fixed and added back to the system.

4.5 Conclusions

In this work, we proposed a proactive fault-tolerant Lyapunov-based MPC that can account for a known future fault and work for complete fault rejection. We proved practical stability of a closed-loop nonlinear system with the proposed proactive fault-tolerant LMPC. The proposed controller was demonstrated through a chemical process consisting of two CSTRs in series followed by a flash separator. The simulated process demonstrated that the proactive fault-tolerant LMPC was able to achieve practical stability of the closed-loop system. However, sensor faults or even process abnormal events which are very often encountered in practice, also have a significant effect on the controller performance. Thus we plan to explore these types of faults in a future work.

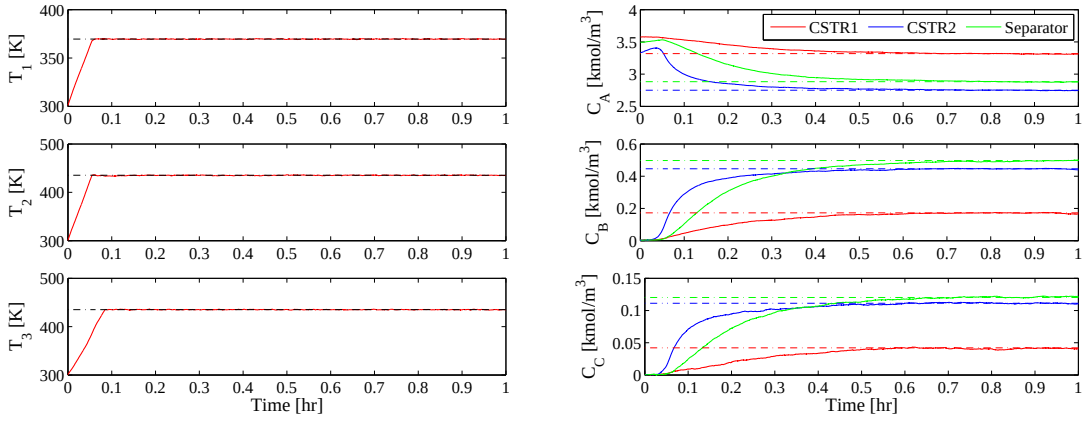

(a) (b)

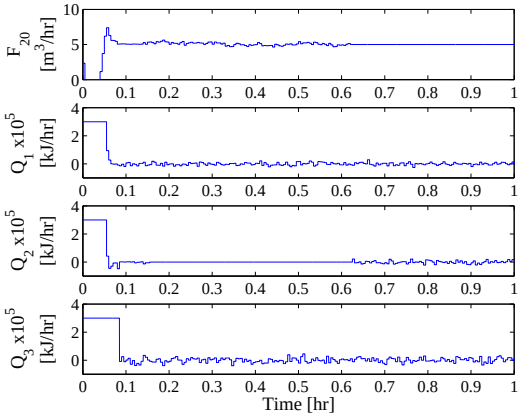

(c)

Figure 4.10: The closed-loop process state and manipulated input trajectories (solid lines) and set-points (dashed lines): (a) vessel temperatures, (b) species concentrations and (c) manipulated inputs with the proposed proactive fault-tolerant LMPC. The maximum available control energy in the faulty actuator of Q_2 follows the logistic function with the given parameters. At $t = 0.625$ *hr*, the proactive fault-tolerant controller adds the repaired Q_2 actuator back to the closed-loop system.

Chapter 5

Economic Model Predictive Control of Transport-Reaction Processes

5.1 Introduction

This chapter presents the development of economic model predictive control (EMPC) systems for transport-reaction processes that are described by nonlinear parabolic partial differential equations (PDEs). Through the application of Galerkin's method, finite-dimensional ordinary differential equation models are first derived that capture the dominant dynamics of the parabolic PDEs. The reduced-order models are then used to formulate finite-dimensional EMPC systems of varying dimension depending on the type of state constraints imposed. The EMPC systems are applied to a non-isothermal tubular reactor, described by two nonlinear parabolic PDEs, where a second-order chemical reaction takes place. A state constraint that bounds the reactor temperature as well as an input constraint that bounds the available reactant material over a fixed period of operation are considered in the formulations of the EMPC systems which use the average reaction rate along the length of the reactor as the economic cost function. Closed-loop simulations are conducted

where a low-order EMPC system and a high-order EMPC system are separately applied to a high-order discretization of the reactor model of PDEs, and they demonstrate that the EMPC systems operate the process in a time-varying fashion to improve the economic cost over steady-state operation and meet input and state constraints.

5.2 Preliminaries

5.2.1 Class of Parabolic PDE Systems

In this work, we consider parabolic partial differential equation systems with a state-space representation of the following form:

$$\frac{\partial \bar{x}}{\partial t} = A\frac{\partial \bar{x}}{\partial z} + B\frac{\partial^2 \bar{x}}{\partial z^2} + Wu(t) + f(\bar{x}(z,t)) \tag{5.1}$$

subject to the boundary conditions:

$$\begin{aligned} \frac{\partial \bar{x}}{\partial z} &= g_0\bar{x}, \quad z = 0; \\ \frac{\partial \bar{x}}{\partial z} &= g_1\bar{x}, \quad z = 1; \end{aligned} \tag{5.2}$$

and the initial condition:

$$\bar{x}(z,0) = \bar{x}_0(z) \tag{5.3}$$

where $\bar{x}(z,t) = [\bar{x}_1(z,t) \cdots \bar{x}_{n_x}(z,t)]'$ denotes the state vector of the system, the notation $\bar{x}'$ denotes the transpose of $\bar{x}$, $f(\bar{x}(z,t))$ denotes a nonlinear vector function, $z \in [0,1]$ is the spatial coordinate, $t \in [0,\infty)$ is the time, A, B, W, g_0 and g_1 are matrices and vectors of appropriate dimensions, $u(t)$ denotes the n_u-dimensional manipulated input vector and is

subject to the following input constraints:

$$u_{min} \leq u(t) \leq u_{max} \tag{5.4}$$

where u_{min} and u_{max} are the lower and upper bound vectors of the manipulated input $u(t)$. Moreover, the system states are also subject to the following constraints:

$$x_{min} \leq \int_0^1 r_x(z)\bar{x}(z,t)dz \leq x_{max} \tag{5.5}$$

where x_{min} and x_{max} are the lower and upper state constraint, respectively. The function $r_x(z) \in L_2(0,1)$ is the state constraint distribution function used to describe how the state constraint is enforced in the spatial domain $[0,1]$ and $L_2(0,1)$ is used to denote the space of measurable functions that are square-integrable on the interval $[0,1]$.

5.2.2 Galerkin's Method

To present our results, we first formulate the system of PDEs as an infinite dimensional system in the Hilbert space $\mathscr{H}([0,1];\mathbb{R}^{n_x})$, with $\mathscr{H}$ being the space of measurable vector functions defined on $[0,1]$, with inner product and norm:

$$\begin{aligned} &(\omega_1,\omega_2) = \int_0^1 (\omega_1(z),\omega_2(z))_{\mathbb{R}^{n_x}} dz, \\ &\|\omega_1\|_2 = (\omega_1,\omega_1)^{\frac{1}{2}} \end{aligned} \tag{5.6}$$

where ω_1,ω_2 are two elements of $\mathscr{H}([0,1];\mathbb{R}^{n_x})$ and the notation $(\cdot,\cdot)_{\mathbb{R}^{n_x}}$ denotes the standard inner product in $\mathbb{R}^{n_x}$. The state function $x(t)$ on the state-space $\mathscr{H}$ is defined as

$$x(t) = \bar{x}(z,t), \quad t > 0, \quad 0 \leq z \leq 1, \tag{5.7}$$

and the operator $\mathscr{A}$ is defined as

$$\mathscr{A}x = A\frac{d\bar{x}}{dz} + B\frac{d^2\bar{x}}{dz^2}, \quad 0 \leq z \leq 1. \tag{5.8}$$

Then, the system of Eq. 5.1 takes the following infinite-dimensional quasi-linear form:

$$\dot{x}(t) = \mathscr{A}x(t) + \mathscr{B}u(t) + \mathscr{F}(x(t)), \quad x(0) = x_0 \tag{5.9}$$

where $x_0 = \bar{x}_0(z)$, $\mathscr{B}u(t) = Wu(t)$ and $\mathscr{F}(x(t))$ is a nonlinear vector function in the Hilbert space. For the operator $\mathscr{A}$, the eigenvalue problem takes the form

$$\mathscr{A}\phi_k = \lambda_k\phi_k, \quad k = 1, \ldots, \infty \tag{5.10}$$

subject to

$$\begin{aligned} \frac{d\phi_k}{dz}(0) &= g_0\phi_k(0), \\ \frac{d\phi_k}{dz}(1) &= g_1\phi_k(1) \end{aligned} \tag{5.11}$$

where ϕ_k is an eigenfunction corresponding to the k-th eigenvalue and $\bar{\phi}_k$ is an adjoint eigenfunction of the operator $\mathscr{A}$.

Assumption 5.1 below characterizes the class of parabolic PDEs considered in this work and states that the eigenspectrum of operator $\mathscr{A}$ can be partitioned into a finite part consisting of m slow eigenvalues which are close to the imaginary axis and a stable infinite complement containing the remaining fast eigenvalues which are far in the left-half of the complex plane, and that the separation between the slow and fast eigenvalues of $\mathscr{A}$ is large. We also note that the large separation of slow and fast modes of the spatial operator in parabolic PDEs ensures that a controller which exponentially stabilizes the closed-loop ODE system, also stabilizes the closed-loop infinite-dimensional system.[9] This assumption

is satisfied by the majority of diffusion-convection-reaction processes.[25]

Assumption 5.1

1. *$Re(\lambda_1) \geq Re(\lambda_2) \geq \cdots \geq Re(\lambda_j) \geq \cdots$, where $Re(\lambda_j)$ denotes the real part of the eigenvalue, λ_j.*

2. *The eigenspectrum of $\mathscr{A}$, $\sigma(\mathscr{A})$, is defined as the set of all eigenvalues of $\mathscr{A}$, i.e. $\sigma(\mathscr{A}) = \{\lambda_1, \lambda_2, \cdots\}$. $\sigma(\mathscr{A})$ can be portioned as $\sigma(\mathscr{A}) = \sigma_1(\mathscr{A}) \cup \sigma_2(\mathscr{A})$, where $\sigma_1(\mathscr{A})$ consists of the first m finite eigenvalues, i.e. $\sigma_1(\mathscr{A}) = \{\lambda_1, \cdots, \lambda_m\}$, and $|Re(\lambda_1)|/|Re(\lambda_m)| = O(1)$.*

3. *$Re(\lambda_{m+1}) < 0$ and $|Re(\lambda_1)|/|Re(\lambda_{m+1})| = O(\varepsilon)$ where $\varepsilon < 1$ is a small positive number.*

Next, we apply standard Galerkin's method to the infinite-dimensional system of Eq. 5.9 to derive a finite-dimensional system. Let $\mathscr{H}_s$ and $\mathscr{H}_f$ be modal subspaces of $\mathscr{A}$ defined as $\mathscr{H}_s = \text{span}\{\phi_1, \phi_2, \ldots, \phi_m\}$ and $\mathscr{H}_f = \text{span}\{\phi_{m+1}, \phi_{m+2}, \ldots\}$. The existence of $\mathscr{H}_s$ and $\mathscr{H}_f$ follows from the properties of $\mathscr{A}$. Defining the orthogonal projection operators, P_s and P_f, which projects the state x onto the subspaces $\mathscr{H}_s$ and $\mathscr{H}_f$ of $\mathscr{A}$, respectively (i.e., $x_s = P_s x \in \mathscr{H}_s$ and $x_f = P_f x \in \mathscr{H}_f$), the state x of the system of Eq. 5.9 can be decomposed as

$$x = x_s + x_f = P_s x + P_f x \tag{5.12}$$

Applying P_s and P_f to the system of Eq. 5.9 and using the above decomposition for x, the system of Eq. 5.9 can be re-written in the following equivalent form:

$$\begin{aligned} \dot{x}_s(t) &= \mathscr{A}_s x_s(t) + \mathscr{F}_s(x_s(t), x_f(t)) + \mathscr{B}_s u(t), \quad x_s(0) = P_s x(0) = P_s x_0 \\ \dot{x}_f(t) &= \mathscr{A}_f x_f(t) + \mathscr{F}_f(x_s(t), x_f(t)) + \mathscr{B}_f u(t), \quad x_f(0) = P_f x(0) = P_f x_0 \end{aligned} \tag{5.13}$$

where $\mathscr{A}_s = P_s\mathscr{A}$, $\mathscr{B}_s = P_s\mathscr{B}$, $\mathscr{A}_f = P_f\mathscr{A}$, $\mathscr{B}_f = P_f\mathscr{B}$, $\mathscr{F}_f = P_f\mathscr{F}$, $\mathscr{F}_s = P_s\mathscr{F}$. In the above system, $\mathscr{A}_s = \text{diag}\{\lambda_j\}$, $j = 1, \ldots, m$ is a diagonal matrix of dimension $m \times m$ and may contain unstable eigenvalues (i.e., $Re(\lambda_j) > 0$). The operator $\mathscr{A}_f$ is an unbounded exponentially stable differential operator. Neglecting the fast modes, the resulting ODE system is

$$\dot{x}_s(t) = \mathscr{A}_s x_s(t) + \mathscr{F}_s(x_s(t), 0) + \mathscr{B}_s u(t), \quad x_s(0) = P_s x_0 \tag{5.14}$$

which is a finite-dimensional system that describes the slow (dominate) dynamics of the PDEs of Eq. 5.1 and may be used for standard model-based control synthesis

Remark 5.1 *Whenever the eigenfunction ϕ_j of the operator $\mathscr{A}$ cannot be calculated analytically, one can still use Galerkin's method to perform model reduction by using empirical eigenfunction of the system of PDEs as basis functions in $\mathscr{H}_s$ and $\mathscr{H}_f$ (such empirical eigenfunctions can be extracted from detailed numerical simulations of the system of PDEs using Karhunen-Loeve expansion; see Ref[69])*

5.3 Economic Model Predictive Control Problem Formulation

We consider the application of economic model predictive control (EMPC) to the infinite-dimensional system of Eq. 5.9 to optimize an economic measure. We assume that the EMPC receives state measurements continuously and synchronously at sampling periods

denoted as $t_k = k\Delta$ with $k = 0, 1, \ldots$. The EMPC optimization problem has the form

$$\max_{u \in S(\Delta)} \quad \int_{t_k}^{t_{t_{k+N}}} L(\tilde{x}(\tau), u(\tau)) d\tau \tag{5.15a}$$

$$\text{s.t.} \quad \dot{\tilde{x}}(t) = \mathscr{A}\tilde{x}(t) + \mathscr{F}(\tilde{x}(t)) + \mathscr{B}u(t) \tag{5.15b}$$

$$\tilde{x}(t_k) = x(t_k) \tag{5.15c}$$

$$u_{min} \leq u(t) \leq u_{max}, \ \forall t \in [t_k, t_{k+N}) \tag{5.15d}$$

$$x_{min} \leq (r_x, \tilde{x}(t)) \leq x_{max}, \ \forall t \in [t_k, t_{k+N}) \tag{5.15e}$$

where Δ is the sampling period, $S(\Delta)$ is the family of piecewise constant functions with sampling period Δ, N is the prediction horizon, $\tilde{x}(t)$ is the predicted state function evolution with input $u(t)$ computed by the EMPC and $x(t_k)$ is the state measurement. In the optimization problem of Eq. 5.15, the cost function of Eq. 5.15a defined as $L(\tilde{x}(\tau), u(\tau))$ is formulated to directly account for the economics of the system of PDEs. The constraint of Eq. 5.15b is the system of PDEs in the Hilbert space used to predict the future evolution of the system of PDEs with the initial condition of Eq. 5.15c obtained through state feedback. The constraints of Eq. 5.15d-5.15e are the available control energy and state constraints, respectively. The optimal solution to this optimization problem is $u^*(t|t_k)$ defined for $t \in [t_k, t_{k+N})$. The EMPC applies the control action computed for the first sampling period to the system in a sample-and-hold fashion for $t \in [t_k, t_{k+1})$. The EMPC is resolved at the next sampling period, t_{k+1}, after receiving a new state measurement, $x(t_{k+1})$. The infinite dimensional nature of the controller of Eq. 5.15 in this case, however, renders it unsuitable for the purpose of practical implementation.

5.3.1 Low-order Economic Model Predictive Control Formulation

In this formulation, a Lyapunov-based EMPC (LEMPC) system (see Ref[65] for results on LEMPC) is designed on the basis of the low-order, finite-dimensional slow subsystem of Eq. 5.14 describing the evolution of x_s (the fast subsystem is neglected). The low-order EMPC law is obtained by solving, in a receding horizon fashion, the following finite-dimensional optimization problem:

$$\max_{u\in S(\Delta)} \quad \int_{t_k}^{t_{t_{k+N}}} L(\tilde{x}_s(\tau),u(\tau))d\tau \tag{5.16a}$$

$$\text{s.t.} \quad \dot{\tilde{x}}_s(t) = \mathscr{A}_s\tilde{x}_s(t) + \mathscr{F}_s(\tilde{x}_s(t),0) + \mathscr{B}_s u(t) \tag{5.16b}$$

$$\tilde{x}_s(t_k) = P_s x(t_k) \tag{5.16c}$$

$$u_{min} \leq u(t) \leq u_{max},\ \forall t \in [t_k,t_{k+N}) \tag{5.16d}$$

$$x_{min} \leq (r_x,\tilde{x}_s(t)) \leq x_{max},\ \forall t \in [t_k,t_{k+N}) \tag{5.16e}$$

$$(\tilde{x}_s(t),P\tilde{x}_s(t)) \leq \bar{\rho},\ \forall t \in [t_k,t_{k+N}) \tag{5.16f}$$

The constraints of Eq. 5.16b-5.16c are used to predict the future evolution of the slow subsystem with the initial condition given in Eq. 5.16c. The constraints of Eq. 5.16d-5.16e are the available control energy and the state constraints, respectively. The constraint of Eq. 5.16f is a quadratic Lyapunov function (P is an $m \times m$ dimensional positive definite matrix) of the slow subsystem and ensures that the predicted state trajectory is restricted inside a predefined stability region which is a level set of the Lyapunov function (see Ref[65] for a complete discussion of this issue).

Remark 5.2 *The reduced-order EMPC formulation may achieve suboptimal solutions compared to the infinite dimensional EMPC problem, but it is not possible to quantify how suboptimal the solution obtained via the reduced-order formulation is (due to the inability to compute the solution of the infinite-dimensional problem).*

Remark 5.3 *To improve the accuracy of the slow finite-dimensional x_s-subsystem, the finite-dimensional approximation of the system of Eq. 5.14 may be obtained through combination of Galerkin's method with approximate inertial manifolds. This approach can be used to further reduce the dimension of the x_s-subsystem and ensure that it is of an appropriately low-order suitable for controller design and on-line controller implementation system.*[25]

5.3.2 High-order Economic Model Predictive Control Formulation

Accounting for the evolution of the fast subsystem is important for the purpose of satisfying state constraints. To formulate a finite dimensional EMPC optimization problem, the fast subsystem is truncated at the l-th fast state (i.e., the $l+1, l+2, \ldots$ states are discarded). The notation $\hat{\cdot}$ is used to denote the finite-dimensional truncation of the fast subsystem. The computational complexity associated with accounting for the fast subsystem could be eased by neglecting the nonlinearity in the dynamic model of the fast modes, while retaining the nonlinear dynamics of the slow modes (so as to not adversely effect the task of stabilization). The term $\hat{\mathscr{A}_f}$ behaves like $1/\varepsilon$ (in Assumption 5.1), where ε is a small parameter. Therefore, $\hat{\mathscr{A}_f}$ is much greater than $\hat{\mathscr{F}_f}$ and $\hat{\mathscr{F}_f}$ can be neglected from the equation (see Ref[25] for more discussion and analysis of this approximation). Using this

approximation, the EMPC formulation takes the following form:

$$\max_{u \in S(\Delta)} \quad \int_{t_k}^{t_{t_{k+N}}} L(\tilde{x}(\tau), u(\tau)) d\tau \tag{5.17a}$$

$$\text{s.t.} \quad \dot{\tilde{x}}_s(t) = \mathscr{A}_s \tilde{x}_s(t) + \mathscr{F}_s(\tilde{x}_s(t), \hat{x}_f(t)) + \mathscr{B}_s u(t) \tag{5.17b}$$

$$\dot{\hat{x}}_f(t) = \hat{\mathscr{A}}_f \hat{x}_f(t) + \hat{\mathscr{B}}_f u(t) \tag{5.17c}$$

$$\tilde{x}_s(t_k) = P_s x(t_k), \quad \hat{x}(t_k) = \hat{P}_f x(t_k) \tag{5.17d}$$

$$\check{x}(t) = \tilde{x}_s(t) + \hat{x}_f(t) \tag{5.17e}$$

$$u_{min} \leq u(t) \leq u_{max}, \ \forall t \in [t_k, t_{k+N}) \tag{5.17f}$$

$$x_{min} \leq (r_x, \check{x}(t)) \leq x_{max}, \ \forall t \in [t_k, t_{k+N}) \tag{5.17g}$$

$$(\check{x}(t), P\check{x}(t)) \leq \bar{\rho} \tag{5.17h}$$

In the optimization problem of Eq. 5.17, the constraint of Eq. 5.17c is the finite-dimensional truncation of the fast subsystem (nonlinear part of the dynamics being neglected) which is used to predict the evolution of the fast subsystem states, and $\check{x}(t)$ is used to denote the vector of all the states (i.e., both the slow subsystem and fast subsystem states). The cost function and the remaining constraints are similar to Eq. 5.16.

Remark 5.4 *We choose a certain number of modes of the dynamic system of Eqs. 5.17b-5.17c for the synthesis of the high-order EMPC formulation to make sure that further increase in the number of modes leads to identical numerical results.*

Remark 5.5 *State constraints arise either due to the necessity to keep the process state variables within acceptable ranges to avoid, for example, runaway reactions (in which case they need to be enforced at all times and treated as hard constraints) or due to the desire to maintain process state variables within desirable bounds dilated by performance considerations (in which case they may be relaxed, and treated as soft constraints). In the*

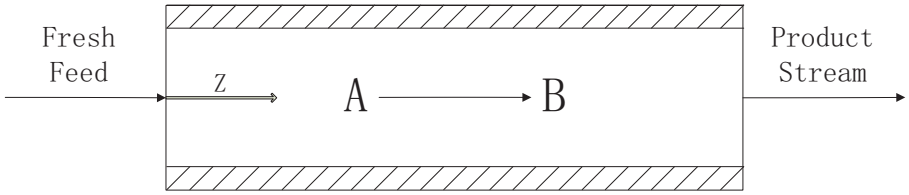

Figure 5.1: A tubular reactor with reaction A $\rightarrow$ B.

formulations presented in this work, we consider state constraints that are hard constraints but could also be treated as soft ones; for predictive controller formulations where the state constraints are handled as soft constraints, see, e.g., Refs.[100,122]

5.4 Application To A Tubular Reactor

In this section, we apply the low-order and high-order EMPC systems to a transport-reaction chemical process example. First, we present the model of the transport-reaction process which is a tubular reactor. Second, we apply Galerkin's method to the chemical process example to construct a reduced-order model in modal space. Finally, we present a series of simulations with EMPC systems formulated with various state and input constraints to assess the performance of the closed-loop system under the EMPC.

5.4.1 Reactor Description

We consider a non-isothermal tubular reactor shown in Fig. 5.1, where an irreversible second-order reaction of the form A $\rightarrow$ B takes place. The reaction is exothermic and a cooling jacket of constant temperature is used to remove heat from the reactor. Under the standard assumptions of constant density (ρ) and heat capacity (C_p) of the reacting fluid, and constant axial fluid velocity (v), the dynamic model of the process can be derived from mass and energy balances and takes the following form:

$$\begin{aligned}
\frac{\partial T}{\partial t} &= -v\frac{\partial T}{\partial z} + \frac{k}{\rho C_p}\frac{\partial^2 T}{\partial z^2} + \left(\frac{-\Delta H k_0}{\rho C_p}\right)\exp\left(\frac{-E}{RT}\right)C_A^2 - \frac{hA_s}{\rho C_p}(T - T_C) \\
\frac{\partial C_A}{\partial t} &= -v\frac{\partial C_A}{\partial z} + D_A\frac{\partial^2 C_A}{\partial z^2} - k_0\exp\left(\frac{-E}{RT}\right)C_A^2
\end{aligned} \tag{5.18}$$

where T and C_A denote the temperature and concentration of species A in the reactor, respectively, k and D_A are the thermal conductivity and mass diffusivity of the reacting fluid, respectively, k_0, E and $(-\Delta H)$ represent the pre-exponential constant, activation energy, and the heat of the reaction, respectively, h is the heat transfer coefficient between the reactor and the cooling jacket, A_s is the surface area of the reactor walls, and T_c is the jacket temperature. The system is subject to the boundary conditions:

$$\begin{aligned}
z = 0 \quad &: \quad \frac{\partial T}{\partial z} = \frac{\rho C_p v}{k}(T - T_f),\ \frac{\partial C_A}{\partial z} = \frac{v}{D_A}(C_A - C_{Af}); \\
z = L \quad &: \quad \frac{\partial T}{\partial z} = 0,\ \frac{\partial C_A}{\partial z} = 0;
\end{aligned} \tag{5.19}$$

where T_f and C_{Af} denote the inlet temperature and concentration of species A in the reactor and L is the length of the reactor. In this case, we choose the inlet concentration of species A, C_{Af} as the manipulated input. In order to simplify the presentation of our results, we introduce the following dimensionless variables:

$$\begin{gathered}
\bar{t} = \frac{tv}{L}, \qquad \bar{z} = \frac{z}{L}, \qquad Pe_1 = \frac{\rho C_p v L}{k}, \qquad Pe_2 = \frac{vL}{D_A}, \\
\bar{x}_1 = \frac{T - T_0}{T_0}, \quad \bar{x}_2 = \frac{C_A - C_{A0}}{C_{A0}}, \quad u = \frac{C_{Af} - C_{A0}}{C_{A0}}, \qquad \gamma = \frac{E}{RT_0}, \\
T_s = \frac{T_c - T_0}{T_0}, \quad T_i = \frac{T_f - T_0}{T_0}, \qquad \beta_T = \frac{hA_s L}{\rho C_p v}, \qquad B_T = \frac{-(\Delta H)C_{A0}}{\rho C_p T_0}, \\
B_C = \frac{k_0 C_{A0} e^{-E/RT_0} L}{v}
\end{gathered} \tag{5.20}$$

where T_0 and C_0 are reference temperature and concentration, respectively, to write the system of Eqs. 5.18-5.19 in the following form:

$$\begin{aligned}
\frac{\partial \bar{x}_1}{\partial \bar{t}} &= -\frac{\partial \bar{x}_1}{\partial \bar{z}} + \frac{1}{Pe_1}\frac{\partial^2 \bar{x}_1}{\partial \bar{z}^2} + B_T B_C \exp\left(\frac{\gamma \bar{x}_1}{1+\bar{x}_1}\right)(1+\bar{x}_2)^2 + \beta_T(T_s - \bar{x}_1) \\
\frac{\partial \bar{x}_2}{\partial \bar{t}} &= -\frac{\partial \bar{x}_2}{\partial \bar{z}} + \frac{1}{Pe_2}\frac{\partial^2 \bar{x}_2}{\partial \bar{z}^2} - B_C \exp\left(\frac{\gamma \bar{x}_1}{1+\bar{x}_1}\right)(1+\bar{x}_2)^2
\end{aligned} \tag{5.21}$$

subject to the following boundary conditions:

$$\begin{aligned}
\bar{z} = 0 \quad &: \quad \frac{\partial \bar{x}_1}{\partial \bar{z}} = Pe_1(\bar{x}_1 - T_i), \frac{\partial \bar{x}_2}{\partial \bar{z}} = Pe_2(\bar{x}_2 - u); \\
\bar{z} = 1 \quad &: \quad \frac{\partial \bar{x}_1}{\partial \bar{z}} = 0, \frac{\partial \bar{x}_2}{\partial \bar{z}} = 0;
\end{aligned} \tag{5.22}$$

Furthermore, in order to simplify the computation of the eigenvalues and eigenfunctions of the spatial differential operator which will be used in our calculations, we insert the non-homogeneous part of the boundary conditions of Eq. 5.22 into the differential equation and obtain the following nonlinear PDEs for the process (we suppress the bar notation for $\bar{t}$ and $\bar{z}$):[119]

$$\begin{aligned}
\frac{\partial \bar{x}_1}{\partial t} &= -\frac{\partial \bar{x}_1}{\partial z} + \frac{1}{Pe_1}\frac{\partial^2 \bar{x}_1}{\partial z^2} + \delta(z-0)T_i + B_T B_C \exp\left(\frac{\gamma \bar{x}_1}{1+\bar{x}_1}\right)(1+\bar{x}_2)^2 + \beta_T(T_s - \bar{x}_1) \\
\frac{\partial \bar{x}_2}{\partial t} &= -\frac{\partial \bar{x}_2}{\partial z} + \frac{1}{Pe_2}\frac{\partial^2 \bar{x}_2}{\partial z^2} + \delta(z-0)u - B_C \exp\left(\frac{\gamma \bar{x}_1}{1+\bar{x}_1}\right)(1+\bar{x}_2)^2
\end{aligned} \tag{5.23}$$

where δ is the standard Dirac function, subject to the following transformed boundary conditions:

$$\begin{aligned}
z = 0 \quad &: \quad \frac{\partial x_1}{\partial z} = Pe_1 x_1, \ \frac{\partial x_2}{\partial z} = Pe_2 x_2; \\
z = 1 \quad &: \quad \frac{\partial x_1}{\partial z} = 0, \ \frac{\partial x_2}{\partial z} = 0;
\end{aligned} \tag{5.24}$$

Finally, we present the solution to the eigenvalue problem of the spatial differential

operator of the process, i.e.,:

$$-\frac{d\phi_{ij}}{dz}+\frac{1}{Pe_i}\frac{d^2\phi_{ij}}{dz^2}=\lambda_{ij}\phi_{ij}, \tag{5.25}$$

subject to

$$\begin{aligned} z=0 \quad &: \quad \frac{d\phi_{ij}}{dz}=Pe_i\phi_{ij}; \\ z=1 \quad &: \quad \frac{d\phi_{ij}}{dz}=0; \end{aligned} \tag{5.26}$$

for $i=1,2$, $j=1,\ldots,\infty$. The index i is used to denote the ith partial differential equation and the index j is used to denote the j-th eigenmode. The solution of the eigenvalue problem of the spatial differential operator of the i-th partial differential equation can be obtained by utilizing standard techniques from linear operator theory and is of the form:

$$\begin{aligned} &\lambda_{ij}=-\frac{\bar{a}_{ij}^2}{Pe_i}-\frac{Pe_i}{4}, \\ &\phi_{ij}(z)=B_{ij}\exp\left(Pe_i\frac{z}{2}\right)\left(\cos(\bar{a}_{ij}z)+\frac{Pe_i}{2\bar{a}_{ij}}\sin(\bar{a}_{ij}z)\right), \\ &\bar{\phi}_{ij}(z)=\exp\left(-Pe_iz\right)\phi_{ij}(z), \end{aligned} \tag{5.27}$$

for $i=1,2$, $j=1,\ldots,\infty$ where λ_{ij}, ϕ_{ij} and $\bar{\phi}_{ij}$ denote the eigenvalues, eigenfunctions and adjoint eigenfunctions of the spatial differential operator of the i-th partial differential equation, respectively. The parameters B_{ij} and $\bar{a}_{ij}$ can be calculated from the following formulas:

$$\begin{aligned} &B_{ij}=\left[\int_0^1\left(\cos(\bar{a}_{ij}z)+\frac{Pe_i}{2\bar{a}_{ij}}\sin(\bar{a}_{ij}z)\right)^2dz\right]^{-1/2}, \\ &\tan\bar{a}_{ij}=\frac{Pe_i\bar{a}_{ij}}{\bar{a}_{ij}^2-(Pe_i/2)^2}, \end{aligned} \tag{5.28}$$

for $i=1,2$, $j=1,\ldots,\infty$.

The following typical values are given to the process parameters: $Pe_1=7$, $Pe_2=7$,

$B_T = 2.5$, $B_C = 0.1$, $\beta_T = 2$, $T_s = 0$, $T_f = 0$ and $\gamma = 10$. In all simulations reported below, the second-order finite-difference method was used to discretize, in space, the two parabolic PDEs describing the tubular reactor and obtain a 400th-order set of ODEs in time describing the tubular reactor behavior; this discretized model was used to describe the process dynamics in all simulations. We note that further increase on the order of the process model led to identical open-loop and closed-loop simulation results.

Remark 5.6 *The Péclet numbers (Pe_1 and Pe_2) essentially quantify the ratio of convective transport phenomena to diffusive transport phenomena. If these numbers are large, convective transport phenomena dominate over the diffusive transport phenomena. If it is small, diffusive transport phenomena dominate over the convective transport phenomena. For processes with $Pe_1 = Pe_2 = c$ where c is a constant on the order of 1, both transport mechanisms are significant and the diffusive and convective phenomena are comparable in importance for both the mass and heat transfer. In this work, we are considering processes where both the diffusive and convective phenomena play an important role like in most industrially-important transport-reaction processes. The choice of $Pe_1 = Pe_2 = 7$ reflects this point: mass and heat transport are fully coupled (i.e., no time scale separation where the assumption can be made that one of the two equations is at steady-state) and both the diffusive and convective phenomena have to be accounted for.*

However, this choice of Péclet numbers is not a limitation of our approach as we can still construct a model on the basis of separation of time scales in the modal space. As pointed out below, the first four eigenvalues (for each partial differential equation) of the spatial differential operator are $\lambda_{11} = \lambda_{21} = -2.36$, $\lambda_{12} = \lambda_{22} = -4.60$, $\lambda_{13} = \lambda_{23} = -9.14$, and $\lambda_{14} = \lambda_{24} = -16.29$. From this analysis, we observe a separation in magnitudes of the first two eigenvalues from the second two eigenvalues. Following our previous work (e.g., Ref[25]), the error associated with the reduced-order model constructed with the

first two eigenvalues will have error on the order of $\varepsilon = |\lambda_1|/|\lambda_3| = \mathscr{O}(0.1)$. *Please see the "Case 3: High-order Economic Model Predictive Control Formulation With Both State and Input Constraints" subsection which contains a closed-loop simulation with* $Pe_1 = 1$ *and* $Pe_2 = 7$.

5.4.2 Galerkin's Method

To simplify the presentation of the results, we will work with the amplitudes of the eigenmodes of the PDEs. To reduce the PDEs of Eq. 5.23 into an ODE model, we take advantage of the orthogonality property of the eigenfunctions. Specifically, using Galerkin's method, we first derive a high-order ODE system for each of the PDEs that describes the temporal evolution of the amplitudes corresponding to the first l_i eigenmodes. The state $\bar{x}_i(z,t)$ for $i = 1, 2$ can be written as the sum of the amplitudes and eigenfunctions of the first l_i eigenmodes:

$$\bar{x}_i(z,t) = \sum_{j=1}^{l_i} a_{ij}(t)\phi_{ij}(z) \tag{5.29}$$

where $a_{ij}(t)$ and $\phi_{ij}(z)$ are the amplitude and eigenfunction associated with the j-th eigenvalue of spatial differential operator of the i-th partial differential equation. Substituting the right-hand side of Eq. 5.29 into the i-th partial differential equation and taking inner product of the resulting system with the adjoint eigenfunction, we can construct the temporal evolution of the amplitudes of the i-th PDE:

$$\begin{aligned} \dot{a}_{s,i}(t) &= A_{s,i}a_{s,i}(t) + F_{s,i}(a_s(t), a_f(t)) + B_{s,i}u(t), \\ \dot{a}_{f,i}(t) &= A_{f,i}a_{f,i}(t) + F_{f,i}(a_s(t), a_f(t)) + B_{f,i}u(t), \end{aligned} \qquad i = 1, 2 \tag{5.30}$$

where $a_{s,i}(t) = [a_{s,i1}(t), a_{s,i2}(t), \cdots, a_{s,ij}(t), \cdots, a_{s,im_i}]'$ with elements $a_{s,ij}(t) \in \mathbb{R}$ associated with the amplitudes of the first m_i eigenmodes and $a_{f,i}$ is a vector of similar structure to $a_{s,i}(t)$ and is associated with the next $m_i + 1$ to l_i eigenmodes. The notation $a_s(t)$, $a_f(t)$,

and $a(t)$ is used to denote the following vectors:

$$a_s(t) = \begin{bmatrix} a_{s,1}(t) \\ a_{s,2}(t) \end{bmatrix}, \quad a_f(t) = \begin{bmatrix} a_{f,1}(t) \\ a_{f,2}(t) \end{bmatrix}, \quad a(t) = \begin{bmatrix} a_s(t) \\ a_f(t) \end{bmatrix} \tag{5.31}$$

The matrix $A_{s,i} = \text{diag}\{\lambda_{ij}\}$ is a $m_i \times m_i$ matrix (i.e, $j = 1, \ldots, m_i$), the matrix $A_{f,i} = \text{diag}\{\lambda_{ij}\}$ is a $(l_i - m_i) \times (l_i - m_i)$ matrix (i.e, $j = m_i + 1, \ldots, l_i$), and the matrices $B_{s,i}$ and $B_{f,i}$ and the nonlinear vector fields $F_{s,i}$ and $F_{f,i}$ can be constructed through the appropriate inner product, e.g.,

$$B_{s,i} = \begin{bmatrix} (\bar{\phi}_{i1}(z), \delta(z-0)) \\ (\bar{\phi}_{i2}(z), \delta(z-0)) \\ \vdots \\ (\bar{\phi}_{im_i}(z), \delta(z-0)) \end{bmatrix} \tag{5.32}$$

The initial conditions of the ODEs in Eq. 5.30 are

$$a_{s,i}(0) = \begin{bmatrix} (\bar{\phi}_{i1}(z), \bar{x}(z,0)) \\ (\bar{\phi}_{i2}(z), \bar{x}(z,0)) \\ \vdots \\ (\bar{\phi}_{im_i}(z), \bar{x}(z,0)) \end{bmatrix}, \quad a_{f,i} = \begin{bmatrix} (\bar{\phi}_{i(m_i+1)}(z), \bar{x}(z,0)) \\ (\bar{\phi}_{i(m_i+2)}(z), \bar{x}(z,0)) \\ \vdots \\ (\bar{\phi}_{il_i}(z), \bar{x}(z,0)) \end{bmatrix} \tag{5.33}$$

After truncating the fast subsystem of Eq. 5.30, we can construct a low-order finite-dimensional model for the first $j = 1, \ldots, m_i$ eigenmodes of each partial differential equation:

$$\dot{a}_{s,i}(t) \quad = \quad A_{s,i}a_{s,i}(t) + F_{s,i}(a_s(t), 0) + B_{s,i}u(t), \quad i = 1, 2 \tag{5.34}$$

with initial conditions constructed using a similar procedure as in Eq. 5.33. Using Eq. 5.27, the first four eigenvalues of the spatial operator of the i-th partial differential equation are $\lambda_{11} = \lambda_{21} = -2.36$, $\lambda_{12} = \lambda_{22} = -4.60$, $\lambda_{13} = \lambda_{23} = -9.14$, $\lambda_{14} = \lambda_{24} = -16.29$. These

values indicate that the eigenspectrum exhibits a two-time-scale property. Therefore, we consider the first 2 eigenvalues, namely $m_1 = m_2 = 2$, as the dominant/slow eigenmodes and the remaining infinite eigenmodes as the fast ones. We will refer to ODE system of Eq. 5.34 with $m_1 = m_2 = 2$ as the low-order model.

We can also account for the fast subsystem by retaining the first l_i eigenmodes of each partial differential equation. As described previously in the "High-order Economic Model Predictive Control Formulation" subsection, the nonlinear part of the fast subsystem can be neglected to improve the computational efficiency. The resulting ODE system is given by

$$\begin{aligned} \dot{a}_{s,i}(t) &= A_{s,i}a_{s,i}(t) + F_{s,i}(a_s(t), a_f(t)) + B_{s,i}u(t), \quad i = 1, 2 \\ \dot{a}_{f,i}(t) &= A_{f,i}a_{f,i}(t) + B_{f,i}u(t), \quad i = 1, 2 \end{aligned} \tag{5.35}$$

To determine the amount of eigenmodes to retain, a series of open-loop and closed-loop simulations were preformed. Based on these simulation results, the same open-loop and closed-loop results are obtained with a 400th-order discretization, obtained by Galerkin's method ($m_1 = m_2 = 2$ and $l_1 = l_2 = 200$), of the two parabolic PDEs as with the 400-th order set of ODEs obtained through the second-order finite-difference method. We will refer to the ODE system of Eq. 5.35 with $m_1 = m_2 = 2$ and $l_1 = l_2 = 200$ simply as the high-order model.

Remark 5.7 *In this example, the same number of eigenmodes for each of the two PDEs are retained. However, this is not necessary, in general, and hence, the need for the index i.*

5.4.3 Implementation of EMPC to a Tubular Reactor

We now proceed with the description and implementation of the EMPC formulations. To solve the EMPC optimization problem at each sampling period, the open-source interior

point solver Ipopt[139] was used. To numerically integrate the finite-dimensional ODE model of the transport-reaction process, explicit Euler's method was used with an interation step of 10^{-5}. For the EMPC formulations, we consider a quadratic Lyapunov function of form

$$V(a) = a'(t)Pa(t) \tag{5.36}$$

where P is an m_i by m_i and l_i by l_i identity matrix for the low-order and high-order model, respectively and $\bar{\rho} = 3$ which has been chosen through closed-loop simulations of the PDE system of Eq. 5.23 with the low-order EMPC formulated below as an estimate of the closed-loop stability region. The control objective that we consider is to maximize the total reaction rate along the length of the reactor and over one process operation period for $t_f = 1$. The economic measure used to accomplish this objective is

$$L(x,u) = \int_0^1 r(z,t)dz \tag{5.37}$$

where $r(z,t) = k_0 \exp(\frac{-E}{RT})C_A^2$ is the reaction rate in the tubular reactor.

The control input is subject to constraints as follows: $-1 \leq u \leq 1$. We also consider that there is limitation on the amount of reactant material which can be used over the period t_f. Specifically, the control input trajectory of u should satisfy the following constraint:

$$\frac{1}{t_f}\int_0^{t_f} u(\tau)d\tau = 0.5 \tag{5.38}$$

This constraint means that the total amount of reactant during one period is fixed. We will refer to Eq. 5.38 as the reactant material constraint or the integral input constraint. Since the EMPC is evaluated at discrete-time instants during the closed-loop simulation, the reactant

material constraint is enforced as follows:

$$\sum_{i=0}^{M-1} u(t_i) = \frac{t_f}{2\Delta} \tag{5.39}$$

where $M = t_f/\Delta$. Moreover, to ensure that the reactant material constraint is satisfied through the period t_f, the EMPC utilizes the previously computed input $u(t_i), i = 0, 1, \ldots, (k-1)$ to constrain the control input trajectory $u(t)$ $t \in [t_k, t_{k+N})$ at the current sampling time t_k:

$$\frac{M}{2} + \left(M - \frac{t_k}{\Delta} - N\right) u_{min} \leq \sum_{i=0}^{k-1} u^*(t_i) + \sum_{j=k}^{N+k} u(t_j) \leq \frac{M}{2} + \left(M - \frac{t_k}{\Delta} - N\right) u_{max} \tag{5.40}$$

where $M/2$ is the total amount of material that can be supplied to the reactor over one operating period, M is the total number of sampling periods over each operating period, and t_k/Δ is the number sampling periods since the beginning of the operating period. To simplify the notation, we use the notation $u \in g(t_k)$ to denote this constraint.

In terms of the state constraint, we consider that the temperature T along the length of the reactor is subject to the following constraint:

$$x_{1,min} \leq x_1(z,t) \leq x_{1,max} \tag{5.41}$$

where $x_{1,min} = -1$ and $x_{1,max} = 3$ are the lower and upper limits, respectively. Since the models used in the formulations of the EMPC optimization problems are the low-order and high-order models, we cast the state constraint in terms of the amplitudes of the eigenmodes to prevent unnecessary computation required to convert from the modal space back to state space when solving the optimization problem at each sampling period:

$$-1 \leq \sum_{j=1}^{200} a_{1j}(t)\phi_{1j}(z) \leq 3 \tag{5.42}$$

Remark 5.8 *The operating period t_f is chosen to be on the order of the time-scale of the process dynamics and is used for imposing the integral input constraint (i.e., the available amount of reactant material over one operating period is fixed). Since the reaction is second-order, the optimal strategy to maximize the reaction rate (without the integral constraint) would be to feed the maximum allowable amount of reactant material to the reactor for all time. From a practical (economic) perspective, it is more important to address the case where the available reactant material is fixed. For this case, the EMPC determines the optimal distribution method of the reactant material to the reactor to maximize the reaction rate. As the results of the first simulation case (input constraint only) demonstrate, for a fixed amount of reactant material over some finite-time operating window, it is better, from an economic stand-point, to distribute the material in a periodic fashion as this distribution method yields greater average production rates over each operation period compared to uniform in time distribution of the reactant material to the reactor.*

We also note that the input and integral constraints are imposed for two fundamentally different reasons. The input constraint is imposed as a result of the physical limitations of the control actuator or available control actuation (e.g., the limits on available actuation with a flow valve are fully closed or fully open). As pointed out above, the integral material constraint is an economic or practical constraint that the EMPC must satisfy. For example, consider the case where the integral constraint and input constraint are imposed on the EMPC (no state constraint). If the integral constraint was imposed, but not the input constraints, the EMPC would choose to feed in all the material over the first sampling period to maximize the reaction rate which is not practical and most likely not physically possible due to control actuator limitations. If we imposed the input constraint, but not the integral constraint, the EMPC would feed in the maximum allowable material for all time which is not as practical as considering the best method to distribute a fixed amount of reactant material to the reactor over time. Therefore, the input and integral constraints taken together

are not overlapping.

5.4.4 Case 1: Low-order Economic Model Predictive Control Formulation with Input Constraint

In the first set of simulations, we propose a low-order EMPC formulation using the low-order model of Eq. 5.34 and considering only input constraints which takes the following form for the tubular reactor example:

$$\max_{u\in S(\Delta)} \quad \frac{1}{N\Delta}\int_{t_k}^{t_{k+N}}\left(\int_0^1 r(z,\tau)dz\right)d\tau \tag{5.43a}$$

$$\text{s.t.} \quad \dot{a}_{s,i}(t) = A_{s,i}a_{s,i}(t) + F_{s,i}(a_s(t),0) + B_{s,i}u(t), \quad i=1,2 \tag{5.43b}$$

$$a_{s,ij}(t_k) = (\bar{\phi}_{s,ij}(z), \bar{x}_i(z,t_k)), \quad i=1,2,\ j=1,2 \tag{5.43c}$$

$$-1 \leq u(t) \leq 1,\ \forall t \in [t_k, t_{k+N}) \tag{5.43d}$$

$$u \in g(t_k) \tag{5.43e}$$

$$a_s'(t)Pa_s(t) \leq \bar{\rho} \tag{5.43f}$$

where $g(t_k)$ is the control input constraint to make the computed input profile over the entire operating period, t_f, satisfy the integral reactant material constraint. The economic cost function of Eq. 5.43a that the EMPC works to maximize is the reaction rate in the tubular reactor. The EMPC of Eq. 5.43 is implemented with a prediction horizon $N=3$ and sampling time $\Delta = 0.01$.

For an initial condition $x(z,0)=0$, the manipulated input and closed-loop state profiles under the EMPC controller of Eq. 5.43 are shown in Fig. 5.2 and Figs. 5.3-5.4, respectively. It has been pointed out (e.g., Refs[17,117,125]) that by periodic operation through switching between the upper and lower bound on the reactant material feed concentration, the average production rate can be improved owing to the second-order dependence of the reaction rate

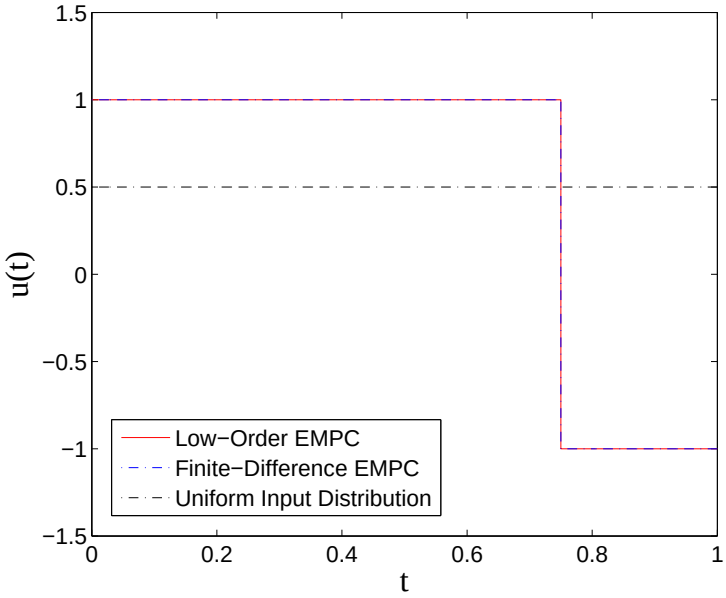

Figure 5.2: Manipulated input profiles under the EMPC formulation of Eq. 5.43 (solid red line), under uniform in time distribution of the reactant material (dotted black line), and under the finite-difference EMPC (dotted blue line) over one operation period. The input profiles of the two EMPCs (solid red line and dotted blue line) are overlapping.

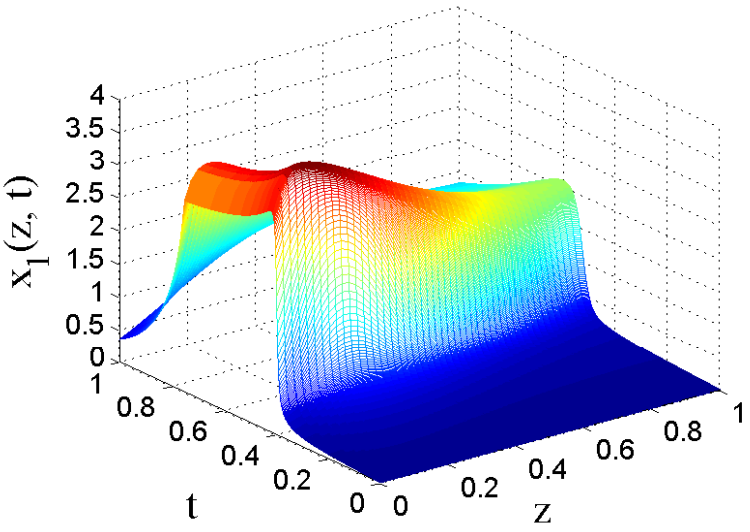

Figure 5.3: Closed-loop profile of x_1 under the low-order EMPC formulation of Eq. 5.43 over one operation period.

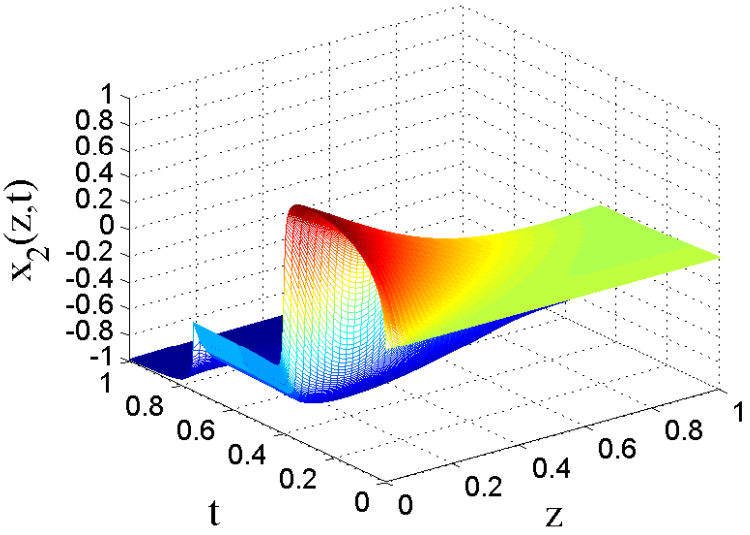

Figure 5.4: Closed-loop profile of x_2 under the low-order EMPC formulation of Eq. 5.43 over one operation period.

on reactant concentration. Thus, to achieve the maximum reaction rate over one operation period, the EMPC feeds the maximum allowable amount of reactant material to the reactor at the beginning of the process operation period. After a while, the EMPC needs to satisfy the reactant material constraint so it decreases the amount of reactant material fed to the reactor to the lowest allowable amount as displayed in Fig. 5.2. We also completed a simulation where the reactant material is fed to the reactor uniformly in time distribution of the reactant material and the input profile is given in Fig. 5.2 (dotted black line). The corresponding closed-loop evolution of the state profiles are given in Figs. 5.5-5.6.

In order to confirm that the economic measure from the manipulated input profile under the low-order EMPC formulation is better than that from uniform in time distribution of the reactant material, we compare the reaction rate values along the length of the reactor from these two input distribution profiles in Fig. 5.7. The average reaction rate along the length of the reactor (i.e., $J = \frac{1}{L}\int_0^L r(z,t)dz$) under the low-order EMPC formulation of Eq. 5.43 increases much faster than that from uniform in time distribution of the reactant

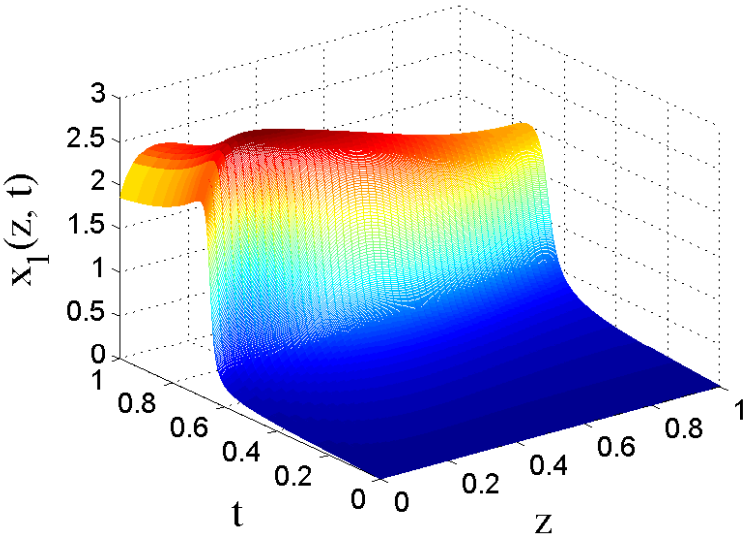

Figure 5.5: Closed-loop profile of x_1 under uniform in time distribution of the reactant material over one operation period.

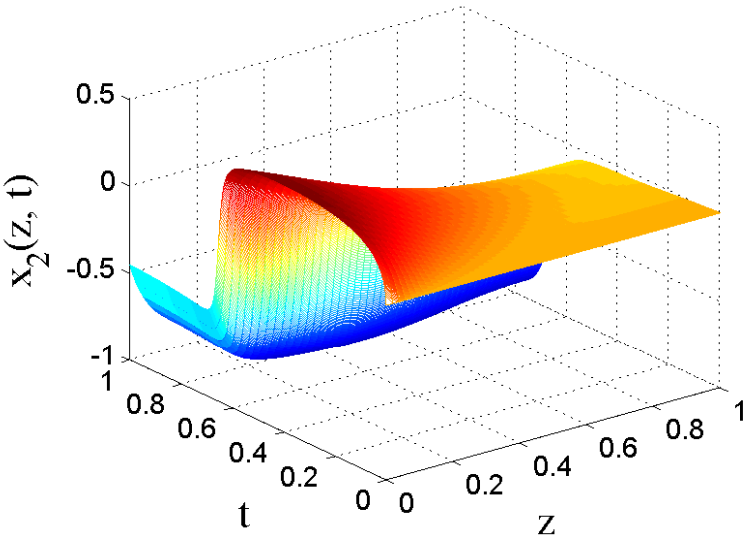

Figure 5.6: Closed-loop profile of x_2 under uniform in time distribution of the reactant material over one operation period.

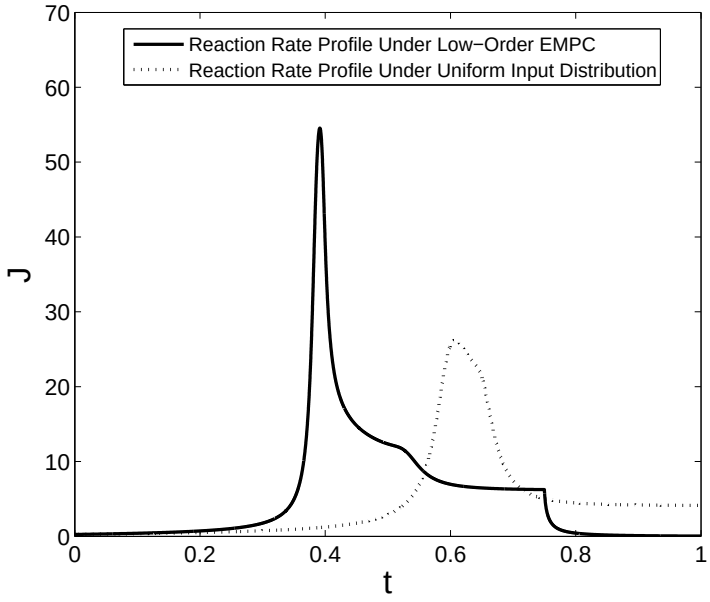

Figure 5.7: Average reaction rate J along the length of the reactor (i.e., $J = \frac{1}{L}\int_0^L r(z,t)dz$) under the low-order EMPC formulation of Eq. 5.43 over one operation period (solid line) and under uniform in time distribution of the reactant material (dashed line).

material because of the second-order reaction and the EMPC input distribution. Over this one operation period, the total reaction rate from the system under the EMPC formulation is about 15.45% higher than that from the closed-loop system under flat input distribution.

To verify the accuracy of the low-order EMPC, we formulate an EMPC with the 400-order finite-difference method, which we refer to as the finite-difference EMPC, to compare the closed-loop evolution obtained under the finite-difference EMPC with the low-order EMPC. The manipulated input profile under the finite-difference method is also shown in Fig. 5.2. From this simulation, the same input profile is computed by the high-order finite-difference EMPC as the low-order EMPC. However, the low-order model uses four ODEs to predict the future evolution of the system of PDEs; while, the high-order finite-difference EMPC uses 400 ODEs. From Fig. 5.8, we observe a significant computational improvement with using the low-order EMPC. Furthermore, if we formulate an EMPC

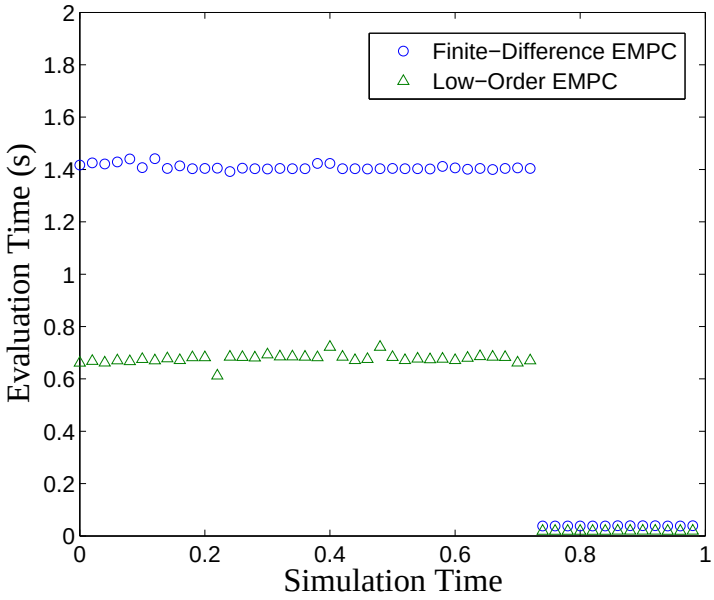

Figure 5.8: Computational time required to solve the low-order EMPC optimization problem and the finite-difference EMPC optimization problem over one operation period.

with a fourth-order model obtained through the finite-difference method and apply it to the system of PDEs, the resulting EMPC does not compute the optimal trajectory as it cannot accurately predict the future evolution of the system.

Since chemical reactors are typically operated continuously over long periods of time, we conduct another simulation of multiple (twenty) consecutive periods of operation. The reactant material constraint is enforced over each of the 20 consecutive operating periods where the system at the beginning of each period starts from a different initial condition. Fig. 5.9 displays the manipulated input profiles under the EMPC controller of Eq. 5.43 and Figs. 5.10-5.11 depict the closed-loop evolution of the two states under the low-order EMPC formulation of Eq. 5.43, respectively. After two operation periods in the twenty-period operation simulation under the low-order EMPC of Eq. 5.43, the closed-loop economic measure becomes constant over each operation period as shown in Fig. 5.12. The total reaction rate over each operation period under the low-order EMPC after two opera-

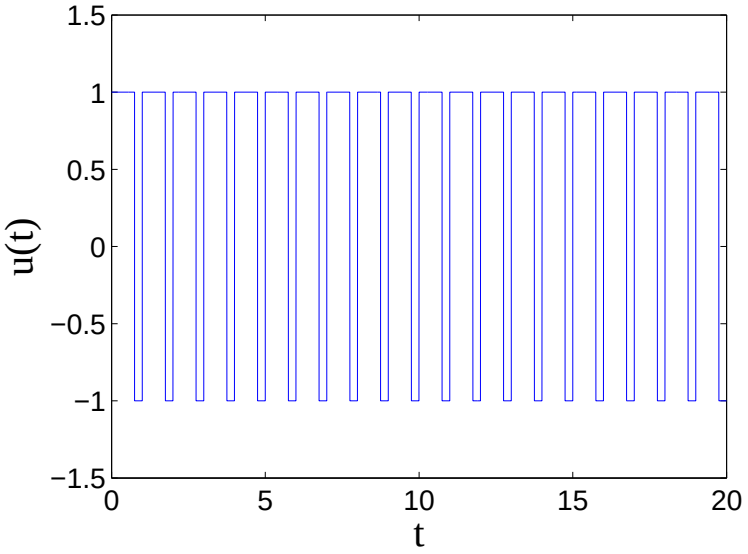

Figure 5.9: Twenty-period operation manipulated input profile under the low-order EMPC formulation of Eq. 5.43.

tion periods is still 3.89% greater than that of the case under uniform in time distribution of the reactant material.

Remark 5.9 *Regarding the oscillations (e.g., Figs. 5.9-5.12 where the evolution of the tubular reactor is simulated over 20 operating intervals and the process evolution appears to be oscillatory), we point out that this is not open-loop periodic behavior or a numerical issue. This behavior is enforced by the EMPC to maximize the cost over many periods. We refer the interested reader to any of the literature on periodically operated reactors (e.g., Refs[17, 125]) for more commentary on this issue.*

5.4.5 Case 2: High-order Economic Model Predictive Control Formulation With State and Actuator Constraints

Secondly, we consider the addition of a state constraint and use the high-order EMPC formulation of Eq. 5.17 with the high-order model of Eq. 5.35; the average reactant material

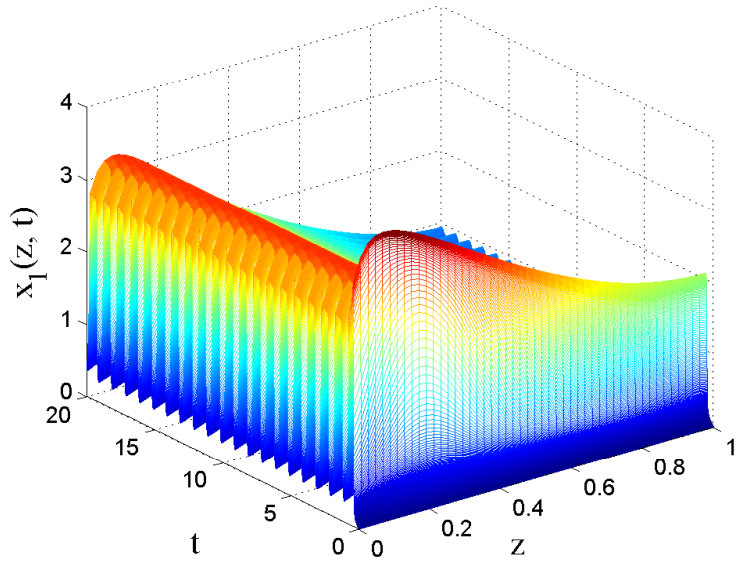

Figure 5.10: Twenty-period operation closed-loop profile of x_1 under the low-order EMPC formulation of Eq. 5.43.

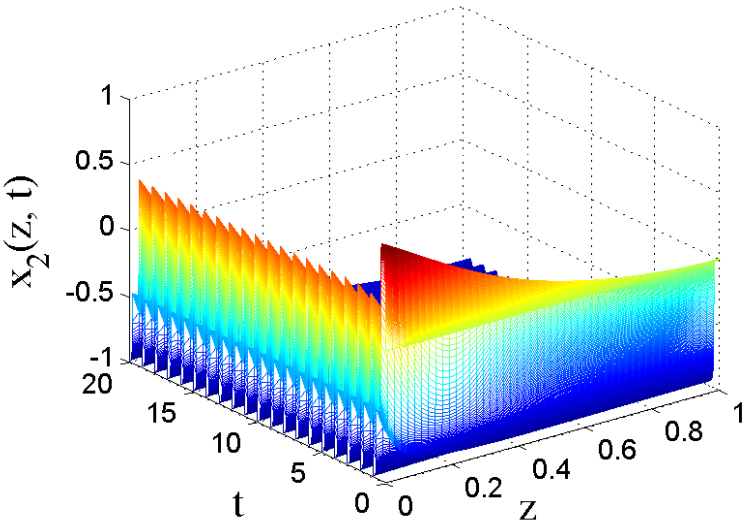

Figure 5.11: Twenty-period operation closed-loop profile of x_2 under the low-order EMPC formulation of Eq. 5.43.

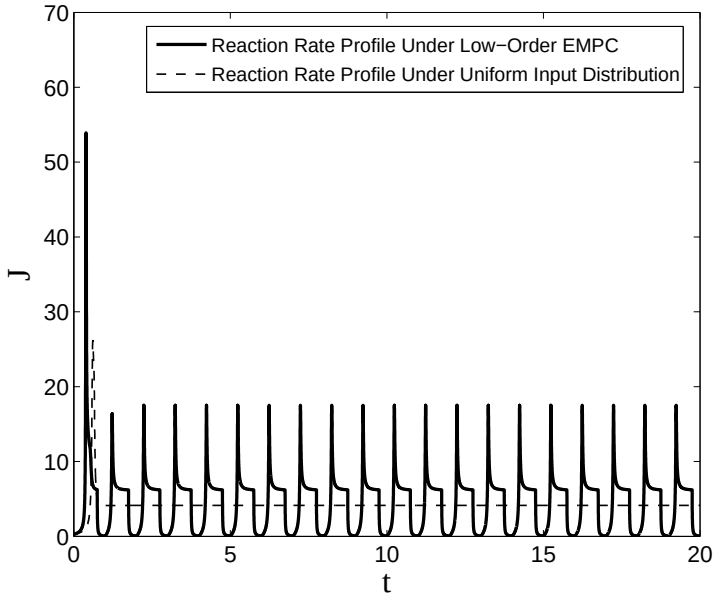

Figure 5.12: Average reaction rate along the length of the reactor J (i.e., $J = \frac{1}{L}\int_0^L r(z,t)dz$) under the low-order EMPC formulation of Eq. 5.43 over a twenty-period operation (solid line) and under uniform in time distribution of the reactant material (dashed line).

constraint is removed. The high-order EMPC formulation for this chemical process example has the following form:

$$\max_{u\in S(\Delta)} \quad \frac{1}{N\Delta}\int_{t_k}^{t_{k+N}} \left(\int_0^1 r(z,\tau)dz\right) d\tau \tag{5.44a}$$

$$\text{s.t.} \quad \dot{a}_{s,i}(t) = A_{s,i}a_{s,i}(t) + F_{s,i}(a_s(t), a_f(t)) + B_{s,i}u(t), \quad i = 1,2 \tag{5.44b}$$

$$\dot{a}_{f,i}(t) = A_{f,i}a_{f,i}(t) + B_{f,i}u(t), \quad i = 1,2 \tag{5.44c}$$

$$a_{s,ij}(t_k) = (\bar{\phi}_{s,ij}(z), \bar{x}_i(z,t_k)), \quad i = 1,2,\ j = 1,2 \tag{5.44d}$$

$$a_{f,ij}(t_k) = (\bar{\phi}_{f,ij}(z), \bar{x}_i(z,t_k)), \quad i = 1,2,\ j = 3,\ldots,200 \tag{5.44e}$$

$$-1 \leq \sum_{j=1}^{200} a_{1j}(t)\phi_{1j}(z) \leq 3 \tag{5.44f}$$

$$-1 \leq u(t) \leq 1,\ \forall t \in [t_k, t_{k+N}) \tag{5.44g}$$

$$a'(t)Pa(t) \leq \bar{\rho} \tag{5.44h}$$

The EMPC of Eq. 5.44 is implemented with a prediction horizon $N = 5$ and sampling time $\Delta = 0.02$. The prediction horizon N and sampling time Δ are greater than Case 1 to increase the overall prediction horizon length which helps to guarantee that the temperature does not violate its upper or lower limit. For this case, the initial condition is the steady state of the system under uniform input distribution, $u = 0.5$, as shown in the Figs. 5.5-5.6.

The manipulated input and closed-loop state profiles under the high-order EMPC of Eq. 5.44 are shown in Fig. 5.13 and Figs. 5.14-5.15, respectively. Fig. 5.14 and Fig. 5.15 show the closed-loop evolution of the states under the EMPC formulation of Eq. 5.44. From Fig. 5.13, the EMPC initially feeds in more reactant material to the reactor to increase the reaction rate. Since the reaction is exothermic, the temperature in the reactor also increases. When the temperature approaches the maximum allowable temperature, the input reactant concentration decreases to avoid the temperature in the reactor from exceeding $x_{1,max} = 3$. After this phase, the high-order EMPC maintains operation at a steady-state associated with the maximum temperature in the reactor being equal to the maximum allowable temperature. For this simulation, the corresponding maximum temperature in the reactor trajectory is shown in Fig. 5.16.

We compare the closed-loop evolution of the tubular reactor under the high-order EMPC and under the high-order finite-difference EMPC formulated with the state constraint (no integral input constraint). The manipulated input profile computed by the finite-difference EMPC is shown in Fig. 5.13 (dotted blue line) along with the profile of the high-order EMPC. The closed-loop state trajectories under the finite-difference EMPC is shown in Figs.5.17-5.18. The overall difference between the two input trajectories is small as shown in Fig. 5.13 and as a result, the closed-loop states under the high-order EMPC and under the finite-difference EMPC evolve in a similar fashion. Since both EMPCs use a 400-order model albeit obtained through different methods, the computational time required to solve the EMPC optimization problems are comparable.

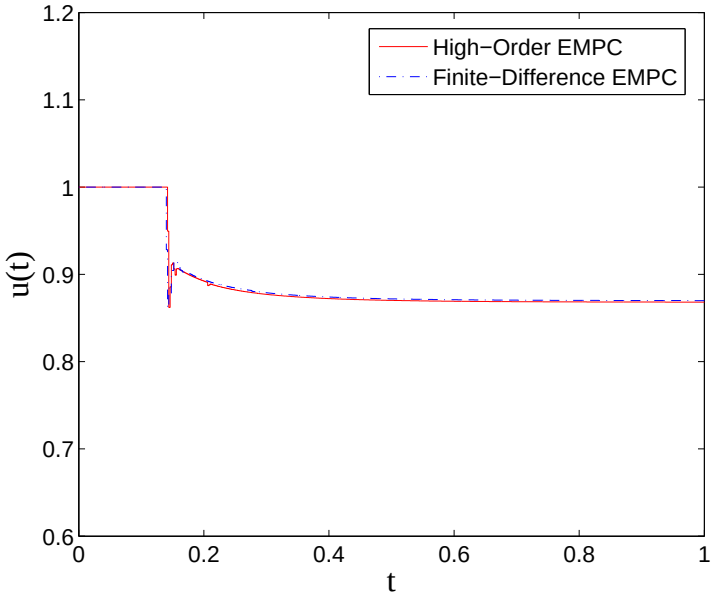

Figure 5.13: Manipulated input profile under the high-order EMPC formulation of Eq. 5.44 (solid red line) and under the finite-difference EMPC (dotted blue line) over one operation period.

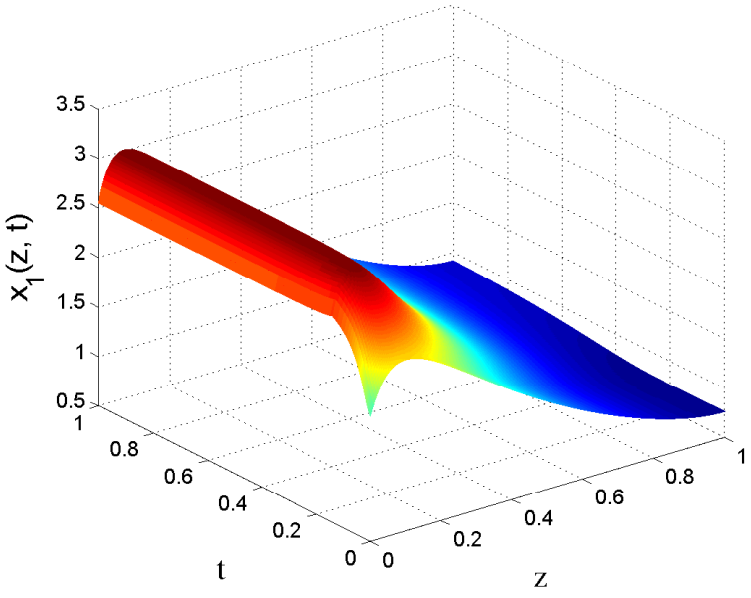

Figure 5.14: Closed-loop profile of x_1 under the high-order EMPC formulation of Eq. 5.44 over one operation period.

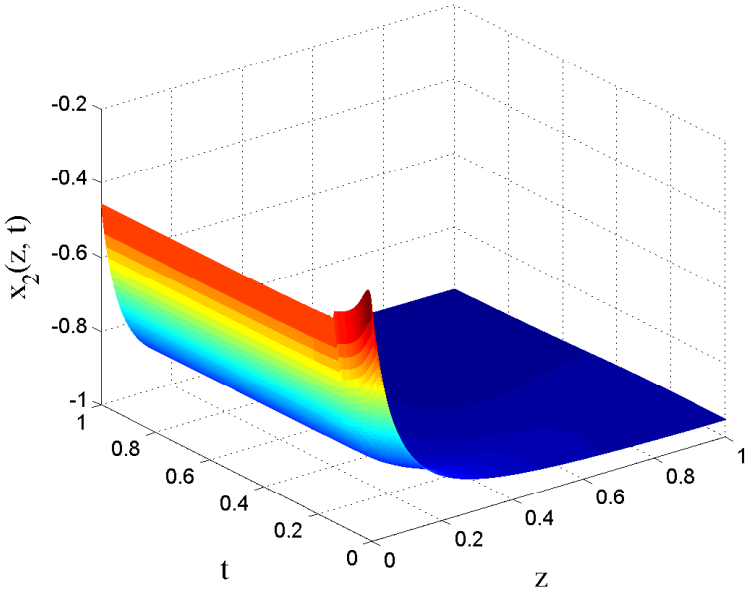

Figure 5.15: Closed-loop profile of x_2 under the high-order EMPC formulation of Eq. 5.44 over one operation period.

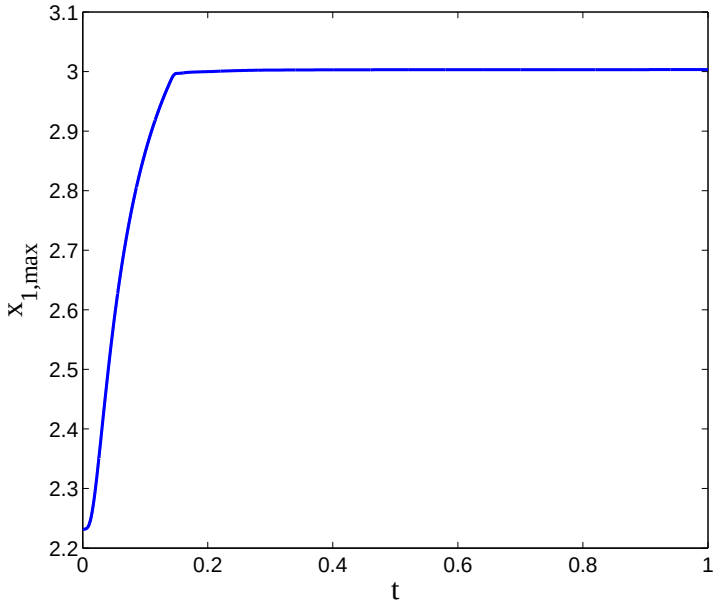

Figure 5.16: Closed-loop profile of the maximum value of x_1 along the length of the reactor under the high-order EMPC formulation of Eq. 5.44 over one operation period.

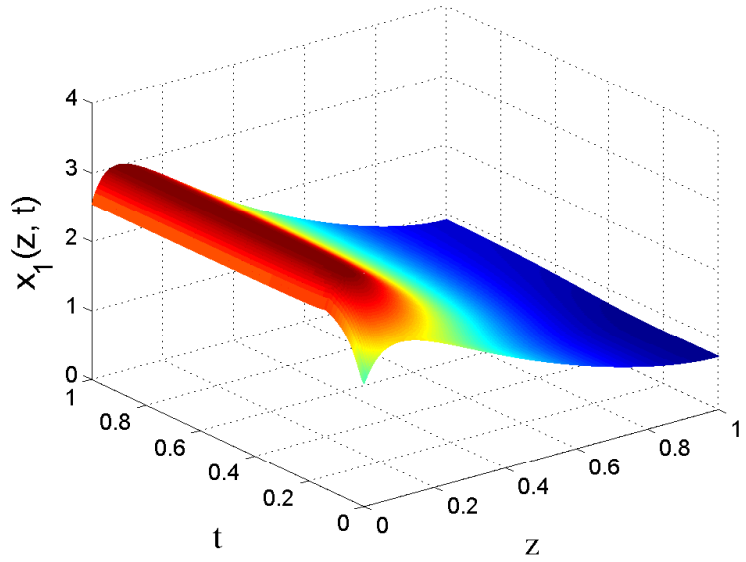

Figure 5.17: Closed-loop profile of x_1 under the finite-difference EMPC formulation with the state constraint over one operation period.

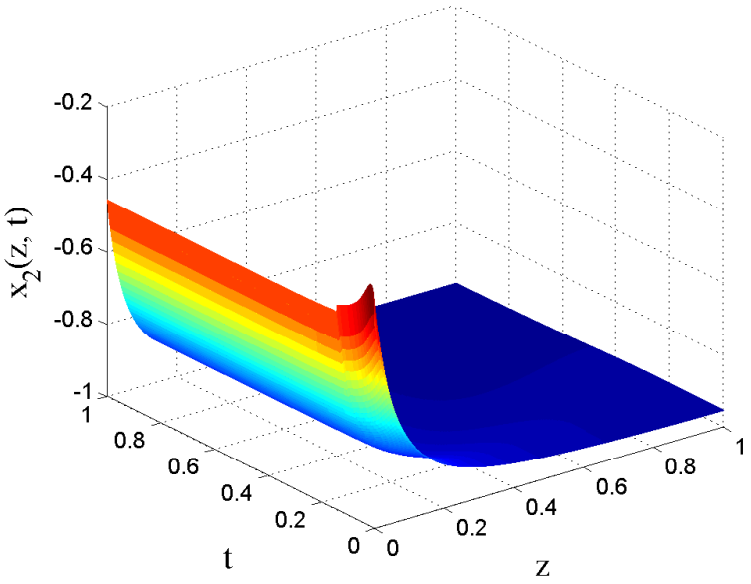

Figure 5.18: Closed-loop profile of x_2 under the finite-difference EMPC formulation with the state constraint over one operation period.

5.4.6 Case 3: High-order Economic Model Predictive Control Formulation With Both State and Input Constraints

Finally, we add the reactant material constraint into the high-order EMPC formulation and thus, the high-order EMPC formulation considering both the state and input constraints for this chemical process example has the following form:

$$\max_{u\in S(\Delta)} \quad \frac{1}{N\Delta}\int_{t_k}^{t_{k+N}}\left(\int_0^1 r(z,\tau)dz\right)d\tau \tag{5.45a}$$

$$\text{s.t.} \quad \dot{a}_{s,i}(t) = A_{s,i}a_{s,i}(t) + F_{s,i}(a_s(t),a_f) + B_{s,i}u(t), \quad i=1,2 \tag{5.45b}$$

$$\dot{a}_{f,i}(t) = A_{f,i}a_{f,i}(t) + B_{f,i}u(t), \quad i=1,2 \tag{5.45c}$$

$$a_{s,ij}(t_k) = (\bar{\phi}_{s,ij}(z), \bar{x}(z,t_k)), \quad i=1,2,\ j=1,2 \tag{5.45d}$$

$$a_{f,ij}(t_k) = (\bar{\phi}_{f,ij}(z), \bar{x}_i(z,t_k)), \quad i=1,2,\ j=3,\ldots,200 \tag{5.45e}$$

$$-1 \leq \sum_{j=1}^{200} a_{1j}(t)\phi_{1j}(z) \leq 3 \tag{5.45f}$$

$$-1 \leq u(t) \leq 1,\ \forall t \in [t_k, t_{k+N}) \tag{5.45g}$$

$$u \in g(t_k) \tag{5.45h}$$

$$a'(t)Pa(t) \leq \bar{\rho} \tag{5.45i}$$

We consider the prediction horizon $N=5$ and sampling time $\Delta = 0.02$. For this case, the initial condition is the steady-state of the system under uniform input distribution, $u=0.5$, as shown in the Figs. 5.5-5.6.

Fig. 5.19 and Fig. 5.20 show the closed-loop evolution of the states under the EMPC formulation of Eq. 5.45. The corresponding manipulated input profiles are given in Fig. 5.21 (solid line). Here, again, the EMPC initially feeds in the maximum allowable reactant material until the maximum allowable temperature in the reactor is reached and the EMPC feeds less reactant material to the reactor to maintain operation at the maximum allowable

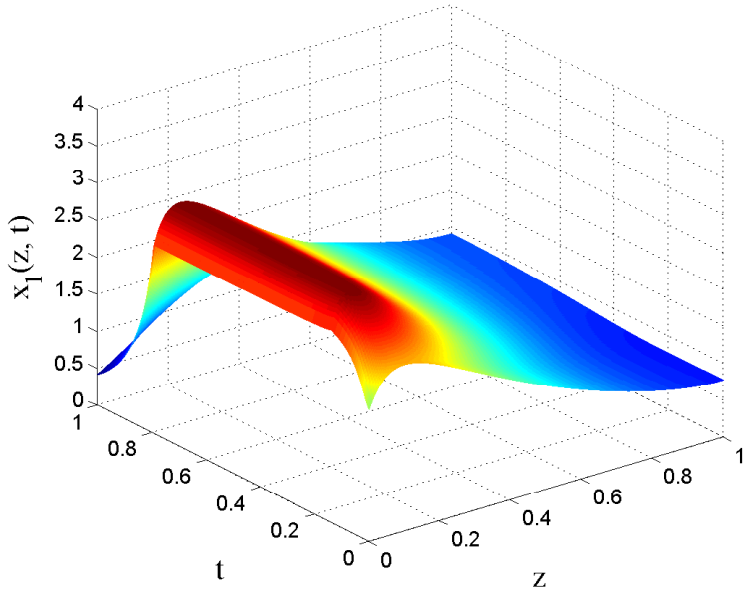

Figure 5.19: Closed-loop profile of x_1 under the high-order EMPC formulation of Eq. 5.45 over one operation period.

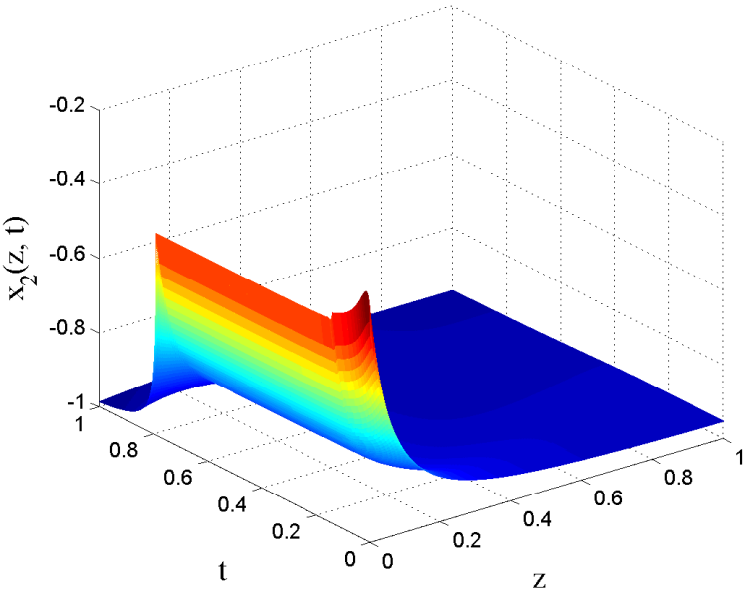

Figure 5.20: Closed-loop profile of x_2 under the high-order EMPC formulation of Eq. 5.45 over one operation period.

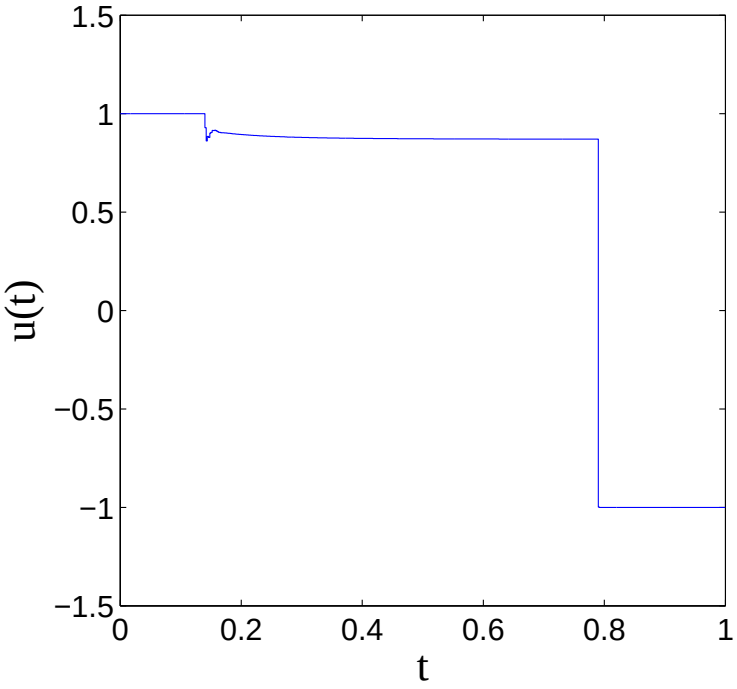

Figure 5.21: Manipulated input profile under the high-order EMPC formulation of Eq. 5.45 over one operation period.

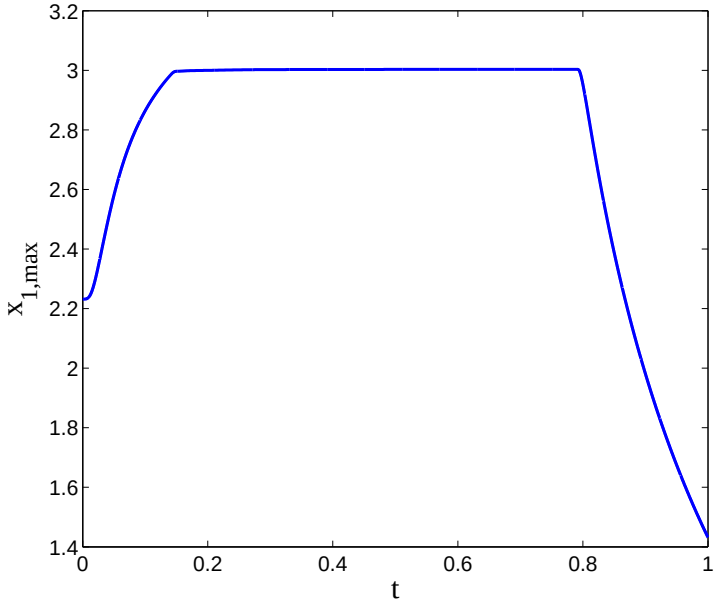

Figure 5.22: Closed-loop profile of the maximum value of x_1 along the length of the reactor under the high-order EMPC formulation of Eq. 5.45 over one operation period.

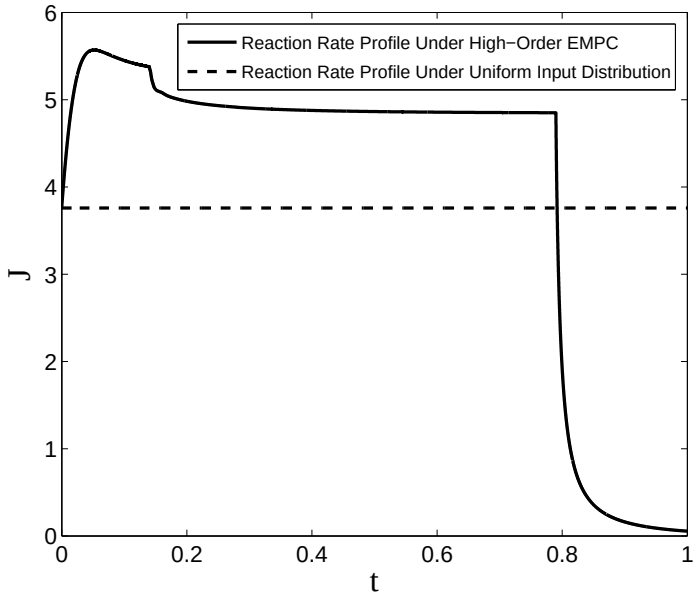

Figure 5.23: Average reaction rate along the length of the reactor J (i.e., $J = \frac{1}{L}\int_0^L r(z,t)dz$) under the high-order EMPC formulation of Eq. 5.45 over one operation period (solid line) and under uniform in time distribution of the reactant material (dashed line).

temperature. In the beginning, the optimal input trajectory follows a similar path to Case 2 since the input constraint has no effect on the choice of the optimal input value. After some time, the reactant material constraint needs to be satisfied so the input reactant concentration decreases at $t = 0.8$ to satisfy the constraint. The corresponding highest temperature in the reactor also decreases when the input is limited by the reactant material constraint as shown in Fig. 5.22.

For this case study, in order to confirm that the economic measure from the control input profile under the high-order EMPC formulation is better than that from the system under uniform in time distribution of the reactant material, we compare the reaction rate along the length of the reactor from these two input distribution profiles, shown in Fig. 5.23. Since the initial condition for this case study is the steady-state of the system under uniform input distribution, the overall reaction rate is a constant throughout the operation period when

the reactant material is distributed uniformly in time to the reactor. On the other hand, the average reaction rate along the length of the reactor, J, under the EMPC formulation of Eq. 5.45 increases dramatically because of the second-order reaction and after some time, it reaches a steady state when the input is held constant. Lastly, it drops to zero since the reactant material constraint needs to be satisfied over one operation period. Over this one operation period, the total reaction rate from the system under the EMPC formulation is still 6.91% higher than that from the system under uniform in time distribution of the reactant material.

To demonstrate that the EMPC performance is not associated with the specific process parameters, we conduct another simulation were $Pe_1 = 1$. This represents the case where the time-scales of heat diffusive and convective phenomena are roughly equivalent and the heat convective phenomena are slower than the mass convective phenomena compared to the case where $Pe_1 = 7$. As a result of the slower heat convection, the temperature does not increase as much over the course of the one operating period simulation compared to the case with $Pe_1 = 7$. To demonstrate the ability of the high-order EMPC to satisfy state constraint, we set the maximum allowable temperature to be $x_{1,max} = 2$. The manipulated input and closed-loop state profiles are shown in Fig. 5.24-5.26, respectively. Over the one operation period (with $Pe_1 = 1$), the total reaction rate from the system under the high-order EMPC is 7.09%. For the case of $x_{1,max} = 3$ and $Pe_1 = 1$, we have also verified that the EMPC will compute the same input profile as Case 1 because the upper bound on the temperature is never reached over the course of one operating period.

Remark 5.10 *While the argument can be made that the optimal operating policy of the first simulation (the EMPC formulated with an input constraint only) can be determined through physical intuition owing to the second order reaction rate, our motivation for performing this simulation is to demonstrate that the EMPC, formulated with a low-order model (in*

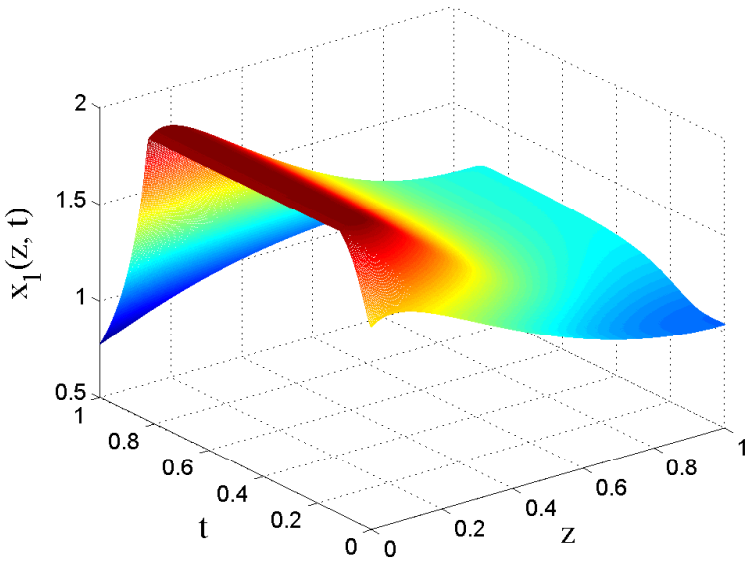

Figure 5.24: Closed-loop profile of x_1 under the high-order EMPC formulation of Eq. 5.45. For this case, the heat transfer Péclet number is $Pe_1 = 1$.

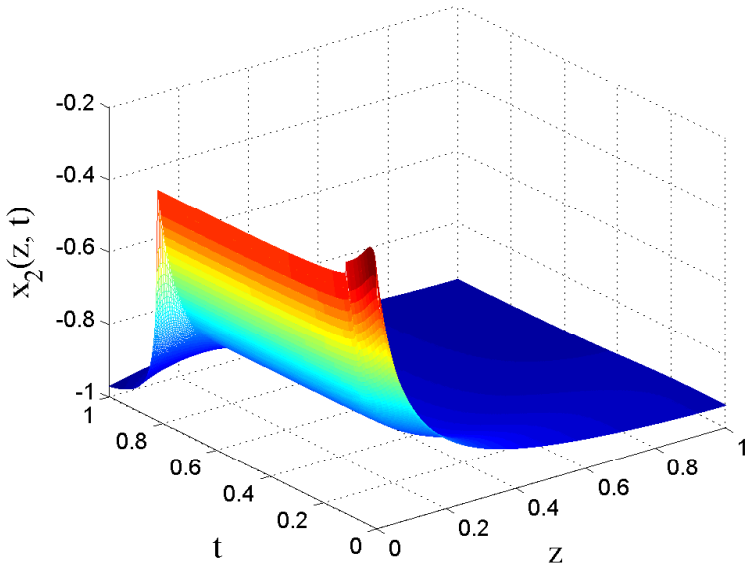

Figure 5.25: Closed-loop profile of x_2 under the high-order EMPC formulation of Eq. 5.45. For this case, the heat transfer Péclet number is $Pe_1 = 1$.

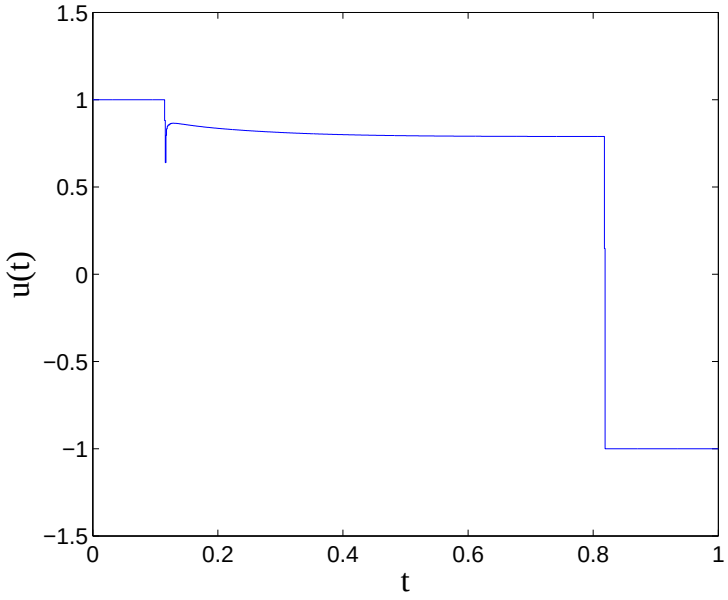

Figure 5.26: Manipulated input profile under the high-order EMPC formulation of Eq. 5.45. For this case, the heat transfer Péclet number is $Pe_1 = 1$.

this case, the model is constructed with the first four (2×2) modes only), can return the optimal operating strategy. In the subsequent simulation studies, we demonstrate the ability of EMPC to determine more complex optimal operating strategy in real-time while also accounting for other process constraints. Specifically, the EMPC is able to return the optimal operating strategy by considering a state constraint that limits the maximum allowable operating temperature in the reactor.

5.5 Conclusion

In this work, we developed low-order and high-order finite-dimensional economic model predictive (EMPC) systems, through the application of Galerkin's method and involvement of singular perturbation arguments, for transport-reaction processes described by nonlinear systems of parabolic PDEs. The formulated EMPC systems were applied to a tubular

reactor example described by two nonlinear parabolic PDEs, where the average reaction rate along the length of the reactor was used as the cost function. Closed-loop simulations demonstrated that in the absence of state constraint, the low-order EMPC system is sufficient to meet the constraint on the availability of the reactant material over one operation period, and yields improved closed-loop economic performance compared to when the reactant material is fed uniformly in time to the reactor by requesting a suitable time-varying reactor operation. On the other hand, when a state constraint on the maximum value of the temperature along the length of the reactor is imposed, the use of a high-order (yet computationally efficient) EMPC system allows to account for the process dynamics with sufficient accuracy and meet both the input and state constraints simultaneously while improving the economic cost over uniform in time feeding of the reactant material.

Chapter 6

Economic Model Predictive Control of Parabolic PDE Systems: Addressing State Estimation and Computational Efficiency

6.1 Introduction

This chapter presents several EMPC systems which are formulated and applied to a non-isothermal tubular reactor where a second-order chemical reaction takes place. First, an output feedback EMPC formulation is presented. Second, a reduced-order model (ROM) of the PDEs is constructed on the basis of historical data-based empirical eigenfunctions by applying Karhunen-Loève expansion to formulate a computationally efficient EMPC system. Several EMPC systems each using a different ROM (i.e., different number of modes and derived from either using analytical sinusoidal/cosinusoidal eigenfunctions or empirical eigenfunctions) are applied to the non-isothermal tubular reactor example. The

model accuracy, computational time and closed-loop economic performance of the closed-loop tubular reactor under the different EMPC systems is compared and discussed.

6.2 Preliminaries

6.2.1 Parabolic PDEs

We consider quasi-linear parabolic PDEs with measured outputs of the form:

$$\frac{\partial \bar{x}}{\partial t} = A\frac{\partial \bar{x}}{\partial z} + B\frac{\partial^2 \bar{x}}{\partial z^2} + Wu(t) + f(\bar{x}(z,t)) \tag{6.1}$$

$$y_j(t) = \int_0^1 c_j(z)\bar{x}(z,t)dz \tag{6.2}$$

for $j = 1, \ldots, p$, with the boundary conditions:

$$\left.\frac{\partial \bar{x}}{\partial z}\right|_{z=0} = g_0\bar{x}(0,t), \quad \left.\frac{\partial \bar{x}}{\partial z}\right|_{z=1} = g_1\bar{x}(1,t) \tag{6.3}$$

for $t \in [0,\infty)$ and the initial condition:

$$\bar{x}(z,0) = \bar{x}_0(z) \tag{6.4}$$

where $z \in [0,1]$ is the spatial coordinate, $t \in [0,\infty)$ is the time, $\bar{x}'(z,t) = [\bar{x}_1(z,t) \cdots \bar{x}_{n_x}(z,t)]$ is the vector of the state variables ($\bar{x}'$ denotes the transpose of $\bar{x}$), $f(\bar{x}(z,t))$ denotes a nonlinear vector function, $y_j(t)$ is the j-th measured output, and $c_j(z)$ are known smooth functions of z ($j = 1, \ldots, p$) whose functional form depends on the type of the measurement sensor. The notation A, B, W, g_0 and g_1 is used to denote (constant) matrices of appropriate dimensions. The control input vector is denoted as $u(t) \in \mathbb{R}^{n_u}$ and is subject to the following

constraints:

$$u_{min} \leq u(t) \leq u_{max} \tag{6.5}$$

where u_{min} and u_{max} are the lower and upper bound vectors of the manipulated input vector, $u(t)$. Moreover, the system states are also subject to the following state constraints:

$$x_{i,min} \leq \int_0^1 r_{x_i}(z)\bar{x}_i(z,t)dz \leq x_{i,max}, \quad i = 1, \ldots, n_x \tag{6.6}$$

where $x_{i,min}$ and $x_{i,max}$ are the lower and upper state constraint for the i-th state, respectively. The function $r_{x_i}(z) \in L_2(0,1)$ where $L_2(0,1)$ is the space of measurable, square-integrable functions on the interval $[0,1]$ is the state constraint distribution function.

6.2.2 Galerkin's Method

We first formulate the system of PDEs of Eqs. 6.1-6.4 as an infinite dimensional system in the Hilbert space $\mathscr{H}([0,1];\mathbb{R}^{n_x})$, with $\mathscr{H}$ being the space of measurable vector functions defined on $[0,1]$, with inner product and norm:

$$\begin{aligned} (\omega_1, \omega_2) &= \int_0^1 (\omega_1(z), \omega_2(z))_{\mathbb{R}^{n_x}} dz, \\ \|\omega_1\|_2 &= (\omega_1, \omega_1)^{\frac{1}{2}} \end{aligned} \tag{6.7}$$

where ω_1, ω_2 are two elements of $\mathscr{H}([0,1];\mathbb{R}^{n_x})$ and the notation $(\cdot,\cdot)_{\mathbb{R}^{n_x}}$ denotes the standard inner product in $\mathbb{R}^{n_x}$. The state function $x(t)$ on the state-space $\mathscr{H}$ is defined as

$$x(t) = \bar{x}(z,t), \quad t > 0, \quad 0 \leq z \leq 1, \tag{6.8}$$

and the operator $\mathscr{A}$ is defined as

$$\mathscr{A}x = A\frac{d\bar{x}}{dz} + B\frac{d^2\bar{x}}{dz^2}, \quad 0 \leq z \leq 1. \tag{6.9}$$

and the measured output operator is defined as:

$$\mathscr{C}x(t) = [(c_1(\cdot), \bar{x}(\cdot,t)), \cdots, (c_p(\cdot), \bar{x}(\cdot,t))]' \tag{6.10}$$

Then, the system of Eqs. 6.1-6.4 takes the following form:

$$\dot{x}(t) = \mathscr{A}x(t) + \mathscr{B}u(t) + \mathscr{F}(x(t)), \quad x(0) = x_0 \tag{6.11}$$

$$y(t) = \mathscr{C}x(t) \tag{6.12}$$

where $x_0 = \bar{x}_0(z)$, $\mathscr{B}u(t) = Wu(t)$ and $\mathscr{F}(x(t))$ is a nonlinear vector function in the Hilbert space. The eigenvalue problem for $\mathscr{A}$ takes the form

$$\mathscr{A}\phi_k = \lambda_k\phi_k, \quad k = 1, \ldots, \infty \tag{6.13}$$

subject to

$$\left.\frac{d\phi_k}{dz}\right|_{z=0} = g_0\phi_k(0), \quad \left.\frac{d\phi_k}{dz}\right|_{z=1} = g_1\phi_k(1) \tag{6.14}$$

where ϕ_k is an eigenfunction corresponding to the k-th eigenvalue λ_k and $\bar{\phi}_k$ is an adjoint eigenfunction of the operator $\mathscr{A}$.

Assumption 6.1 below characterizes the class of parabolic PDEs considered in this work and states that the eigenspectrum of operator $\mathscr{A}$ can be partitioned into a finite part consisting of m slow eigenvalues which are close to the imaginary axis and a stable infinite complement containing the remaining fast eigenvalues which are far in the left-half of the

complex plane, and that the separation between the slow and fast eigenvalues of $\mathscr{A}$ is large. We also note that the large separation of slow and fast modes of the spatial operator in parabolic PDEs ensures that a controller which exponentially stabilizes the closed-loop ODE system, also stabilizes the closed-loop infinite-dimensional system.[9] This assumption is satisfied by the majority of diffusion-convection-reaction processes.[25]

Assumption 6.1

1. *$Re(\lambda_1) \geq Re(\lambda_2) \geq \cdots \geq Re(\lambda_j) \geq \cdots$, where $Re(\lambda_j)$ denotes the real part of the eigenvalue, λ_j.*

2. *The eigenspectrum of $\mathscr{A}$, $\sigma(\mathscr{A})$, is defined as the set of all eigenvalues of $\mathscr{A}$, i.e. $\sigma(\mathscr{A}) = \{\lambda_1, \lambda_2, \cdots\}$. $\sigma(\mathscr{A})$ can be partitioned as $\sigma(\mathscr{A}) = \sigma_1(\mathscr{A}) \cup \sigma_2(\mathscr{A})$, where $\sigma_1(\mathscr{A})$ consists of the first m finite eigenvalues, i.e. $\sigma_1(\mathscr{A}) = \{\lambda_1, \cdots, \lambda_m\}$, and $|Re(\lambda_1)|/|Re(\lambda_m)| = O(1)$.*

3. *$Re(\lambda_{m+1}) < 0$ and $|Re(\lambda_1)|/|Re(\lambda_{m+1})| = O(\varepsilon)$ where $\varepsilon < 1$ is a small positive number.*

Next, we apply standard Galerkin's method[119] to the infinite-dimensional system of Eqs. 6.11-6.12 to derive a finite-dimensional subsystem. Let $\mathscr{H}_s$ and $\mathscr{H}_f$ be modal subspaces of $\mathscr{A}$ defined as $\mathscr{H}_s = \text{span}\{\phi_1, \phi_2, \ldots, \phi_m\}$ and $\mathscr{H}_f = \text{span}\{\phi_{m+1}, \phi_{m+2}, \ldots\}$, where $\phi_i, i = 1, \ldots, \infty$ are the eigenfunctions of $\mathscr{A}$. Using the orthogonal projection operators, P_s and P_f, which project the state x onto the subspaces $\mathscr{H}_s$ and $\mathscr{H}_f$ of $\mathscr{A}$, respectively ($x_s = P_s x \in \mathscr{H}_s$ and $x_f = P_f x \in \mathscr{H}_f$), the state x of the system of Eq. 6.11 can be written as

$$x = x_s + x_f = P_s x + P_f x \tag{6.15}$$

Applying P_s and P_f to the system of Eqs. 6.11-6.12 and using the above decomposition for

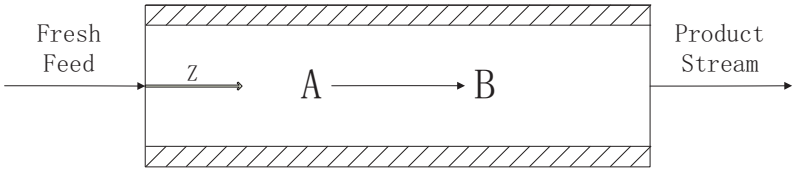

Figure 6.1: A tubular reactor with reaction A $\rightarrow$ B.

x, Eqs. 6.11-6.12 can be re-written as:

$$\begin{aligned}
\dot{x}_s(t) &= \mathscr{A}_s x_s(t) + \mathscr{A}_s x_f(t)(\equiv 0) + \mathscr{F}_s(x_s(t), x_f(t)) + \mathscr{B}_s u(t), \quad x_s(0) = P_s x_0, \\
\dot{x}_f(t) &= \mathscr{A}_f x_f(t) + \mathscr{A}_f x_s(t)(\equiv 0) + \mathscr{F}_f(x_s(t), x_f(t)) + \mathscr{B}_f u(t), \quad x_f(0) = P_f x_0, \\
y(t) &= \mathscr{C}_s x_s(t) + \mathscr{C}_f x_f(t)
\end{aligned} \tag{6.16}$$

where $\mathscr{A}_s = P_s\mathscr{A}$, $\mathscr{B}_s = P_s\mathscr{B}$, $\mathscr{A}_f = P_f\mathscr{A}$, $\mathscr{B}_f = P_f\mathscr{B}$, $\mathscr{F}_f = P_f\mathscr{F}$, $\mathscr{F}_s = P_s\mathscr{F}$, $\mathscr{C}_s = \mathscr{C}P_s$, and $\mathscr{C}_f = \mathscr{C}P_f$. Specifically, $\mathscr{A}_s = \text{diag}\{\lambda_j\}$, $j = 1, \ldots, m$ is a diagonal matrix of dimension $m \times m$ and may contain unstable eigenvalues (i.e., $Re(\lambda_j) > 0$). Note that since the sunspace of $\mathscr{A}$ are spanned by eigenfunctions of $\mathscr{A}$, then $\mathscr{A}_s x_f(t) \equiv 0$ and $\mathscr{A}_f x_x(t) \equiv 0$ based on the fact that the eigenfunctions are orthogonal to each other. The operator $\mathscr{A}_f$ is an unbounded exponentially stable differential operator. The first subsystem (i.e., first equation) of Eq. 6.16 is referred to as the slow subsystem; while, the second subsystem is referred to as the fast subsystem. Neglecting the fast subsystem, we obtain the ODE system describing the dominant dynamics of the PDEs:

$$\begin{aligned}
\dot{x}_s(t) &= \mathscr{A}_s x_s(t) + \mathscr{F}_s(x_s(t), 0) + \mathscr{B}_s u(t), \quad x_s(0) = P_s x_0 \\
y(t) &= \mathscr{C}_s x_s(t)
\end{aligned} \tag{6.17}$$

6.2.3 Tubular Reactor Example

A chemical process example of industrial importance of the form of Eq. 6.1 is used to demonstrate the EMPC systems formulated in this work. Specifically, consider a tubular

reactor shown in Fig. 6.1, where an exothermic, irreversible second-order reaction of the form A $\rightarrow$ B takes place. A cooling jacket of constant temperature is used to remove heat from the reactor. The states of the tubular reactor are temperature and concentration of A in the reactor, and the input is the inlet concentration of A. In order to simplify the presentation of our results below, we use dimensionless variables and obtain the following nonlinear model of parabolic PDEs for the process (details and model notation can be found in[85] and[119]):

$$\begin{aligned}
\frac{\partial \bar{x}_1}{\partial t} &= -\frac{\partial \bar{x}_1}{\partial z} + \frac{1}{Pe_1}\frac{\partial^2 \bar{x}_1}{\partial z^2} + B_T B_C \exp\left(\frac{\gamma \bar{x}_1}{1+\bar{x}_1}\right)(1+\bar{x}_2)^2 \\
&\quad +\beta_T(T_s - \bar{x}_1) + \delta(z-0)T_i \\
\frac{\partial \bar{x}_2}{\partial t} &= -\frac{\partial \bar{x}_2}{\partial z} + \frac{1}{Pe_2}\frac{\partial^2 \bar{x}_2}{\partial z^2} - B_C \exp\left(\frac{\gamma \bar{x}_1}{1+\bar{x}_1}\right)(1+\bar{x}_2)^2 + \delta(z-0)u
\end{aligned} \tag{6.18}$$

where δ is the standard Dirac function, subject to the following boundary conditions:

$$\begin{aligned}
z = 0 \quad &: \quad \frac{\partial \bar{x}_1}{\partial z} = Pe_1 \bar{x}_1, \; \frac{\partial \bar{x}_2}{\partial z} = Pe_2 \bar{x}_2; \\
z = 1 \quad &: \quad \frac{\partial \bar{x}_1}{\partial z} = 0, \; \frac{\partial \bar{x}_2}{\partial z} = 0;
\end{aligned} \tag{6.19}$$

The following typical values are given to the process parameters: $Pe_1 = 7$, $Pe_2 = 7$, $B_T = 2.5$, $B_C = 0.1$, $\beta_T = 2$, $T_s = 0$, $T_f = 0$ and $\gamma = 10$. In all simulations reported below, second-order finite-difference method was used to discretize, in space, the two parabolic PDEs of Eq. 6.18 to be two 101th-order set of ODEs (further increase on the order of discretization led to identical open-loop and closed-loop results); this discretized model was used to describe the process dynamics. The following simulations were carried out using Java programming language in a Intel Core $i7, 3.40\ GHz$ computer with a 64-bit Windows 7 Professional operating system.

6.3 Methodological Framework for Output Feedback EMPC for Systems of PDEs

6.3.1 State-Estimation Using Output Feedback Methodology

The objective of this section is to propose state estimation-based EMPC formulations that make use of a finite number, p, of measured outputs $y_j(t)$ $(j = 1, \cdots, p)$ to compute estimates of x_s and x_f. The state estimation scheme is based on a direct inversion of the measured output operator to obtain estimates of the slow modes, $\hat{x}_s(t)$ and the concept of the approximate inertial manifolds to obtain estimates of the fast modes, $\hat{x}_f(t)$ in the system of Eq. 6.16. To develop this estimation scheme, we must impose an assumption on the number of measured outputs. We assume that the number of measured outputs is equal to the number of slow modes (i.e., $p = m$) and the distribution functions of the measured outputs are chosen such that $\mathscr{C}_s^{-1}$ exists. Under this assumption, an estimate of the slow subsystem state, $\hat{x}_s(t)$ can be obtained as follows:

$$\hat{x}_s(t) = \mathscr{C}_s^{-1} y(t) \tag{6.20}$$

where $\hat{x}_s(t)$ is an estimate of $x_s(t)$.

Since the accuracy of the estimated modes through the reconstruction of the spatially distributed partial differential equation states is limited by the number of available measurement points, we introduce the derivation of the estimation for the fast subsystem state, $x_f(t)$ to achieve additional accuracy of the state estimation scheme. In the infinite-dimensional system described by Eq. 6.16, the fast dynamics, $\dot{x}_f(t)$ can be ignored compared with that of the slow dynamics, $\dot{x}_s(t)$ given that $\mathscr{A}_f$ includes eigenvalues with large negative real part[25] ($\mathscr{A}_f$ is exponentially stable). Thus, the equation of the fast state, $x_f(t)$ can be ap-

proximately expressed as the following equality:

$$\mathscr{A}_f x_f(t) + \mathscr{B}_f u(t) + \mathscr{F}_f(x_s(t), x_f(t)) = 0 \tag{6.21}$$

The fast state x_f is equal to zero at its quasi-steady-state (we note that $\bar{x}(z,t) = 0$ is a steady-state of the nominal system of PDEs with $u(t) \equiv 0$). Accounting for the fact that $\mathscr{A}_f$ includes eigenvalues with large negative real parts, we can neglect the fast subsystem state, $x_f(t)$ in the nonlinear term, $\mathscr{F}_f(x_s, x_f)$. Using the estimated slow subsystem state, $\hat{x}_s$ to calculate the approximate fast subsystem state, Eq. 6.21 becomes

$$\mathscr{A}_f \hat{x}_f(t) + \mathscr{B}_f u(t) + \mathscr{F}_f(\hat{x}_s(t), 0) = 0 \tag{6.22}$$

where $\hat{x}_f(t)$ is the estimated fast state. An explicit form for the estimated fast state can be derived:

$$\hat{x}_f(t) = -\mathscr{A}_f^{-1}[\mathscr{B}_f u(t) + \mathscr{F}_f(\hat{x}_s(t), 0)] \tag{6.23}$$

Remark 6.1 *The accuracy of the finite-dimensional ODE model with m slow modes is of order* $\varepsilon = |Re\{\lambda_1(\mathscr{A})\}|/|Re\{\lambda_{m+1}(\mathscr{A})\}|$ *(*$O(\varepsilon)$*). This means under state feedback the closeness of the closed-loop system state of PDEs to the closed-loop system state of ODEs is* $O(\varepsilon)$*. Closed-loop stability under output feedback works not only for the slow and fast modes but also the real state as long as the estimation error is negligible. This occurs when m is chosen to be sufficiently large such that* ε *is sufficiently small. Specifically, to achieve the same level of closeness for the output feedback case (*$O(\varepsilon)$*), the number of measurements must be equal to the number of slow modes (i.e.,* $p = m$*). When there are more available measurement points than the slow modes, i.e.,*$p > m$*, one can pick m measurement points from the all p points and use them in the reduced order model. However, the discrepancy between the closed-loop partial differential equation state under output*

feedback with more than m measurements and the one of the closed-loop partial differential equation state under output feedback with m measurements will be indistinguishable since the achieved closed-loop system performance is limited by the number of slow modes (m) used in the design of the EMPC. In this work, from both the open-loop and closed-loop system simulation, we have good state estimation accuracy by picking m sufficiently large and choosing the measurement points such that the inverse of the matrix $\mathscr{C}_s$ exists.

6.3.2 Output Feedback Economic Model Predictive Control Formulation

Utilizing the estimates $\hat{x}_s$ and $\hat{x}_f$ of Eq. 6.20 and Eq. 6.23, respectively, we formulate a state estimation-based Lyapunov-based EMPC for the system of Eq. 6.16 to dynamically optimize an economic cost function. We assume that the output measurements are available continuously and synchronously at sampling instants denoted as $t_k = k\Delta$ with $k = 0, 1, \ldots$. Accounting for x_f is important for increasing state estimation accuracy of PDEs and satisfying state constraints. To formulate a finite-dimensional EMPC problem, the fast subsystem is truncated at the l-th fast state. With the estimated slow and fast modes, of Eq. 6.20 and

Eq. 6.23, respectively, the EMPC formulation takes the following form:

$$\max_{u \in S(\Delta)} \quad \int_{t_k}^{t_{k+N}} L(\check{x}(\tau), u(\tau)) d\tau \tag{6.24a}$$

$$\text{s.t.} \quad \dot{\tilde{x}}_s(t) = \mathscr{A}_s \tilde{x}_s(t) + \mathscr{F}_s(\tilde{x}_s(t), \tilde{x}_f(t)) + \mathscr{B}_s u(t) \tag{6.24b}$$

$$\tilde{x}_s(t_k) = \mathscr{C}_s^{-1} y(t_k) \tag{6.24c}$$

$$\tilde{x}_f(t) = -\mathscr{A}_f^{-1}[\mathscr{B}_f u(t) + f_f(\tilde{x}_s(t), 0)] \tag{6.24d}$$

$$\check{x}(t) = \tilde{x}_s(t) + \tilde{x}_f(t) \tag{6.24e}$$

$$u_{min} \leq u(t) \leq u_{max}, \ \forall t \in [t_k, t_{k+N}) \tag{6.24f}$$

$$x_{i,min} \leq (r_{x_i}, \check{x}_i(t)) \leq x_{i,max}, \ i = 1, \ldots, n_x, \ \forall t \in [t_k, t_{k+N}) \tag{6.24g}$$

$$\check{x}'(t) P \check{x}(t) \leq \bar{\rho} \tag{6.24h}$$

where Δ is the sampling period, $S(\Delta)$ is the family of piecewise constant functions with sampling period Δ, N is the prediction horizon, $\tilde{x}_s(t)$ and $\tilde{x}_f(t)$ are the predicted evolution of the slow subsystem state and fast subsystem state, respectively, with input $u(t)$ computed by the EMPC and $y(t_k)$ is the output measurement at the sampling time t_k.

In the optimization problem of Eq. 6.24, the objective function of Eq. 6.24a describes the dynamic economics of the process which the EMPC maximizes over a horizon t_N. The constraint of Eq. 6.24b is used to predict the future evolution of the slow subsystem with the initial condition given in Eq. 6.24c (i.e., the estimate of $x_s(t_k)$ computed from the output $y(t_k)$). The constraint of Eq. 6.24d is the finite-dimensional truncation of the fast subsystem which is used to predict the evolution of the fast subsystem states. The symbol $\check{x}(t)$ is used to denote the finite dimensional truncated state vector (i.e., both the slow subsystem and the fast subsystem states). The constraints of Eq. 6.24f-6.24g are the available control action and the state constraints, respectively. Finally, the constraint of Eq. 6.24h ensures that the predicted state trajectory is restricted inside a predefined stability region which is

a level set of the Lyapunov function (see[65] for a complete discussion of this issue). The optimal solution to this optimization problem is $u^*(t|t_k)$ defined for $t \in [t_k, t_{k+N})$. The EMPC applies the control action computed for the first sampling period to the system in a sample-and-hold fashion for $t \in [t_k, t_{k+1})$. The EMPC is resolved at the next sampling period, t_{k+1}, after receiving a new output measurement, $y(t_{k+1})$.

Remark 6.2 *In the formulation of the state estimation-based Lyapunov-based EMPC of Eq. 6.24, Eq. 6.24h defines a stability region of the closed-loop system. This stability region is typically characterized with an explicit stabilizing state feedback controller.*[65,66] *To account for the fact that additional uncertainty may be introduced by using an output feedback controller over a state feedback controller due to the estimation error, the stability region, computed using an explicit stabilizing state feedback controller, may be reduced for the output feedback case and a sufficiently large number of slow modes m (as well as number of output measurements p) can always be found to ensure that closed-loop stability under output feedback is accomplished.*

6.3.3 Implementation of Output Feedback EMPC

The output feedback EMPC is applied to the tubular reactor. To solve the EMPC problem, the open-source interior point solver Ipopt[139] was used. Explicit Euler's method was used with an sufficiently small integration step of 1×10^{-4} to numerically integrate the finite-dimensional ODE model of the transport-reaction process. The cost function that we consider is to maximize the overall reaction rate along the length of the reactor. The economic cost that the EMPC works to maximize over the prediction horizon is

$$L(\bar{x}, u) = \int_0^1 r(z,t)dz \tag{6.25}$$

where

$$r(z,t) = B_C \exp\left(\frac{\gamma \bar{x}_1}{1+\bar{x}_1}\right)(1+\bar{x}_2)^2 \tag{6.26}$$

is the reaction rate.

Regarding input and state constraints, the manipulated input is subject to constraints as follows: $-1 \leq u \leq 1$. Owing to economic considerations, the amount of reactant material available over the period t_f is fixed. Specifically, the input trajectory should satisfy:

$$\frac{1}{t_f}\int_0^{t_f} u(\tau)\, d\tau = 0.5 \tag{6.27}$$

where $t_f = 1.0$. To simplify the notation, we use the notation $u \in g(t_k)$ to denote this constraint. Constraints on the minimum and maximum temperatures along the length of the reactor are considered as state constraints, Namely, the temperature along the length of the reactor must satisfy the following inequalities:

$$x_{1,min} \leq \bar{x}_1(z,t) \leq x_{1,max} \tag{6.28}$$

for all $z \in [0,1]$ where $x_{1,min} = -1$ and $x_{1,max} = 3$ are the lower and upper limits, respectively.

Since the system of PDEs of Eq. 6.18 consists of two PDEs, the index i ($i = 1, 2$) is used to denote the i-th partial differential equation of Eq. 6.18. We assume the tubular reactor has $p_1 + p_2$ sensors where the first p_1 sensors measures the temperature (i.e., the state corresponding to the first partial differential equation of Eq. 6.18) at measurement points $z_{s,1j} \in [0,1]$ for $j = 1, 2, \ldots, p_1$, and the next p_2 sensors measures the concentration of A (i.e., the second state) at measurement points $z_{s,2j} \in [0,1]$ for $j = 1, 2, \ldots, p_2$. Thus, the output measurements consist of the state measurements at a finite number of points in

the spatial domain (i.e., $x_i'(t_k) = [x_i(z_{s,i1}, t_k) \cdots x_i(z_{s,ip_i}, t_k)]$) and can be written as

$$y_{ij}(t_k) = \bar{x}_i(z_{s,ij}, t_k), \quad i = 1, 2, \quad j = 1, 2, \ldots, p_i$$

where the output measurement vector, $y'(t_k) = [y_1'(t_k)\, y_2'(t_k)]$ and

$$y_i'(t_k) = [y_{i1}(t_k) \cdots y_{ip_i}(t_k)], \quad i = 1, 2\,.$$

We assume the number of measurements satisfies $p_i = m_i$ where m_i refers to the number of total slow modes retained from the i-th partial differential equation in the construction of the model of Eq. 6.24b. Since point-wise measurements are considered, the following measurement distribution function is used:

$$c_{ij}(z) = \delta(z - z_{s,ij}), \quad i = 1, 2, \quad j = 1, 2, \ldots, p_i \tag{6.29}$$

where δ is the standard Dirac function. Each measurement point, $z_{s,ij}$ in the spatial domain is assumed to be at $z_{s,ij} = (j-1)/(p_i - 1)$. The choice of measurement points satisfies the assumption that $\mathscr{C}_{s,i}^{-1}$ exists.

The state $\bar{x}_i(z,t)$ can be decomposed into the sum of the amplitudes and the eigenfunctions of the first l_i eigenmodes:

$$\bar{x}_i(z,t) \approx \sum_{j=0}^{l_i} a_{ij}(t)\phi_{ij}(z), \quad i = 1, 2 \tag{6.30}$$

where $a_{ij}(t)$ and $\phi_{ij}(z)$ is the amplitude and eigenfunctions associated with the j-th eigenvalue of the spatial operator $\mathscr{A}$. Utilizing the decomposition of Eq. 6.30, the estimated slow mode vector, $a_{s,i}'(t_k) = [a_{s,i1}(t_k) \cdots a_{s,ip_i}(t_k)]$ (recall that $m_i = p_i$) can be written in the

following form:

$$y_i(t_k) = \mathscr{C}_{s,i} x_i(t_k) = C_{s,i} a_{s,i}(t_k) = \begin{pmatrix} \phi_{i1}(z_{s,i1}) & \phi_{i2}(z_{s,i1}) & \dots & \phi_{ip}(z_{s,i1}) \\ \phi_{i1}(z_{s,i2}) & \phi_{i2}(z_{s,i2}) & \dots & \phi_{ip}(z_{s,i2}) \\ \vdots & \vdots & \ddots & \vdots \\ \phi_{i1}(z_{s,ip_i}) & \phi_{i2}(z_{s,ip_i}) & \dots & \phi_{ip}(z_{s,ip_i}) \end{pmatrix} \begin{pmatrix} a_{s,i1}(t_k) \\ a_{s,i2}(t_k) \\ \vdots \\ a_{s,ip_i}(t_k) \end{pmatrix} \tag{6.31}$$

for $i = 1, 2$. The estimated slow modes are:

$$\hat{a}_{s,i}(t_k) = C_{s,i}^{-1} y_i(t_k) = \begin{pmatrix} \phi_{i1}(z_{s,i1}) & \phi_{i2}(z_{s,i1}) & \dots & \phi_{ip}(z_{s,i1}) \\ \phi_{i1}(z_{s,i2}) & \phi_{i2}(z_{s,i2}) & \dots & \phi_{ip}(z_{s,i2}) \\ \vdots & \vdots & \ddots & \vdots \\ \phi_{i1}(z_{s,ip_i}) & \phi_{i2}(z_{s,ip_i}) & \dots & \phi_{ip}(z_{s,ip_i}) \end{pmatrix}^{-1} \begin{pmatrix} \bar{x}_i(z_{s,i1}, t_k) \\ \bar{x}_i(z_{s,i2}, t_k) \\ \vdots \\ \bar{x}_i(z_{s,ip_i}, t_k) \end{pmatrix} \tag{6.32}$$

where $\hat{a}_{s,i}(t_k)$ is an estimate of $a_{s,i}(t_k)$ from the output measurement, $y(t_k)$.

Since the decomposition of Eq. 6.30 provides a simplified method for describing the temporal evolution of the system of PDEs, the reduced-order model used in the EMPC (Eq. 6.24b and Eq. 6.24d) is written in terms of the temporal evolution of the amplitudes of each eigenmode. After applying the decomposition of Eq. 6.30 to Eq. 6.16 and multiplying both sides by the adjoint eigenfunction, the resulting reduced-order model has the following form:

$$\begin{aligned} \dot{a}_s(t) &= A_s a_s(t) + F_s(a_s(t), a_f(t)) + B_s u(\cdot) \\ \dot{a}_f(t) &= A_f a_f(t) + F_f(a_s(t), a_f(t)) + B_f u(\cdot) \\ y(t) &= C_s a_s(t) + C_f a_f(t) \end{aligned} \tag{6.33}$$

which is used as the reduced-order model in the EMPC systems. Note that $A_s = \text{diag}\{\lambda_j\}$, $j = 1, \dots, m$ is a diagonal matrix of dimension $l_1 \times l_1$ and $A_f = \text{diag}\{\lambda_j\}$, $j = l_1 + 1, \dots, l_2$ is a diagonal matrix of dimension $(l_2 - l_1) \times (l_2 - l_1)$. Therefore, the quadratic Lyapunov

function of Eq. 6.24h is also written in terms of the amplitudes and has the form:

$$V(a(t)) = a'(t)Pa(t) \tag{6.34}$$

where $a(t)$ denotes a vector consisting of the amplitudes of all retained eigenmodes (i.e., both $a_s(t)$ and $a_f(t)$) for each partial differential equation, P is an $(l_1+l_2)\times(l_1+l_2)$ identity matrix and $\bar{\rho}=3$ is used in the formulations of the EMPC systems below.

Case 1: Low-order Output Feedback EMPC System

In this set of simulations, a low-order output feedback EMPC system of the form of Eq. 6.24 (the fast modes are neglected) is formulated for the tubular reactor with the economic cost function of Eq. 6.25, the input constraint of Eq. 6.27 and the state constraint of Eq. 6.28. The low-order output feedback EMPC is given by the following optimization problem:

$$\max_{u\in S(\Delta)} \quad \frac{1}{N\Delta}\int_{t_k}^{t_{k+N}}\left(\int_0^1 r(z,\tau)dz\right)d\tau \tag{6.35a}$$

$$\text{s.t.} \quad \dot{\tilde{a}}_{s,i}(t) = A_{s,i}\tilde{a}_{s,i}(t) + F_{s,i}(\tilde{a}_s(t),0) + B_{s,i}u(t), \quad i=1,2 \tag{6.35b}$$

$$\tilde{a}_{s,i}(t_k) = C_s^{-1}y_i(t_k), \quad i=1,2 \tag{6.35c}$$

$$-1 \le u(t) \le 1, \ \forall t \in [t_k, t_{k+N}) \tag{6.35d}$$

$$u(t) \in g(t_k) \tag{6.35e}$$

$$-1 \le \sum_{j=1}^{m_1}\tilde{a}_{s,1j}(t)\phi_{1j}(z) \le 3 \tag{6.35f}$$

$$\tilde{a}_s'(t)P\tilde{a}_s(t) \le \bar{\rho} \tag{6.35g}$$

where the notation $\tilde{a}_s$ denotes the predicted temporal evolution of the amplitudes of the slow modes, the prediction horizon is $N=3$ and the sampling time is $\Delta=0.01$. The constraint of Eq. 6.35e is the integral input constraint of Eq. 6.27 formulated for the sampling time

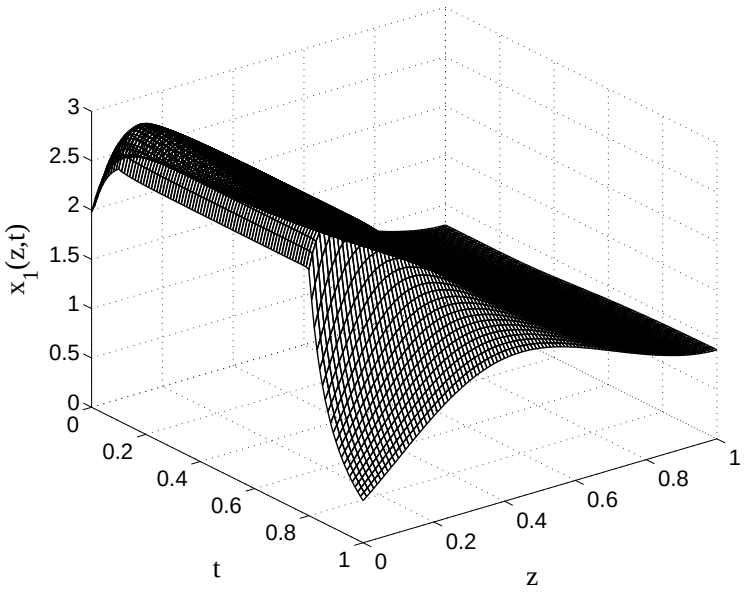

Figure 6.2: Closed-loop profile of x_1 of the tubular reactor under the low-order output feedback EMPC system of Eq. 6.35 based on 21 slow modes over one operation period.

t_k to ensure that the integral input constraint is satisfied over the window $t_f = 1.0$. The tubular reactor is initialized with a transient state profile (i.e., not the steady-state profile corresponding to the steady-state input $u_s = 0.5$). For the reactor, two EMPC systems are formulated with the following low-order model of the system of PDEs:

1. The low-order model based on 11 slow modes only (i.e., $m_1 = m_2 = 11$).

2. The low-order model based on 21 slow modes only (i.e., $m_1 = m_2 = 21$).

where the measured output points consists of the state measurements at $m_1 = 11$ or $m_1 =$ 21 points which are evenly spaced in the spatial domain. Additionally, the reactor under uniform in time distribution of the reactant material over $t_f = 1.0$ is also considered for comparison purposes.

The closed-loop state profiles of the reactor over one period $t_f = 1.0$ under the output feedback EMPC formulated with the low-order model based on 21 slow modes is displayed

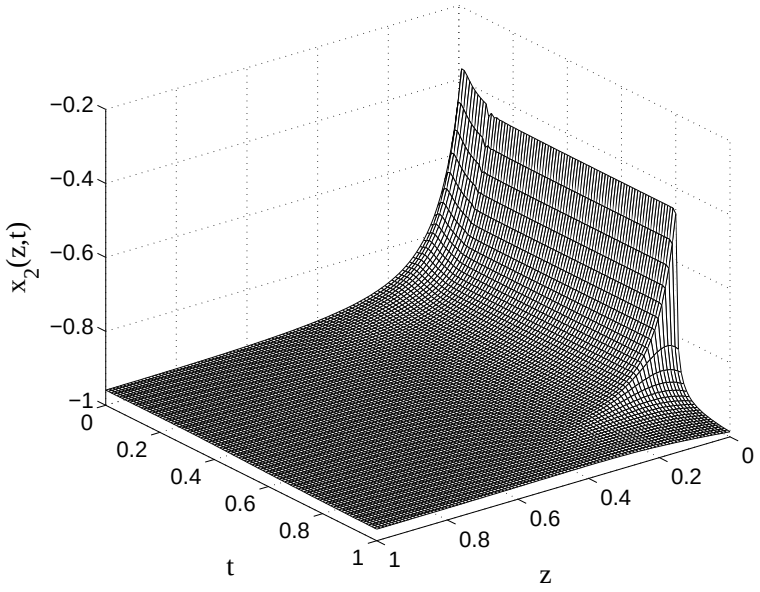

Figure 6.3: Closed-loop profile of x_2 of the tubular reactor under the low-order output feedback EMPC system of Eq. 6.35 based on 21 slow modes over one operation period.

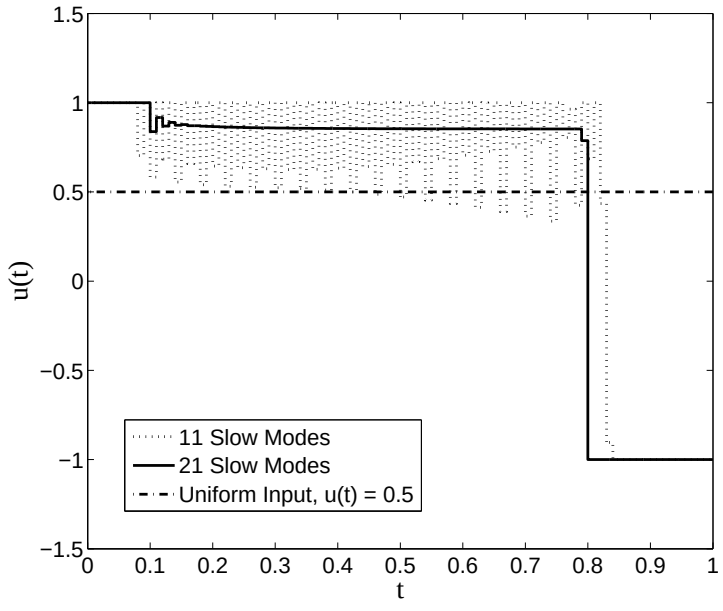

Figure 6.4: Manipulated input profiles of the low-order output feedback EMPC systems of Eq. 6.35 based on 11 and 21 slow modes, respectively, and uniform in time distribution of the reactant material over one operation period.

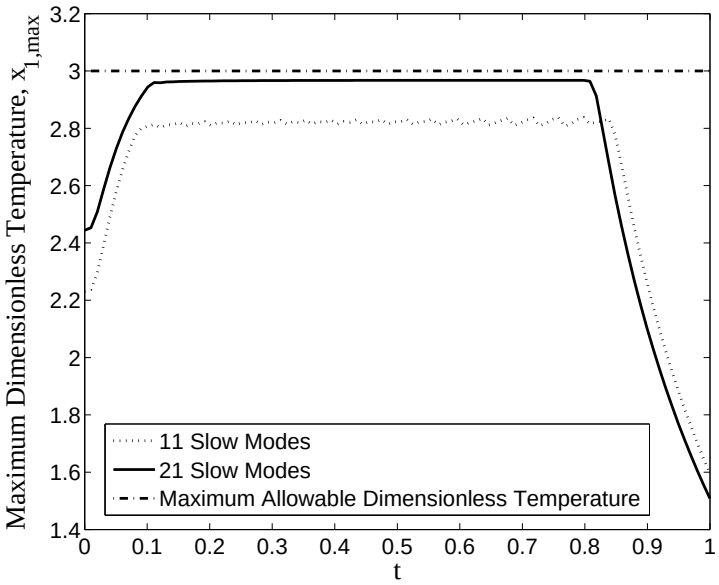

Figure 6.5: Maximum temperature x_1, profiles of the tubular reactor under the low-order output feedback EMPC systems of Eq. 6.35 based on 11 and 21 slow modes, respectively, over one operation period.

in Figs. 6.2-6.3. The computed manipulated input profiles from the low-order output feedback EMPC systems formulated based on 11 and 21 slow modes, respectively, over one period are shown in Fig. 6.4. From Fig. 6.4, the output feedback EMPC system based on 21 slow modes computes a smoother manipulated input profile than that of the output feedback EMPC system based on 11 slow modes. The maximum temperature profiles of the tubular reactor under the EMPC systems are shown in Fig. 6.5. Since the temperature directly influences the reaction rate, the optimal operating strategy is to operate the reactor at the maximum allowable temperature. From Fig. 6.5, both EMPC systems operate the tubular reactor with a maximum temperature less than the maximum allowable which is a consequence of the error associated with the low-order models. Since the low-order model based on 21 slow modes is able to more accurately compute the state profile, the output feedback EMPC system formulated with this low-order model operates the reactor at a greater temperature than the other EMPC system.

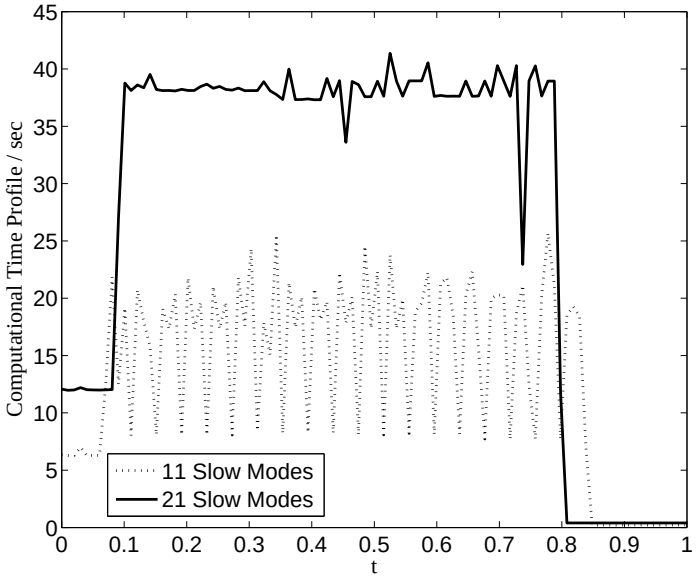

Figure 6.6: Computational time profiles of the low-order output feedback EMPC system of Eq. 6.35 based on 11 and 21 slow modes, respectively, over one operation period.

Over one period $t_f = 1$, the total reaction rate of the process under the EMPC system based on 21 slow modes is 5.13% greater than that of EMPC system based on 11 slow modes and 8.45% greater than that of the system under uniform in time distribution of the reactant material. Moreover, the computational time profiles for these two EMPC systems of Eq. 6.35 is given in Fig. 6.6. The EMPC system based on 11 slow modes has a significant advantage in the computational efficiency since it uses fewer modes in the reduced-order model.

Remark 6.3 *Regarding the chattering in the computed input profile (Fig. 6.4), the chattering is not caused by the numerical integration. A smaller integration time step size was tested and the same input profile was obtained.*

Case 2: High-order Output Feedback EMPC System

In the second set of simulations, a high-order output feedback EMPC system of the form of Eq. 6.24 is formulated for the tubular reactor and has the form:

$$\max_{u\in S(\Delta)} \quad \frac{1}{N\Delta}\int_{t_k}^{t_{k+N}}\left(\int_0^1 r(z,\tau)dz\right)d\tau \tag{6.36a}$$

$$\text{s.t.} \quad \dot{\tilde{a}}_{s,i}(t) = A_{s,i}\tilde{a}_{s,i}(t) + F_{s,i}(\tilde{a}_s(t),\tilde{a}_f(t)) + B_{s,i}u(t) \tag{6.36b}$$

$$\tilde{a}_{f,i}(t) = -A_{f,i}^{-1}[B_{f,i}u(t) + F_{f,i}(\tilde{a}_s(t),0)] \tag{6.36c}$$

$$\tilde{a}_{s,i}(t_k) = C_{s,i}^{-1}y_i(t_k), \quad i = 1,2 \tag{6.36d}$$

$$-1 \leq \sum_{j=1_1}^{l}\tilde{a}_{1j}(t)\phi_{1j}(z) \leq 3 \tag{6.36e}$$

$$-1 \leq u(t) \leq 1, \ \forall t \in [t_k, t_{k+N}) \tag{6.36f}$$

$$u(t) \in g(t_k) \tag{6.36g}$$

$$\tilde{a}'(t)P\tilde{a}(t) \leq \bar{\rho} \tag{6.36h}$$

where $\tilde{a}_s$ is the predicted temporal evolution of the amplitudes of the slow modes, $\tilde{a}_f$ is the predicted temporal evolution of the amplitudes of the fast modes, and $\tilde{a}$ is a vector consisting of both $\tilde{a}_s$ and $\tilde{a}_f$. The prediction horizon of the EMPC is $N = 3$ and the sampling time is $\Delta = 0.01$. The high-order model of Eqs. 6.36b-6.36c is based on 11 slow modes and 19 fast modes (i.e., $m_1 = m_2 = 11$ and $l_1 = l_2 = 30$). Two other model formulations are considered for comparison purposes:

1. The low-order output feedback EMPC system of Eq. 6.35 based on 11 slow modes.

2. A high-order EMPC system with full state feedback like in[83] based on 30 modes (11 slow modes).

Again, the system with uniform in time distribution of the reactant material over one operation period is also considered.

The closed-loop state profiles of the reactor under the high-order output feedback EMPC of Eq. 6.36 is displayed in Figs. 6.7-6.8. The manipulated input profiles computed by the high-order output feedback EMPC system of Eq. 6.36 is shown in Fig. 6.9; while, the input profile computed by the high-order state feedback EMPC system is shown in Fig. 6.10. From Fig. 6.9, chattering in the input profiles computed by the high-order output feedback EMPC systems is observed. The additional 19 fast modes in the high-order output feedback EMPC system helps reduce this compared to the low-order output feedback EMPC of Eq. 6.35. Correspondingly, the differences in the maximum temperature profiles among the three EMPC systems is shown in Fig. 6.11. The total reaction rate over one operation period of the process under the high-order output feedback EMPC system is 0.89% greater than that of the process under the low-order output feedback EMPC system and only 0.73% less than that of the process under the EMPC system with full state feedback. In summary, the above comparison results demonstrate that the additional fast modes in Eq. 6.36 can improve the accuracy of model prediction.

Moreover, the computational time profiles for these 3 different EMPC systems of Eq. 6.36 are given in Fig. 6.12. From Fig. 6.12, the computational efficiency of the EMPC system of Eq. 6.36 based on 30 modes (11 slow modes) is comparable to that of the full state feedback EMPC system based on 30 modes (11 slow modes). Based on the above results, from a practical point of view, comparable total economic cost and computational time is achieved while using much fewer measurement points with the high-order output feedback EMPC system than that resulting from the full state feedback EMPC system.

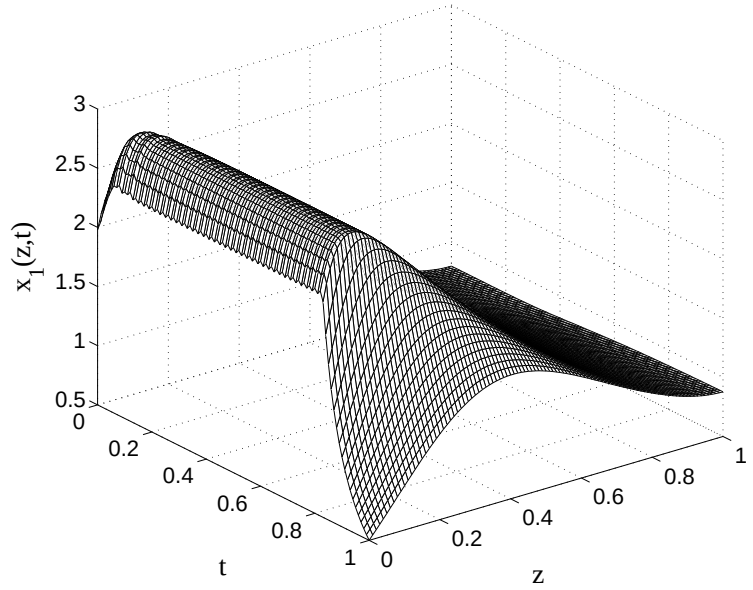

Figure 6.7: Closed-loop profile of x_1 of the process under the high-order output feedback EMPC system of Eq. 6.36 based on 30 modes (11 slow modes) over one operation period.

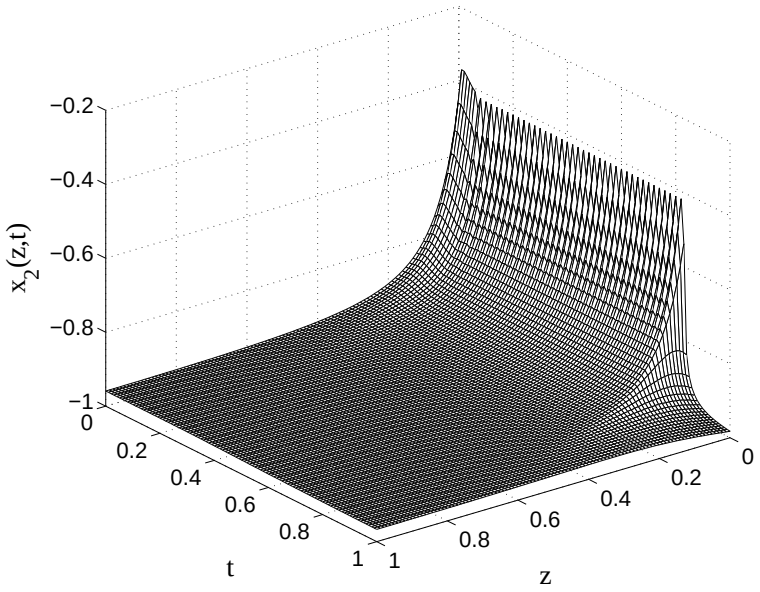

Figure 6.8: Closed-loop profile of x_2 of the process under the high-order output feedback EMPC system of Eq. 6.36 based on 30 modes (11 slow modes) over one operation period.

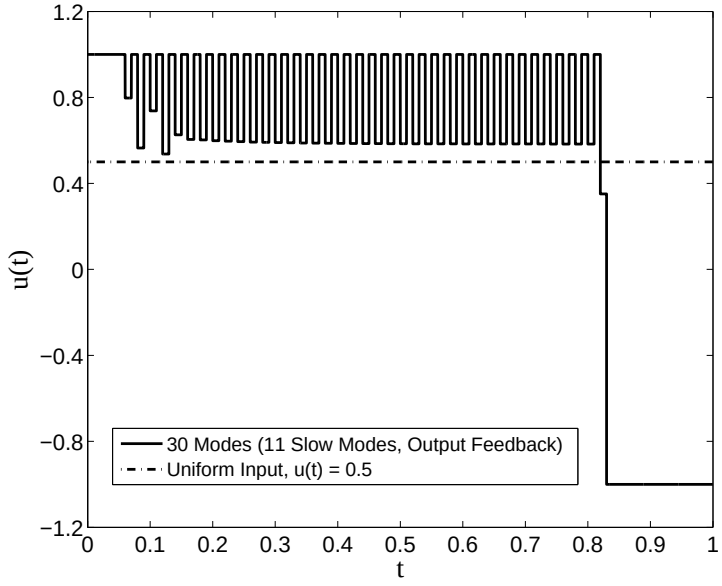

Figure 6.9: Manipulated input profiles of the high-order output feedback EMPC system of Eq. 6.36 based on 30 modes (11 slow modes) and uniform in time distribution of the reactant material over one operation period.

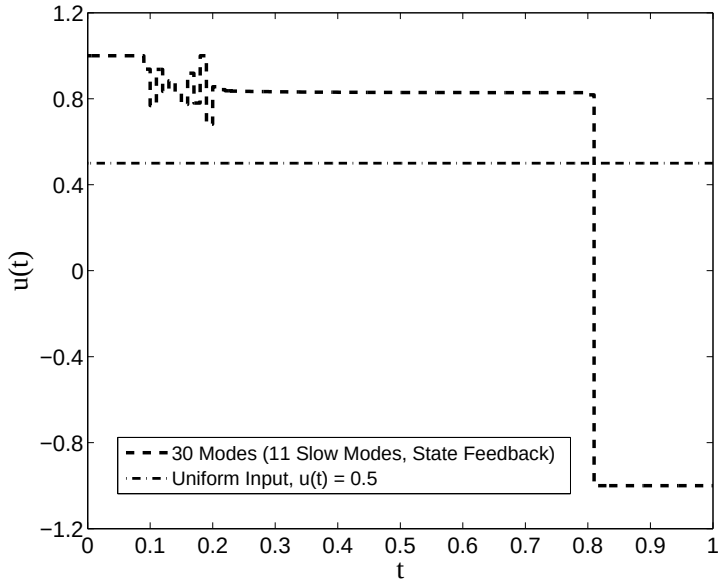

Figure 6.10: Manipulated input profiles of the high-order full state feedback EMPC system based on 30 modes (11 slow modes) and uniform in time distribution of the reactant material over one operation period.

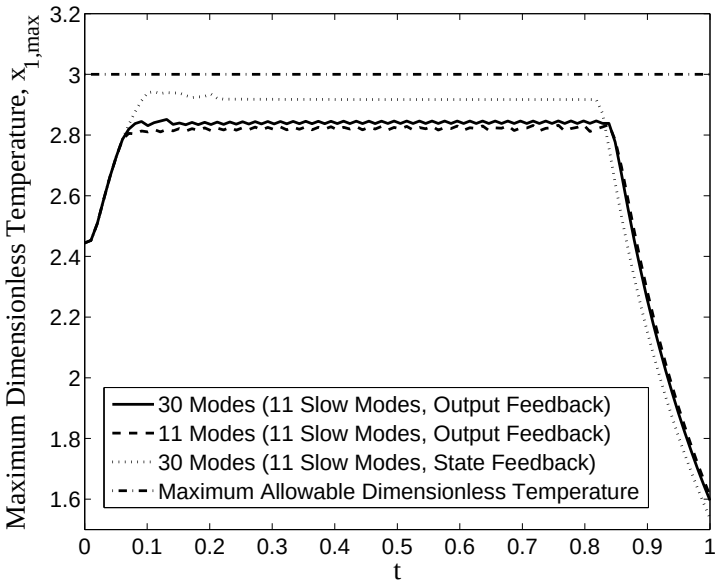

Figure 6.11: Maximum temperature x_2, profiles of the low-order output feedback EMPC system of Eq. 6.35 based on 11 slow modes, the high-order output feedback EMPC system of Eq. 6.36 based on 30 modes (11 slow modes), the high-order full state feedback EMPC system based on 30 modes (11 slow modes) over one operation period.

Case 3: Measurement Noise Effect on Low-Order Output Feedback EMPC System

In this case, the effect of bounded measurement noise on the output measurement is considered. Process noise is added to each of the 2 states and modeled as bounded Gaussian white noise with 0 mean, unit variance, and bounds given by $wn = [0.10.05]$ which is 3% and 5% of the maximum state value. The low-order output feedback EMPC system based on 11 slow modes as Case 1 adopts is applied to operate the process. The closed-loop manipulated input profile of the reactor under the low-order output feedback EMPC is displayed in Fig. 6.13. Comparing Fig. 6.13 with the manipulated input profile of the low-order output feedback EMPC without output measurement noise in Fig. 6.4, we can see the noise results in more serious input fluctuation phenomenon. The maximum temperature profiles of the EMPC systems with measurement noise is shown in Fig. 6.14 and the EMPC system can still control the reactor operating below the maximum allowable temperature and achieve

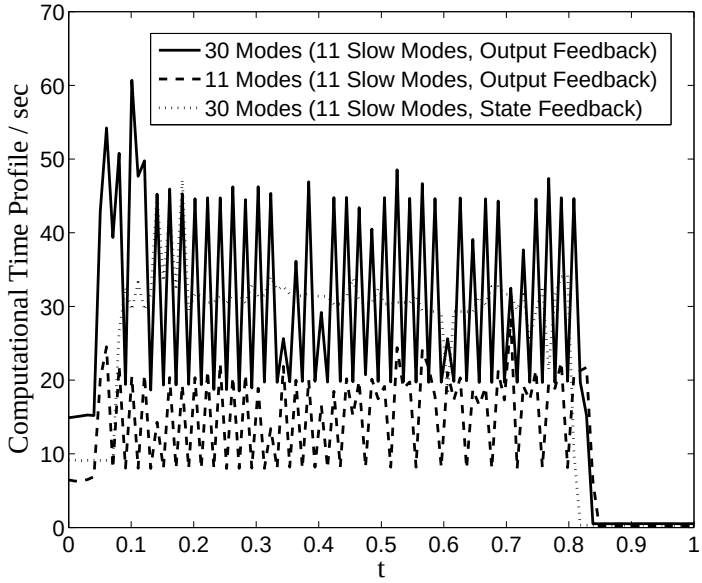

Figure 6.12: Computational time profiles of the low-order output feedback EMPC system of Eq. 6.35 based on 11 slow modes, the high-order output feedback EMPC system of Eq. 6.36 based on 30 modes (11 slow modes), the high-order full state feedback EMPC system based on 30 modes (11 slow modes) over one operation period.

robustness.

6.4 Methodological Framework for Low-Order EMPC Using Empirical Eigenfunctions

As another way to derive a reduced-order model (ROM) for the system of Eq. 6.11, empirical eigenfunctions may be used as basis functions in Galerkin's method. This method can lead to improved computational efficiency over using analytical sinusoidal/cosinusoidal eigenfunctions. In this section, the overall approach is summarized followed by several closed-loop simulations of the closed-loop tubular reactor under an EMPC with a model constructed from empirical eigenfunctions. Both state feedback and output feedback implementation of the EMPC systems formulated for the tubular reactor example are considered.

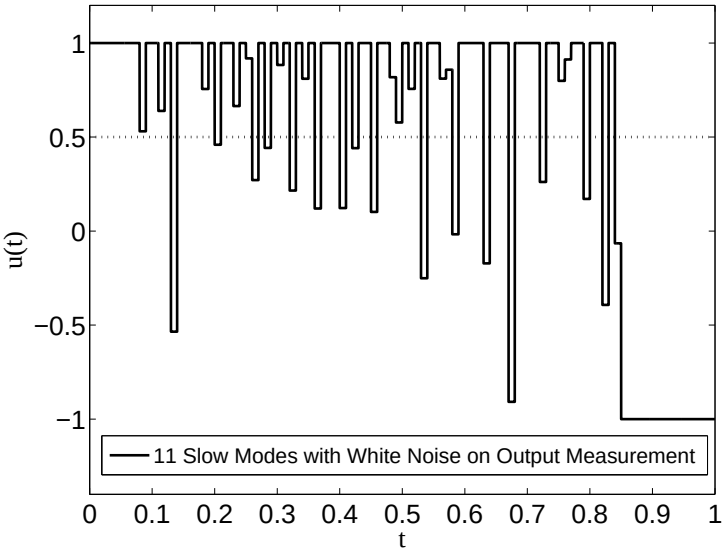

Figure 6.13: Manipulated input profiles of the low-order output feedback EMPC system with white noise on output measurement based on 11 slow modes and uniform in time distribution of the reactant material over one operation period.

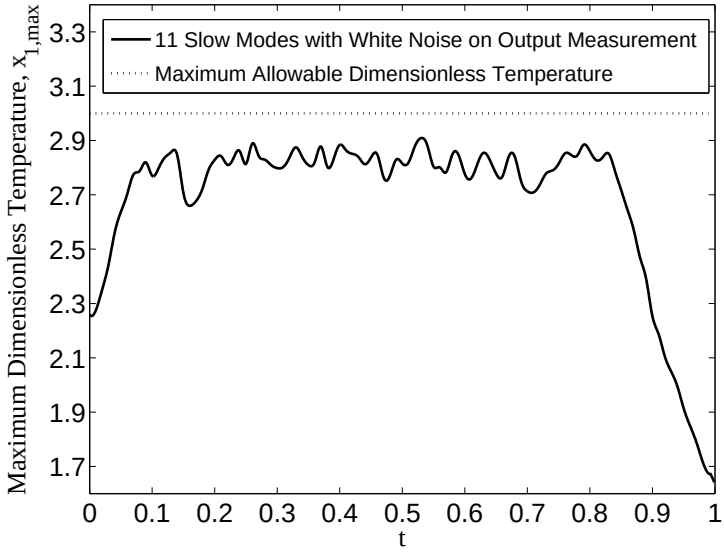

Figure 6.14: Maximum temperature x_1, profiles of the low-order output feedback EMPC system with white noise on output measurement based on 11 slow modes and maximum allowable dimensionless temperature over one operation period.

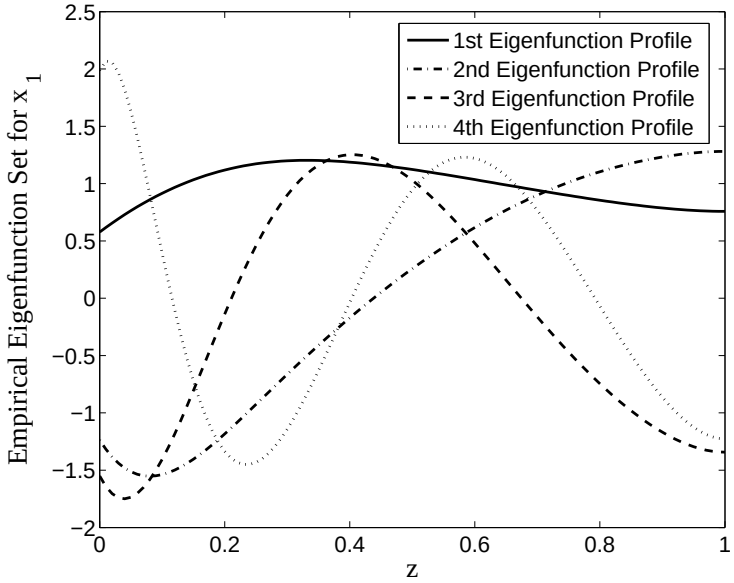

Figure 6.15: First 4 empirical eigenfunction set for x_1 from an ensemble of 2500 system solutions.

6.4.1 Implementation of Karhunen-Loève Expansion

In order to compute the empirical eigenfunctions, we first derive and solve a high-order and convergent discretization of the PDE of Eq. 6.18. In detail, 20 different initial conditions and arbitrary (constant) input values, $u(t)$ were applied to the process model to get the spatiotemporal solution profiles. Consequently, from each simulation solution profile, 125 uniformly sampled solutions (which are typically called "snapshots") were taken and combined to generate an ensemble of 2500 solutions. The Karhunen-Loève (K-L) expansion was applied to the developed ensemble of solutions to compute empirical eigenfunctions that describe the dominant spatial solution patterns embedded in the ensemble where the Jacobian in the K-L expansion is calculated through a finite-difference. After truncating the eigenfunctions with relatively small eigenvalues (smaller than 1×10^{-5}), we were left with the first 4 eigenvalues which occupy more than 99.99% of the total energy included in the entire ensemble. The first 4 of these empirical eigenfunctions profiles for each state

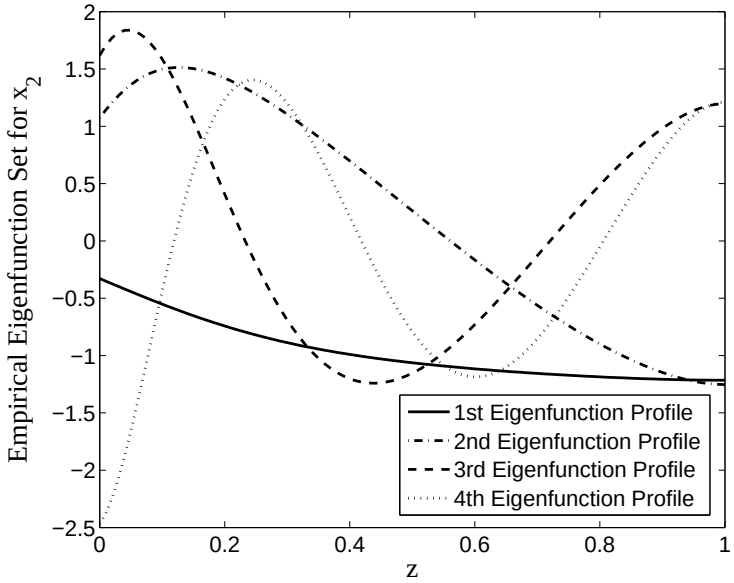

Figure 6.16: First 4 empirical eigenfunction set for x_2 from an ensemble of 2500 system solutions.

are presented in Fig. 6.15 and Fig. 6.16. Note that in contrast to the sinusoidal/cosinusoidal eigenfunctions, these empirical eigenfunctions are not symmetric with respect to the center of the spatial domain owing to the nonlinear term f and the input $u(t)$.

The methodology used to carry out the order reduction and EMPC design is summarized below.

1. Initially, we form an ensemble of solutions of the PDEs of Eq. 6.1 for different values of manipulated input variables $u(t)$.

2. Then, we apply Karhunen-Loève (K-L) expansion to this ensemble to derive a set of empirical eigenfunctions (dominant spatial patterns that minimize the mean square error over all the ensemble elements).[6]

3. The empirical eigenfunctions are used as basis functions within a Galerkin's model reduction framework to transform the infinite dimensional nonlinear system of PDEs

into a ROM in the form of a low-dimensional nonlinear ODE system.

4. Finally, an EMPC formulation is developed with the ROM and applied to the tubular reactor example.

Remark 6.4 *As a practical implementation note, we point out that even though the increase of the eigenfunctions applied to the series expansion of Eq. 6.18 could improve the accuracy of the computed approximate model, eigenfunctions that have high frequency spatial profiles with small eigenvalues are discarded because of the probable round off errors. For this case, the descending first* 5 *empirical eigenvalues are listed as follows: for* $\bar{x}_1(z,t)$*,* $\lambda_{1,1} = 2.365, \lambda_{1,2} = 1.157 \times 10^{-1}, \lambda_{1,3} = 4.926 \times 10^{-2}, \lambda_{1,4} = 9.315 \times 10^{-4}, \lambda_{1,5} = 7.255 \times 10^{-6}$ *and for* $\bar{x}_2(z,t)$*,* $\lambda_{2,1} = 9.719 \times 10^{-1}, \lambda_{2,2} = 1.371 \times 10^{-1}, \lambda_{2,3} = 5.138 \times 10^{-2}, \lambda_{2,4} = 9.405 \times 10^{-4}, \lambda_{2,5} = 8.930 \times 10^{-6}$.

6.4.2 Galerkin's Method with Empirical Eigenfunctions Functions

To reduce the partial differential equation model of Eq. 6.18 into an ODE model, we take advantage of the orthogonality of the empirical eigenfunctions obtained from the K-L expansion. Specifically, using Galerkin's method, we first derive a low-order ODE system for each of the PDEs describing the temporal evolution of the amplitudes corresponding to the first m_i eigenfunctions. The low-order finite-dimensional model for the first $j = 1, \ldots, m_i$ eigenfunctions of the i-th partial differential equation has the following form:

$$\dot{a}_{s,i}(t) = A_{s,i} a_{s,i}(t) + F_{s,i}(a_s(t), 0) + B_{s,i} u(t), \quad i = 1, 2 \tag{6.37}$$

where $a'_{s,i}(t) = [a_{s,i1}(t) \cdots a_{s,im_i}(t)]$ is a vector of the amplitudes of the first m_i eigenfunctions.

To present the effectiveness of empirical eigenfunctions in capturing the dominant

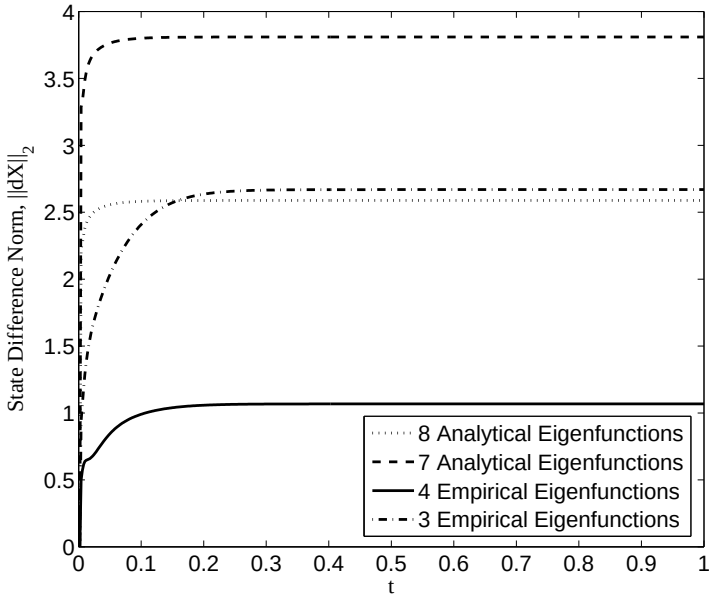

Figure 6.17: L_2 norm of the closed-loop evolution profiles of Eq. 6.18 using 4 different ROMs with respect to the evolution profile from the higher-order discretization finite difference method.

trends that appear during closed-loop process evolution, we let the process evolve starting from a certain initial condition and under a constant input value, $u(t) = 1$. Four different ROMs are presented and compared to show the ROM accuracy in the context of EMPC handling manipulated input and state constraints. Specifically, the following ROMs are considered:

1. ROM using 8 analytical sinusoidal/cosinusoidal eigenfunctions (e.g., 8 eigenfunctions for each partial differential equation state; 16 eigenfunctions total).

2. ROM using 7 analytical sinusoidal/cosinusoidal eigenfunctions.

3. ROM using 4 empirical eigenfunctions.

4. ROM using 3 empirical eigenfunctions.

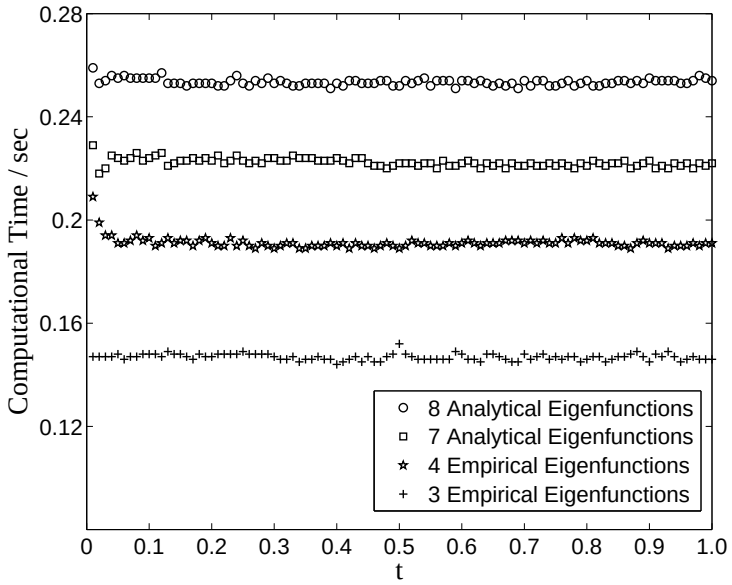

Figure 6.18: Computational time profiles of Eq. 6.18 using 4 different ROMs.

We compared the L_2 norm, denoted as $||dX||_2$ which is the sum of state difference at each state measurement point, i.e., $||dX||_2^2 = \sum_{j=1}^{101}(x_{i,j} - \hat{x}_{i,j})^2, i = 1,2$ where $x_{i,j}$ is the point state measurement from reduced order model and $\hat{x}_{i,j}$ comes from the finite difference method, of the closed-loop evolution profile of the system under these 4 different situations with respect to the evolution profile from the higher-order discretization finite difference method (i.e., the two 101th-order set of ODEs obtained by discretizing, in space, the two parabolic PDEs of Eq. 6.18) under the same initial condition and input value in Fig. 6.17. From the Fig. 6.17, comparing the L_2 norm between the ROM using 4 empirical eigenfunctions and the ROM using 8 analytical eigenfunctions, the ROM constructed from the empirical eigenfunctions is more accurate than the accuracy of the ROM constructed from analytical eigenfunctions with more modes. Furthermore, we compared the computational efficiency under the above two different model reduction methods. The comparison of the computational time corresponding to these 4 different ROMs is given in Fig. 6.18. The ROM based on empirical eigenfunctions shows its advantage on the computational

efficiency compared with the ROM based on the analytical sinusoidal/cosinusoidal eigenfunctions.

6.4.3 Implementation of EMPC

The implementations details of the EMPC are the same as for the output feedback case (see the "Implementation of Output Feedback EMPC" subsection) except for two differences. First, the availability of the full state profile across the entire spatial domain is assumed at each sampling instance except for the third case study below and second, the reduced-order model used in the EMPC is constructed using empirical eigenfunctions as basis functions.

Case 1: Low-order EMPC System with Input Constraints Only

In this set of simulations, we consider an EMPC formulation using the model of Eq. 6.37 and considering only input constraints which is of the form:

$$\max_{u\in S(\Delta)} \quad \frac{1}{N\Delta}\int_{t_k}^{t_{k+N}}\left(\int_0^1 r(z,\tau)dz\right)d\tau \tag{6.38a}$$

$$\text{s.t.} \quad \dot{\tilde{a}}_{s,i}(t) = A_{s,i}\tilde{a}_{s,i}(t) + F_{s,i}(\tilde{a}_s(t),0) + B_{s,i}u(t) \tag{6.38b}$$

$$\tilde{a}_{s,ij}(t_k) = (\bar{\phi}_{s,ij}(z), \bar{x}_i(z,t_k)), \quad j = 1,\ldots,m_i,\ i = 1,2 \tag{6.38c}$$

$$-1 \le u(t) \le 1,\ \forall t \in [t_k, t_{k+N}) \tag{6.38d}$$

$$u \in g(t_k) \tag{6.38e}$$

$$\tilde{a}_s'(t)P\tilde{a}_s(t) \le \bar{\rho} \tag{6.38f}$$

where the notation is similar to the notation of the EMPC formulations in the previous sections. The EMPC of Eq. 6.38 is applied with a prediction horizon $N = 2$ and a sampling time $\Delta = 0.01$.

The closed-loop behavior of the tubular reactor under an EMPC formulated with four

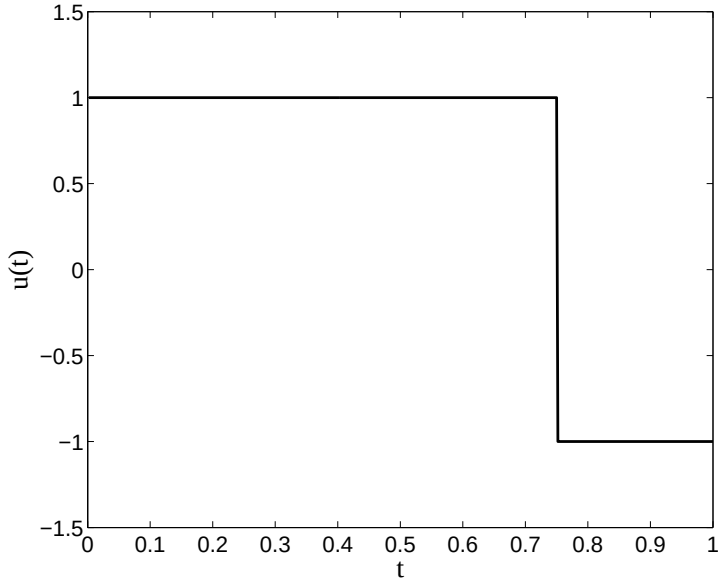

Figure 6.19: Manipulated input profiles of the EMPC formulation of Eq. 6.38 using 4 different ROMs over one operation period (profiles are overlapping).

different ROM was considered: ROMs based on 3 and 4 empirical eigenfunctions and ROMs based on 7 and 8 analytical sinusoidal/cosinusoidal eigenfunctions. For $x(z,0) = 0$, all of these 4 ROMs achieve the same manipulated input and closed-loop state profiles under the EMPC of Eq. 6.38 which are shown in Fig. 6.19 and Figs. 6.20-6.21, respectively. We emphasize here on the computational efficiency under the above two different methods. The comparison of the computational time corresponding to these 4 different situations is given in Fig. 6.22. The ROM based on empirical eigenfunctions shows its advantage on the computational efficiency compared with the ROM based on the analytical sinusoidal/cosinusoidal eigenfunctions.

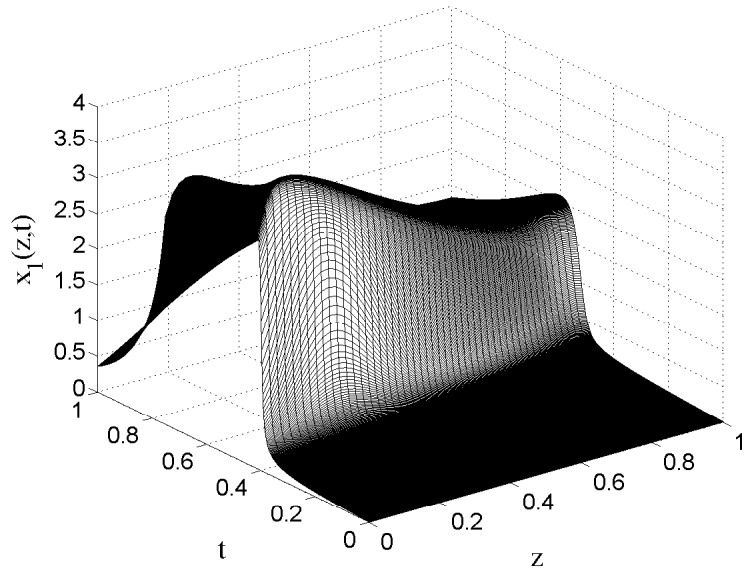

Figure 6.20: Closed-loop profile of x_1 of the EMPC formulation of Eq. 6.38 using 4 different ROMs over one operation period (profiles are overlapping).

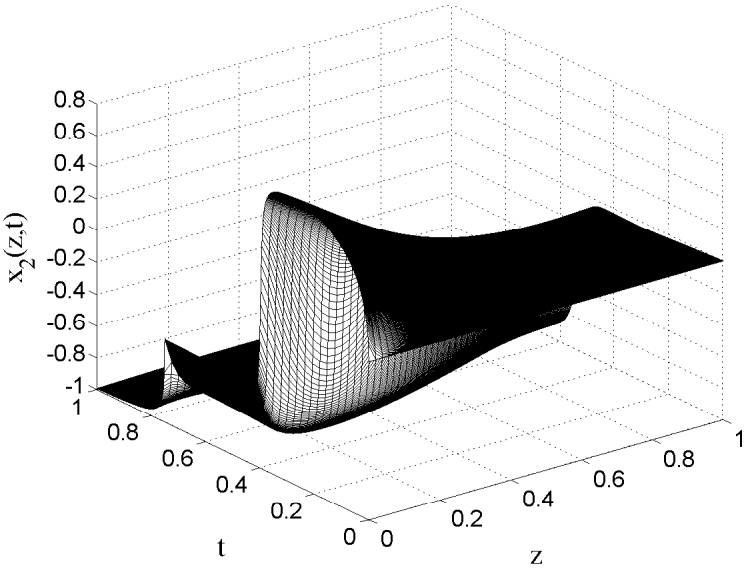

Figure 6.21: Closed-loop profile of x_2 of the EMPC formulation of Eq. 6.38 using 4 different ROMs over one operation period (profiles are overlapping).

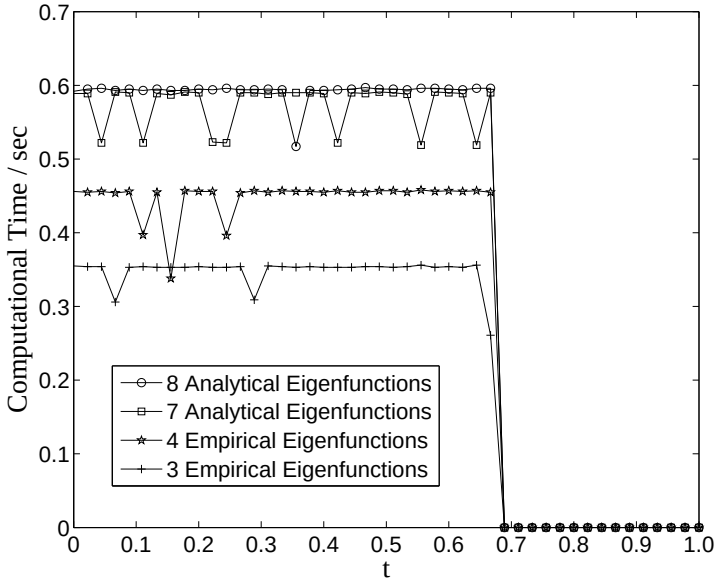

Figure 6.22: Computational time profiles of the EMPC formulation of Eq. 6.38 using 4 different ROMs over one operation period.

Case 2: Low-order EMPC System With State and Input Constraints

In this case, the state constraint of Eq. 6.28 into the EMPC formulation and thus, the EMPC formulation takes the form:

$$\max_{u\in S(\Delta)} \quad \frac{1}{N\Delta}\int_{t_k}^{t_{k+N}}\left(\int_0^1 r(z,\tau)dz\right)d\tau \tag{6.39a}$$

$$\text{s.t.} \quad \dot{\tilde{a}}_{s,i}(t) = A_{s,i}\tilde{a}_{s,i}(t) + F_{s,i}(\tilde{a}_s(t),0) + B_{s,i}u(t) \tag{6.39b}$$

$$\tilde{a}_{s,ij}(t_k) = (\bar{\phi}_{s,ij}(z), \bar{x}_i(z,t_k)), \quad j = 1,\ldots,m_i,\, i = 1,2 \tag{6.39c}$$

$$-1 \leq \sum_{j=1}^{m_i} \tilde{a}_{s,1j}(t)\phi_{1j}(z) \leq 3 \tag{6.39d}$$

$$-1 \leq u(t) \leq 1,\ \forall t \in [t_k, t_{k+N}) \tag{6.39e}$$

$$u \in g(t_k) \tag{6.39f}$$

$$\tilde{a}'(t)P\tilde{a}(t) \leq \bar{\rho} \tag{6.39g}$$

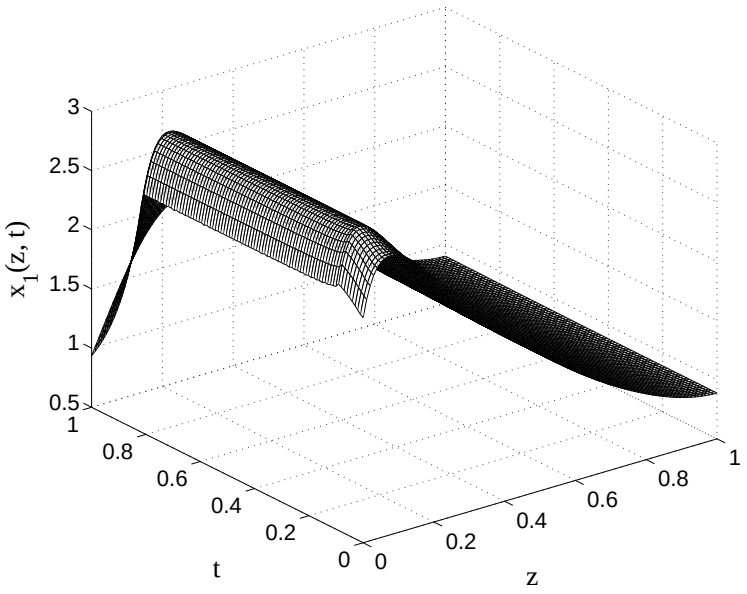

Figure 6.23: Closed-loop profile of x_1 of EMPC formulation of Eq. 6.39 using the ROM based on 4 empirical eigenfunctions over one operation period.

We consider a prediction horizon $N = 3$ and a sampling time $\Delta = 0.01$. For this case, the initial condition is the steady-state of the system under uniform input distribution, $u = 0.5$, as shown in the Figs. 6.23-6.24.

We compared the simulation results from the ROM based on 4 empirical eigenfunctions (i.e., $m_1 = m_2 = 4$) and ROMs based on 8 and 12 sinusoidal/cosinusoidal eigenfunctions, respectively, for $x(z,0)$ equal to the steady-state of the system under constant input value, $u(t) = 0.8$. Figs. 6.23-6.24 show the closed-loop evolution of the states under the EMPC formulation of Eq. 6.39 from the ROM based on 4 empirical eigenfunctions. The manipulated input profiles for the above 3 different ROMs are given in Fig. 6.25, which have the same behavior as the ones in Case 1. For the input profile of ROM based on 4 empirical eigenfunctions in Fig. 6.25 (solid line), the vibration is caused by the over-estimated maximum temperature by the ROM in EMPC, which is also seen in Fig. 6.26 (solid line).

For this case study, we compared the integral of the reaction rate along the length of

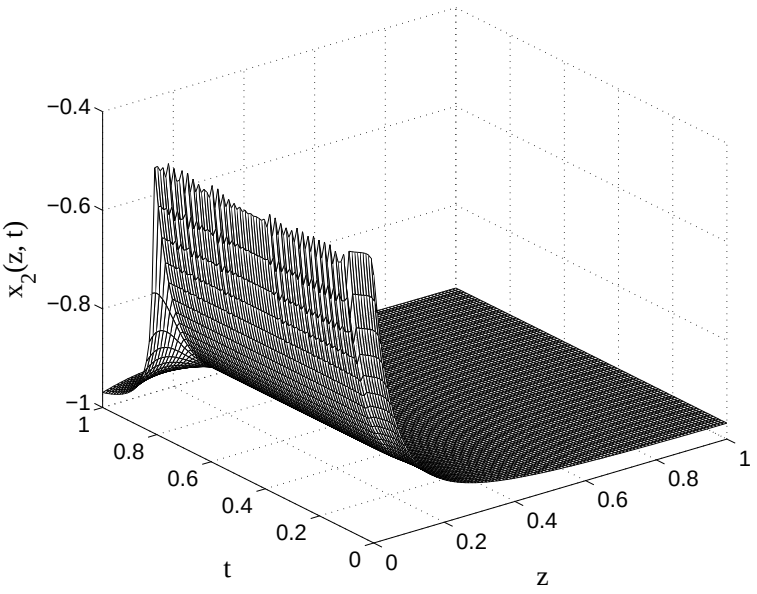

Figure 6.24: Closed-loop profile of x_2 of EMPC formulation of Eq. 6.39 using the ROM based on 4 empirical eigenfunctions over one operation period.

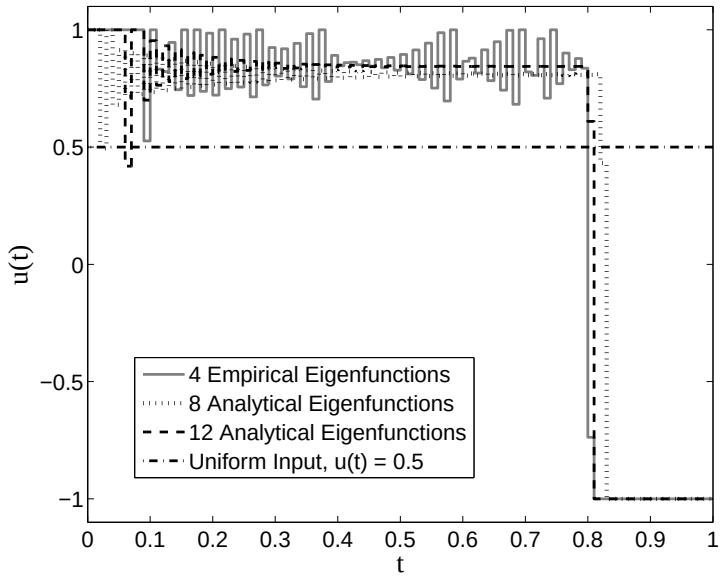

Figure 6.25: Manipulated input profiles of the EMPC formulation of Eq. 6.39 using 3 different ROMs and uniform in time distribution of the reactant material profile over one operation period.

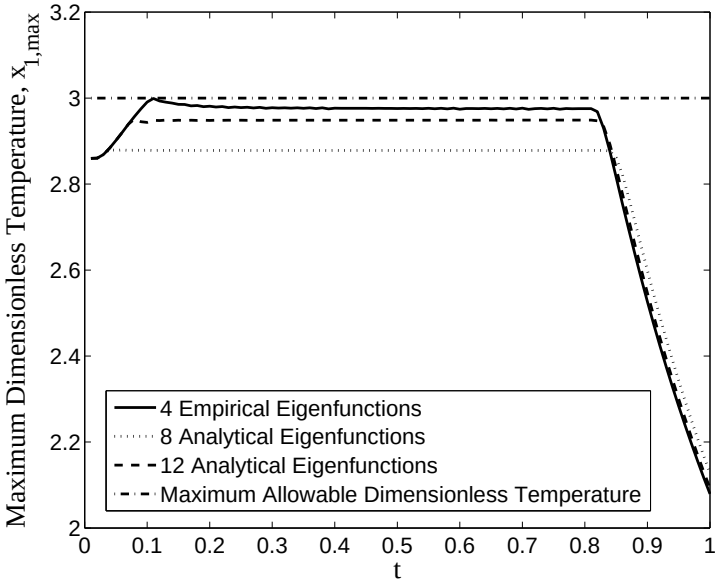

Figure 6.26: Maximum temperature x_1, profiles of the EMPC formulation of Eq. 6.39 using 3 different ROMs over one operation period.

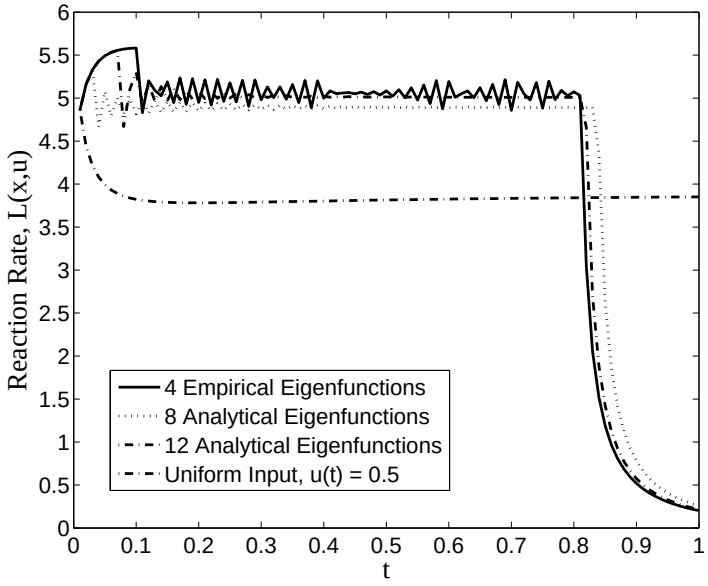

Figure 6.27: The integral of the reaction rate along the length of the reactor of the tubular reactor under the EMPC formulation of Eq. 6.39 using 3 different ROMs and under uniform in time distribution of the reactant material over one operation period.

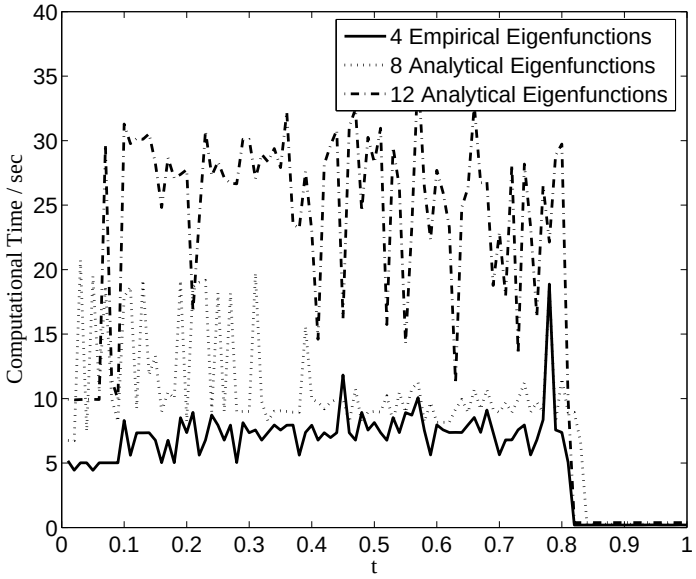

Figure 6.28: Computational time profiles of the EMPC formulation of Eq. 6.39 using 3 different ROMs over one operation period.

the reactor among the above 3 different ROMs and the case of the system under uniform in time distribution of the reactant material, i.e., $u(t) = 0.5$, as shown in Fig. 6.27. From Fig. 6.27, for the cases of 3 different ROMs, the average reaction rates under the EMPC significantly increase initially because of the second-order reaction rate dependence. The economic cost decrease since the reactant material fed to the reactor decreases to satisfy of the reactant material constraint. Over t_f, the total reaction rate from the system under the EMPC formulation from the ROM on the basis of 4 empirical eigenfunctions is 11.25% greater than that from the system under uniform in time distribution of the reactant material. The total economic cost of the ROM on the basis of 4 empirical eigenfunctions is 0.79% and 1.85% greater than that of the ROM on the basis of 8 and 12 analytical eigenfunctions, respectively. This can be explained from the point that the empirical eigenfunctions capture more information on the nonlinear terms and the input effect in the original model of PDEs which is not considered by the analytical eigenfunctions.

The comparison of the computational time corresponding to the EMPC systems based on the above 3 different ROMs is given in Fig. 6.28. The ROM based on 4 empirical eigenfunctions shows its advantage on the computational efficiency compared with the ROM based on both 8 and 12 analytical eigenfunctions.

Case 3: Low-order Output Feedback EMPC System With State and Input Constraints

In this set of simulations, a low-order output feedback EMPC system (Eq. 6.35) based on a ROM using empirical eigenfunctions is formulated and applied to the tubular reactor. The tubular reactor is initialized with $x(z,0)$ equal to the steady-state of the system under constant input value, $u(t) = 0.6$. For the reactor, the low-order output feedback EMPC system based on the ROM using 4 empirical eigenfunctions is compared with the low-order output feedback EMPC system based on 11 slow modes only (i.e., $m_1 = m_2 = 11$). Additionally, the reactor under uniform in time distribution of the reactant material over $t_f = 1.0$ is also considered for comparison purposes.

We compared the simulation results from the low-order output feedback EMPCs using the ROM based on 4 empirical eigenfunctions (i.e., $m_1 = m_2 = 4$) and ROMs based on 11 sinusoidal/cosinusoidal eigenfunctions, respectively. Figs. 6.29-6.30 show the closed-loop evolution of the states under the EMPC formulation of Eq. 6.35 from the ROM based on 4 empirical eigenfunctions. The manipulated input profiles for the above 2 different ROMs are given in Fig. 6.31. For the input profile of ROM based on 4 empirical eigenfunctions in Fig. 6.31 (solid line), the vibration is caused by the over-estimated maximum temperature by the ROM in EMPC, which is also seen in Fig. 6.32 (solid line). Different from the simulation results in Section 6.4.3, the EMPC using the ROM based on 4 empirical eigenfunctions have a higher amplitude of fluctuation on the input profile and also a much lower maximum temperature in the reactor. This difference results from the limited number of

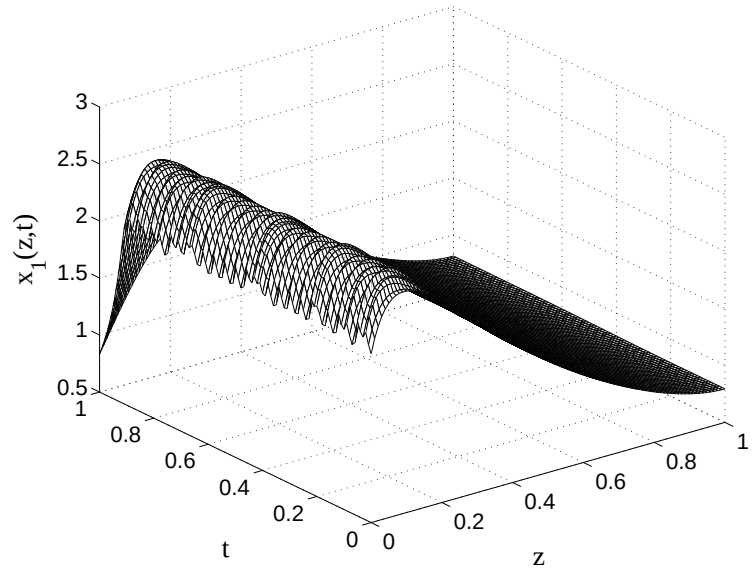

Figure 6.29: Closed-loop profile of x_1 of EMPC formulation of Eq. 6.35 using the ROM based on 4 empirical eigenfunctions over one operation period.

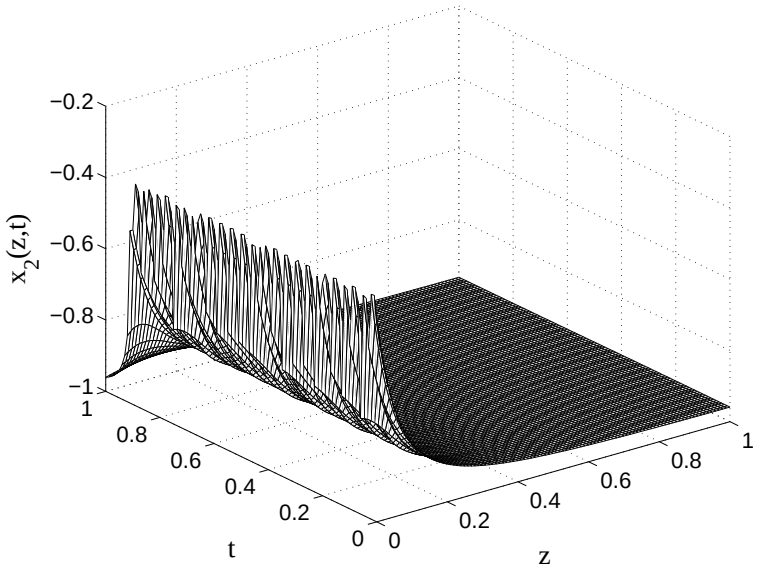

Figure 6.30: Closed-loop profile of x_2 of EMPC formulation of Eq. 6.35 using the ROM based on 4 empirical eigenfunctions over one operation period.

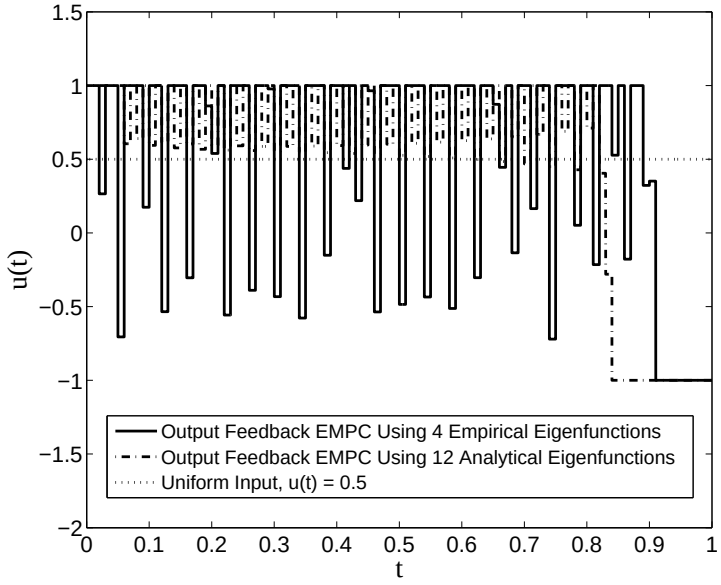

Figure 6.31: Manipulated input profiles of the EMPC formulation of Eq. 6.35 using the ROM based on 4 empirical eigenfunctions and the ROM based on 11 analytical eigenfunctions and uniform in time distribution of the reactant material profile over one operation period.

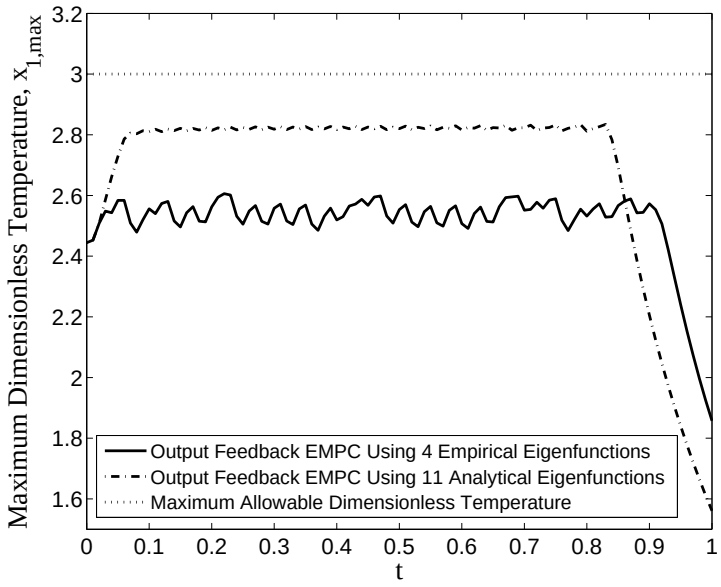

Figure 6.32: Maximum temperature x_1, profiles of the EMPC formulation of Eq. 6.35 using the ROM based on 4 empirical eigenfunctions and the ROM based on 11 analytical eigenfunctions and maximum allowable dimensionless temperature over one operation period.

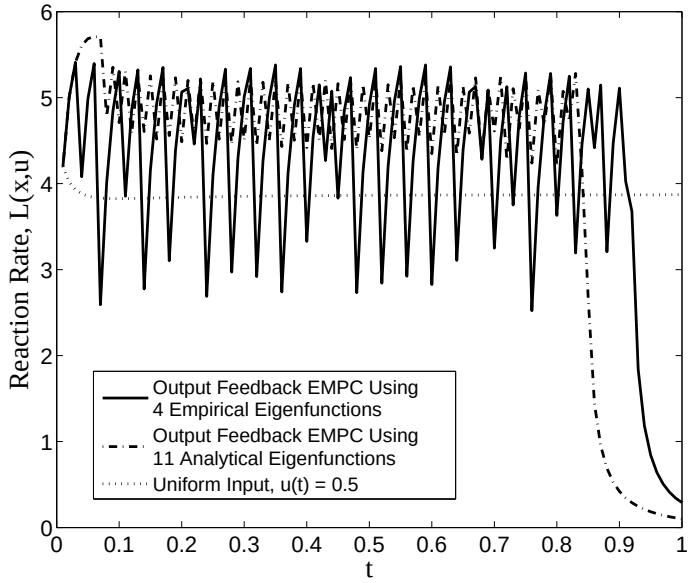

Figure 6.33: The integral of the reaction rate along the length of the tubular reactor under the EMPC formulation of Eq. 6.35 using the ROM based on 4 empirical eigenfunctions and the ROM based on 11 analytical eigenfunctions and uniform in time distribution of the reactant material profile over one operation period.

measurement points used with the EMPC using the ROM based on 4 empirical eigenfunctions (i.e., $p_1 = p_2 = m_1 = m_2 = 4$) compared to the EMPC using the ROM based on 11 analytical eigenfunctions (i.e., $p_1 = p_2 = m_1 = m_2 = 11$).

For this case study, we also compared the integral of the reaction rate along the length of the reactor among the above 2 different ROMs and the case of the system under uniform in time distribution of the reactant material, i.e., $u(t) = 0.5$, as shown in Fig. 6.33. From Fig. 6.33, the total reaction rate over t_f from the system under the EMPC formulation from the ROM on the basis of 4 empirical eigenfunctions is still 9.45% greater than that from the system under uniform in time distribution of the reactant material and meanwhile, 1.46% less than that of the ROM on the basis of 11 analytical eigenfunctions.

6.5 Conclusions

In this work, two types of EMPC systems for quasi-linear systems of PDEs were presented: (1) an output feedback EMPC system, and (2) an EMPC system formulated with a reduced-order model derived using empirical eigenfunctions as basis functions. The EMPC systems were applied to a tubular reactor of industrial importance. Through time-varying operation, the EMPC systems yielded improved closed-loop economic performance over steady-state operation. Additionally, constructing a ROM on the basis of historical data-based empirical eigenfunctions by applying Karhunen-Loève expansion demonstrated computational benefits over using analytical sinusoidal/cosinusoidal eigenfunctions as basis functions.

Chapter 7

Handling State Constraints and Economics in Feedback Control of Transport-Reaction Processes

7.1 Introduction

This chapter presents the development of an EMPC scheme with model reduction technology and a standard discretization method to deal with state estimation accuracy and computational efficiency. First, the APOD method is applied to parabolic systems of PDEs by considering process control system computational efficiency and some specific constraints imposed on the process (i.e., state and input constraints), and then a novel EMPC design integrating APOD method with a high-order finite-difference method is proposed to improve the EMPC scheme's performance on dealing with hard state constraint over the traditional EMPC scheme with APOD method only. The proposed EMPC method is applied to a non-isothermal tubular reactor where a second-order chemical reaction takes place and the computational efficiency, state and input constraint satisfaction, and closed-loop economic

performance are evaluated. These results are mainly based on Ref.[87]

7.2 Preliminaries

7.2.1 Parabolic PDEs

We consider parabolic PDEs of the form:

$$\frac{\partial x}{\partial t} = A\frac{\partial x}{\partial z} + B\frac{\partial^2 x}{\partial z^2} + Wu(t) + f(x) \tag{7.1}$$

with the boundary conditions:

$$\left.\frac{\partial x}{\partial z}\right|_{z=0} = g_0 x(0,t), \quad \left.\frac{\partial x}{\partial z}\right|_{z=1} = g_1 x(1,t) \tag{7.2}$$

for $t \in [0,\infty)$ and the initial condition:

$$x(z,0) = x_0(z) \tag{7.3}$$

where $z \in [0,1]$ is the spatial coordinate, $t \in [0,\infty)$ is the time, $x(z,t) = [x_1(z,t) \cdots x_{n_x}(z,t)]^T \in \mathbb{R}^{n_x}$ is the vector of the state variables (x^T denotes the transpose of x), and $f(x)$ denotes a nonlinear vector function. The notation A, B, W, g_0 and g_1 is used to denote (constant) matrices of appropriate dimensions. The control input vector is denoted as $u(t) \in \mathbb{R}^{n_u}$ and is subject to the following constraints:

$$u_{min} \leq u(t) \leq u_{max} \tag{7.4}$$

where u_{min} and u_{max} are the lower and upper bound vectors of the manipulated input vector, $u(t)$. Moreover, the system states are also subject to the following state constraints:

$$x_{i,min} \leq \int_0^1 r_{x_i}(z) x_i(z,t)\, dz \leq x_{i,max} \tag{7.5}$$

for $i = 1, \ldots, n_x$ where $x_{i,min}$ and $x_{i,max}$ are the lower and upper state constraint for the i-th state, respectively. The function $r_{x_i}(z) \in L_2(0,1)$ where $L_2(0,1)$ is the space of measurable square-integrable functions on the interval $[0,1]$, is the state constraint distribution function.

7.2.2 Galerkin's Method with POD-Computed Basis Functions

To reduce the model of PDEs of Eq. 7.1 into an model of ODEs, we take advantage of the orthogonality of the empirical eigenfunctions obtained from POD ([69, 127]). Specifically, using Galerkin's method ([27, 53]), a low-order ODE system for the PDEs of Eq. 7.1 describing the temporal evolution of the amplitudes corresponding to the first m_i eigenfunctions of the i-th partial differential equation state in Eq. 7.1 has the following form:

$$\begin{aligned} \dot{a}_s(t) &= \mathscr{A}_s a_s(t) + \mathscr{F}_s(a_s(t)) + \mathscr{W}_s u(t) \\ x_i(z,t) &\approx \sum_{j=1}^{m_i} a_s^{ij}(t)\phi_{ij}(z), \quad i = 1, \ldots, n_x \end{aligned} \tag{7.6}$$

where $a_s(t) = [a_{s,1}^T(t) \cdots a_{s,n_x}^T(t)]^T$ is a vector of the total eigenmodes, $a_{s,i}(t) = [a_s^{i1}(t) \cdots a_s^{im_i}(t)]^T$ is a vector of the amplitudes of the first m_i eigenfunctions, $a_s^{ij}(t)$ is the $j-th$ eigenmode of $i-th$ partial differential equation, $\mathscr{A}_s$ and $\mathscr{W}_s$ are constant matrices, $\mathscr{F}_s(a_s(t))$ is a nonlinear smooth vector function of the modes obtained by applying weighted residual method to Eq. 7.1, and $\{\phi_{ij}(z)\}_{j=1:m_i}$ are the first m_i dominant empirical eigenfunctions computed from POD for the i-th PDE state, $x_i(z,t)$.

7.3 EMPC of Systems of Parabolic PDEs with State and Control Constraints

7.3.1 Adaptive Proper Orthogonal Decomposition

Compared with POD, APOD is a more computationally efficient algorithm because it only needs an ensemble of a small number of snapshots in the beginning. It can complete the recursive update of the computation of the dominant eigenfunctions, while keeping the size of the ensemble small to reduce the computational burden of updating the ensemble once a new process state measurement is available. Moreover, APOD can also adaptively adjust the number of the basis eigenfunctions under a desired energy occupation requirement, η. Out of N possible eigenvalues from the covariance matrix of the ensemble, the most dominant m eigenvalues of the covariance matrix occupies η energy of the whole ensemble, i.e., $\sum_{j=1}^{m} \lambda_j / \sum_{j=1}^{N} \lambda_j \leq \eta$. Then, the computational efficiency of the control system whose construction is based on the ROM with the dominant eigenfunctions will be improved due to the adaptive property of APOD.[136] Since the basis eigenfunctions are updated on-line, the initial ensemble of process snapshots may contain significantly less process solution data than POD. More details of the APOD methodology can be found in[136] and.[115] The implementation steps of the APOD methodology can be summarized as follows:

1. At $t < 0$, generate an ensemble of solutions of the PDE system (e.g., Eq. 7.1) for single manipulated input value $u(t)$ from certain initial condition;

    1.1. Apply POD to this ensemble to derive a set of first $m_i(t_0)$ most dominant empirical eigenfunctions for each state $x_i, \quad i = 1, \ldots, n_x$ which occupy η energy of the chosen ensemble ;[6]

    1.2. Construct a ROM in the form of a low-dimensional nonlinear ODE system

based on these empirical eigenfunctions within a Galerkin's model reduction framework from the infinite dimensional nonlinear system of PDEs;

2. The ensemble (or basis eigenfunctions) is updated based on a constant update frequency with the update period, Δ (constant). In the context of EMPC, the update period, Δ, is equal to the sampling time in EMPC. For all k, repeat: at $t = t_k = k\Delta > 0$, when the new process state measurements are available, update the ensemble by utilizing the most important snapshots approach [115] which analyzes the contribution of the current snapshots in the ensemble and replaces the snapshot that corresponds to the lowest contribution of representativeness with new state measurement to keep the size of the ensemble;

   2.1. Recompute the dominant eigenvalues corresponding to the first $m_i(t_{k-1})$ eigenfunctions by constructing small scale matrix to reduce the computational burden;

   2.2. Adopt orthogonal power iteration methodology to get the $(m_i(t_{k-1})+1)-th$ dominant eigenvalue;

   2.3. Get the new size of the basis eigenfunctions, $m_i(t_k)$ which should still occupy η energy of the updated ensemble (the new size of the basis eigenfunctions, $m_i(t_k)$, may increase, decrease or keep the same compared with $m_i(t_{k-1})$);

7.3.2 Methodological Framework for Finite-Dimensional EMPC Using Adaptive Proper Orthogonal Decomposition

EMPC Using Adaptive POD

Utilizing the empirical eigenfunctions from APOD, we formulate a state feedback Lyapunov-based EMPC for the system of Eq. 7.1 to dynamically optimize an economic cost function.

We assume that the state profile across the entire spatial domain is available synchronously at sampling instants denoted as $t_k = k\Delta$ with $k = 0, 1, \ldots$. To formulate a finite-dimensional EMPC problem, the first m_i modes of Eq. 7.6 are adopted to construct the ROM, and the EMPC formulation takes the following form:

$$\max_{u \in S(\Delta)} \quad \int_{t_k}^{t_{k+N}} L_e(\tau)\, d\tau \tag{7.7a}$$

$$\text{s.t.} \quad \dot{a}_s(t) = \mathscr{A}_s a_s(t) + \mathscr{F}_s(a_s(t)) + \mathscr{W}_s u(t), \tag{7.7b}$$

$$a_s^{ij}(t_k) = \int_0^1 \phi_{ij}(z) x_i(z,t_k)\, dz,$$

$$\text{for } j = 1, \ldots, m_i \tag{7.7c}$$

$$\hat{x}_i(z,t) = \sum_{j=1}^{m_i} a_s^{ij}(t)\phi_{ij}(z), \tag{7.7d}$$

$$u_{min} \leq u(t) \leq u_{max}, \tag{7.7e}$$

$$x_{i,min} \leq \int_0^1 r_{x_i}(z)\hat{x}_i(z,t)\, dz \leq x_{i,max}, \tag{7.7f}$$

$$a_s^T(t) P a_s(t) \leq \bar{\rho} \tag{7.7g}$$

where the constraints are enforced for all $t \in [t_k, t_{k+N})$ and $i = 1, \ldots, n_x$, Δ is the sampling period, $S(\Delta)$ is the family of piecewise constant functions with sampling period Δ, N is the prediction horizon, $\hat{x}_i(z,t)$ is the predicted evolution of state variables with input $u(t)$ computed by the EMPC and $x_i(z,t_k)$ is the state measurement at the sampling time t_k. Since the empirical eigenfunctions derived from the APOD procedure are all self-adjoint, i.e., $\{\bar{\phi}_{ij}(z)\} = \{\phi_{ij}(z)\}$ (more details can be found in[69,127]), we can use the empirical eigenfunction $\{\phi_{ij}(z)\}$ directly to calculate the estimated eigenmode amplitude $a_s^{ij}(t_k)$ by taking advantage of the orthogonality property of the eigenfunctions in Eq. 7.7c.

In the optimization problem of Eq. 7.7, the objective function of Eq. 7.7a describes the temporal economic cost of the process which the EMPC maximizes over a horizon $N\Delta$.

The constraint of Eq. 7.7b is used to predict the future evolution of the subsystem based on the first m_i dominant eigenfunctions with the initial condition given in Eq. 7.7c (i.e., the estimate of $a_s^{ij}(t_k)$ computed from the state measurement $x_i(z,t_k)$). The constraints of Eq. 7.7e-7.7f are the available control action and the state constraints, respectively. Finally, the constraint of Eq. 7.7g ensures that the predicted state trajectory is restricted inside a predefined stability region, $\bar{\rho}$ which is a level set of a quadratic Lyapunov function $V(a_s) = a_s^T P a_s$ where P is a positive definite matrix (see[65] for a complete discussion of this issue). The optimal solution to this optimization problem is $u^*(t|t_k)$ defined for $t \in [t_k, t_{k+N})$. The EMPC applies the control action computed for the first sampling period to the system in a sample-and-hold fashion for $t \in [t_k, t_{k+1})$. The EMPC is resolved at each sampling period, t_{k+1}, after receiving a new state measurement of each state, $x_i(z,t_{k+1})$ and updated basis functions, $\{\phi_{ij}(z)\}$ from APOD.

EMPC Scheme of Integrating APOD and Finite-Difference Method to Avoid State Constraint Violation and Improve Computational Efficiency

Although APOD only needs an ensemble of a small number of snapshots which can improve the computational efficiency of the eigenfunction update calculation, smaller size of ensemble usually results in a single or a few dominant eigenfunctions. The accuracy of the ROM based on fewer eigenfunctions computed from an ensemble of small size is usually worse than that of the ROM constructed by adopting more eigenfunctions from a large ensemble of snapshots. However, as pointed out in,[114] eigenfunctions that have high frequency spatial profiles (corresponding to small empirical eigenvalues) should be discarded because of potentially significant round-off errors. In this situation, only a single or a few eigenfunctions can be adopted from APOD keeping the dimension of the reduced-order model low. So there exists the trade-off between the ROM accuracy and computational efficiency of APOD in practical implementation. Moreover, under a dynamic operation of

a process, the state error between the estimated state value from ROM and the actual state value cannot be predicted (i.e., it is almost impossible to predict whether the estimated state value will be an overestimate or an underestimate of the actual state value). From the point of view of practical implementation, when the process faces some specific state constraints, a controller which is constructed based on the ROM may produce an input trajectory misleading the process to violate state constraints.

To circumvent this problem, we propose an EMPC methodology to avoid potential state constraint violation. The methodology integrating APOD and a high-order finite-difference method in EMPC is designed to improve the computational efficiency compared to using EMPC with a model constructed from a high-order finite-difference method only. Before a detailed algorithm of the methodology can be presented, we define the following notation which will be used in the algorithm. To ensure that the state constraint is satisfied, we will make use of the following two inequalities to define a so-called alert region:

$$\int_0^1 r_{x,i}(z)x_i(z,t)\,dz \geq x_{i,max}^{alert}, \tag{7.8a}$$

$$\int_0^1 r_{x,i}(z)x_i(z,t)\,dz \leq x_{i,min}^{alert} \tag{7.8b}$$

where $x_{i,max}^{alert} < x_{i,max}$ and $x_{i,min}^{alert} > x_{i,min}$ are tuning parameters chosen to ensure that the state constraints are always satisfied under the EMPC methodology described below. With abuse of notation, we use $x_i(z,t) \in \Omega_i$ to denote the fact that one of the inequalities of Eq. 7.8 is satisfied for the state profile of the i-th partial differential equation state, and we use $x_i(z,t) \notin \Omega_i$ to denote that neither inequalities are satisfied. Also, Ω_i is referred to as the i-th state constraint alert region. The abbreviation EMPC-FD will denote an EMPC scheme formulated with a model from a high-order finite-difference method, while EMPC-APOD will be used to denote an EMPC with a model resulting from APOD. The corresponding input trajectory from each EMPC will be denoted as $u_{FD}(t|t_k)$ and $u_{APOD}(t|t_k)$, respectively.

The algorithm is initialized with POD, that is an ensemble of solutions of the system of PDEs of Eq. 7.1 are collected, m_i is derived by applying standard POD method to the initial ensemble for each state, and an EMPC with a model generated through POD computes the control action for the first sampling period (i.e., from $t = 0$ to $t = \Delta$). The control action applied to the system over the first sampling period is denoted as $u^*(t_0) = u_{POD}(t_0|t_0)$ and $k = 0$.

Considering that the APOD procedure (i.e., updating the empirical eigenfunctions) is computationally expensive especially when the size of the ensemble is large, the state measurement value $x(z,t_k)$ is adopted to update the basis eigenfunctions by APOD procedure for ROM construction at $t = t_{k+1}$ which is completed during the sampling time between $t = t_k$ and $t = t_{k+1}$. In other words, the APOD update is performed over the sampling period t_k to t_{k+1} in parallel to the EMPC calculation that is done at a sampling instance t_k. The detailed steps of EMPC system flow chart which integrates the APOD methodology with a finite-difference method are explained as follows:

Basis Update Procedure

1. At t_k, obtain a measurement of the state profile, go to Step 2.

2. Use the state profile measurement $x(z,t_k)$ to complete the APOD procedure and compute the number of the basis eigenfunctions for the next sampling period, $m(t_{k+1})$ where $m(t_{k+1}) = [m_1(t_{k+1}) \cdots m_{n_x}(t_{k+1})]^T$ is a vector containing the number of basis eigenfunctions for each partial differential equation state; go to Step 3.

3. If $u^*(t_k) = u_{FD}(t_k)$, go to Step 4; otherwise, go to Step 5.

4. Enforce the number of the basis eigenfunctions to be increased by 1 for the i-th partial differential equation state (each): $m_i(t_{k+1}) = m_i(t_{k+1}) + 1$ (increase the ROM accuracy by using more eigenfunctions since the process enters into the state constraint

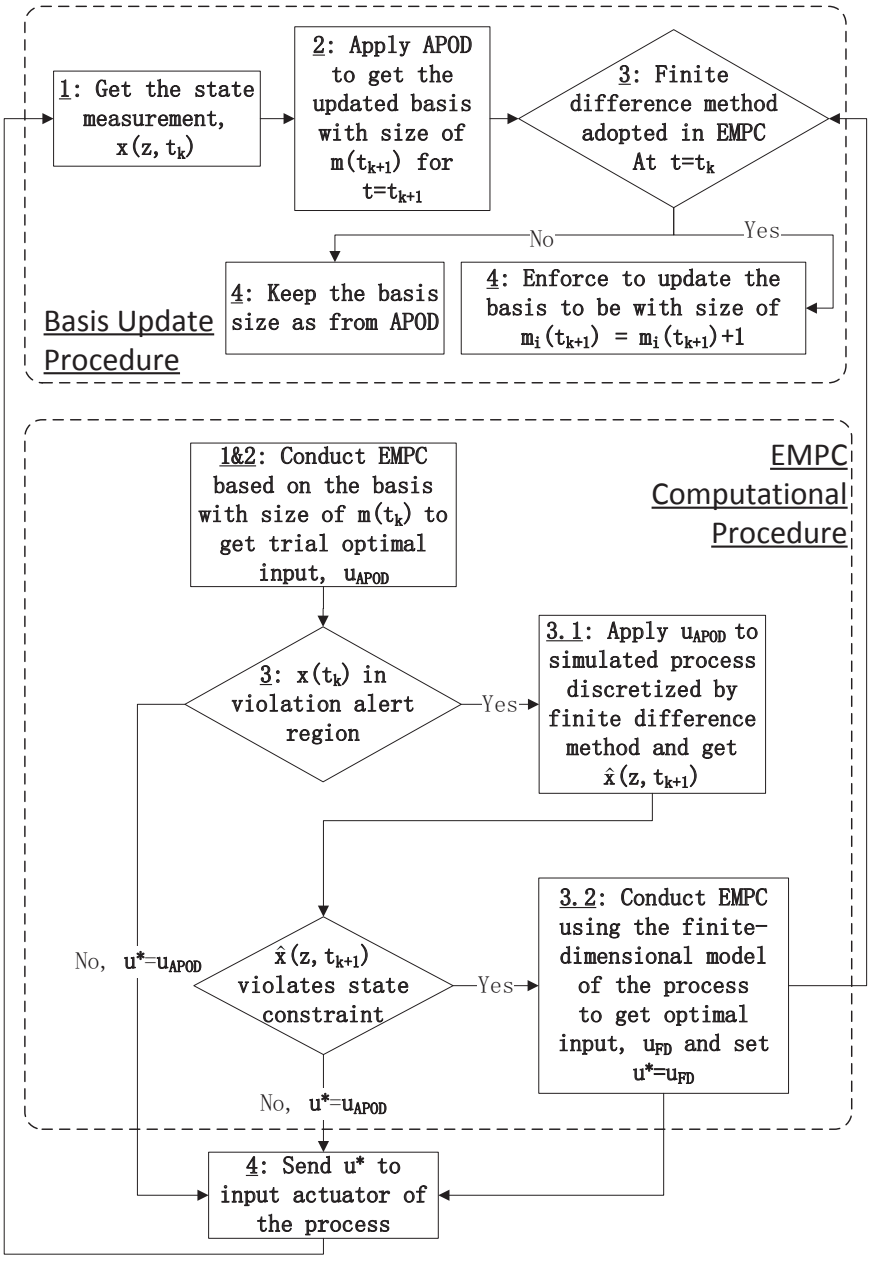

Figure 7.1: EMPC system flow chart which integrates the APOD methodology with a finite-difference method to increase the computational efficiency and avoid potential state constraint violation.

alert region) and update the basis eigenfunctions for the i-th partial differential equation state; go to Step 5.

5. $k \leftarrow k+1$; go to Step 1.

EMPC Computational Procedure

1. Obtain a measurement of the state profile at t_k; go to Step 2.

2. Solve the EMPC-APOD problem using the updated basis eigenfunctions with the size of $m(t_k)$ and get the trial input trajectory, $u_{APOD}(t|t_k)$; go to Step 3.

3. If $x_i(z,t_k) \in \Omega_i$, go to Step 3.1. Else, set the actual optimal input trajectory, $u^*(t_k) = u_{APOD}(t_k|t_k)$; go to Step 4.

   3.1. Apply the trial optimal input trajectory u_{APOD} to the finite-difference model and compute the predicted state at the next sampling time instant, $\hat{x}(z,t_{k+1})$. If $\hat{x}_i(z,t_{k+1})$ violates the state constraints, go to Step 3.2. Else, $u^*(t_k) = u_{APOD}(t_k|t_k)$ and go to Step 4.

   3.2 Solve the EMPC-FD problem to compute new trial input trajectory, $u_{FD}(t|t_k)$, and set $u^*(t_k) = u_{FD}(t_k|t_k)$; go to Step 4.

4. Apply the optimal control action $u^*(t_k)$ over the sampling period from $t = t_k$ to $t = t_{k+1}$ and $k \leftarrow k+1$; go to Step 1.

Fig. 7.1 illustrates the designed EMPC system flow chart for increasing the computational efficiency and avoiding potential state constraint violation. With respect to the APOD update cycle length, the availability of the full state profile across the entire spatial domain is assumed at each sampling instance (i.e., $t = t_k = k\Delta$) and the update cycle of APOD is equal to the sampling time of EMPC, Δ. Based on the proposed methodology, the

computational time of APOD procedure (Steps 2 and 3 noted as "Basis Update Procedure" in the Fig. 7.1) is not accounted for in the total EMPC calculation time (Steps 3.1 and 3.2 noted as "EMPC Computational Procedure" in the Fig. 7.1).

Remark 7.1 *We note here that in practice, the sampling time length Δ should be longer than the time needed to complete the APOD procedure otherwise the EMPC system will not be able to get the updated basis eigenfunctions at the new sampling time instant $t = t_{k+1}$. On the other hand, since the state measurements are available only at every Δ, large Δ may result in APOD missing the appearance of new process dynamics when the process goes through different regions in the state-space. Based on this consideration, the sampling should be chosen properly.*

Remark 7.2 *By setting the state constraint alert region of state constraint, the EMPC based on the ROM from APOD or POD method with few modes may lead to state constraint violation. However, the EMPC system based on a high-order discretization of the system of PDEs by finite-difference method can provide more accurate optimal manipulated input values to avoid potential state constraint violation.*

Remark 7.3 *In terms of the effectiveness of eigenfunctions, eigenfunctions that have high frequency spatial profiles (i.e., corresponding to small eigenvalues) should be discarded because of potentially significant round-off errors. When implementing the proposed methodology, the eigenfunctions corresponding to eigenvalues smaller than λ_{min} are not included to avoid round-off errors. This consideration is implemented in Steps* 1 *and* 2.1 *of Fig. 7.1. Furthermore, one may set the maximum number of basis functions used in APOD to avoid using eigenfunctions with high frequency spatial profiles.*

Remark 7.4 *Since the energy occupation percentage η has no direct relationship with the state prediction accuracy, to ensure the state constraint satisfaction during the whole*

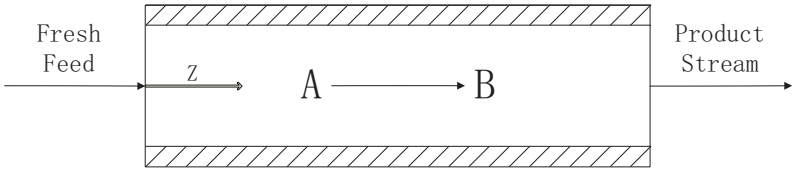

Figure 7.2: A tubular reactor with reaction $A \rightarrow B$.

process operation, the state violation alert region Ω_i should be large enough for a specific energy occupation requirement. For the process state outside the chosen state violation alert region Ω_i, the EMPC using APOD only is assumed to not lead the process to violate the state constraint under its ROM's accuracy.

7.4 Application to a Tubular Reactor Modeled by a System of Parabolic PDEs

7.4.1 Reactor Description

We consider a tubular reactor, where an exothermic, irreversible second-order reaction of the form $A \rightarrow B$ takes place as displayed in Fig. 7.2. A cooling jacket of constant temperature is used to remove heat from the reactor. The states of the tubular reactor are temperature and concentration of reactant species A in the reactor, and the input is the inlet concentration of the reactant species A. In order to simplify the presentation of our results below, we use dimensionless variables and obtain the following nonlinear model of

parabolic PDEs for the process (details and model notation can be found in[85] and[119]):

$$\begin{aligned}
\frac{\partial x_1}{\partial t} &= -\frac{\partial x_1}{\partial z} + \frac{1}{Pe_1}\frac{\partial^2 x_1}{\partial z^2} + \beta_T(T_s - x_1) \\
&\quad + B_T B_C \exp\left(\frac{\gamma x_1}{1+x_1}\right)(1+x_2)^2 + \delta(z-0)T_i \\
\frac{\partial x_2}{\partial t} &= -\frac{\partial x_2}{\partial z} + \frac{1}{Pe_2}\frac{\partial^2 x_2}{\partial z^2} \\
&\quad - B_C \exp\left(\frac{\gamma x_1}{1+x_1}\right)(1+x_2)^2 + \delta(z-0)u
\end{aligned} \tag{7.9}$$

where δ is the standard Dirac function, subject to the following boundary conditions:

$$\begin{aligned}
z = 0 \quad &: \quad \frac{\partial x_1}{\partial z} = Pe_1 x_1, \ \frac{\partial x_2}{\partial z} = Pe_2 x_2; \\
z = 1 \quad &: \quad \frac{\partial x_1}{\partial z} = 0, \ \frac{\partial x_2}{\partial z} = 0;
\end{aligned} \tag{7.10}$$

The following typical values are given to the process parameters: $Pe_1 = 7$, $Pe_2 = 7$, $B_T = 2.5$, $B_C = 0.1$, $\beta_T = 2$, $T_s = 0$, $T_i = 0$ and $\gamma = 10$. The following simulations were carried out using Java programming language in a Intel Core $i7, 3.40\ GHz$ computer with a 64-bit Windows 7 Professional operating system.

7.4.2 Implementation of EMPC with Adaptive Proper Orthogonal Decomposition

We formulate an EMPC system like that of Eq. 7.7 for the tubular reactor with the ROM derived from the procedure described above. Ipopt[139] was used to solve the EMPC optimization problem. To numerically integrate the ODE model, explicit Euler's method was used with an integration step of 1×10^{-5} (dimensionless). Central finite-difference method was adopted to discretize, in space, the two parabolic PDEs and obtain a set of 101 ODEs in

time for each partial differential equation state (further increase on the order of discretization led to identical open-loop and closed-loop simulation results); this discretized model was also used to describe the process dynamics. In the first case studies reported below, with respect to EMPC settings, we used a prediction horizon, $N = 3$ and sampling time length, $\Delta = 0.01$ (dimensionless) which can sufficiently capture the appearance of new patterns by the newly available snapshots as the process moves through different regions in the state-space.

The cost function of Eq. 7.7 considered involves maximizing the overall reaction rate along the length of the reactor in the prediction horizon, t_k to t_{k+N} and over one operation period with $t_f = 1$. The temporal economic cost along the length of the reactor then takes the form:

$$L_e(t) = \int_0^1 r(z,t)dz \tag{7.11}$$

where $r(x_1(z,t),x_2(z,t)) = B_C \exp\left(\frac{\gamma x_1(z,t)}{1+x_1(z,t)}\right)(1+x_2(z,t))^2$ is the reaction rate (dimensionless) in the tubular reactor.

The control input is subject to constraints as follows: $-1 \leq u \leq 1$. Owing to practical considerations, the amount of reactant material which can be fed to the tubular reactor over the period t_f is fixed. Specifically, $u(t)$ satisfies the following constraint over the period:

$$\frac{1}{t_f}\int_0^{t_f} u(\tau)d\tau = 0.5 \tag{7.12}$$

which will be referred to as the reactant material constraint. Details on the implementation of this constraint can by found in[85] and.[84] Furthermore, the temperature (dimensionless) along the length of the reactor is subject to the following constraint:

$$x_{1,\min} \leq \min(x_1(z,t)), \quad \max(x_1(z,t)) \leq x_{1,\max} \tag{7.13}$$

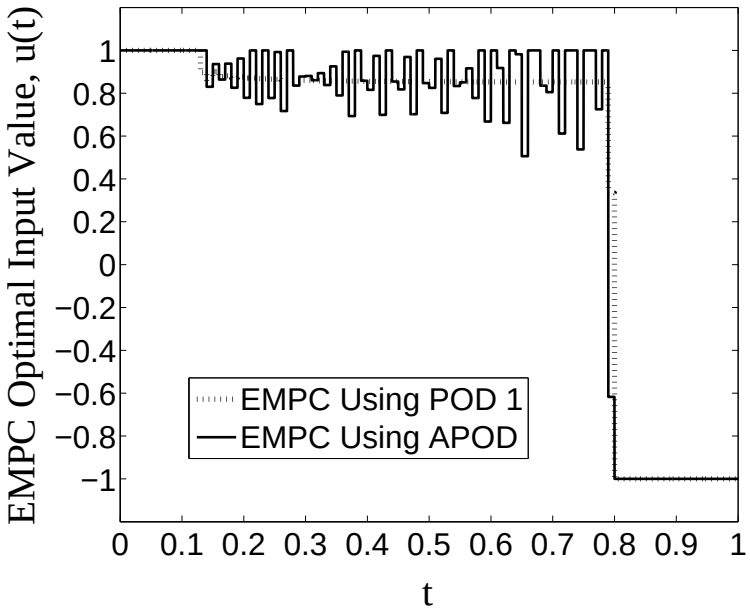

Figure 7.3: Manipulated input profiles of the EMPC system of Eq. 7.7 based on POD 1 (dotted line) and APOD using Ensemble 1 (solid line) over one operation period.

where $x_{1,\min} = -1$ and $x_{1,\max} = 3$ are the lower and upper limits, respectively.

To design the Lyapunov-based EMPC, a quadratic Lyapunov function of the following form was adopted for the constraint of Eq. 7.7g:

$$V(a_s(t)) = a_s^T(t) P a_s(t) \tag{7.14}$$

where P is an identity matrix of approximate dimension and $\bar{\rho} = 3$ (see[65] for more details on Lyapunov-based EMPC).

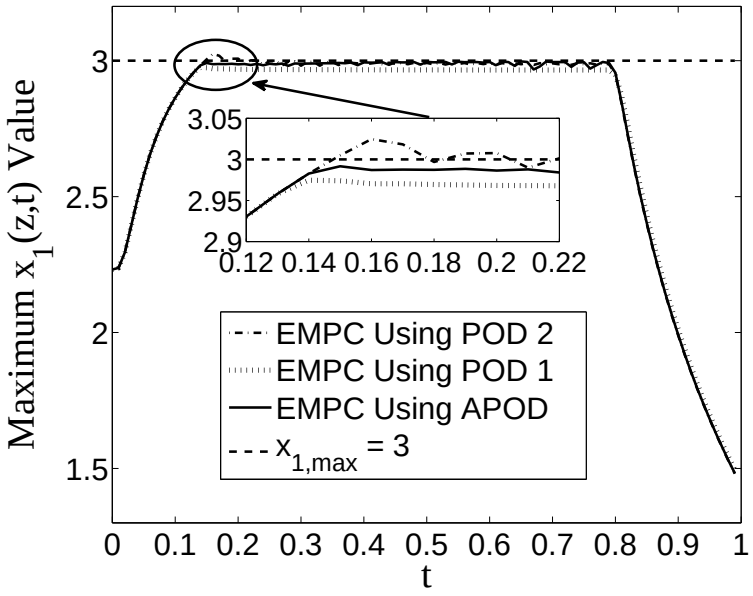

Figure 7.4: Maximum $x_1(z,t)$ profiles of the process under the EMPC system of Eq. 7.7 based on POD 1 (dotted line), POD 2 (dash-dotted line)and APOD using Ensemble 1 (solid line) over one operation period.

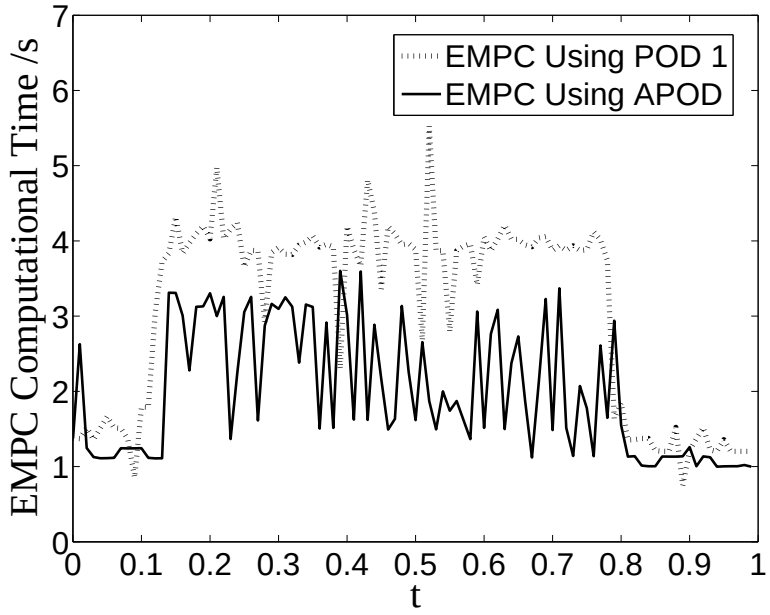

Figure 7.5: EMPC computational time profiles for the EMPC system of Eq. 7.7 based on POD 1 (dotted line) and APOD using Ensemble 1 (solid line) over one operation period.

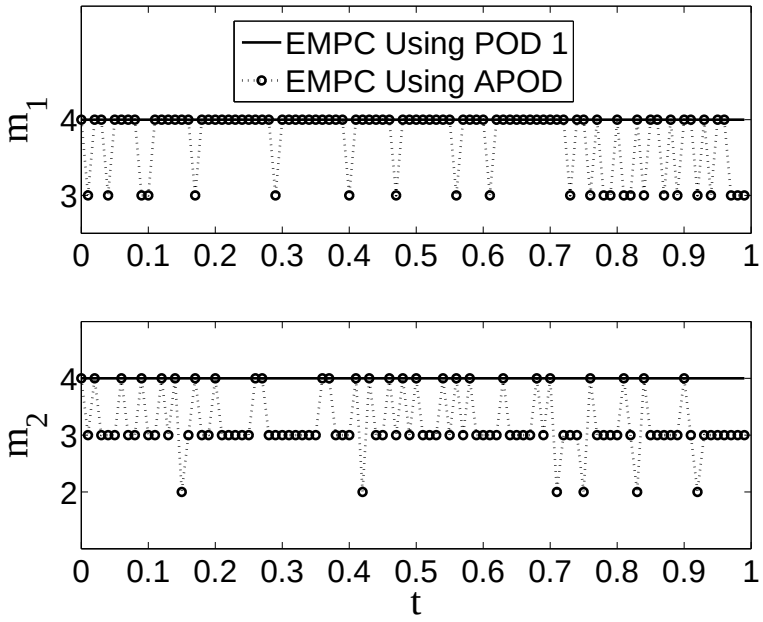

Figure 7.6: Numbers of dominant eigenfunctions based on POD 1 (solid line) and APOD using Ensemble 2 (dotted line with circles) over one operation period.

7.4.3 Simulation Study

Case 1: APOD Compared to POD

This case study is introduced to demonstrate the effectiveness of the APOD method to capture process dynamic information (i.e., accurate reduced order model) when compared with the traditional POD method; this comparison is conducted under the assumption that both APOD and POD method are applied to a large snapshot ensemble.

To compute the empirical eigenfunctions, we use the set of 101 ODEs of each partial differential equation in Eq. 7.9 (i.e., 101 discretized points). In detail, 15 different initial conditions and arbitrary (constant) input values, $u(t)$ were applied to the process model to get the spatiotemporal solution profiles with a time length of 2 (dimensionless). Consequently, from each simulation solution profile, 200 uniformly sampled snapshots were taken and combined to generate an ensemble of 3000 solutions which is noted as Ensem-

ble 1. The POD method was applied to the developed ensemble of solutions to compute empirical eigenfunctions that describe the dominant spatial solution patterns embedded in the ensemble where the Jacobian in the POD method is calculated through a central finite-difference method. After truncating the eigenfunctions with relatively small eigenvalues ($\lambda_{ij} < \lambda_{min} = 1 \times 10^{-5}$), we were left with the first 4 eigenvalues for each state which occupy more than 99.99% (i.e., $\eta = 99.99\%$) of the total energy included in the entire ensemble. These 4 eigenfunctions for each partial differential equation state are utilized for the POD method and as the initial eigenfunctions for APOD method to construct the ROM. To demonstrate the ability of APOD to capture the dominant trends that appear during closed-loop process evolution as the process goes through different regions of the state-space, we use EMPC of Eq. 7.7 based on POD using Ensemble 1 and based on APOD using Ensemble 1 (as the starting ensemble) to the tubular reactor, respectively. For the POD method, we constructed 2 ROMs which use the first 3 and 4 dominant eigenfunctions of the previously constructed eigenfunctions, respectively, for the EMPC system of Eq. 7.7. The EMPC utilizing ROM with 4 eigenfunctions is denoted as EMPC based on POD 1 and the other is denoted as EMPC based on POD 2.

The maximum temperature (dimensionless) profiles of the tubular reactor under the EMPC systems of Eq. 7.7 based on POD 1, POD 2 and APOD using Ensemble 1 are shown in Fig. 7.4. Since the temperature directly influences the reaction rate (i.e., higher temperature leads to higher reaction rate), the optimal operating strategy is to operate the reactor at the maximum allowable temperature. From Fig. 7.4, the EMPC system based on POD 1 and APOD operate the tubular reactor with a maximum temperature less than the maximum allowable which is a consequence of the error associated with the ROM. However, the process under the EMPC system based on POD 2 violates the state constraint imposed on $x_1(z,t)$ due to fewer eigenfunctions used for constructing the ROM in the EMPC system of Eq. 7.7. On the other hand, since the APOD is able to more accurately compute the

state profile owing to its continuously updated dominant eigenfunctions, the EMPC system formulated with the ROM using APOD eigenfunctions operates the reactor at a greater temperature than the other EMPC system as demonstrated by the magnified plot in Fig. 7.4.

The computed manipulated input profiles from the EMPC systems of Eq. 7.7 based on POD 1 and APOD using Ensemble 1, respectively, over one period are shown in Fig. 7.3. From Fig. 7.3, the EMPC system based on APOD computes a less smooth manipulated input profile than that of the EMPC system based on POD 1 due to its continuously updated dominant eigenfunctions so that new process dynamics information is included in the dominant eigenfunctions. These updated dominant eigenfunctions improved the ROM which may be different from the previous ones when compared with the dominant eigenfunctions POD 1 used which are kept the same during the whole operation period. Due to more accurate ROMs produced by APOD method, over one period $t_f = 1$, the total reaction rate of the process of Eq. 7.11 under the EMPC system based on APOD is 1.18% greater than that of the EMPC system based on POD 1.

Here, we have compared the EMPC calculation time for the EMPC systems of Eq. 7.7 based on POD 1 and APOD using Ensemble 1. As displayed in Fig. 7.5, the EMPC based on APOD achieves 38.8% improvement on the average computational time compared with that of the EMPC based on POD 1. As shown in Fig. 7.6, the APOD can adaptively adjust the required minimum number of eigenfunctions to satisfy the energy occupation requirement for each state while the number of the eigenfunctions utilized by the POD 1 is fixed at $m_1 = m_2 = 4$. ROM using $m_1 = m_2 = 4$ of eigenfunctions increases the computational burden to the EMPC optimization problem based on POD 1 since the size of the dynamic model of Eq. 7.7b is higher when compared with EMPC using APOD method. In terms of computational time of the recursive APOD procedure for updating basis eigenfunctions, it requires 45.2 s on the average for the case of EMPC based on APOD using Ensemble 1. We note here that the APOD is completed before the EMPC problem is solved at $t = t_k$

($k = 0,\ 1,\ \ldots$) which follows the methodology we proposed in Fig. 7.1. Therefore, for the EMPC calculation time in Fig. 7.5, the time of completing the APOD procedure is not included.

Case 2: APOD with An Ensemble of Small Size

As we pointed out in Case 1, although the EMPC system based on APOD scheme using Ensemble 1 yields high state-approximation accuracy of the resulting ROM and of the process economic performance owing to the fact that the APOD continuously updates the dominant eigenfunctions, the APOD procedure and EMPC calculation is more computationally expensive when compared with that of the EMPC system based on a set of 101 ODEs for each partial differential equation state. The computational efficiency difference is mainly caused by the number of the eigenfunctions adopted for constructing the ROM of the system of PDEs. Below, we construct the EMPC scheme using the APOD method with a small snapshot ensemble and demonstrate its advantage on computational efficiency and ability to on-line capture dynamic process information.

Based on the above consideration, in this case, we reduce the size of the ensemble by adopting an ensemble of 125 snapshots denoted as Ensemble 2 and apply Ensemble 2 to the APOD procedure for EMPC system of Eq. 7.7. The required energy occupation is still the same ($\eta = 99.99\%$). Moreover, from the practical point of applying the APOD to the process, the APOD procedure is completed by using the full state profile at $t = t_{k-1}$ for the dominant eigenfunctions at $t = t_k$ as we show in Fig. 7.1 which means the APOD can be completed during the sampling time. In detail, as long as we update the APOD during the sampling time, using the state value at the previous sampling time, $x(t_{k-1})$, we can complete the APOD update and this computational time has no effect on the EMPC computational efficiency. The computed manipulated input profiles from the EMPC systems of Eq. 7.11 based on APOD using Ensemble 1 and APOD using Ensemble 2, respectively,

over one period are compared in Fig. 7.7. From Fig. 7.7, the EMPC system based on APOD using Ensemble 2 computes a less smooth manipulated input profile than that of the EMPC system based on APOD using Ensemble 1 due to the fact that fewer snapshots are used to get the dominant eigenfunctions. In terms of the process economic cost of Eq. 7.11, over one period $t_f = 1$, the total reaction rate of the process under the EMPC system based on APOD using Ensemble 2 is only 0.83% smaller than that of EMPC system based on APOD using Ensemble 1 and 1.74% smaller than that of the EMPC system based on the set of 101 ODEs for each partial differential equation state.

We have compared the EMPC calculation time for the above EMPC system based on APOD using Ensemble 1, APOD using Ensemble 2, and a model of a set of 101 ODEs for each partial differential equation state in Fig. 7.8. As displayed in Fig. 7.8, the EMPC calculation time for the EMPC system based on APOD using Ensemble 2 is less than compared with that of the the EMPC system based on APOD using Ensemble 1. The computational time of EMPC system based on Ensemble 2 is 12.5% less than that of the EMPC system based on model of a set of 101 ODEs for each partial differential equation state. This computational efficiency improvement of EMPC system based on APOD using Ensemble 2 comes from the fact that fewer number of dominant eigenfunctions are adopted for constructing the ROM as compared in Fig. 7.9. We set a 99.99% energy occupation requirement for the APOD using Ensemble 1 and the corresponding number of eigenfunctions for each state is kept at $m_i = 4,\ i = 1,2$ over one operation period; while for the EMPC based on the APOD using Ensemble 2, the corresponding number of eigenfunctions for each state adaptively changes as different process dynamics are collected and integrated into the dominant eigenfunctions. Moreover, the APOD using Ensemble 2 which has a much smaller size of ensemble also decreases the computational time of the APOD update procedure to 0.24 s.

Since Ensemble 2 with a size of 125 snapshots only reflects part of process dynamics, it

may not contain enough process dynamic behavior to guarantee the accuracy of the ROM of the system of PDEs. Especially, when there exists a specific state constraint, the ROM may not be a good approximation of the original system of PDEs to help the EMPC avoid the state constraint violation due to its poor or incomplete state representation. In other words, the ROM either from POD or APOD may overestimate or underestimate the state value of Eq. 7.7b in the EMPC optimization problem of Eq. 7.7. For the state constraint in this case, when the ROM underestimates the state value of $\hat{x}_1(t)$, it may mislead the EMPC to compute and implement a higher optimal input value to the actual process which may result in the state constraint violation on $x_1(t)$ due to the second-order exothermic reaction rate. Here, we constructed another ensemble of 125 snapshots from different process solutions which is noted as Ensemble 3. We constructed EMPC systems using both of these 2 ensembles and applied them to the process. The maximum temperature (dimensionless) profiles of the tubular reactor under the EMPC systems of Eq. 7.7 based on APOD using Ensemble 2 and APOD using Ensemble 3 are shown in Fig. 7.10. From Fig. 7.10, the EMPC system based on APOD using Ensemble 2 operates the process around the maximum allowable temperature but at some points, it is close to the state constraint. While, from the magnified plot of Fig. 7.10, the EMPC system based on APOD using Ensemble 3 violates the state constraint around $t = 0.51$.

Remark 7.5 *The number of snapshots affects not only the computational burden but also the state constraint satisfaction. A large size of ensemble usually results in more dominant eigenfunctions and at the same time, it increases the EMPC and APOD computational time; but more eigenfunctions can improve the ROM accuracy and help the EMPC system to avoid the state constraint violation. Therefore, the choice of the number of snapshots (i.e., the number of the dominant eigenfunctions) is a tradeoff between the computational efficiency and reduced order model accuracy.*

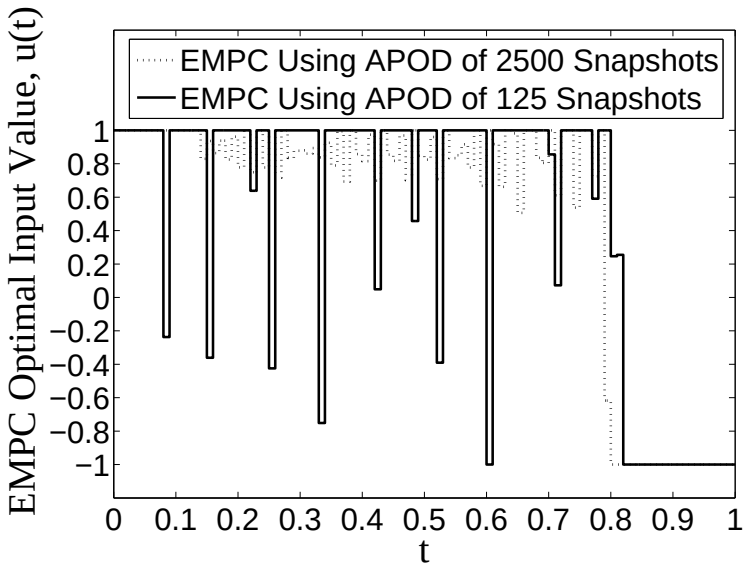

Figure 7.7: Manipulated input profiles of the EMPC systems of Eq. 7.7 based on APOD using Ensemble 1 (dotted line) and on APOD (solid line) using Ensemble 2 over one operation period.

1. *For POD method, the ensemble must have enough snapshots which contain as much global process dynamics as possible to help the EMPC system predict the state value more accurately. Since POD is only conducted once, it has no effect on the EMPC computational burden which only depends on how many modes/energy occupation is required.*

2. *For APOD method, the number of snapshots depends on the model accuracy although the ROM can be updated during the closed-loop operation. More snapshots will increase the APOD computational burden. But it will help the system avoid the state constraint violation. As long as the APOD update time is less than the sampling time size, we can use as many snapshots as possible, but large number of snapshots usually decreases the computational efficiency of the EMPC system.*

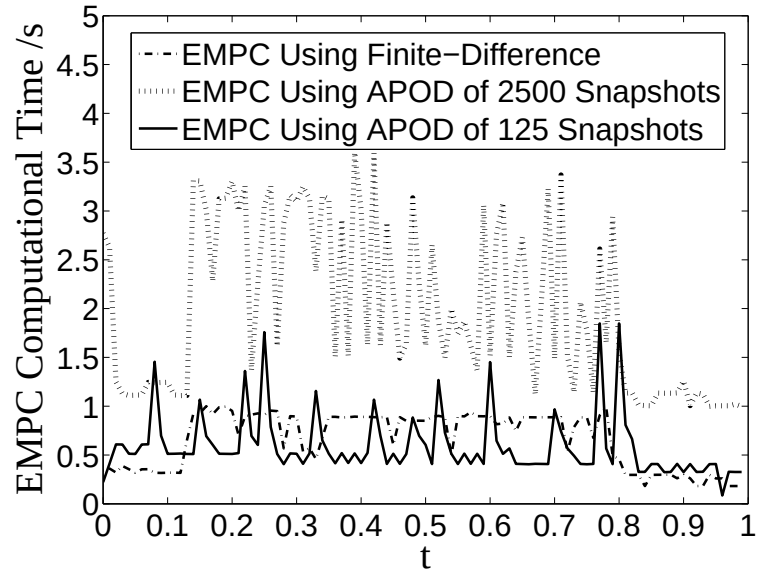

Figure 7.8: EMPC calculation time profiles of the process under the EMPC systems of Eq. 7.7 based on APOD using Ensemble 1 (dotted line), on APOD using Ensemble 2 (solid line), and a set of 101 ODEs for each partial differential equation state (dash-dotted line) over one operation period.

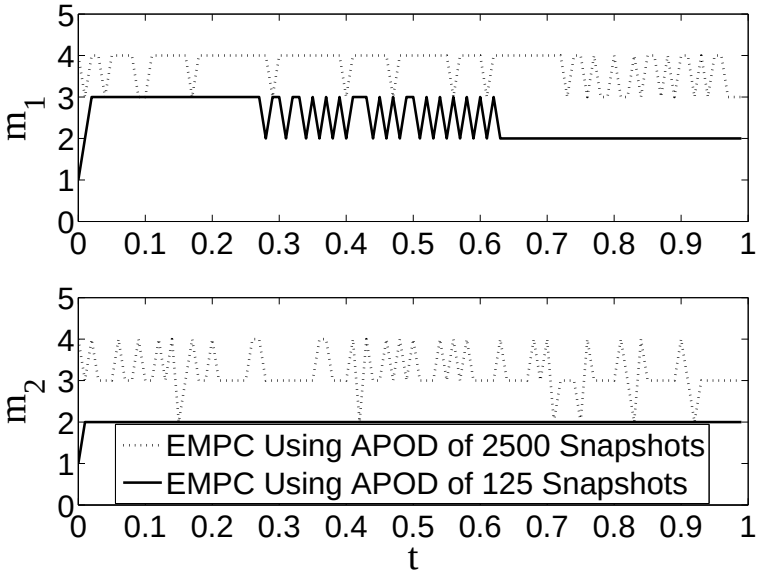

Figure 7.9: Number of dominant eigenfunctions based on APOD using Ensemble 1 (dotted line) and on APOD using Ensemble 2 (solid line) over one operation period.

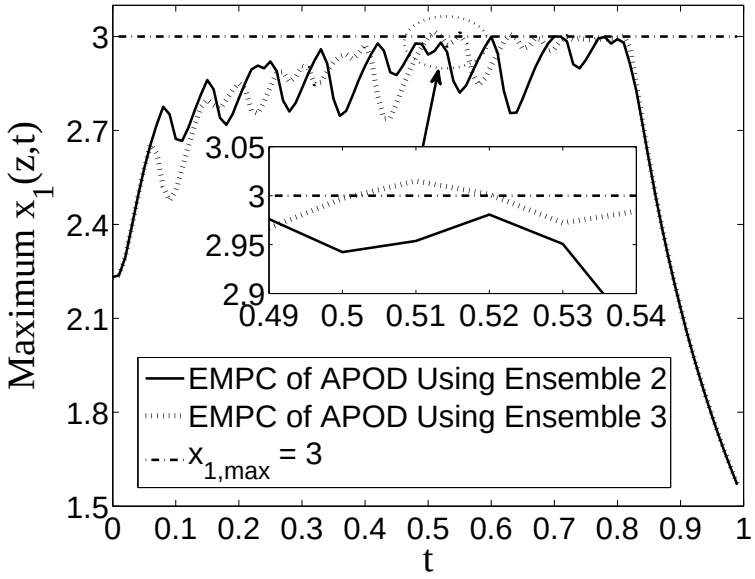

Figure 7.10: Maximum x_1 profiles of the process under the EMPC systems of Eq. 7.7 based on APOD using Ensemble 2 (solid line) and on APOD using Ensemble 3 (dotted line) over one operation period.

Case 3: Proposed Flow Chart of Integrating APOD with Finite-Difference Method

Based on the weakness of APOD with a small snapshot ensemble in state estimation accuracy which is shown by Case 2, in this case study, the proposed method of integrating APOD and finite differences is applied to construct the predictive models in EMPC scheme to achieve both computational efficiency and high reduced-order model accuracy (i.e., state estimation accuracy) so that the state constraint violation can be successfully avoided.

A set of 101 ODEs for each partial differential equation state as the result of applying central finite-difference method to each partial differential equation state is integrated into the EMPC scheme. An ensemble of 150 snapshots which is noted as Ensemble 4 is initially adopted for the EMPC system based on APOD method. We still request that the dominant eigenfunctions occupy $\eta = 99.99\%$ of the total energy of the ensemble. The EMPC system of Eq. 7.7 based on the finite-difference method resulting in a set of 101 ODEs for each

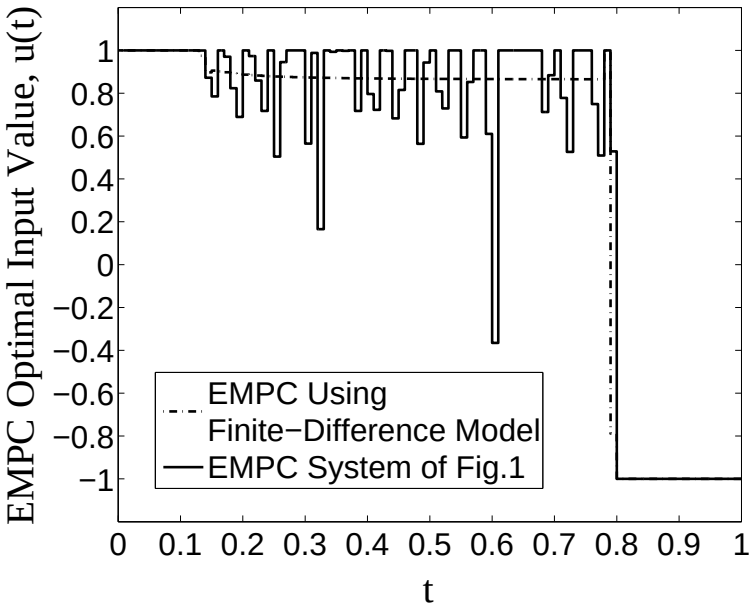

Figure 7.11: Manipulated input profiles of the EMPC system of Fig. 7.1 (solid line) and the EMPC system of Eq. 7.7 based on the finite-difference method (dash-dotted line) over one operation period.

partial differential equation state is taken as the comparison method for the proposed EMPC formulation. The same prediction horizon, sampling time and integration step are adopted as the previous case. We assume the state violation alert region, Ω_1, for dimensionless temperature, $x_1(z,t)$, is defined as:

$$\Omega_1 := \{x \in \mathbb{R} \mid |\max(x_1(z,t_k)) - x_{1,\max}| \leq 0.05\} \tag{7.15}$$

The computed manipulated input profiles over one period $t_f = 1.0$ from the EMPC system of Fig. 7.1 and the EMPC system of Eq. 7.7 based on the finite-difference method over one period are shown in Fig. 7.11. From Fig. 7.11, the EMPC system of Eq. 7.7 based on the finite-difference method computes a smoother manipulated input profile than that of the EMPC of Fig. 7.1. The temporal economic cost profiles of the process under the

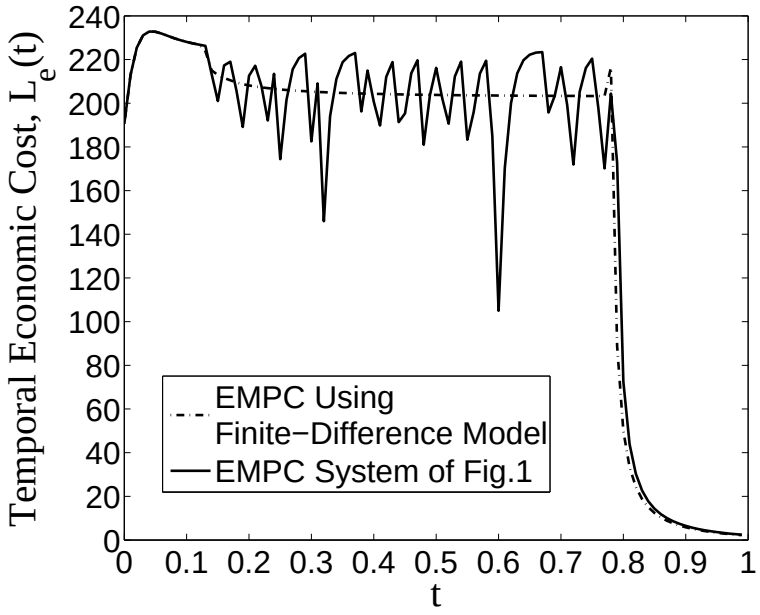

Figure 7.12: Temporal economic cost along the length of the reactor, $L_e(t)$, of the EMPC system of Fig. 7.1 (solid line) and the EMPC system of Eq. 7.7 based on the finite-difference method (dash-dotted line) over one operation period.

EMPC of Fig. 7.1 and the EMPC system of Eq. 7.7 based on the finite-difference method are shown in Fig. 7.12. From Fig. 7.12, over one period $t_f = 1$, the total reaction rate of the process under the EMPC of Fig. 7.1 is only 0.33% smaller than that of the EMPC system of Eq. 7.7 based on the finite-difference model.

With respect to the performance of the EMPC optimal input value, we have compared the maximum temperature (dimensionless) profiles of the tubular reactor under the EMPC systems as shown in Fig. 7.13. From Fig. 7.13, we see that the EMPC system of Fig. 7.1 can operate the process at the maximum allowable temperature and meanwhile avoid the state constraint violation issues by adopting the integrated EMPC system based on the finite-difference method when the process state value enters into the alert region of Eq. 7.15.

We finally have compared the calculation time of the EMPC system of Fig. 7.1 and the EMPC system of Eq. 7.7 based on the finite-difference method in Fig. 7.14. As displayed

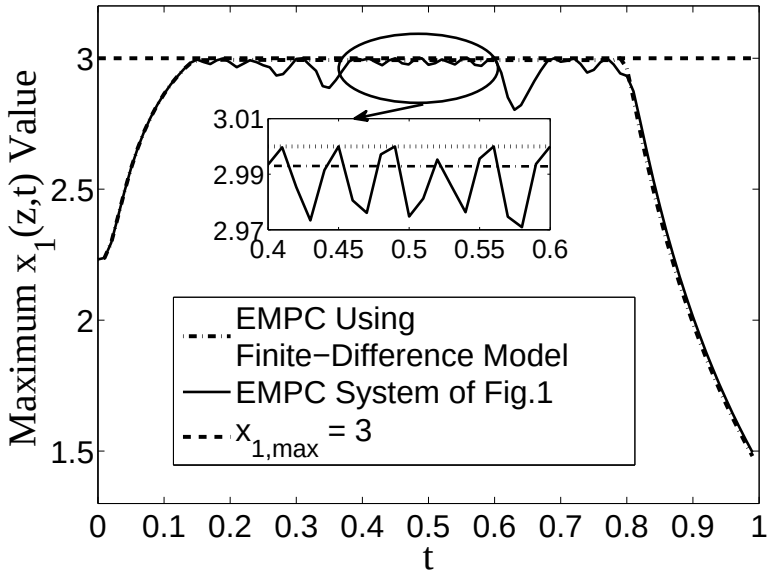

Figure 7.13: Maximum $x_1(z,t)$ profiles under the EMPC system of Fig. 7.1 (solid line) and the EMPC system of Eq. 7.7 based on the finite-difference method (dash-dotted line) over one operation period.

in Fig. 7.14, the EMPC of Fig. 7.1 achieves 8.71% improvement compared with the EMPC system of Eq. 7.7 based on the finite-difference method. In terms of Fig. 7.14, we point out that when the state value enters in the violation alert region, both the EMPC based on APOD method (to get a trial optimal input value) and the EMPC system of Eq. 7.7 based on the finite-difference method (to get an accurate optimal input value to help the EMPC scheme to avoid the state constraint violation if the previous optimal input value leads to constraint violation) are conducted which results in a longer computational time.

Based on the above results and analysis, the proposed EMPC scheme of Fig. 7.1 successfully improves the whole computational efficiency while avoiding the state constraint violation.

Remark 7.6 *We note here that the proposed EMPC scheme of Fig. 7.1 also has its drawbacks and limitations as follows:*

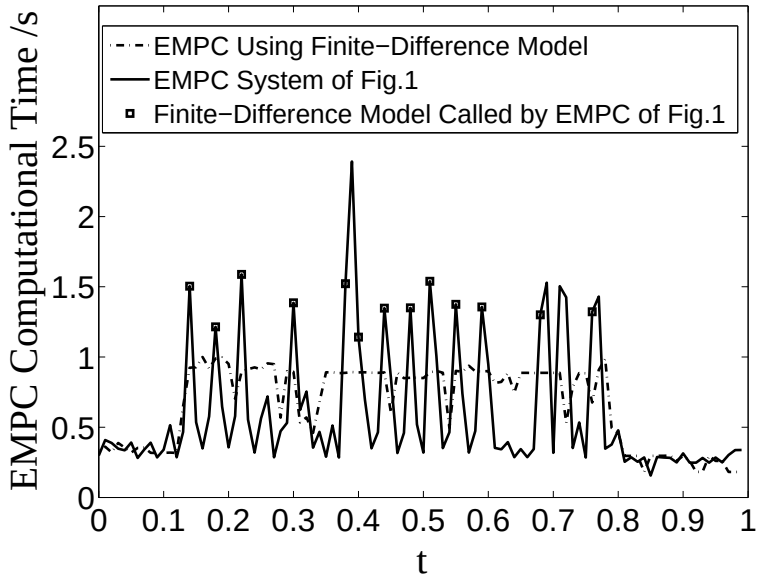

Figure 7.14: EMPC computational time profiles for the EMPC system of Fig. 7.1 (solid line) and the EMPC system of Eq. 7.7 based on the finite-difference method (dash-dotted line) over one operation period.

1. *Due to the automatic transition of the proposed EMPC scheme between APOD and finite-difference method after the process enters into the state violation alert region, the smoothness of the manipulated input trajectories is usually not guaranteed which may increase fluctuations on process state and economic-index trajectories in practice (e.g., production rate). This also reflects APOD method's limitation on capturing the global process dynamics and application on dynamic operation because of its requirement for a relatively smaller size of ensemble.*

2. *The proposed EMPC scheme achieves better computational efficiency compared with EMPC based on finite-difference method. If real-time computational constraints are not critical, EMPC based on a high-order finite-difference method which has a higher model accuracy would be a better choice. In terms of the limitation of the finite-difference method, if the size of the discretized model is large, EMPC based on*

this discretized model requires much more computational time compared with EMPC based APOD method.

Remark 7.7 *To deal with potentially-large fluctuations of the optimal input profile brought by the proposed EMPC scheme of Fig. 7.1, an increase of the prediction horizon and an addition of an input fluctuation penalty term in the economic cost function of Eq. 7.11 may be adopted; such modifications of the presented EMPC scheme have been carried out and have demonstrated the expected benefit in reducing input fluctuations but are omitted here due to space limitations. It is important to note that a longer prediction horizon will definitely sacrifice the computational efficiency of EMPC and an input fluctuation penalty cost may also lead to a degradation of the process economic performance.*

7.5 Conclusion

This work focused on developing an EMPC design for a system of parabolic PDEs which integrated the APOD method and a high-order finite-difference method to deal with control system computational efficiency and state constraint satisfaction. EMPC systems adopting POD, APOD, a high-order spatial discretization by central finite-difference method and the proposed EMPC flow chart were applied to a non-isothermal tubular reactor where a second-order chemical reaction takes place. These EMPC systems were compared with respect to their model accuracy, computational time, APOD update requirements, state constraint satisfaction and closed-loop economic performance of the tubular reactor. The simulation results demonstrated the advantages of APOD on improving computational efficiency of EMPC design, but also demonstrated a potential problem on state constraint violation. To address this issue, an EMPC scheme inheriting the high computational efficiency from APOD and the high state prediction accuracy from high-order finite-difference method was proposed; simulation results demonstrated that this EMPC scheme success-

fully improves the computational efficiency, while avoiding state constraint violations. Future work will focus on developing an output feedback EMPC scheme based on APOD in which the state measurements will be limited to few discrete points along the spatial domain.

Chapter 8

Economic Model Predictive Control of a System of First-Order Hyperbolic PDEs

8.1 Introduction

This chapter presents both state and output feedback EMPC systems that account for both manipulated input and state constraints for a system of first-order hyperbolic PDEs. When measurements of the state variables are available only at a finite number of spatial positions, a pole placement-based state observer technique is adopted to get estimates of the full spatial state profile. The EMPC system is applied to a non-isothermal plug flow reactor whose first-principles model consists of two quasi-linear first-order hyperbolic PDEs. EMPC systems utilizing different numbers of output measurement points and different prediction horizons are applied to this plug flow reactor process. Various results of state estimation accuracy, process economic performance, and computational efficiency are presented and compared.

8.2 Preliminaries

8.2.1 Reactor Description

We focus on a non-isothermal plug flow reactor (PFR) where an irreversible and exothermic second-order reaction of the form $A \rightarrow B$ takes place. The process model in dimensionless variable form consists of two quasi-linear hyperbolic PDEs. The process description details and model notation can be found in[85] (i.e., the PFR model is similar to the tubular reactor model presented in[85] except for the fact that the diffusion term used in the tubular reactor model of[85] is neglected in the PFR model below):

$$\begin{aligned} \frac{\partial x_1}{\partial t} &= -\frac{\partial x_1}{\partial z} + B_T B_C \exp\left(\frac{\gamma x_1}{1+x_1}\right)(1+x_2)^2 \\ &\quad +\beta_T(T_j - x_1) \\ \frac{\partial x_2}{\partial t} &= -\frac{\partial x_2}{\partial z} - B_C \exp\left(\frac{\gamma x_1}{1+x_1}\right)(1+x_2)^2 \end{aligned} \tag{8.1}$$

subject to the following boundary conditions:

$$x_1(0,t) = T_i,\ x_2(0,t) = C_{Ai} = u(t) \tag{8.2}$$

where $x_1(z,t)$ denotes a dimensionless temperature, $x_2(z,t)$ denotes a dimensionless reactant concentration, z and t are the dimensionless spatial coordinate and time variables, respectively. The following typical values are given to the process parameters: $B_T = 2.5$, $B_C = 0.1$, $\beta_T = 2$, $T_i = 0.5$, $T_j = -0.5$, and $\gamma = 10$. Upwind finite-difference scheme is adopted (which can guarantee the stability of the numerical spatial discretization of the process model[59]) to discretize, in space, the two hyperbolic PDEs and obtain a 101st-order system of ODEs in time for each partial differential equation (i.e., a total of 202 ODEs in time). Further increase of the number of discretization points led to identical results. Based

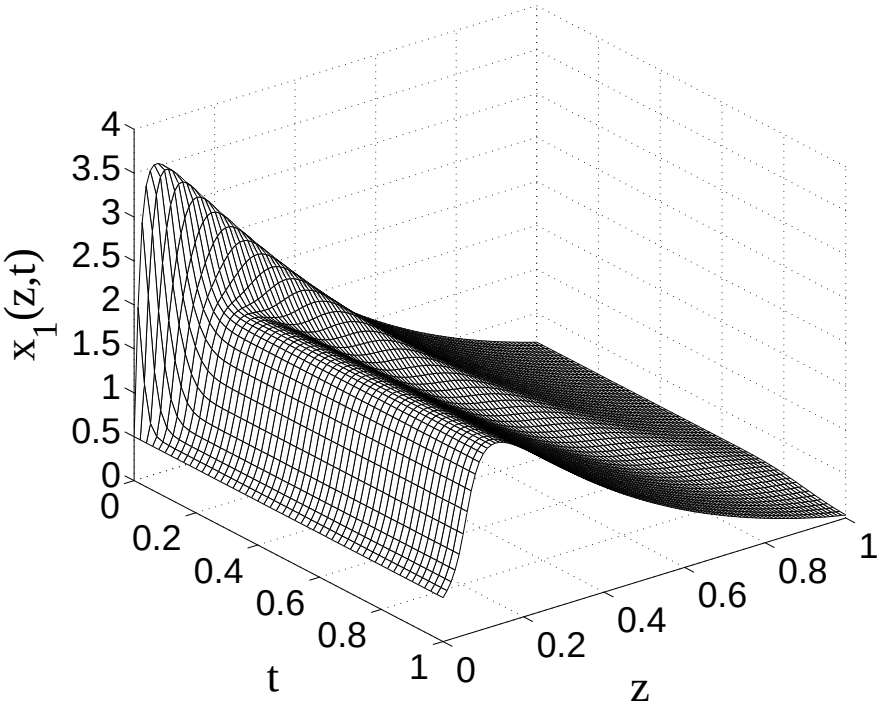

Figure 8.1: Open-loop profile of x_1 of the process model of Eq. 8.1.

on this discretized model, open-loop simulation results for a constant input of $u(t) \equiv 0.0$ are shown in Figs. 8.1-8.2. The state profile is initialized at the steady-state profile corresponding to the steady-state input $u_s = 0.5$.

The process model of Eq. 8.1 can be formulated as follows:

$$\begin{aligned} \frac{\partial x(z,t)}{\partial t} &= A\frac{\partial x(z,t)}{\partial z} + f(x(z,t)) \\ y_j(t) &= \mathscr{C}x(z,t) = \int_0^1 c_j(z)x(z,t)\,dz,\ j = 1,\ldots,p \end{aligned} \tag{8.3}$$

subject to the boundary conditions:

$$x(0,t) = [T_i\ u(t)]' \tag{8.4}$$

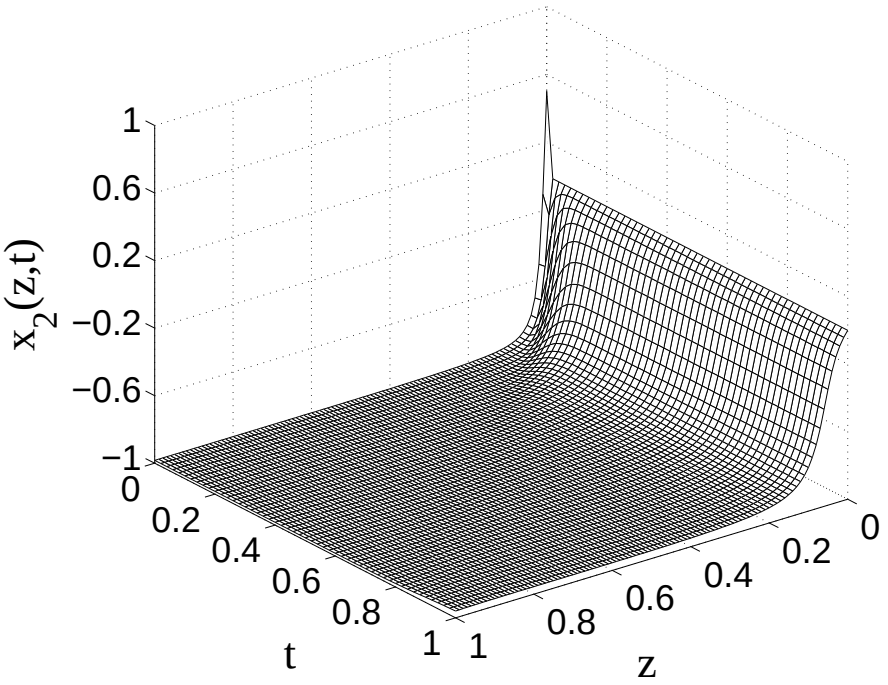

Figure 8.2: Open-loop profile of x_2 of the process model of Eq. 8.1.

and the initial condition:

$$x(z,0) = x_0(z) \tag{8.5}$$

where $x(z,t) = [x_1(z,t)\, x_2(z,t)]'$ denotes the vector of the process state variables, the notation x' is the transpose of x, $z \in [0,1]$ is the spatial coordinate, $t \in [0,\infty)$ is the time, $f(x(z,t))$ denotes a nonlinear vector function, $y_j(t)$ is the j-th measured output ($y(t) = [y_1(t) \cdots y_p(t)]'$ is the measured output vector), $c_j(z)$ are known smooth functions of z ($j = 1, \ldots, p$) whose functional form depends on the type of the measurement sensors, $\mathscr{C}$ is the measured output operator, A is a constant matrix of appropriate dimensions, and $u(t)$ denotes the manipulated input.

8.2.2 EMPC System Constraints and Objective

For the plug flow reactor of Eq. 8.1, the input $u(t)$ is chosen as the reactant concentration (dimensionless) of the inlet stream at $z = 0$ (Eq. 8.2). We assume the manipulated input is subject to constraints as follows:

$$u_{min} \leq u(t) \leq u_{max} \tag{8.6}$$

where $u_{min} = -1$ and $u_{max} = 1$ are the lower and upper bound of the manipulated input, $u(t)$. We assume that there is also a limitation on the amount of reactant material (dimensionless) available over each operating period of length t_p. Specifically, the control input of $u(t)$ should satisfy:

$$\frac{1}{t_p}\int_0^{t_p} u(\tau)\, d\tau = 0.5 \tag{8.7}$$

which will be referred to as the reactant material integral constraint. To ensure that the constraint of Eq. 8.7 is satisfied over the operating period of length t_p when the prediction horizon of the EMPC does not cover the entire operating period, it is implemented according to the strategy described in.[48] In the EMPC formulations below, the constraint will be denoted as $u \in g(t_k)$ to simply the notation.

In terms of the state constraint, we consider that the reactor temperature (dimensionless) is subject to:

$$x_{1,min} \leq x_1(z,t) \leq x_{1,max} \tag{8.8}$$

for all $z \in [0,1]$ and $t \geq 0$ where $x_{1,min} = -1$ and $x_{1,max} = 4.5$ are the lower and upper limits, respectively.

To solve the EMPC problem, the open-source interior point solver Ipopt[139] was used. Explicit Euler's method was used for temporal integration of the 202nd spatial discretization of the PDE model of Eq. 8.1 with an integration step of 1×10^{-3} to numerically

integrate ODE model in EMPC. The dimensionless sampling period of EMPC is $\Delta = 0.01$.

To develop EMPC formulations in the subsequent sections, we use a Lyapunov function of form

$$V(x) = \int_0^1 [x_1^2(z,t) + x_2^2(z,t)]\, dz < \bar{\rho} \tag{8.9}$$

where $x_1(z,t)$ and $x_2(z,t)$ are the spatial state values respectively and $\bar{\rho} = 15$ (see[65] for results on Lyapunov-based EMPC designs).

The cost function that we consider is to maximize the overall reaction rate along the length of the reactor and over one operation period of length $t_p = 1$. The economic cost then takes the form:

$$L_e(t) = \int_0^1 r(z,t)\, dz \tag{8.10}$$

where $r(z,t) = B_C \exp\left(\frac{\gamma x_1(z,t)}{1+x_1(z,t)}\right)(1+x_2(z,t))^2$ is the reaction rate (dimensionless) in the plug flow reactor.

8.3 State Feedback EMPC

8.3.1 State Feedback Economic Model Predictive Control Formulation

We consider the application of a state feedback EMPC to the system of Eq. 8.1 to optimize an economic cost function and handle input and state constraints. Specifically, a Lyapunov-based EMPC (LEMPC) system is designed using the results in[65] with the economic cost function of Eq. 8.10, the input constraint of Eq. 8.6, the state constraint of Eq. 8.8, and the reactant material integral constraint of Eq. 8.7 for the plug flow reactor. The state feedback EMPC receives the (full) state profile of $x(z,t_k)$ of the system of PDEs of Eq. 8.1 synchronously at sampling instants denoted as $t_k = k\Delta$ with $k = 0, 1, \ldots$. The state feedback

EMPC control action is computed by solving the following finite-dimensional optimization problem in a receding horizon fashion:

$$\max_{u\in S(\Delta)} \int_{t_k}^{t_{k+N}} L_e(\tau)\, d\tau \tag{8.11a}$$

$$\text{s.t. } \frac{\partial \tilde{x}(z,t)}{\partial t} = A\frac{\partial \tilde{x}(z,t)}{\partial z} + f(\tilde{x}(z,t)) \tag{8.11b}$$

$$\tilde{x}(z,t_k) = x(z,t_k), \forall z \in [0,1] \tag{8.11c}$$

$$\tilde{x}_1(0,t) = T_i,\ \forall t \in [t_k, t_{k+N}) \tag{8.11d}$$

$$\tilde{x}_2(0,t) = u(t),\ \forall t \in [t_k, t_{k+N}) \tag{8.11e}$$

$$u_{min} \leq u(t) \leq u_{max} \tag{8.11f}$$

$$u(t) \in g(t_k) \tag{8.11g}$$

$$x_{1,min} \leq x_1(z,t) \leq x_{1,max},\ \forall\, z \in [0,1],$$
$$\text{and } \forall t \in [t_k, t_{k+N}) \tag{8.11h}$$

$$V(\tilde{x}) \leq \bar{\rho} \tag{8.11i}$$

where $L_e(\tau)$ is the economic cost, Δ is the sampling period, $S(\Delta)$ is the family of piecewise constant functions with sampling period Δ, N is the prediction horizon, and $\tilde{x}(z,t)$ is the predicted state function evolution with input $u(t)$ computed by the state feedback EMPC.

In the optimization problem of Eq. 8.11, the cost function of Eq. 8.11a accounts for the economics of the system of PDEs (i.e., maximization of the production of product species *B*). The constraint of Eq. 8.11b is used to predict the future evolution of the system of PDEs with the initial condition given in Eq. 8.11c and the boundary conditions given by Eqs. 8.11d-8.11e. The constraints of Eqs. 8.11f-8.11h are the available control action, the integral input constraint, and the state constraints, respectively. The constraint of Eq. 8.11i ensures that the predicted state trajectory is restricted inside a predefined stability region

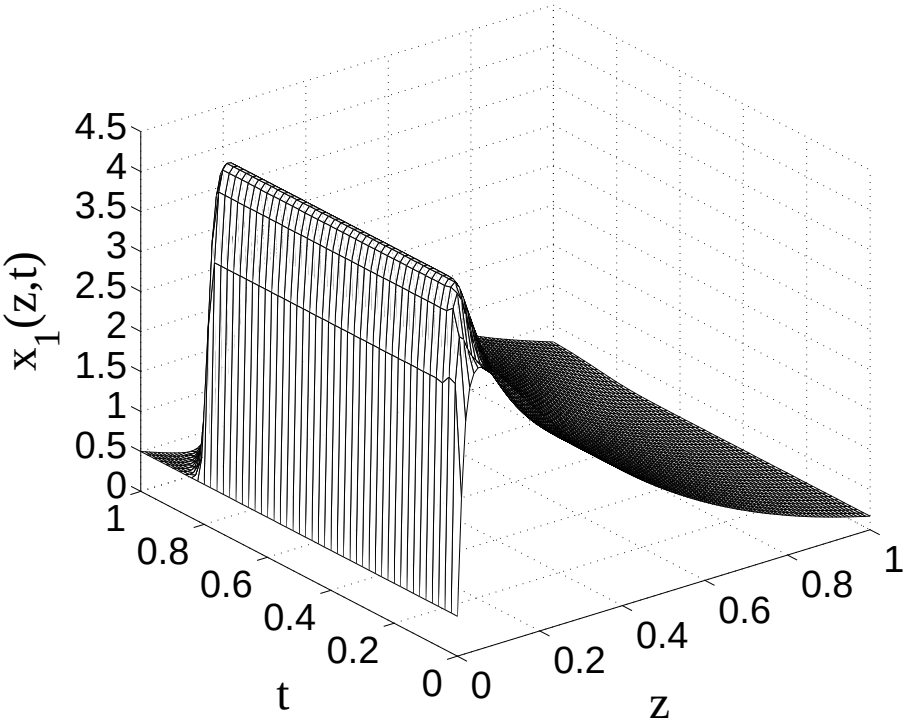

Figure 8.3: Closed-loop profile of x_1 of the process under the state feedback EMPC system of Eq. 8.11 over one operation period.

which is a level set of the Lyapunov function (see[65] for a complete discussion of this issue). The optimal solution to this optimization problem is $u^*(t|t_k)$ defined for $t \in [t_k, t_{k+N})$. The state feedback EMPC applies the control action computed for the first sampling period to the system in a sample-and-hold fashion for $t \in [t_k, t_{k+1})$. The state feedback EMPC is resolved at the next sampling period, t_{k+1}, after receiving a measurement of the state profile, $x(z, t_{k+1})$ for $z \in [0,1]$.

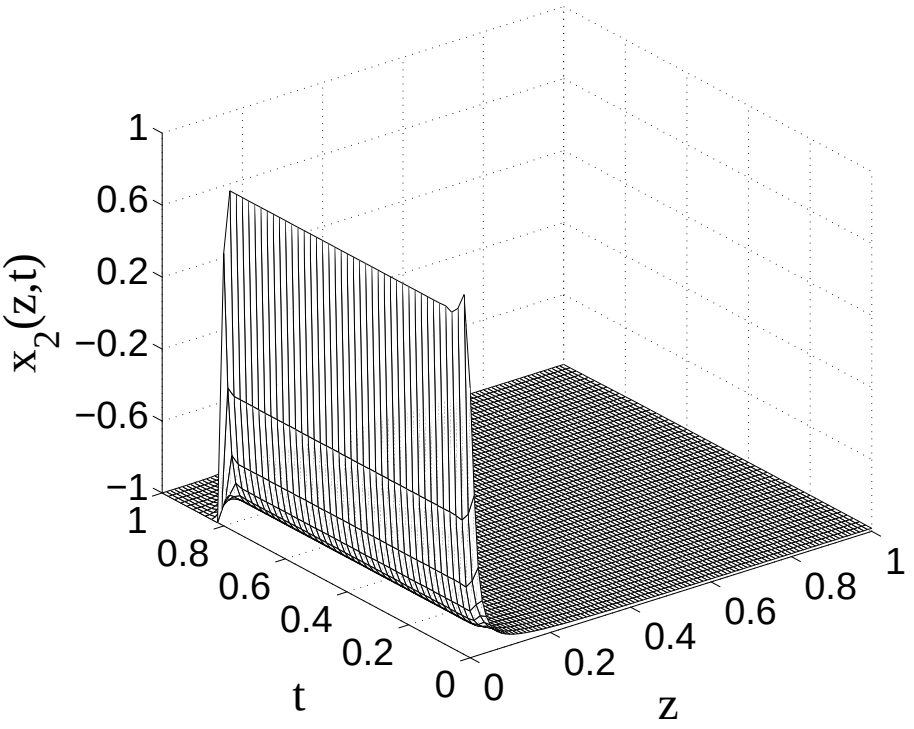

Figure 8.4: Closed-loop profile of x_2 of the process under the state feedback EMPC system of Eq. 8.11 over one operation period.

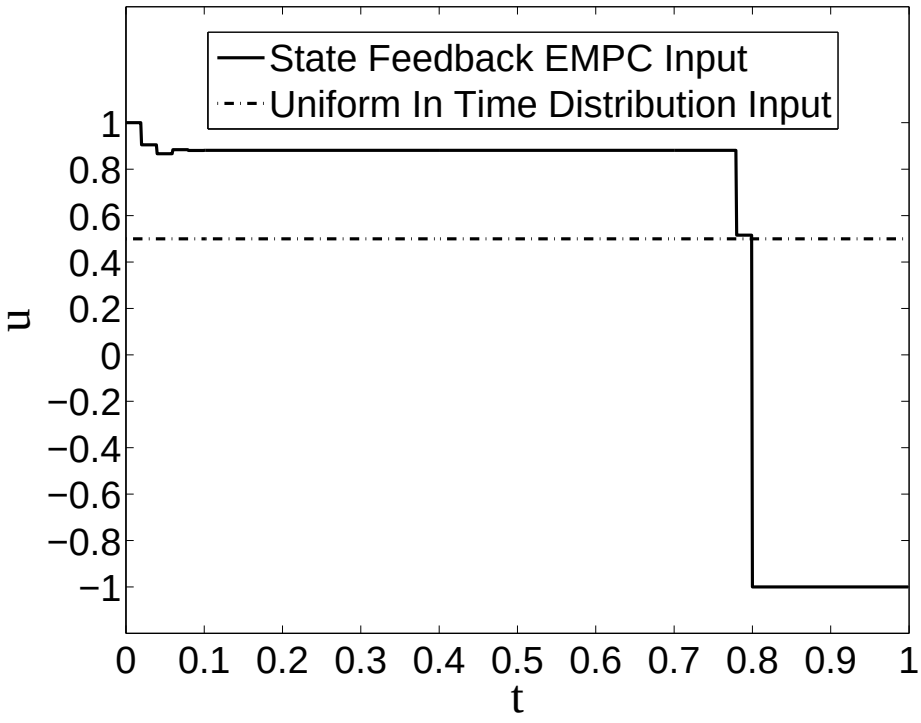

Figure 8.5: Manipulated input profiles of the state feedback EMPC system of Eq. 8.11 and uniform in time distribution of the reactant material over one operation period.

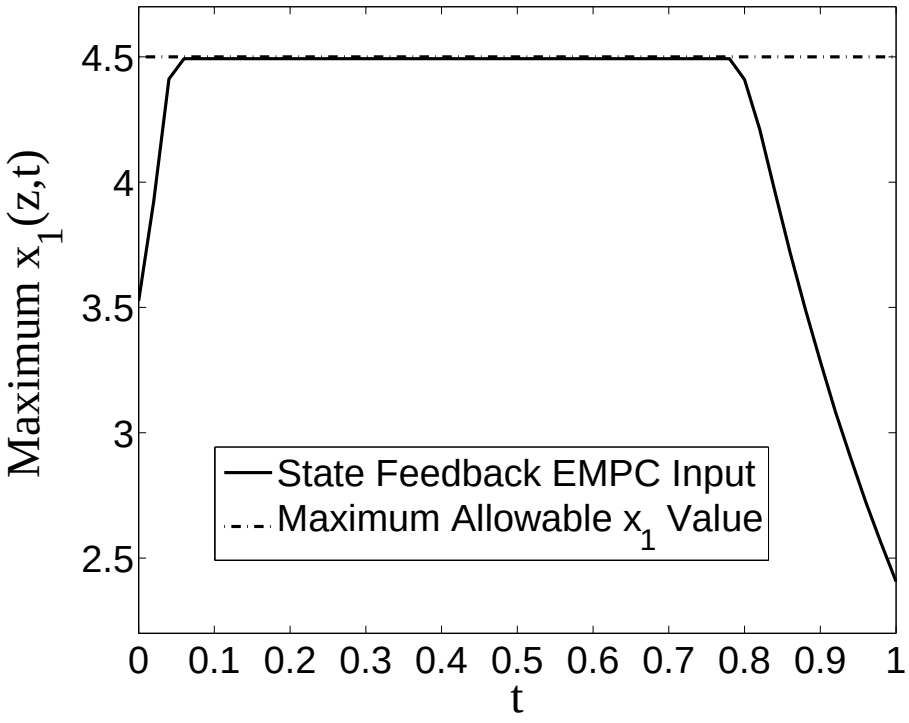

Figure 8.6: Maximum x_1 profiles of the process under the state feedback EMPC system of Eq. 8.11 over one operation period.

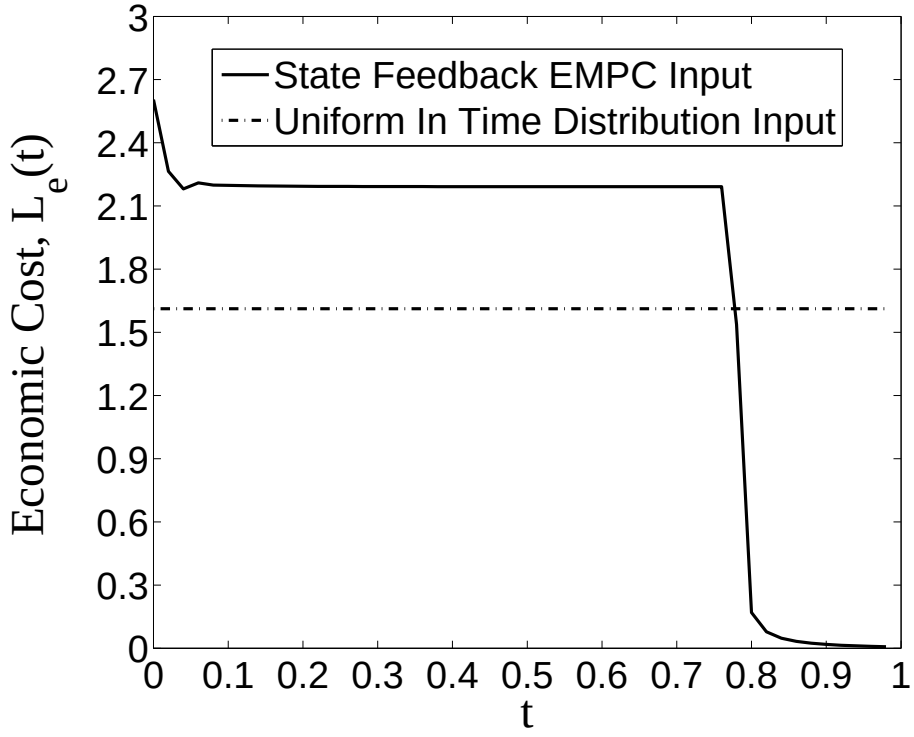

Figure 8.7: Economic cost, $L_e(t)$, along the length of the reactor under the state feedback EMPC system of Eq. 8.11 and under uniform in time distribution of the reactant material over one operation period.

8.3.2 Application of State Feedback EMPC System to the Tubular Reactor

We operate the reactor under the state feedback EMPC system of Eq. 8.11. In detail, we choose the prediction horizon, $N = 3$. The plug flow reactor is initialized with a steady-state profile (i.e., the steady-state profile corresponding to the steady-state input $u_s = 0.5$).

The closed-loop state profiles of the reactor over one period $t_p = 1.0$ under the state feedback EMPC of Eq. 8.11 is displayed in Figs. 8.3-8.4. The computed manipulated input profile from the state feedback EMPC system over one period is shown in Fig. 8.5. From Fig. 8.5, we observe that the state feedback EMPC system varies the optimal input value $u(t)$ in a time-varying fashion. The maximum x_1 value profile of the plug flow reactor under the state feedback EMPC system is shown in Fig. 8.6. Since the temperature directly influences the reaction rate (i.e., the reaction is second-order and exothermic), the optimal operating strategy is to first force the reactor to operate at the maximum allowable value and then, decrease the input to its minimum value to satisfy the integral input constraint. During this one operation period, $t_p = 1$, the economic cost profile of the reactor under the state feedback EMPC system is demonstrated in Fig. 8.7. The average economic cost over one operating period $t_p = 1$, which is denoted as $\bar{L}_e(t)$, is given by

$$\bar{L}_e(t) = \int_0^1 L_e(t)\, dt\,. \tag{8.12}$$

Comparing the process under the state feedback EMPC system to the process under a constant input, the average economic cost is 15.14% greater than that of the reactor under uniform in time distribution of the reactant material. The state feedback EMPC system achieves a significant advantage in maximizing the process economic performance over one operation period through operating the process in a time-varying fashion.

8.4 Output Feedback EMPC

8.4.1 State Estimation Using Output Feedback Methodology

In this section, we consider a state estimation technique that makes use of a finite number, p, of measured outputs $y_j(t)$ ($j = 1, \ldots, p$) to estimate the state vector of the system, $x(z,t)$ in space and time.

This state estimation scheme is designed based on the distributed state observer design approach presented in.[26] The nonlinear state observer is designed to guarantee local exponential convergence of the state estimates to the actual state values. In particular, based on Eq. 8.3, the following state observer will be utilized:

$$\frac{\partial \hat{x}(z,t)}{\partial t} = A\frac{\partial \hat{x}(z,t)}{\partial z} + f(\hat{x}(z,t)) + \mathscr{K}(y(t) - \mathscr{C}\hat{x}(z,t)) \tag{8.13}$$

subject to the boundary conditions:

$$\hat{x}(0,t) = [T_i \; u(t)]' \tag{8.14}$$

and the initial condition:

$$\hat{x}(z,0) = \bar{x}_0(z) \tag{8.15}$$

where $\hat{x}$ is the observer state vector, $\bar{x}_0(z)$ is the initial condition of the observer state which is sufficiently smooth with respect to z, $y(t)$ is the measured output vector which is assumed to be continuously available and $\mathscr{K}$ is a linear operator representing the observer gain which is designed on the basis of the linearization of the system of Eq. 8.13 so that the eigenvalues of the operator $\mathscr{L}_o = \mathscr{L} - \mathscr{K}\mathscr{C}$ lie in the left-half plane. By satisfying this condition, $\mathscr{L}_o$ can generate an exponentially stable semigroup for $\hat{x}(t)$. Specifically, the operator $\mathscr{L}$ is defined on the basis of the linearized form of the Eq. 8.3 at some specific

steady-state profile, denoted as $x_s(z)$, i.e.,:

$$\mathscr{L}x = A\frac{\partial x}{\partial z} + B(z)x \tag{8.16}$$

where

$$B(z) := \left(\frac{\partial f(x)}{\partial x}\right)_{x=x_s(z)} \tag{8.17}$$

If the operator $\mathscr{K}$ is chosen by satisfying the aforementioned condition that the eigenvalues of the operator $\mathscr{L}_o = \mathscr{L} - \mathscr{K}\mathscr{C}$ lie in the left-half of the complex plane, the term $\mathscr{K}(y(t) - \mathscr{C}\hat{x})$ can enforce a fast decay of the discrepancy between the estimated state values and the actual state values of the system of PDEs. In practice, the design of the operator $\mathscr{K}$ depends on whether the output measurements are corrupted by noise or not. Pole placement is often adopted when the output measurements are free of measurement noise, while Kalman filtering theory is often adopted when the output measurements are noisy. For the present work, we assume there is no measurement noise on the output measurements. Therefore, pole placement is utilized to design an appropriate state observer gain for output feedback correction to diminish the state estimation error as fast as possible.

8.4.2 Implementation of State Estimation

We now combine the state observer with the state feedback EMPC to derive an output feedback EMPC formulation. For the case of plug flow reactor of Eq. 8.1, we assume that only p evenly spaced measurement points are available of the state x_1 (temperature); we use these p measurements to estimate the state values of both $x_1(z,t)$ and $x_2(z,t)$ in the whole space and time domain by designing a state observer of the form of Eq. 8.13. Here, each spatial measurement point, z_j, is at $z_j = (j-1)/(p-1)$. Since point-wise measurements

are assumed, the measurement distribution functions are:

$$c_j(z) = \delta(z - z_j) \tag{8.18}$$

for $j = 1, \ldots, p$ where δ is the standard Dirac function. Consequently, each output measurement point value, $y_j(t_k)$, is equal to the partial differential equation state value, x_1 at the corresponding spatial point, z_j, i.e.,:

$$y_j(t) = x_1(z_j, t) \tag{8.19}$$

and the output measurement vector is $y'(t) = [y_1(t) \cdots y_p(t)]$. The operator $\mathscr{K} \in \mathbb{R}^{2\times p}$ is chosen to be:

$$\begin{bmatrix} 1/p & \ldots & 1/p \\ 1/p & \ldots & 1/p \end{bmatrix} \tag{8.20}$$

so that the eigenvalues of the operator $\mathscr{L}_0$ will lie in the left-half of the complex plane.

8.4.3 Application of Output Feedback EMPC System to the Tubular Reactor

We consider the application of output feedback EMPC to the system of Eq. 8.3 of the form:

$$\max_{u \in S(\Delta)} \int_{t_k}^{t_{k+N}} L_e(\tau)\, d\tau \tag{8.21a}$$

$$\text{s.t.} \quad \frac{\partial \tilde{x}(z,t)}{\partial t} = A\frac{\partial \tilde{x}(z,t)}{\partial z} + f(\tilde{x}(z,t)) \tag{8.21b}$$

$$\tilde{x}(z,t_k) = \hat{x}(z,t_k) \tag{8.21c}$$

$$\tilde{x}_1(0,t) = T_i,\ \forall t \in [t_k, t_{k+N}) \tag{8.21d}$$

$$\tilde{x}_2(0,t) = u(t),\ \forall t \in [t_k, t_{k+N}) \tag{8.21e}$$

$$u_{min} \leq u(t) \leq u_{max} \tag{8.21f}$$

$$u(t) \in g(t_k) \tag{8.21g}$$

$$x_{1,min} \leq x_1(z,t) \leq x_{1,max},\ \forall\, z \in [0,1],$$
$$\text{and } \forall t \in [t_k, t_{k+N}) \tag{8.21h}$$

$$V(\tilde{x}) \leq \bar{\rho} \tag{8.21i}$$

where $L_e(\tau)$ is the economic cost of Eq. 8.10, Δ is the sampling period, $S(\Delta)$ is the family of piecewise constant functions with sampling period Δ, N is the prediction horizon, $\tilde{x}(z,t)$ is the predicted state function evolution with input $u(t)$ computed by the output feedback EMPC and $\hat{x}(z,t_k)$ is the state estimate of $x(z,t_k)$ obtained from state observer of Eq. 8.13 at $t = t_k$.

Case 1: Output Feedback EMPC System

For this case, we operate the reactor by using the output feedback EMPC system of Eq. 8.21. In detail, we choose the prediction horizon, $N = 3$ and assume there are $p = 11$ evenly spaced measurement points along the length of the reactor. The plug flow reactor is initialized with the steady-state profile corresponding to the steady-state input $u_s = 0.5$.

The closed-loop state profiles of the plug flow reactor over one period $t_p = 1.0$ under the output feedback EMPC of Eq. 8.21 based on 11 measurements of x_1 are shown in Figs. 8.8-8.9. To check the effectiveness of the state observer, the profile of the state estimation error defined as

$$dx(t) = \sum_{i=1}^{2} \left(\sum_{j=0}^{101} \left(x_i(z_j,t) - \hat{x}_i(z_j,t) \right)^2 \right)^{1/2} \tag{8.22}$$

where z_j, $j = 1, 2, \ldots, 101$ is the discretized spatial coordinate and $dx(t)$ is the metric that defines the estimation error. The estimation error, $dx(t)$ for this case study is shown in Fig. 8.10. From Fig. 8.10, the state estimation error becomes small over time and converges to 0 at the end of the operating period. The optimal manipulated input profile from the output feedback EMPC system based on 11 measurements of x_1 over one period is displayed in Fig. 8.11. The input profile of the output feedback EMPC displays chattering. The chattering is from inaccuracies of the state estimate provided to the EMPC from the state observer. Specifically, it is desirable from an economics perspective to operate the PFR at the maximum temperature. However, the state observer cannot exactly estimate the true state. When the estimated temperature is at or above the state constraint, the EMPC decreases the amount of reactant material fed to the PFR to decrease the temperature (and satisfy the state constraint). If the estimated state is below the state constraint, more reactant material is fed to the PFR to increase the temperature and bring the temperature to the maximum allowable temperature. The maximum x_1 value profile of the plug flow reactor under the output feedback EMPC system is demonstrated in Fig. 8.12. From Fig. 8.12,

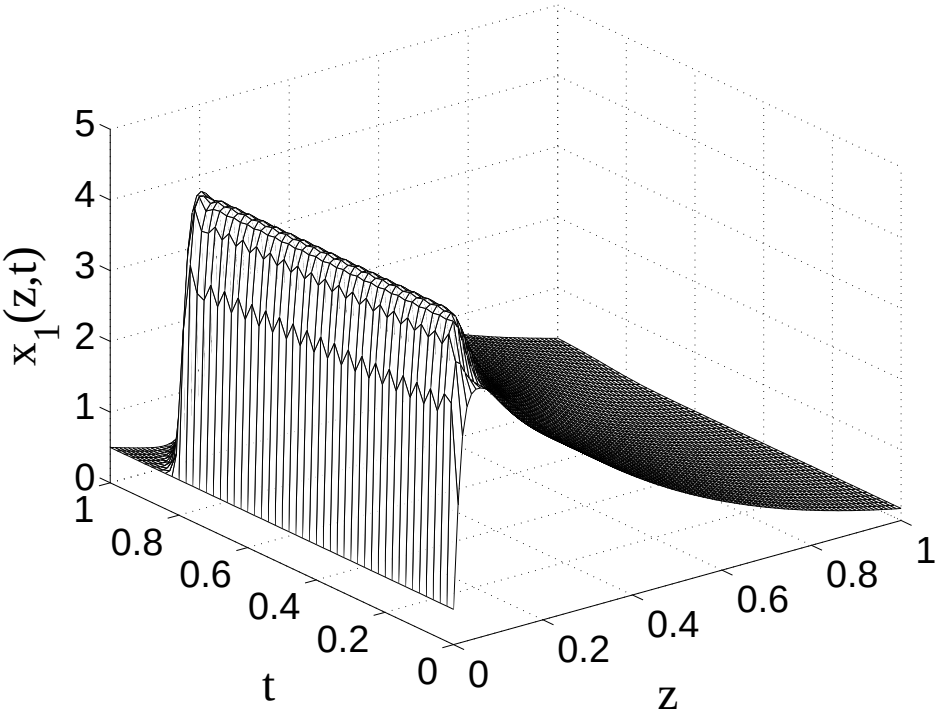

Figure 8.8: Closed-loop profile of x_1 of the process under the output feedback EMPC system of Eq. 8.21 with $N = 3$ based on 11 measurements of x_1 over one operation period.

the output feedback EMPC system is able to operate the reactor at the maximum allowable value over a period of time to maximize the economic cost while not violating the state constraint.

The economic cost profile of the reactor under the output feedback EMPC system is displayed in Fig. 8.13. During this one operation period, the process under the output feedback EMPC system achieves 14.77% improvement on the average economic cost over one operation period than that of the reactor under uniform in time distribution of the reactant material. The output feedback EMPC system demonstrates a significant advantage in maximizing the process economic performance through operating the process in a time-varying fashion over one operation period.

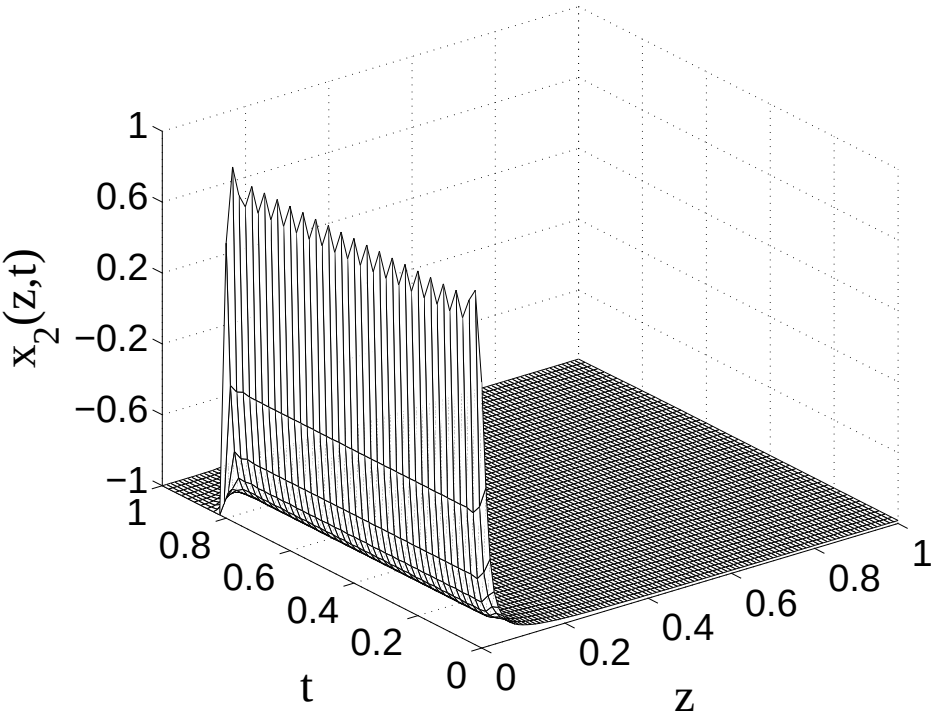

Figure 8.9: Closed-loop profile of x_2 of the process under the output feedback EMPC system of Eq. 8.21 with $N = 3$ based on 11 measurements of x_1 over one operation period.

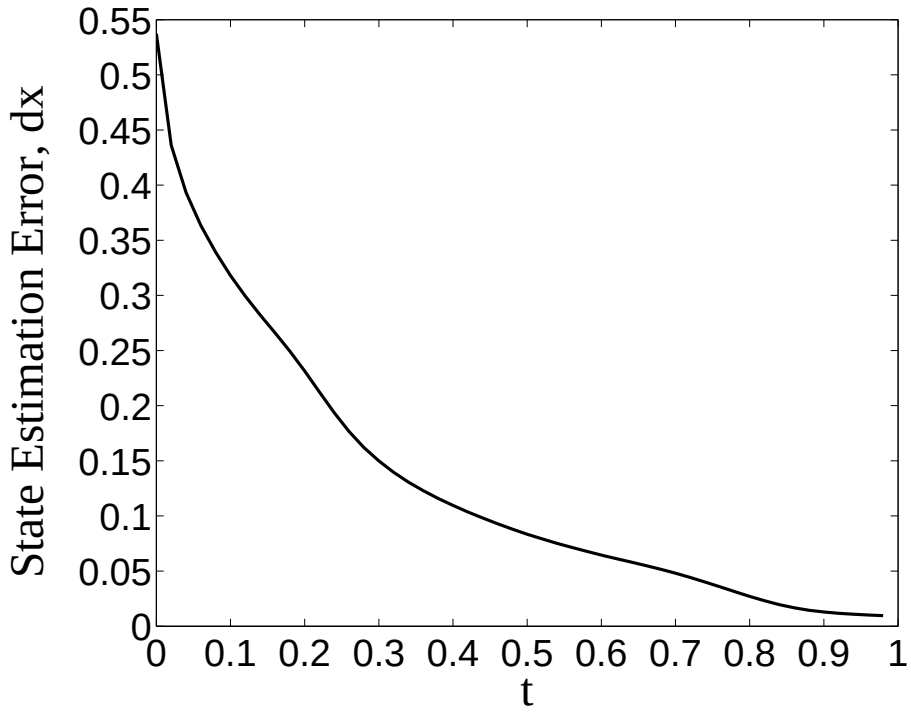

Figure 8.10: State estimation error profile of the process under the output feedback EMPC system of Eq. 8.21 with $N = 3$ based on 11 measurements of x_1 over one operation period.

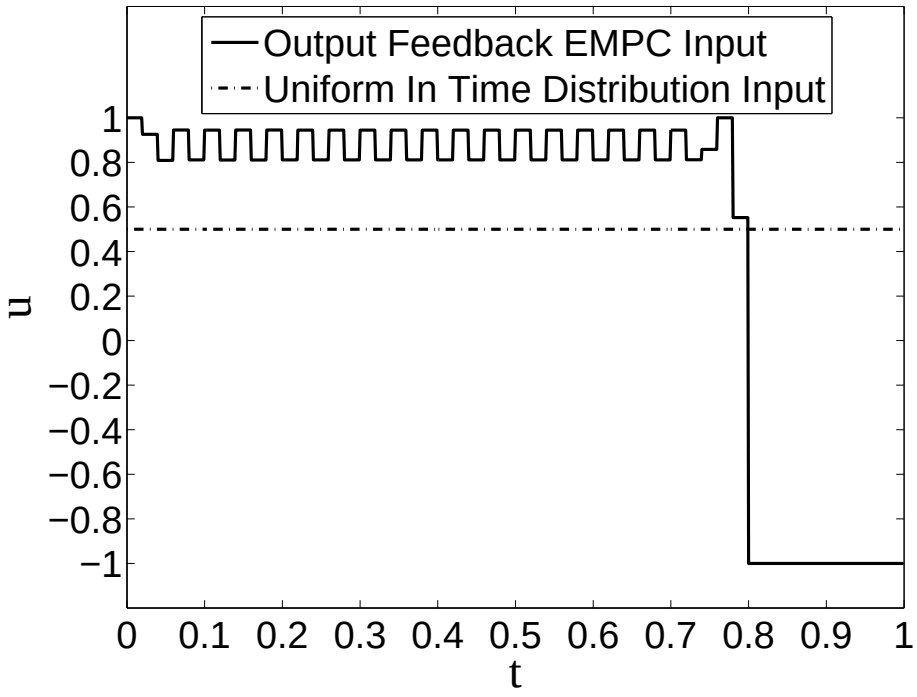

Figure 8.11: Manipulated input profiles of the output feedback EMPC system of Eq. 8.21 with $N = 3$ based on 11 measurements of x_1 and uniform in time distribution of the reactant material over one operation period.

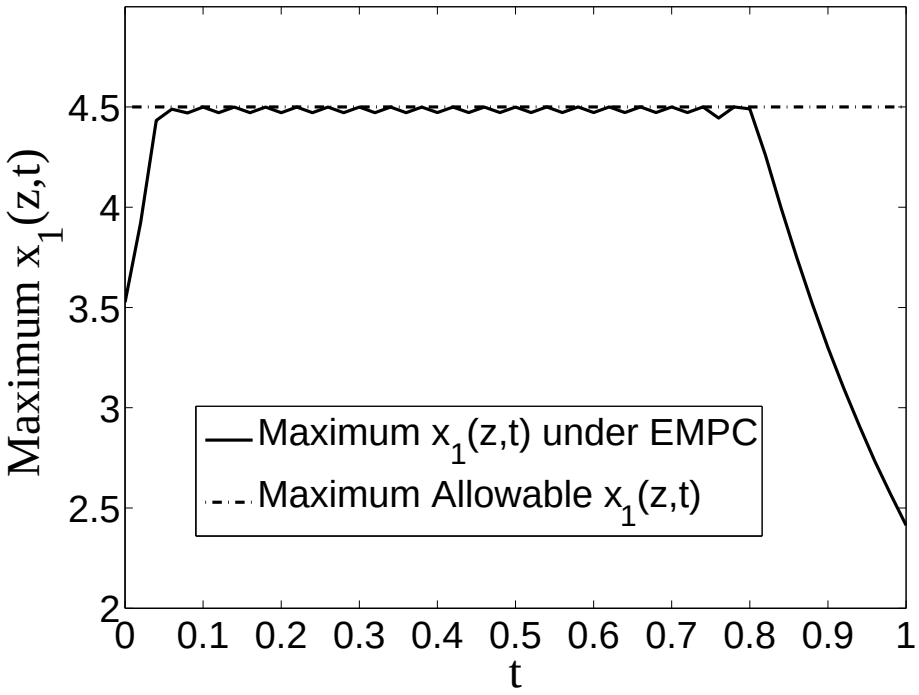

Figure 8.12: Maximum x_1 profiles of the process under the output feedback EMPC system of Eq. 8.21 with $N = 3$ based on 11 measurements of x_1 over one operation period.

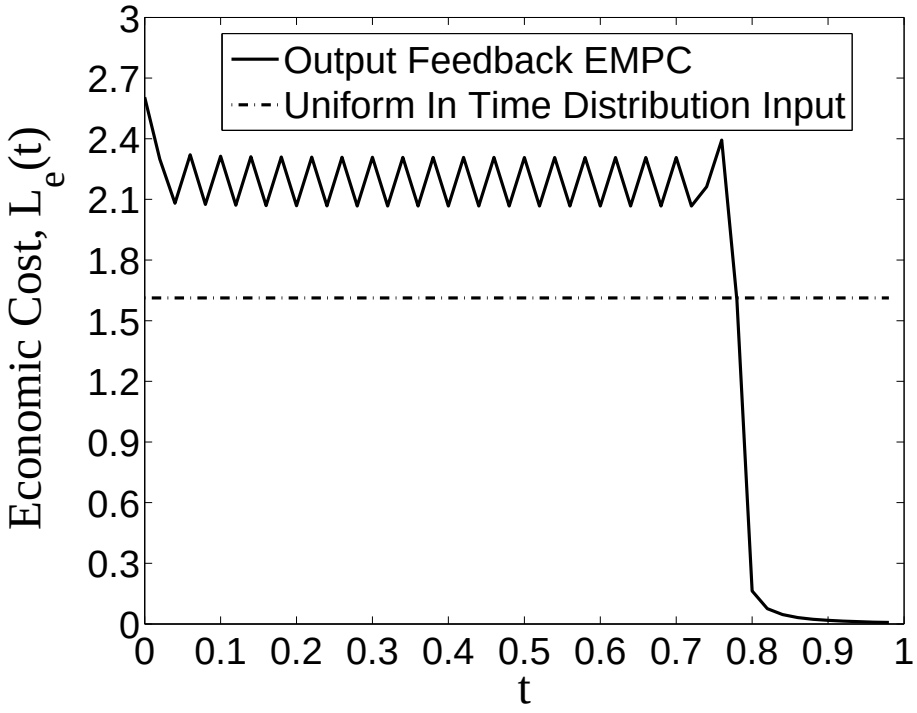

Figure 8.13: Temporal economic cost, $E(t)$, along the length of the reactor under the output feedback EMPC system of Eq. 8.21 with $N = 3$ based on 11 measurements of x_1 and under uniform in time distribution of the reactant material over one operation period.

Case 2: Prediction Horizon Effect on EMPC Application

We operate the process under different prediction horizons ($N < 10$ were considered because $N \geq 10$ is considered impractical based on computation time requirements to the EMPC at each sampling instance). The number of output measurement points on x_1 used was $p = 11$. The closed-loop manipulated input profiles of the output feedback EMPC system of Eq. 8.21 using the above different prediction horizons are displayed in Fig. 8.14. From Fig. 8.14, we can see that the use of a longer prediction horizon reduces the chattering of the manipulated input profiles. The corresponding average economic cost (i.e., $\bar{L}_e(t)$) profiles along the length of the reactor are displayed in Fig. 8.15. Fig. 8.15 demonstrates that the use of a prediction horizon greater than three sampling periods does not show a significant advantage of improving the process economic performance for the output feedback EMPC system of Eq. 8.21. However, as the prediction horizon increases, the computation time required to solve the EMPC at each sampling time increases. The ratio of the average computation time for a given horizon to the average computation time to solve the EMPC with $N = 3$ is shown in Fig. 8.16. The EMPC with $N = 3$ was chosen as the comparison standard because a horizon of $N > 3$ did not result in a significant improvement in the economic performance compared to $N = 3$. Comparing the EMPC with $N = 3$ and that with $N = 7$, for instance, the EMPC with $N = 7$ computation time is approximately six times greater than that of $N = 3$, while the increase in the economic performance is less than 0.0005 (i.e., less than 0.03%).

Case 3: Different Number of Output Measurement Points

For this case, we apply the output feedback EMPC systems of Eq. 8.21 using different numbers of available measurement points, i.e., $p = 6, 11, 21$. Operation over an operation period of $t_p = 1.0$ was considered. Different number of output measurement points bring in

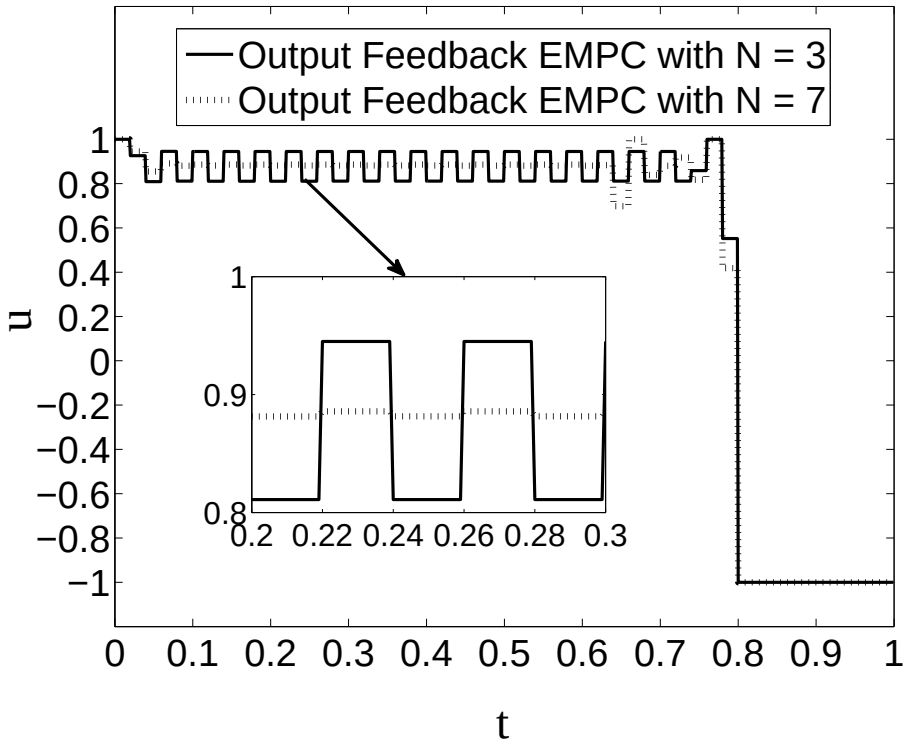

Figure 8.14: Manipulated input profiles of the output feedback EMPC system of Eq. 8.21 based on 11 measurements of x_1 using different prediction horizons, N.

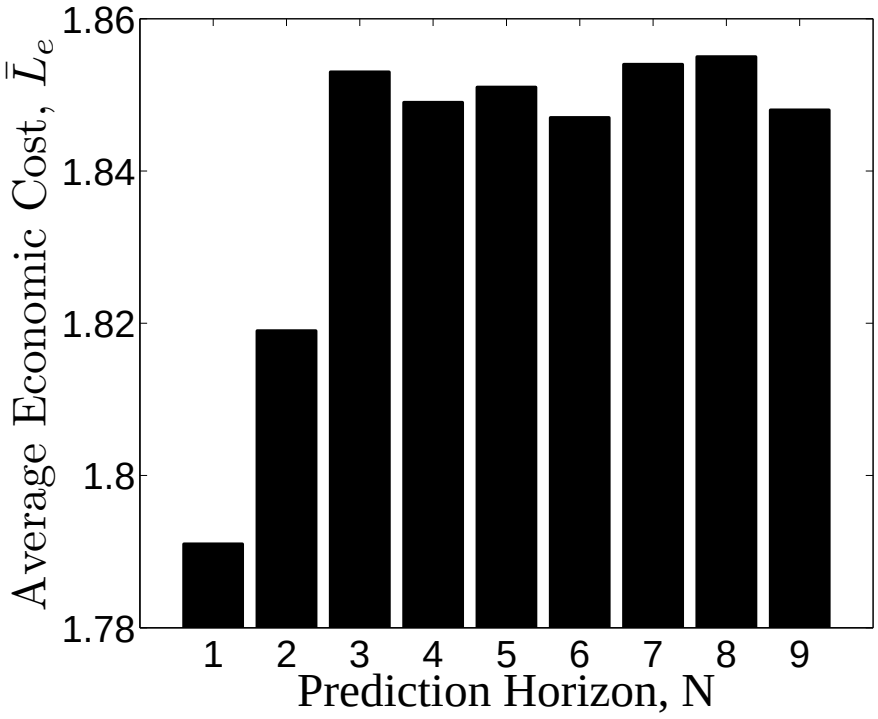

Figure 8.15: Average economic cost, $L_e(t)$, along the length of the reactor under the output feedback EMPC system of Eq. 8.21 based on 11 measurements of x_1 using different prediction horizons, N.

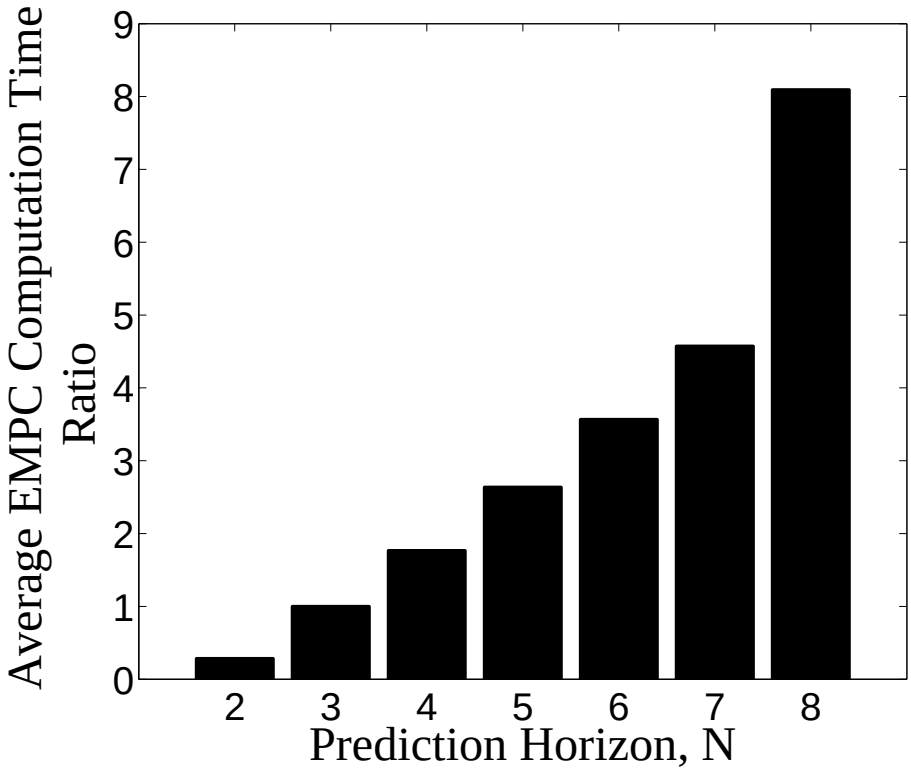

Figure 8.16: The ratio of the average EMPC calculation time with the specified prediction horizon to the average EMPC calculation time with a prediction horizon of $N = 3$.

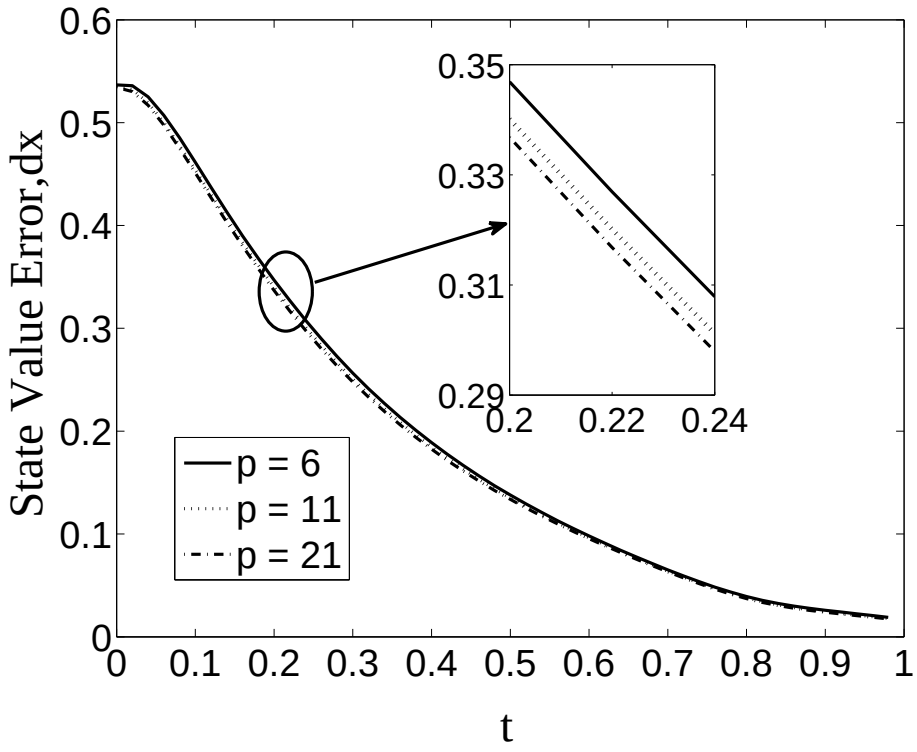

Figure 8.17: State estimation error profiles of the process under the output feedback EMPC system of Eq. 8.21 with $N = 3$ using different numbers of measurement points, p, of x_1.

different state estimation error profiles for the same output feedback control formulation of Eq. 8.13 as shown in Fig. 8.17. From the magnified plot in Fig. 8.17, we can see that more available measurement points can slightly increase state estimation error convergence rate.

8.5 Conclusion

This work presented both state feedback and output feedback EMPC schemes for a system of two coupled hyperbolic PDEs arising in the modeling of a non-isothermal plug flow reactor. Through extensive simulation studies, key metrics like economic closed-loop performance under EMPC versus steady-state operation, impact of horizon length on com-

putation time and economic performance, effect of number of measurement points on state estimation and closed-loop economic performance were evaluated and discussed. Future work will attempt to develop a theoretic framework of the presented computation algorithms.

Chapter 9

Computational Fluid Dynamics Modeling of Industrial Level Steam Methane Reformer

9.1 Introduction

The steam methane reforming (SMR) process, which produces bulk hydrogen gas from methane through catalytic reactions, is the most common commercial method for industrial hydrogen production. A general industrial level SMR process can be described by the schematic of Fig. 9.1. The steam methane reformer (for simplicity, it is denoted as "reformer" in the following context) is the core unit in a SMR process which has separate process side and furnace side that interact through heat exchange on the reforming tubes. In the furnace side, combustion of the furnace side feed, usually a mixture of methane, hydrogen, carbon dioxide, carbon monoxide and air, heats the reforming tubes via radiative heat exchange; in the process side, catalytic reactions take place inside the reforming tubes converting steam and methane into hydrogen and carbon oxides (including CO and

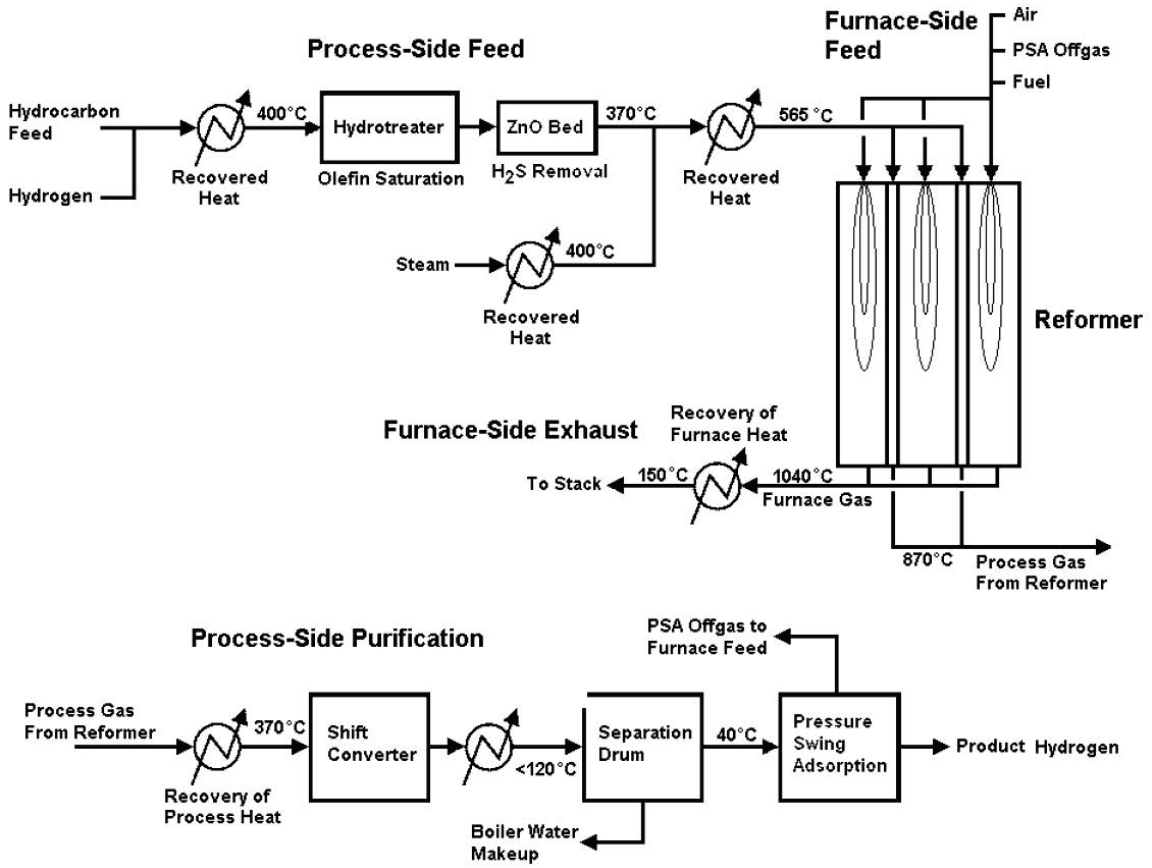

Figure 9.1: Steam methane reforming process diagram.[110]

CO_2) in the reforming tubes. A traditional top-fired, co-current furnace usually includes the top burners which are fed with the furnace side feed, the refractory walls containing the combustion products, the flue gas tunnels transporting the flue gas out of the reformer, and the reforming tubes.

For the last 50 years, extensive work has been performed on the development of reformer first principles models. The mathematical modeling methodology of the complete reformer modeling was first proposed and developed in 1960s.[99] With the improving understanding of both physical and chemical phenomena inside the reformer, more comprehensive mathematical models have been developed considering more detailed and precise radiation mechanisms, combustion models, flue gas flow patterns, reforming reaction kinet-

ics and packed bed reactor models.[89] However, solving these complete reformer models is computationally expensive due to the increasing complexity of the fundamental nonlinear differential equations describing reformer physical-chemical phenomena. Also, for large reformers with complicated geometry, mathematical modeling becomes very difficult in dealing with the geometry characteristics and various boundary conditions.[89]

On the other hand, with the dramatic development of computing power, Computational Fluid Dynamics (CFD) modeling has become an increasingly important platform for reformer modeling and design, combining physical and chemical models with detailed representation of the reformer geometry. When compared with first-principles modeling, CFD is a modeling technique with powerful visualization capabilities to deal with various geometry characteristics and boundary conditions. Moreover, CFD modeling provides more flexibility to modify design parameters without the expense of hardware changes which brings large economic and time savings.[135]

CFD technology has been successful in carrying out the simulation of industrial furnaces[7,63,109,131] and SMR tube reactors, i.e., reforming tubes modeled as packed-bed reactors.[13,18,35,62] Although both the furnace side and the process side have been extensively researched, no work has been done on developing a CFD model of an industrial level reformer. An industrial level reformer usually has a relatively large size and detailed geometry characteristics.[89] To understand the detailed coupling relationship between the process side and the furnace side, a full-size CFD model of a reformer which includes both the furnace and process sides becomes a necessity; meanwhile, it is not suitable to simulate each side separately due to the close interaction between these two sides and the presence of complicated geometry. With the development of commercial CFD software, like ANSYS Fluent, CD-Adapco Star CCM+, and OpenFOAM, new modeling tools and functions are becoming available for developing the CFD model of a complete industrial-level reformer coupling the furnace side and the process side.

In the area of SMR modeling, CFD can be used to design, optimize and even monitor SMR processes. For example, flow profiles of flue gas significantly determine the total energy efficiency of the furnace. Specifically, CFD simulation can provide comprehensive information about a flow field to check flue gas maldistribution, especially in regions where measurements are either difficult or impossible to obtain. Moreover, large-scale configuration and high furnace temperature make furnace condition monitoring difficult. On the other hand, CFD simulation can help reformer designers predict the temperature distribution inside the reformer. During the normal furnace operation, the uniformity of temperature distribution in the furnace chamber is one of the important indices for determining a reformer's performance. In most industrial SMR furnaces, the flame temperature could be up to 2000 K which makes radiation to be the dominant heat transfer mechanism. For heat radiation, nonuniform temperature distribution in the furnace chamber can greatly decrease the radiative heat transfer efficiency. In terms of the reforming tubes, the furnace is required to be operated slightly below the design tube wall temperature to keep the tube wall temperature within the safe margin and eliminate hot spots so that the potential stress-to-rupture of tube materials can be avoided.[14] Also, overheating of reforming tubes can result in carbon formation on the catalyst surface inside the reforming tubes which can further decrease the reaction progress and hydrogen production. Through CFD simulation, these above critical issues can be detected and predicted, and corresponding changes can be applied in the improved reformer design and operational parameters.

Based on the above considerations, in this work, we develop a CFD model of an industrial level reformer including both furnace and process sides. Firstly, the CAD geometry of the objective industrial level reformer is designed. Then, to develop the full-size CFD model of the reformer, a single reforming tube CFD model is developed to simulate the steam methane reforming reactions within porous media. Secondly, we construct a small-scale reformer model with all key characteristics of the full-size reformer and then develop

its CFD model considering both the combustion in the furnace side and the reforming reactions in the process side as designed in the single reforming tube CFD model. Finally, the successful CFD modeling development method of the small-scale reformer model is applied to the full-size reformer. For the CFD simulation, ANSYS ICEM-CFD is adopted as the mesh generation platform, and ANSYS Fluent is used as the CFD simulation platform.

9.2 Steam Methane Reformer Geometry

9.2.1 Industrial Level Geometry

The reformer investigated in this work is a top-fired, co-current reformer designed by Selas Fluid Processing Corporation.[89] Figs. 9.2-9.5 are the computer aided drafting (CAD) plots of the objective steam methane reformer designed in AutoCAD. Fig. 9.2 is an overall view of the furnace, Fig. 9.3 is a detailed top view of the reformer, Fig. 9.4 is a detailed front view of the reformer, and Fig. 9.5 is a detailed side view of the reformer.

The furnace contains seven rows of forty-eight tubes. The tubes have an external diameter of 14.6 *cm*, an internal diameter of 12.6 *cm*, and an exposed length of 12.5 *m*. The rows of tubes are separated by eight rows of twelve burners. Fuel and air enter through the burners, and the fuel combusts over a flame length of $4.5 - 6$ *m*. The burners in the outer lanes which are next to the furnace walls have lower fuel and air flow rates. The reason is that the burners in the outer lanes are adjacent to only one row of tubes, and using the same air and fuel flow rates for all these burners will cause "over-firing" in the outer lanes and "under-firing" in the inner lanes. In detail, the burners in the outer lanes have to be supplied only 60% as much air and fuel as the inner lanes. Correspondingly, the burners in the outer lanes are smaller than the inner row burners as shown in Fig. 9.3.

At the bottom of the furnace, the rows of tubes are separated by the rectangular intru-

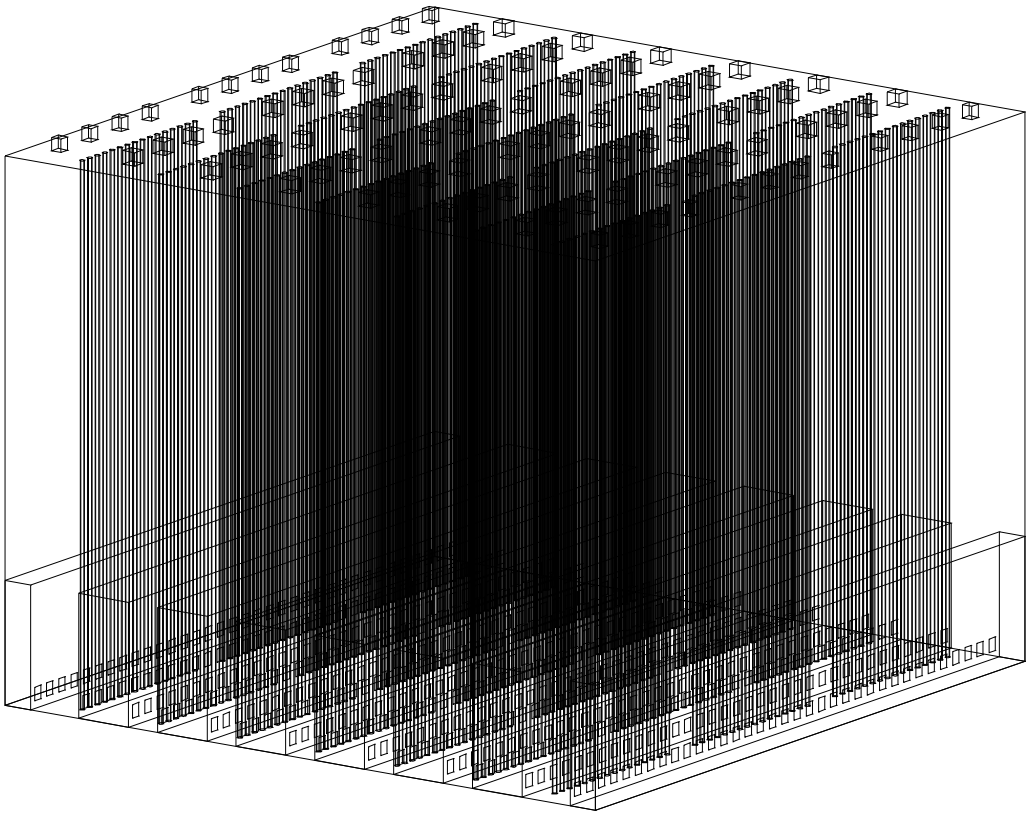

Figure 9.2: Overall view of furnace geometry.

sions known as flue gas tunnels or coffin boxes. The flue gas tunnels extend from the front to the back of the furnace with a height of 2.86 *m* from the floor that allow the furnace flue gas to exit the furnace. Due to the size difference between the burners in the outer lanes and burners in the inner lanes, the width or the opening of the two side flue gas tunnels is smaller than that of the six inner ones. The furnace flue gas enters the tunnels from the furnace chamber and then exits the furnace through the front openings of the coffin boxes, thirty-five extraction ports are distributed in a row along the sides of each flue gas tunnel as shown in Fig. 9.5.

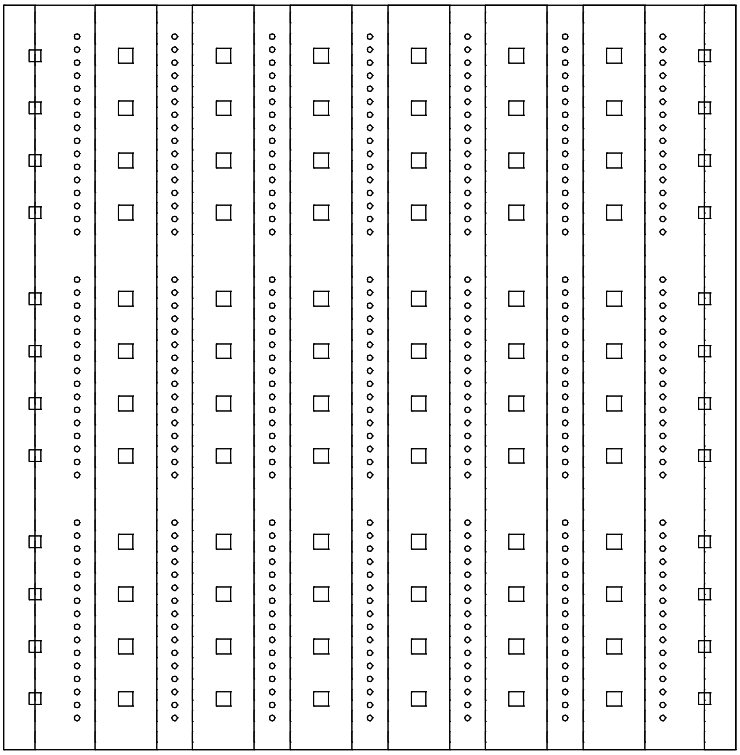

Figure 9.3: Top view of furnace geometry.

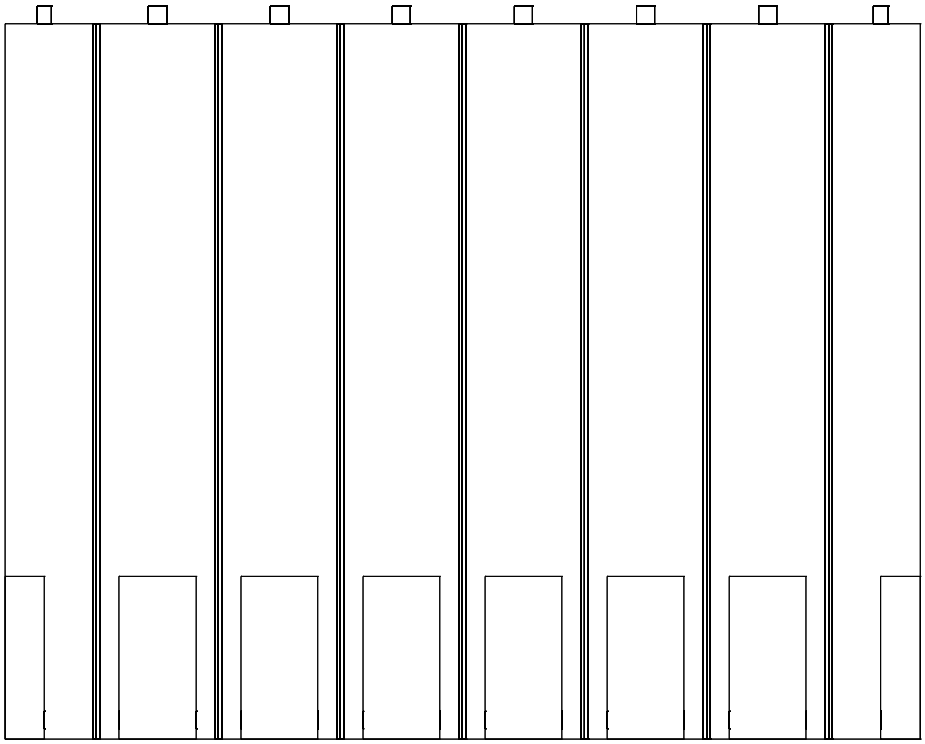

Figure 9.4: Front view of furnace geometry.

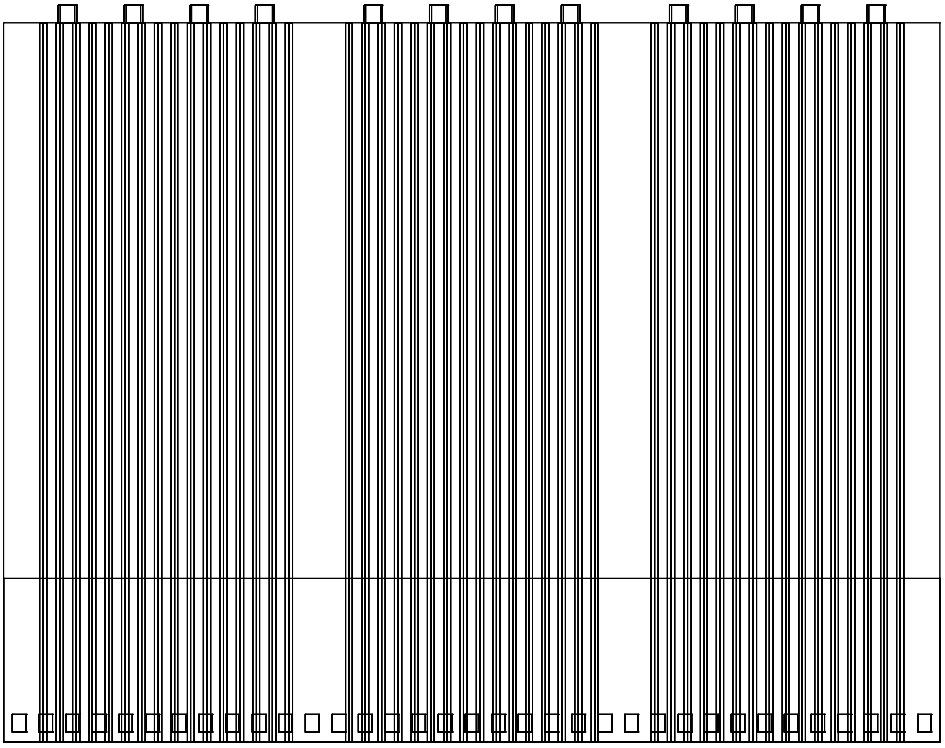

Figure 9.5: Side view of furnace geometry.

9.2.2 SMR Physical Phenomena

As the process gas mixture mainly containing steam and methane flows through the reforming tubes, methane and steam are converted predominantly to hydrogen and carbon dioxide by the catalytic steam methane reforming and water-gas shift reactions. The highly endothermic steam methane reforming reactions are shown in Eqs. 9.1a-9.1b, and the exothermic water-gas shift reaction is shown in Eq. 9.1c where Eq. 9.1c is the sum of Eqs. 9.1a-9.1b. Specially designed nickel oxide over alpha alumina support (i.e., $Ni-\alpha Al_2O$) catalyst particles form a packed bed within the reforming tubes to improve reaction rates. The inside tube surface is in contact with the stationary catalyst and with the moving process gas. The dominant modes of heat transfer inside of the tubes are conduction from the inner tube walls to the network of catalyst particles, convection from the inner tube wall to the process gas, and convection between the process gas and the catalyst particles. These modes of heat transfer work together to transfer heat from hot regions to cold regions and provide the required heat for the endothermic reforming reactions.

$$CH_4(g)+H_2O(g) \quad \rightleftarrows \quad CO(g)+3H_2(g) \qquad \triangle H_1^0=+206\ kJ/mol \tag{9.1a}$$

$$CO(g)+H_2O(g) \quad \rightleftarrows \quad CO_2(g)+H_2(g) \qquad \triangle H_2^0=+164.9\ kJ/mol \tag{9.1b}$$

$$CH_4(g)+2H_2O(g) \quad \rightleftarrows \quad CO_2(g)+4H_2(g) \qquad \triangle H_3^0=-41\ kJ/mol \tag{9.1c}$$

The heat to drive the reforming reactions originates from the combustion side of the furnace. In the furnace, fuel and air combust over the flame length, and the combustion products flow from the top of the furnace to the exit at the bottom through the flue gas tunnels. The energy released by the combustion of furnace fuel can exit the furnace in three ways: through the tube wall to the process side, through the refractory wall to the external environment, or out of the furnace with the bulk flow of flue gas. In high-temperature

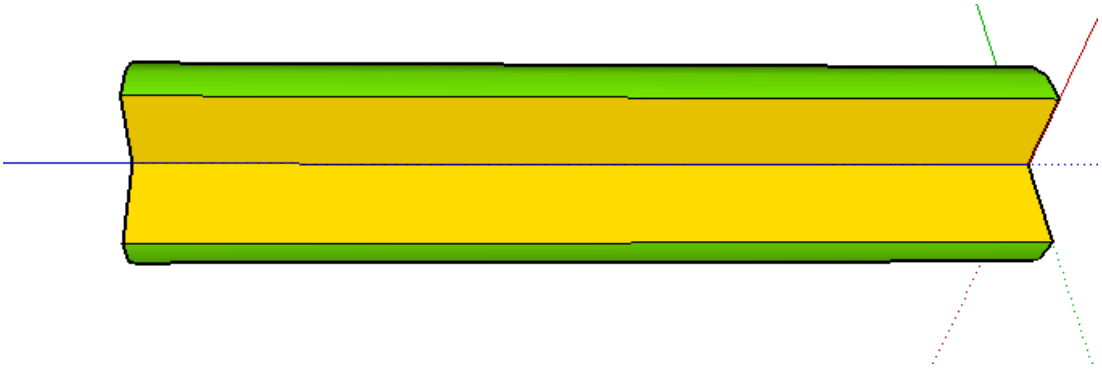

Figure 9.6: 2D axisymmetric tube geometry.

furnaces, the dominant mode of heat transfer to the tube walls and the refractory wall is radiation. In addition to radiative heat transfer, the flue gas transfers energy by bulk gas motion to other regions of the furnace and by convection to the refractory wall and tubes. The refractory wall transfers energy by conduction to the external environment, and receives energy by radiation and by convection from the furnace flue gas. The tubes transfer energy by conduction to the process side and receive energy by radiation and by convection from the furnace flue gas.

9.3 Single Reforming Tube Model

9.3.1 Tube Geometry and Meshing

To develop a full-size CFD model of the reformer, we initially developed a single reforming tube CFD model. Due to the axisymmetric geometry property of the reforming tube as shown in Fig. 9.6, a two-dimensional ($2D$) axisymmetric tube geometry and its corresponding mesh structure were employed. The $2D$ axisymmetric tube mesh which is shown in Fig. 9.7 was constructed in the meshing software ICEM-CFD.

Mesh quality is the most critical issue for accurate and successful CFD modeling. The $2D$ axisymmetric tube mesh only contains 24690 quadrilateral nodes cells, with a 100%

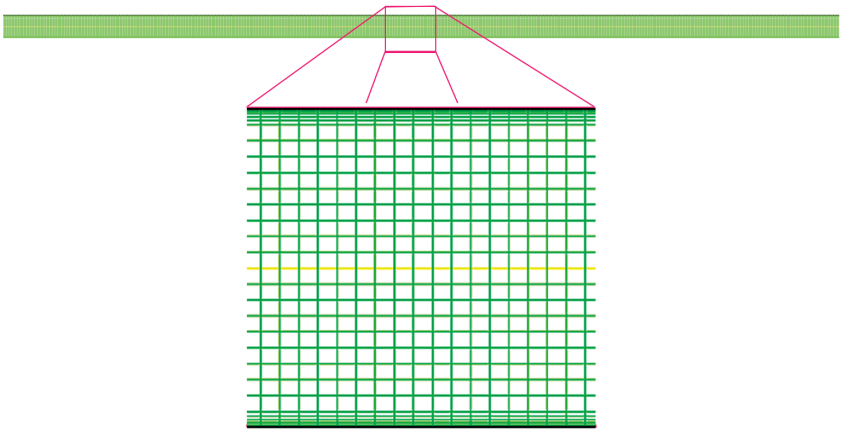

Figure 9.7: 2D axisymmetric tube mesh.

orthogonal quality. Then, the CFD simulation of the single reforming tube only uses half of the tube mesh considering its $2D$ axisymmetric properties. Consequently, this 2D axisymmetric tube mesh brings large computational efficiency over a three-dimensional tube CFD model.

9.3.2 Reforming Reaction Mechanism

The rates of conversion of reactants, i.e., steam and methane, into products, i.e., hydrogen, and the direction of the reforming reactions and the water-gas shift reaction under different conditions (concentration, temperature and pressure) must be accurately accounted for by using a reaction kinetics model. In a reformer, the reforming reactions and water-gas shift reaction occur at the catalyst active sites. In the reforming tubes, reactants need to diffuse from the bulk process gas to the surface of the catalyst and then into the catalyst pores; after the formation of the products, products need to desorb from the catalyst cores and reenters the bulk process gas. However, a kinetic mechanism model that provides a detailed treatment of these catalyst-specific phenomena would be unnecessarily complex. From the point of view of CFD modeling, the packing pattern of catalyst particles inside the packed bed reactor is hard to describe in the packed bed geometry design.

In this single reforming tube CFD model, an intrinsic SMR reaction kinetic mechanism[141] is used to describe the reactions happening inside the reforming tubes. The SMR reaction kinetics are in Eq. 9.2 which is widely adopted in both CFD modeling and mathematical modeling.

$$CH_4(g) + H_2O(g) \rightleftarrows CO(g) + 3H_2(g), \quad r_1 = \frac{k_1}{p_{H_2}^{2.5}} \left(p_{CH_4} p_{H_2O} - \frac{p_{H_2}^3 p_{CO}}{K_1} \right) / DEN^2 \tag{9.2a}$$

$$CO(g) + H_2O(g) \rightleftarrows CO_2(g) + H_2(g), \quad r_2 = \frac{k_2}{p_{H_2}} \left(p_{CO} p_{H_2O} - \frac{p_{H_2} p_{CO_2}}{K_2} \right) / DEN^2 \tag{9.2b}$$

$$CH_4(g) + 2H_2O(g) \rightleftarrows CO_2(g) + 4H_2(g), \quad r_3 = \frac{k_3}{p_{H_2}^{3.5}} \left(p_{CH_4} p_{H_2O}^2 - \frac{p_{H_2}^4 p_{CO_2}}{K_3} \right) / DEN^2 \tag{9.2c}$$

To realize this reaction mechanism in CFD simulation by Fluent, each reversible reaction in Eq. 9.2 is split into two irreversible reactions. The reaction rates in Eq. 9.2 are implemented in Fluent by designing a user defined functions (UDF) file. Since these intrinsic reaction kinetics do not consider the internal and external diffusion resistances onto the catalyst particle, the reaction rates in Eq. 9.2 are multiplied by the effectiveness factor, 0.1.[140]

9.3.3 Compressible Gas

The process side inlet operating conditions of the reforming tubes are given in Table 9.1. Based on the inlet conditions, the Mach number for the jets into the tube is greater than 0.3, and therefore, the density variations due to high static pressure cannot be ignored. Based on this consideration, the compressible ideal gas state equation is adopted to describe the compressibility of the process side gas. From the point of view of CFD simulation, when

Table 9.1: Process side gas inlet operating conditions.

Pressure (kPa)	Temperature (K)	Flow rate (kg/s)	x_{CH_4}	x_{H_20}	x_{CO}	x_{H_2}	x_{CO_2}
3038.5	887	0.1161	0.2487	0.7377	0.0001	0.0018	0.0117

Table 9.2: Reforming reaction catalyst properties.

Density, ρ_c	Heat Capacity, $C_{p,c}$	Thermal Conductivity, k_c	Particle Diameter, D_p
1090 kg/m^3	718 $J/(kg \cdot K)$ at 1100 K	2.7 $w/(m \cdot K)$ at 1100 K	3.5 mm (average)

a pressure-based solver is used, like the one we chose for the simulation in this work, an accurate gas state equation is very critical to simulation accuracy.

A pressure-based solver that enables the pressure-based Navier-Stokes solution algorithm[75] is chosen over the density-based type solver. It is more suited for a wider range of physical models and features which are unavailable to the density-based solver, i.e, premixed combustion model, physical velocity formulation for porous media, and reacting channel model. It also provides more freedom for the simulations while converging to the same results obtained by the density-based solver.

9.3.4 Porous Zone Design

Although the physical catalyst particle is not explicitly considered in the reforming tube modeling, a detailed porous zone model is designed to describe the effect of packing material on the total reaction rate and the pressure drop. To describe porosity, a typical packed bed porosity value for industrial reformers, $\varepsilon_p = 0.609$, is adopted. The property data of one commercial catalyst, Johnson Matthey's Katalco $23-4Q$ catalyst, which we used in this reforming tube simulation, is shown in Table 9.2.[98]

Pressure drop is significant in industrial SMR tubes when the process side gas flows

through the packed bed. To estimate the pressure drop in the porous zone model in the CFD modeling for turbulent flows, a semi-empirical expression, the Ergun equation,[50] which is applicable over a wide range of Reynolds numbers and for many packing patterns, is adopted as follows:

$$\frac{\Delta P}{L} = \frac{150\mu}{D_p^2}\frac{(1-\varepsilon_p)^2}{\varepsilon_p^3}v_\infty + \frac{1.75\rho}{D_p}\frac{(1-\varepsilon_p)}{\varepsilon_p^3}v_\infty^2 \tag{9.3}$$

where ΔP is the pressure drop through the porous media, L is the depth of the porous media, μ is the viscosity of the fluid, ε is the void porosity of the porous media, v_∞ is the bulk velocity of the fluid, ρ is the density of the porous media, $\frac{150\mu}{D_p^2}\frac{(1-\varepsilon_p)^2}{\varepsilon_p^3}$ is the viscous resistance coefficient and $\frac{1.75\rho}{D_p}\frac{(1-\varepsilon_p)}{\varepsilon_p^3}$ is the inertial resistance coefficient. To indicate the directions for which the resistance coefficients are defined, we assume that the viscous and inertial resistance coefficients are both defined in the same manner. In particular, their directions are along direction vectors, $v_1 = [1,0]$ (i.e., the principal axis direction) and $v_2 = [0,1]$ (i.e., the radius direction) in the Cartesian $2D$ coordinate system.

9.3.5 Turbulence and Boundary Layers

Based on the inlet conditions of the process (tube) side gas as shown in Table 9.1, the Reynolds number is calculated to be approximately 5500. To accurately describe the turbulence phenomena inside the reforming tube, we choose the standard two-equation turbulent kinetics energy and turbulent dissipation rate ($k-\varepsilon$) model[78,90] which is developed from the Reynolds-averaged Navier-Stokes (RANS) equations. The $k-\varepsilon$ turbulent model is applicable for many flows, and relatively simple to implement and easy to converge from the point of view of CFD simulation.

Turbulent flows are significantly affected by the walls. The near-wall modeling decides the fidelity of numerical solutions. After all, it is in the near-wall region that the solution

variables have large gradients, and the momentum and other scalar transports occur most vigorously. Therefore, an accurate representation of the flow in the near-wall region determines successful predictions of wall-bounded turbulent flows. For this single reforming tube CFD model, the enhanced wall treatment function in Fluent is applied as the near wall treatment method. The enhanced wall treatment ε-Equation is suitable for complex fluid dynamics especially for those with lightly turbulent flow, and it only requires a few nodes in the boundary layer when using $k-\varepsilon$ model.[74]

For this reforming tube model, boundary layer design is very critical to model the heat convection from the inner wall to the process gas and the heat conduction from the inner wall to the catalyst particles. To get the first node height from the inner wall surface for the boundary layer design, NASA's Viscous Grid Spacing Calculator[1] is adopted based on a suitable Y^+ value.[74] For this specific single reforming tube geometry, five nodes are applied in the boundary layer at the tube inner surface as requested by the two-equation $k-\varepsilon$ model and the enhanced wall treatment function. The first node height is 8.26×10^{-4} m, and the node spacing ratio in the boundary layer is 1.2. The detailed mesh structure for the boundary layer design is demonstrated in Fig. 9.7. We note here that the NASA's Viscous Grid Spacing Calculator[1] uses fixed viscosity, pressure and temperature for the fluid properties which may not be suitable for most SMR calculations. Through a decompiling of the calculator, a revised algorithm based on the original calculator is developed for our specific inlet conditions of the process side gas.

9.3.6 Reforming Tube Boundary Conditions

For an industrial level reformer, the tube skin temperature is usually in the range of 1100 K to 1148 K.[89] For this single reforming tube simulation, we used a pre-defined constant temperature profile for the boundary condition of the tube outer surface (process side) which is

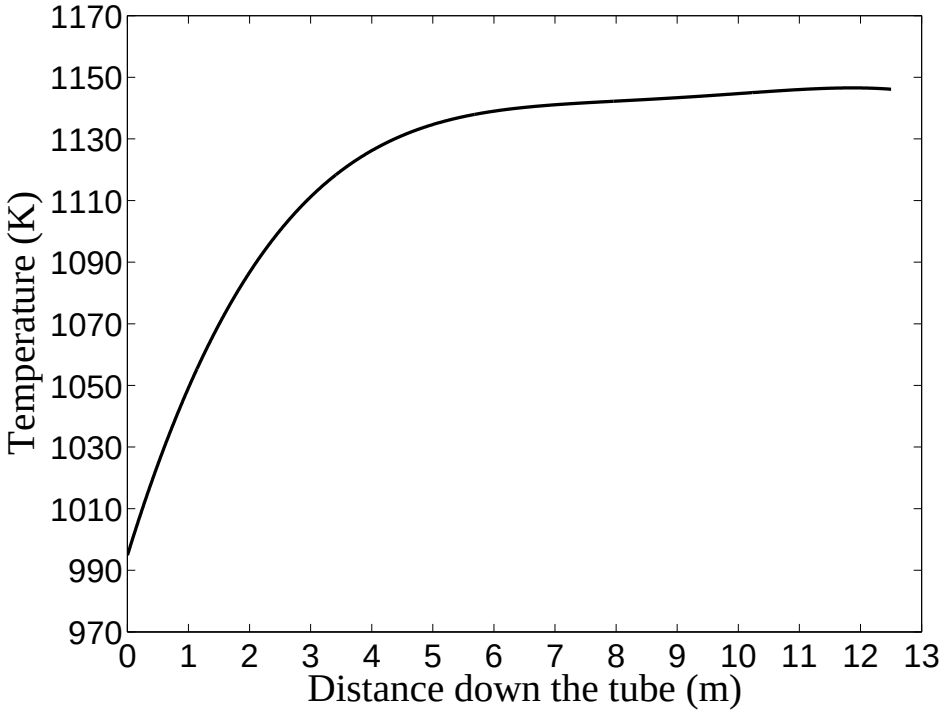

Figure 9.8: User defined tube skin temperature profile.

Table 9.3: Reforming tube material properties.

Density, ρ_t	Heat Capacity, $C_{p,t}$	Thermal Conductivity, k_t	Emissivity, ε_t
7720 kg/m^3	502 $J/(kg \cdot K)$ at 1144 K	29.58 $w/(m \cdot K)$ at 1144 K	0.85 at 1144 K

shown in Fig. 9.8. Under this setting, the reforming tubes are modeled as a heat sink with a constant boundary condition, and the heat is transferred from the outer surface to the inner surface through heat conduction. The corresponding tube material properties are listed in Table 9.3.[33]

9.3.7 Simulation Results

CFD Model of Single Reforming Tube: Results Comparison

Using a parallel computational environment with message passing interface technology, the single reforming tube simulation converges in about 5 minutes with the steady solver in a 4-core CPU desktop computer. The steady-state results of the simulations are displayed in Figs. 9.9-9.16. We note here that due to the large length to diameter ratio of the reforming tube, in all the simulation result plots, the radius is scaled up by 10 times which is convenient for display purposes only. Specifically, in Fig. 9.16, the pressure profile without gradients in the radial direction results from the direction definitions of the resistance coefficients in Section 9.3.4.

Based on the wall temperature profile in Fig. 9.8, the corresponding inner wall temperature profile from the converged model is displayed in Fig. 9.17, and the corresponding heat flux profile is shown in Fig. 9.18.

We compared the single reforming tube CFD model with a typical set of industrial level plant data. Specifically, the typical plant data of a reforming tube outlet is with the same process side inlet conditions, similar catalyst properties, and the same tube geometry structure. All the mole fraction values in Table 9.4 are the area-weighted average values at the tube outlet. We prove that our simulation result is very close to that of the plant data for both temperature and species compositions.

Effects of Porous Media

The intrinsic reaction rates[141] we adopted already account for the existence of catalyst in the reforming tubes. Furthermore, the existence of the porous media in the CFD model is necessary. To establish this point, we conducted two CFD model simulations, i.e., one with the porous zone that we designed in Section 9.3.4 and the other one without the porous

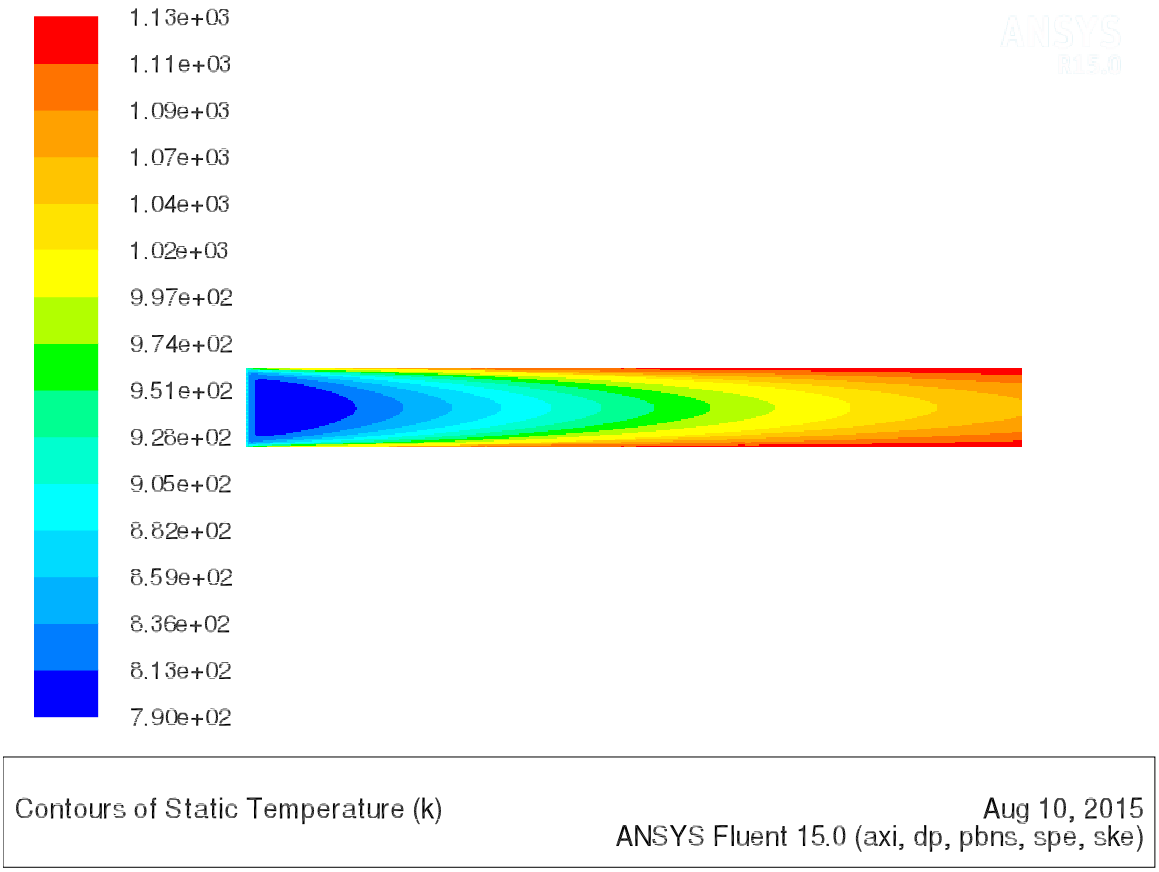

Figure 9.9: Temperature profile inside the reforming tube.

Table 9.4: Single reforming tube results comparison of tube outlets among different sources.

	CFD Result
Temperature (K)	1128.6
Pressure (kPa)	2909.1
x_{H_2O}	0.3554
x_{CH_4}	0.0467
x_{H_2}	0.4621
x_{CO}	0.0825
x_{CO_2}	0.0533
Average Heat Flux ($kW/m^2 \cdot s$)	77.14

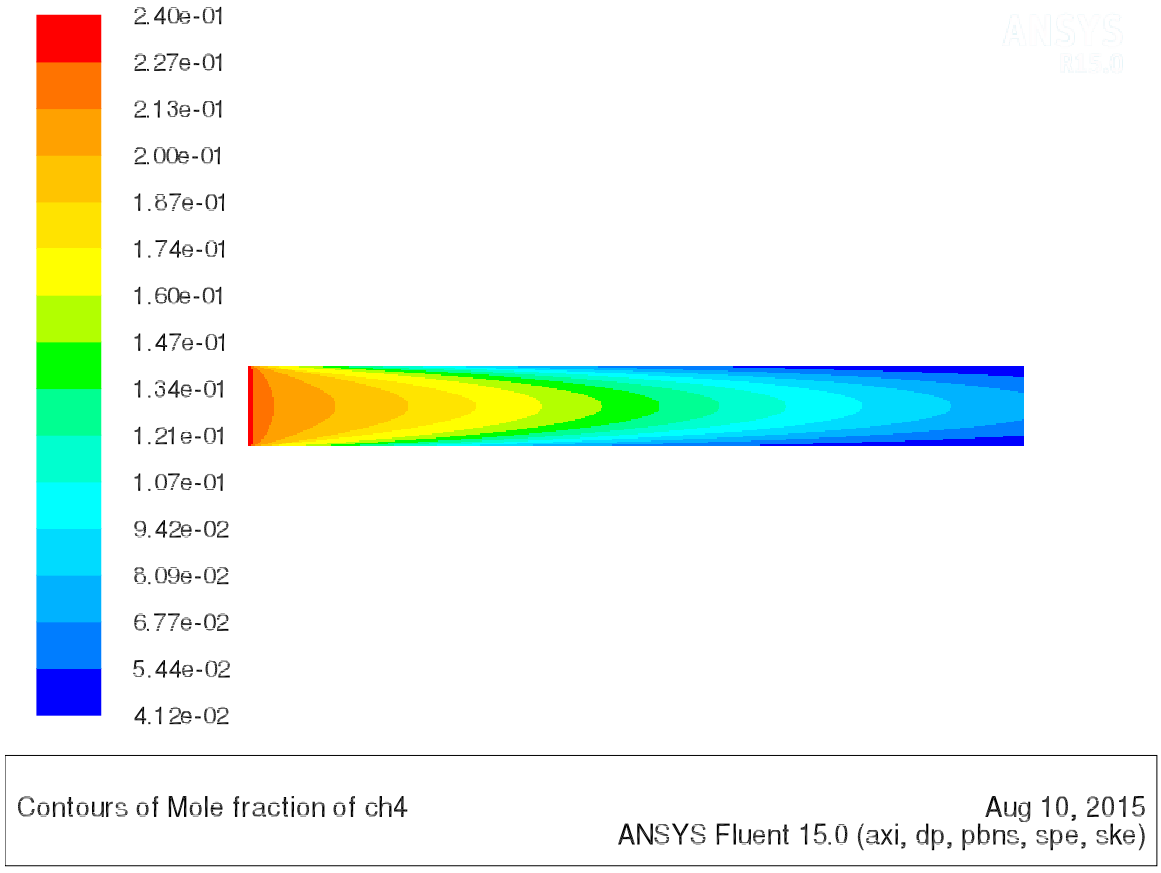

Figure 9.10: CH_4 mole fraction profile inside the reforming tube.

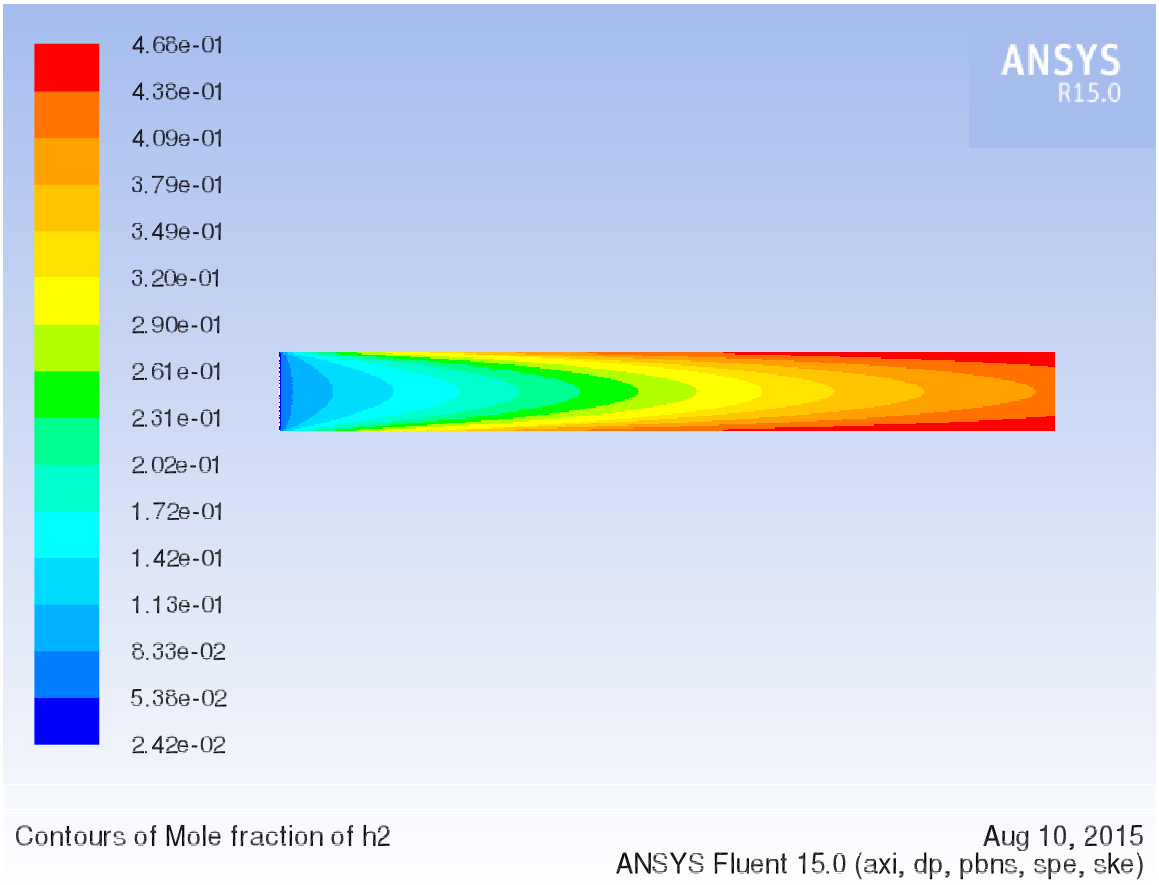

Figure 9.11: H_2 mole fraction profile inside the reforming tube.

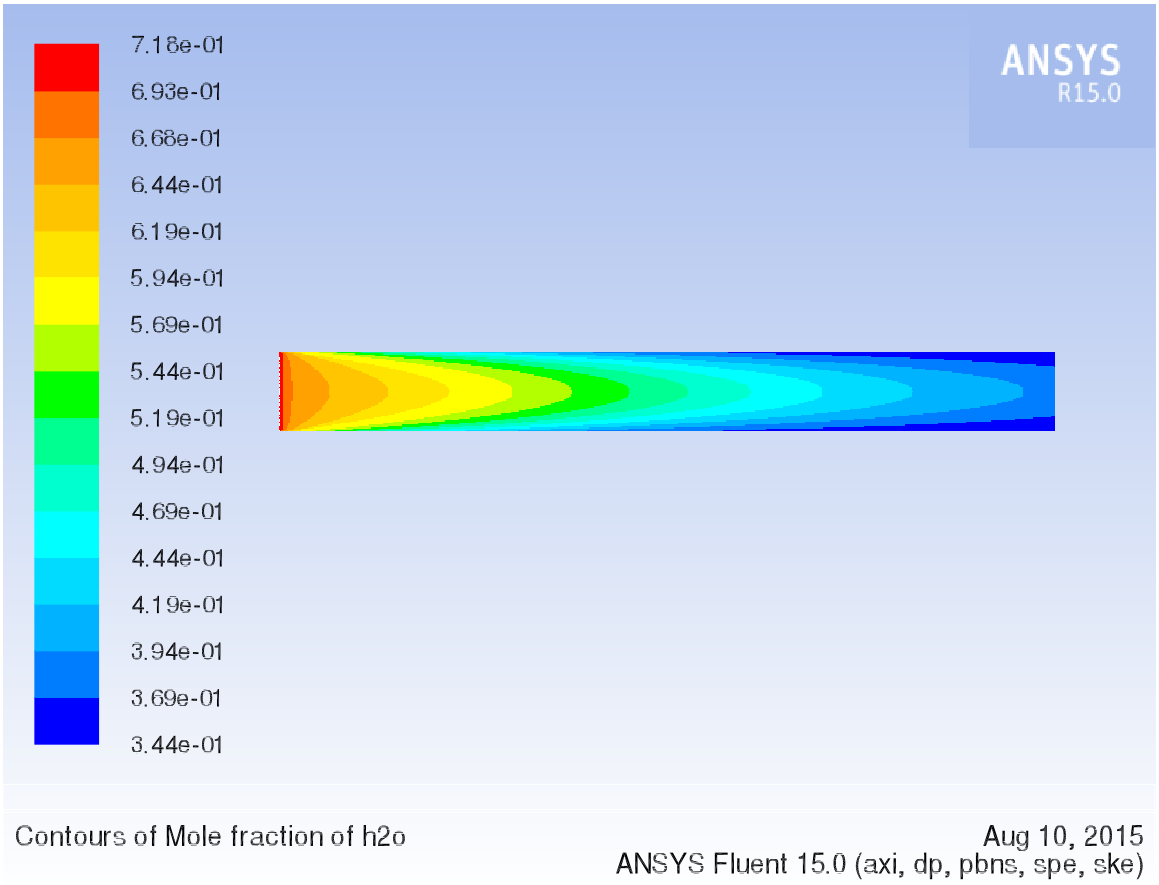

Figure 9.12: H_2O mole fraction profile inside the reforming tube.

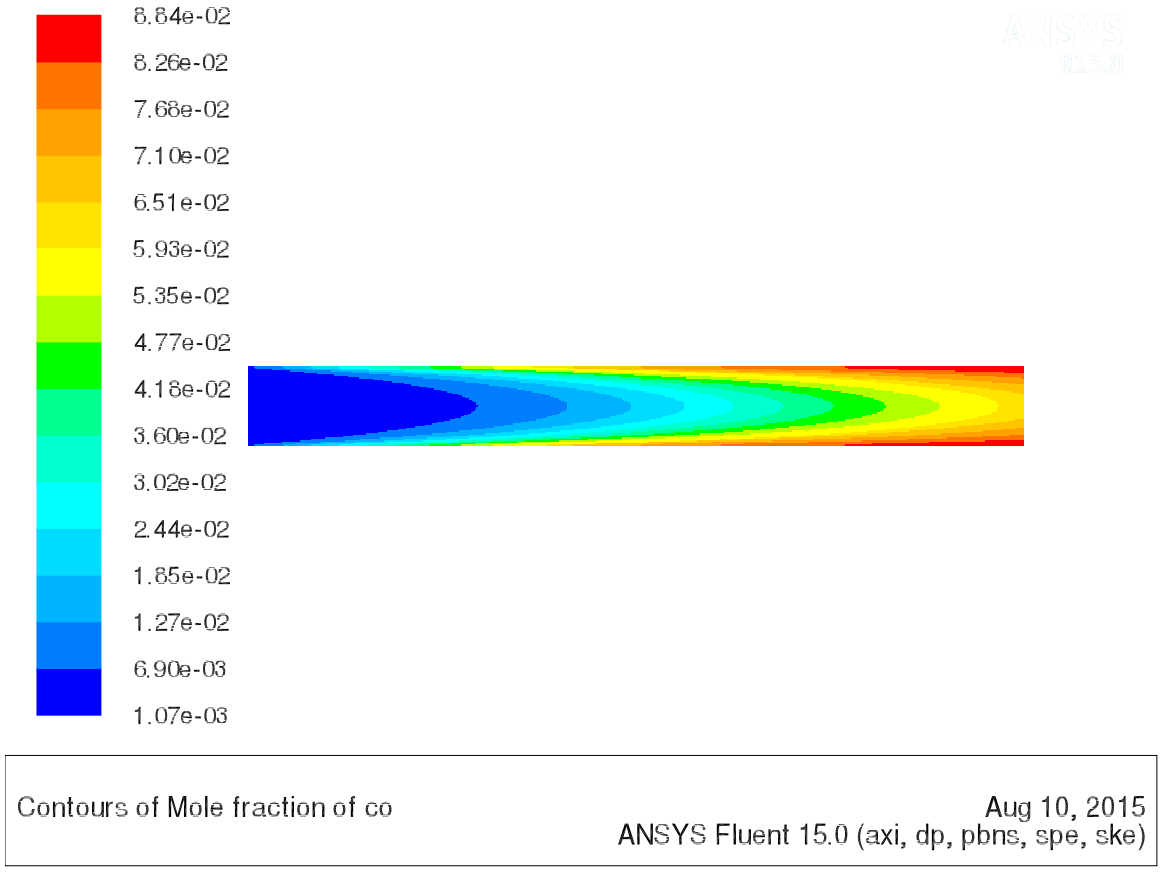

Figure 9.13: *CO* mole fraction profile inside the reforming tube.

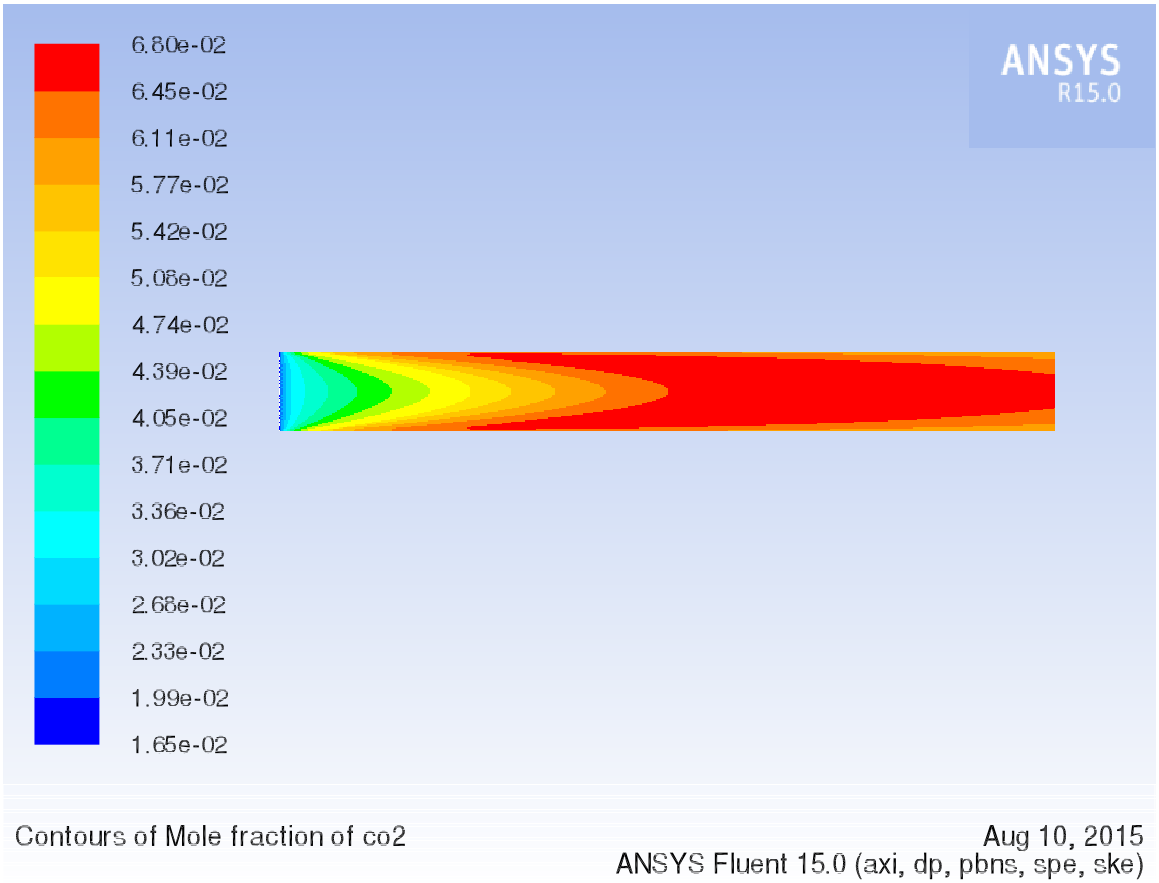

Figure 9.14: CO_2 mole fraction profile inside the reforming tube.

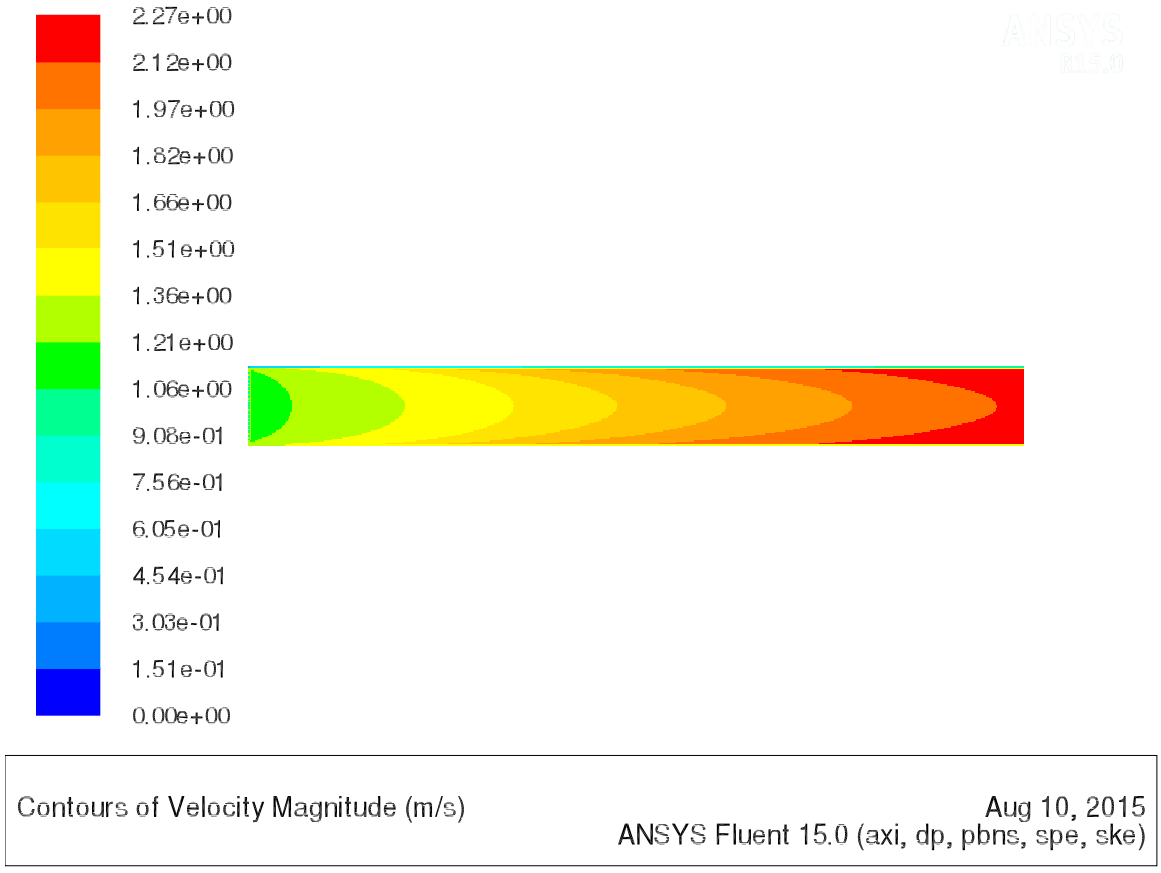

Figure 9.15: Velocity magnitude profile inside the reforming tube.

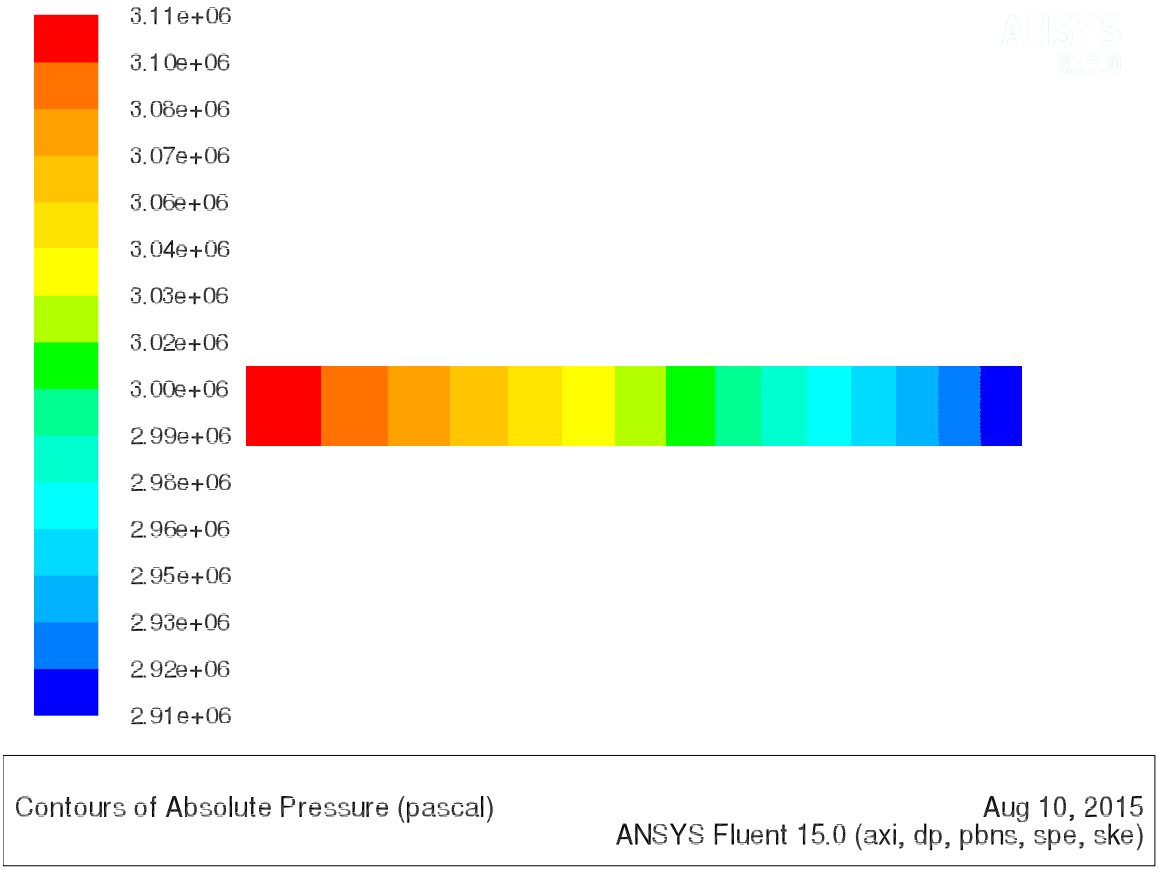

Figure 9.16: Absolute pressure profile inside the reforming tube.

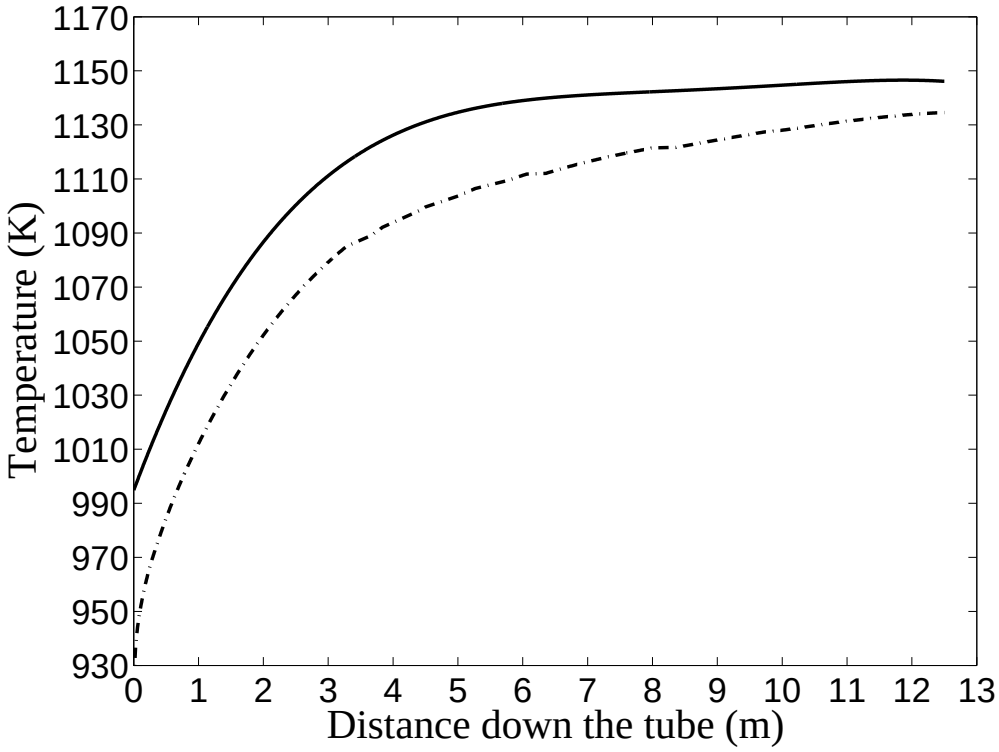

Figure 9.17: Inner (dash-dotted line) and outer (solid line) wall temperature profiles of the reforming tube.

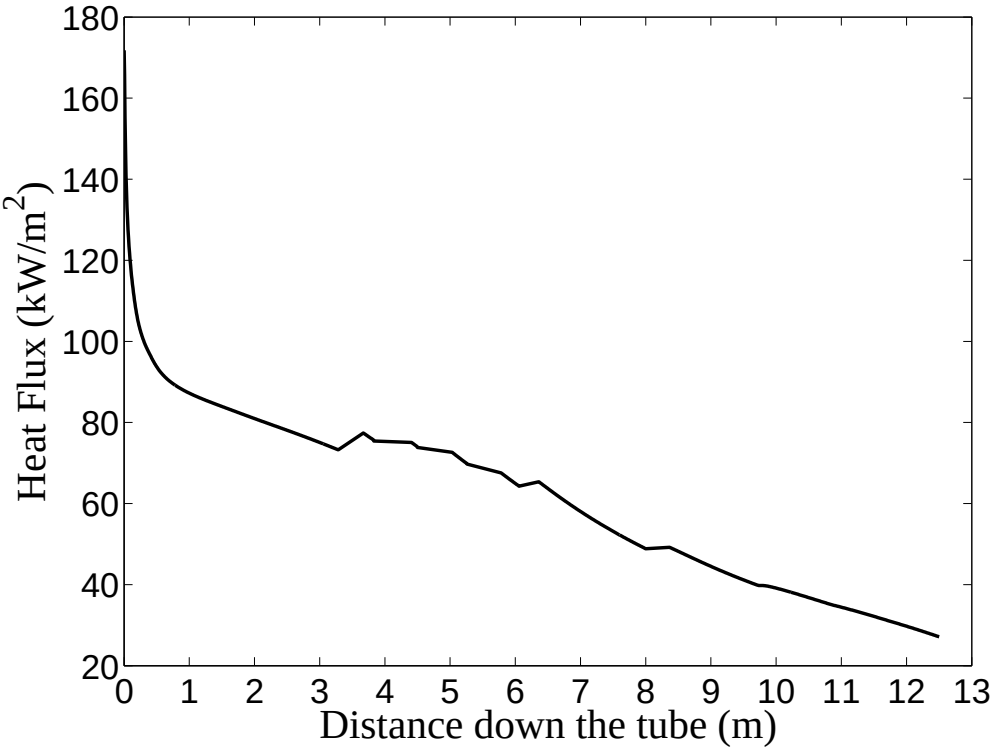

Figure 9.18: Heat flux profile of the reforming tube surface.

zone. However, for the latter CFD model, the intrinsic reaction rates are modified by considering the porosity of the reforming bed since the intrinsic reaction rates[141] are based on unit mass of catalyst. The simulation result of the reforming tube CFD model without the porous zone is shown in Figs. 9.19.

By considering the presence of the catalyst in the reforming tube, more heat can be transferred from the inner wall to the catalyst network by heat conduction. Consequently, a steady state with higher temperature and higher methane conversion rate is reached for the CFD model with porous zones. In detail, comparing Fig. 9.19a with Fig. 9.9, we can see that the porous zone provide much more heat to the packed bed. Moreover, the existence of the porous zone in the reforming tube model increases the residence time of the process side gas, and the product formation rate is increased considerably. From Fig. 9.19b and Fig. 9.11, the H_2 mole fraction at the outlet of the reforming tube without the porous zone is 22% lower than that of the reforming tube with the porous zone due to a shorter residence time and much less heat flux from the tube skin. On the other hand, the catalyst network in the reforming tube increases the friction of the process side gas when it flows through the porous zone. As shown in Fig. 9.19c, the pressure drop of the process gas flow in the reforming tube without the porous zone is negligible. However, for the reforming tube with the porous zone, the pressure of the process gas flow decreases from 3038.5 *kPa* to 2909.1 *kPa* as shown in Fig. 9.16 due to its viscous resistance and inertial resistance of the catalyst particles.

Effects of Equation of State

Due to the high operating pressure of the process side inlet, the compressibility of the process side gas cannot be ignored. To understand the compressibility's effects on the reforming tube, we used three different equations of state of gas, i.e., compressible ideal gas state equation (C-I), Peng-Robinson equation (PR), and Soave-Kwong-Redlich equation

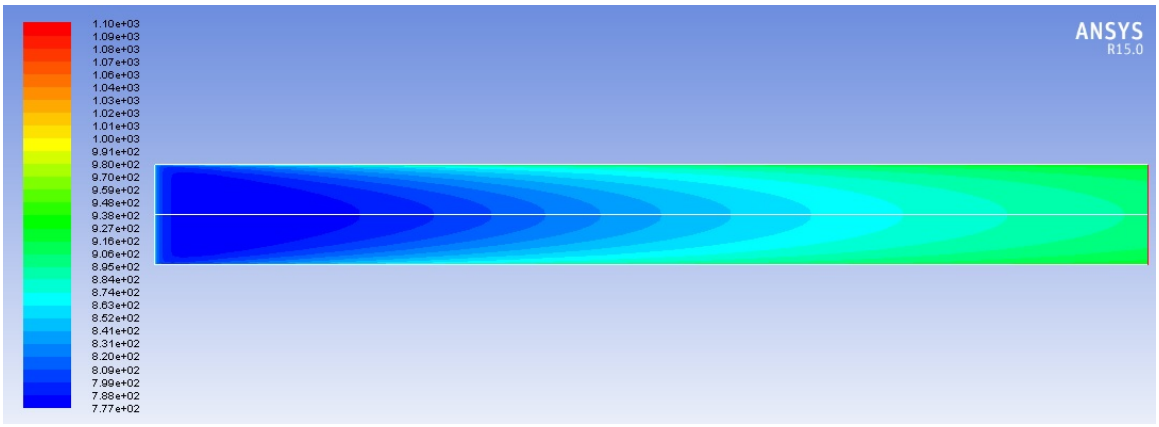

(a) Temperature profile of the reforming tube without the porous zone.

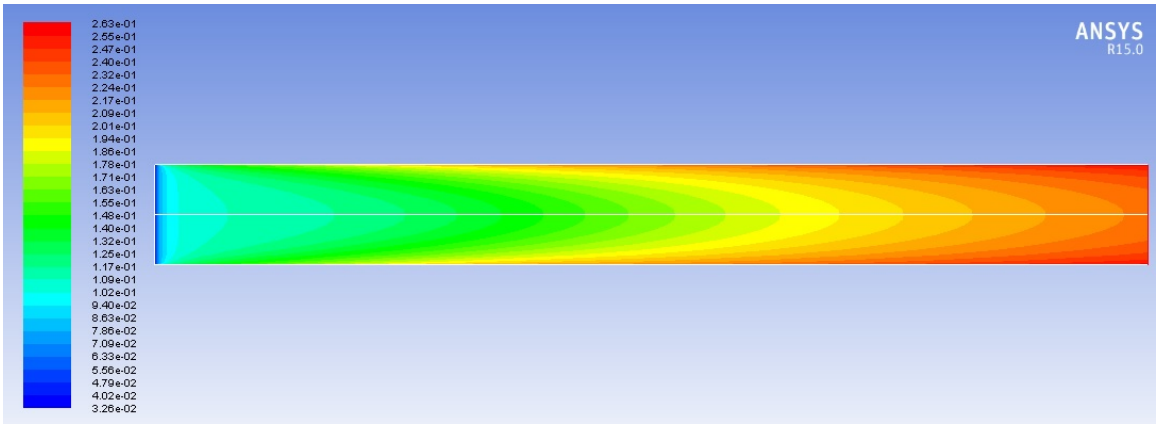

(b) H_2 mole fraction profile of the reforming tube without the porous zone.

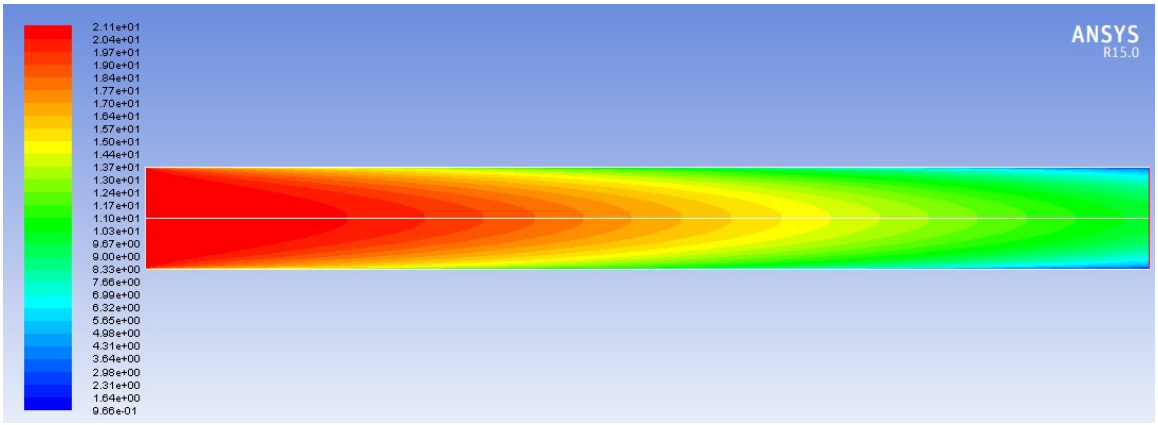

(c) Pressure drop profile of the reforming tube without the porous zone.

Figure 9.19: Effects of porous media on the CFD model of the reforming tube.

Table 9.5: Single reforming tube results comparison of tube outlets under different gas state equations.

	C-I	**SRK**	**PR**
Pressure drop (*kPa*)	129.4	127.5	131.1
T (*K*)	1128.6	1129.4	1130.7
x_{H_2}	0.4621	0.4575	0.4561
x_{H_2O}	0.3554	0.3636	0.3667
x_{CH_4}	0.0467	0.0501	0.0513
x_{CO}	0.0825	0.0811	0.0802
x_{CO_2}	0.0533	0.0477	0.0467
Time cost (s)	312	316	325

(SRK) in the same reforming tube model. The computational efficiency and the simulation results are compared below.

As shown in Table 9.5, the difference of the simulation results from all these three gas state equations of the single reforming tube simulation is negligible. In terms of the computational efficiency of these different gas state equations, the relatively detailed gas state equations, PR and SRK, require more time as demonstrated in Table 9.5 to get the single reforming model converged compared with the compressible ideal gas state equation. Based on the above comparison, the compressible ideal gas state equation is adopted in the following simulations. By doing this, the simulation accuracy is acceptable and at the same time, the computational efficiency of the full-size reformer can also be optimized when three hundred and thirty-six reforming tubes are simulated.

9.4 Small-Scale Reformer Model

9.4.1 Geometry

To model the full-size reformer, we first build a small-scale furnace model which includes both the furnace side and the process side phenomena, as shown in Fig. 9.20. Compared with the full-size model in Fig. 9.2, this small-scale model includes all the key elements of the full-size furnace, i.e., three burners, four reforming tubes and three flue gas tunnels (with flue gas ports). The geometry scales of all these components are consistent with those in the full-size reformer in Fig. 9.2. Similarly, the outer left and right burners are smaller than the ones in the center as requested to avoid overheating of reforming tubes.

9.4.2 Meshing

The most critical part of the CFD process is mesh generation which requires a significant amount of time to obtain a mesh with high quality. For this relatively complex geometry, we designed the mesh in ICEM-CFD using a structured mesh only. A structured mesh/grid results in a smaller number of total mesh elements and better convergence performance in CFD simulation when compared with an unstructured mesh. The generated mesh for the model of Fig. 9.20 has about 1.48 million nodes, which include 1.34 million hexahedrons and 0.22 million quadrilateral cells. The detailed mesh is demonstrated in Figs. 9.21-9.22.

In detail, for both the process gas inlets and furnace gas inlets, the mesh is designed through an O-grid block splitting method, and the detailed mesh of the inlets is designed as shown in Fig. 9.21. At the bottom of the flue gas outlet, there is a more dense mesh designed to avoid reversed flow situations as shown in Fig. 9.22.

For this small-scale reformer, boundary layer is designed not only at the inner surface of the reforming tubes but also at the outer surface to improve the thermal coupling at the

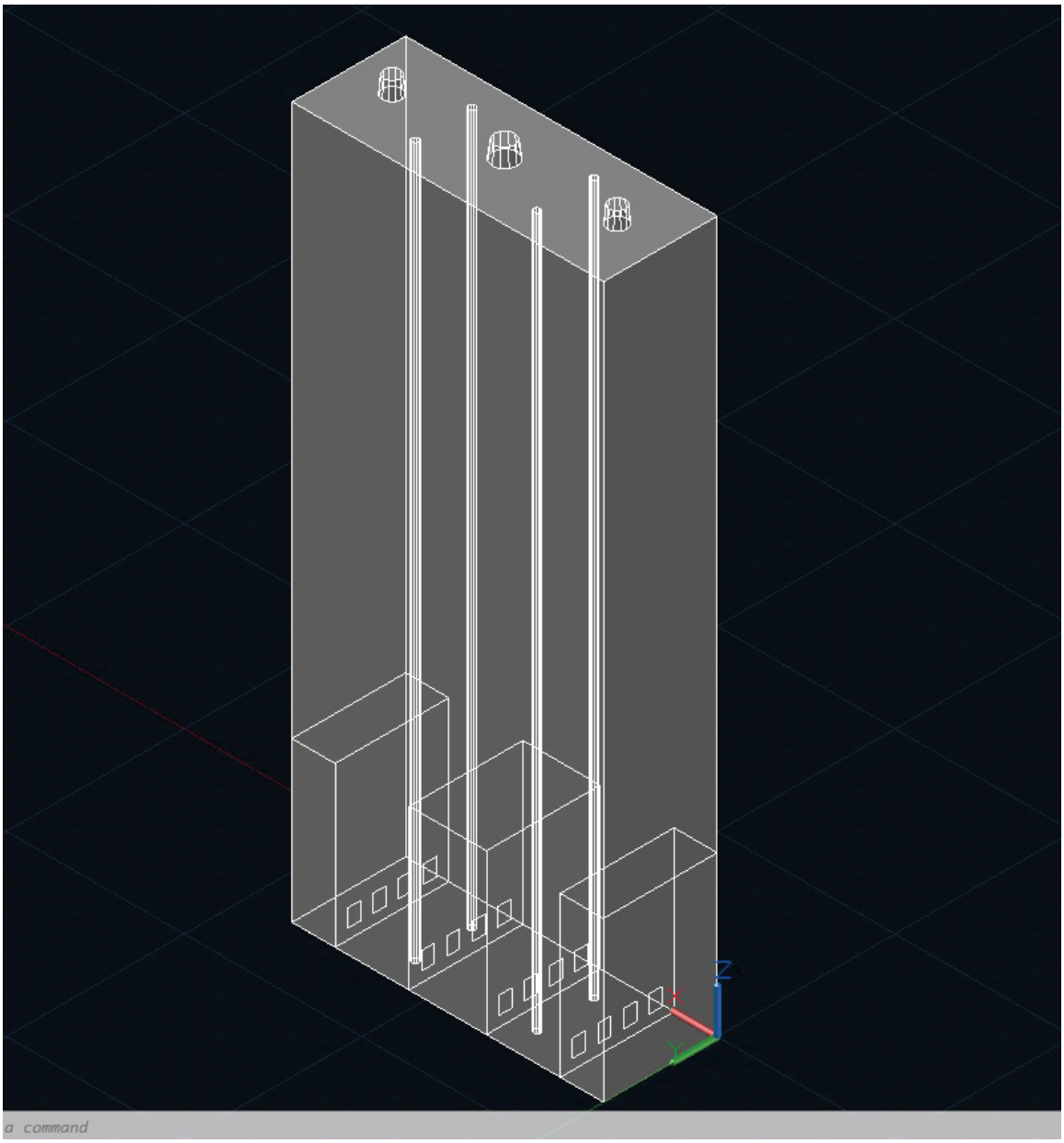

Figure 9.20: CAD geometry of small-scale furnace model.

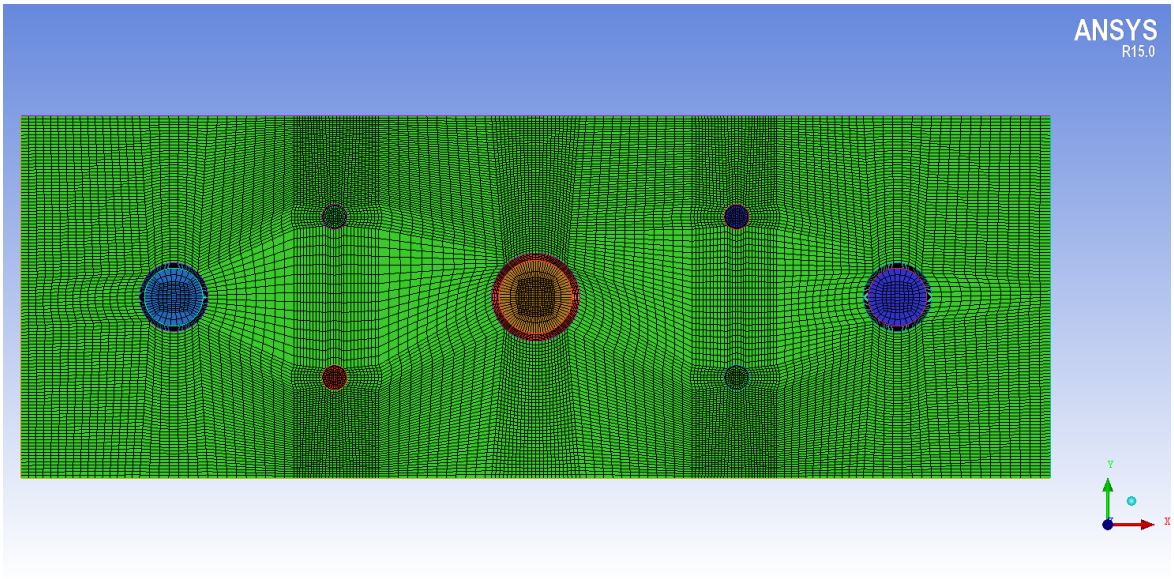

Figure 9.21: Top view of mesh structure of small-scale reformer model.

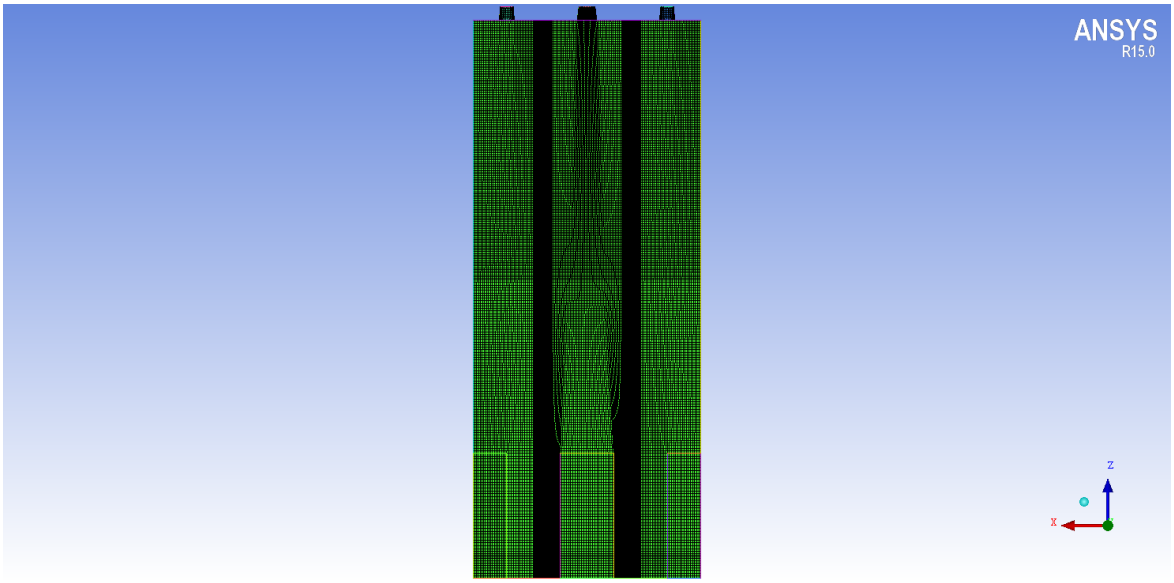

Figure 9.22: Front view of mesh structure of small-scale reformer model.

Table 9.6: Furnace side inlet operating conditions.

Pressure (kPa)	Temperature (K)	Flow rate (kg/s)	x_{CH_4}	x_{H_20}	x_{CO}	x_{H_2}	x_{O_2}	x_{Ar}	x_{N_2}
132.4	524	1.08	0.0517	0.0306	0.0211	0.0540	0.1530	0.0077	0.5793

two sides of the tube wall. Similar to the mesh generation for the single reforming tube CFD modeling, the boundary layer settings for turbulent flow are designed by adopting the revised algorithm based on NASA's Viscous Grid Spacing Calculator. The outer surface of the reforming tube has four nodes in the boundary layer with the first layer height of 6.49×10^{-4} m and the layer spacing ratio of 1.2, and the boundary layer structure of the inner surface of the reforming tube is still the same as that in the single reforming tube CFD model.

9.4.3 Combustion Mechanism

For an industrial reformer, the furnace side gas which is usually composed of three parts, i.e., natural gas, combustion air and tail gas from the secondary reformer is fed to the burners as shown in Fig. 9.1. A typical composition of the furnace side gas fed to the burners is given in Table 9.6 where CO and H_2 come from the tail gas and the inert gas, Ar, is from the combustion air. Based on the composition of the furnace side gas, the combustion is a fuel lean process so that the fuel can be completely combusted. It is noted here that the mass flow rate of 1.08 kg/s is set for the center burner, and as requested by avoiding the over-firing of the left and right burners, the mass flow rate to these two burners is only 60% of that fed to the center burner.

Based on the inlet conditions in Table 9.6, a suitable turbulent gaseous combustion model is applied to describe the turbulence-chemistry interaction of the premixed com-

bustion process. In the premixed flames, the reactants will burn as soon as they enter the computational domain, upstream of the flame stabilizer. To remedy this, ANSYS Fluent provides the finite-rate/eddy-dissipation model where both the Arrhenius reaction rates, and eddy-dissipation reaction rates are calculated.[74] The net reaction rate is taken as the minimum of these two rates. In the eddy-dissipation model, reaction rates are assumed to be controlled by the turbulence which is computationally efficient, and in the finite-rate model, the Arrhenius chemical kinetic calculations are solved. In practice, once the flame is ignited, the eddy-dissipation rate is generally smaller than the Arrhenius rate, and the reactions are mixing limited. Also, only one or two step heat-release mechanisms should be used for the eddy-dissipation model.

Two finite-rate chemistry models are adopted to describe this premixed flow combustion process for CH_4[108] and H_2[10] respectively as shown in Eq. 9.4 and Eq. 9.5. In detail, a two-step CH_4 combustion kinetics model is used whose intrinsic reaction kinetics are described by Eq. 9.4; and an irreversible single step H_2 combustion kinetics model is applied to model the H_2 combustion with the rate of Eq. 9.5b below:

$$CH_4 + 1.5O_2 \rightarrow CO + 2H_2O \tag{9.4a}$$

$$R_1 = 10^{15.22}[CH_4]^{1.46}[O_2]^{0.5217}exp(-20643/T) \tag{9.4b}$$

$$CO + 0.5O_2 \rightarrow CO_2 \tag{9.4c}$$

$$R_2 = 10^{14.902}[CO]^{1.6904}[O_2]^{1.57}exp(-11613/T) \tag{9.4d}$$

$$CO_2 \rightarrow CO + 0.5O_2 \tag{9.4e}$$

$$R_3 = 10^{14.349}[CO_2]exp(-62281/T) \tag{9.4f}$$

Table 9.7: Refractory material properties.

Density, ρ_w	Heat Capacity, $C_{p,w}$	Thermal Conductivity, k_w	Emissivity, ε_w
3950 kg/m^3	718 $J/(kg \cdot K)$ at 1144 K	2.6 $w/(m \cdot K)$ at 1144 K	0.65

$$H_2 + 0.5O_2 \rightarrow H_2O \tag{9.5a}$$

$$R_4 = 1.13 \times 10^{18}[H_2][CO_2]exp(-46.37T_0/T) \tag{9.5b}$$

9.4.4 Radiation

Since the dominant heat transfer mechanism is radiation, a computationally efficient and accurate radiation model plays a significant role in the CFD modeling and simulation. Considering the complex reformer geometry and the complicated coupling of the furnace side and the process side, the radiation model, P-1, is used with the absorption coefficient method of weighted sum of gray gas (WSGG) model. The P-1 model is a relatively simplified radiation model which approximates the angular dependence of the radiative heat transfer equation for a finite number of discrete solid angles. The P-1 model can easily be applied to complicated geometries with curvilinear coordinates.[74] The WSGG-domain-based absorption method in Fluent is a variable coefficient method that uses a length scale, based on the geometry of the model.[70]

To describe the radiation effects from the combustion flame and flue gas to the refractory wall, the thermal properties of the refractory wall are given in Table 9.7.[15]

9.4.5 Initialization

For many complex flow problems such as multiple computational zones with large pressure difference, flow convergence can be accelerated if a better initial solution is used at the start of the calculation. The full multigrid initialization (FMG initialization) can provide an initial and approximate solution at a minimum cost compared to the overall computational expense.[75] For this coupling process, the large pressure difference between the process gas and furnace gas as shown in Table 9.6 and Table 9.1 can cause stability issues for the CFD simulation. In this situation, FMG initialization helps with the solver stability when compared with the standard initialization and the hybrid initialization methods. FMG initialization utilizes the ANSYS Fluent full-approximation storage (FAS) Multigrid technology to obtain the initial solution. Starting from a uniform solution (after performing standard initialization), the FMG initialization procedure constructs the desirable number of geometric grid levels using the procedure outlined in FAS Multigrid.[74] However, compared with other initialization methods, like the standard initialization and hybrid initialization, FMG initialization is more time-consuming.

9.4.6 Simulation Results

To conduct the CFD simulation of this small-scale reformer model, we used three computational nodes in UCLA's Hoffman2 Cluster. A parallel computational environment is utilized based on the message passing interface technology by 48 cores. The CFD simulation of this small-scale reformer model converged in 4 days with 48 cores.

In the furnace side, the combustion flame shapes in the furnace chamber are demonstrated in Fig. 9.23. From Fig. 9.23, we can see that the simulated combustion results in flames with the length between 4.5 m (side flames) and 6 m (central flame) which matches well with the plant data. For this fuel-lean mixing gas, the fuels, CH_4, CO, and H_2, are com-

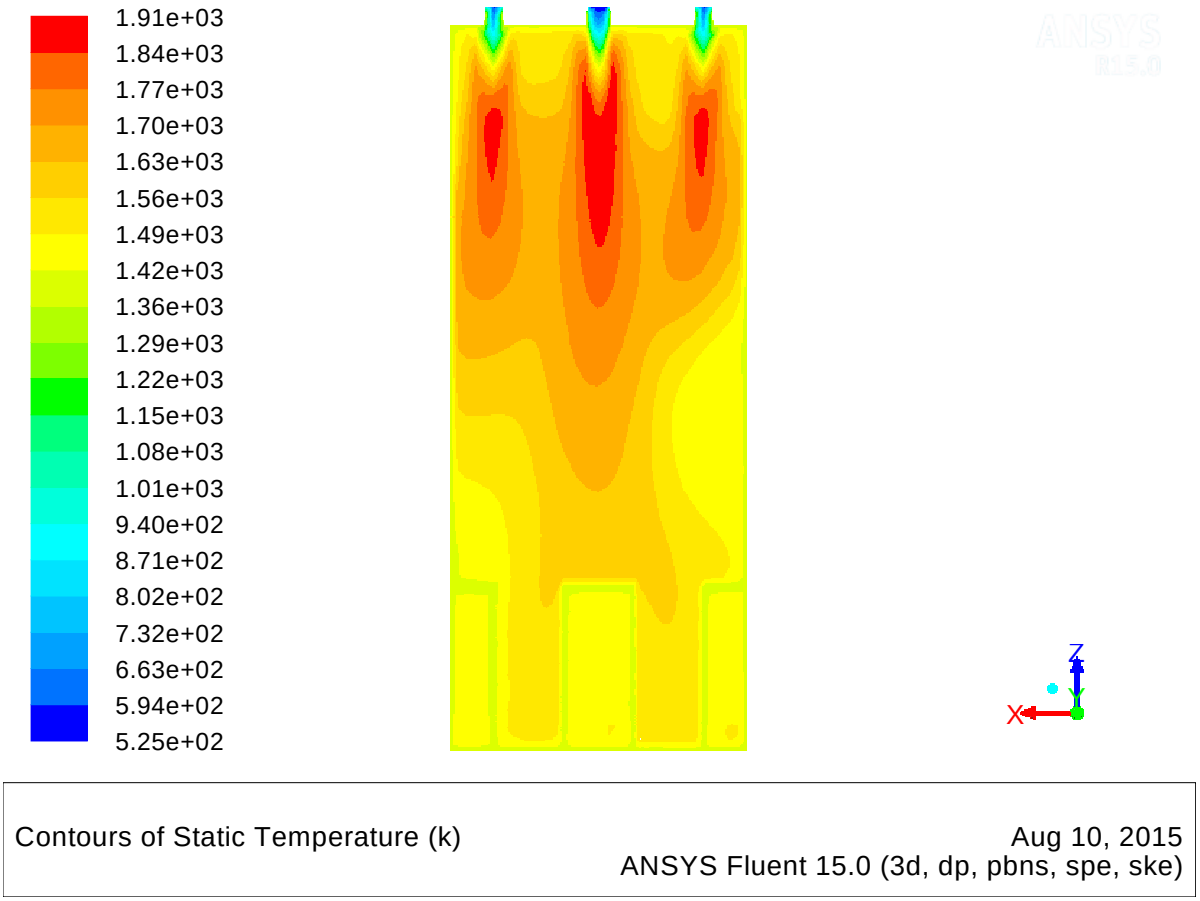

Figure 9.23: Flame shape profile (furnace side) of small-scale reformer model.

pletely combusted, and the mole fraction profiles of these species in the furnace chamber are shown in Figs. 9.24-9.26.

The heat released by the combustion is transferred to the outer wall of the four tubes in this small-scale model. The corresponding tube wall temperature profiles are shown in Fig. 9.28. The maximum temperature on the tube skin, i.e., hot spot, is 1155 K which is below the maximum allowable operating temperature of the tube material. By operating the system at this condition without exceeding the maximum allowable temperature, the tube skin can transfer as much heat flux as possible to the process side. The average heat flux rate at the tube skin of these four reforming tubes is about 79 kW/m^2 which is close to

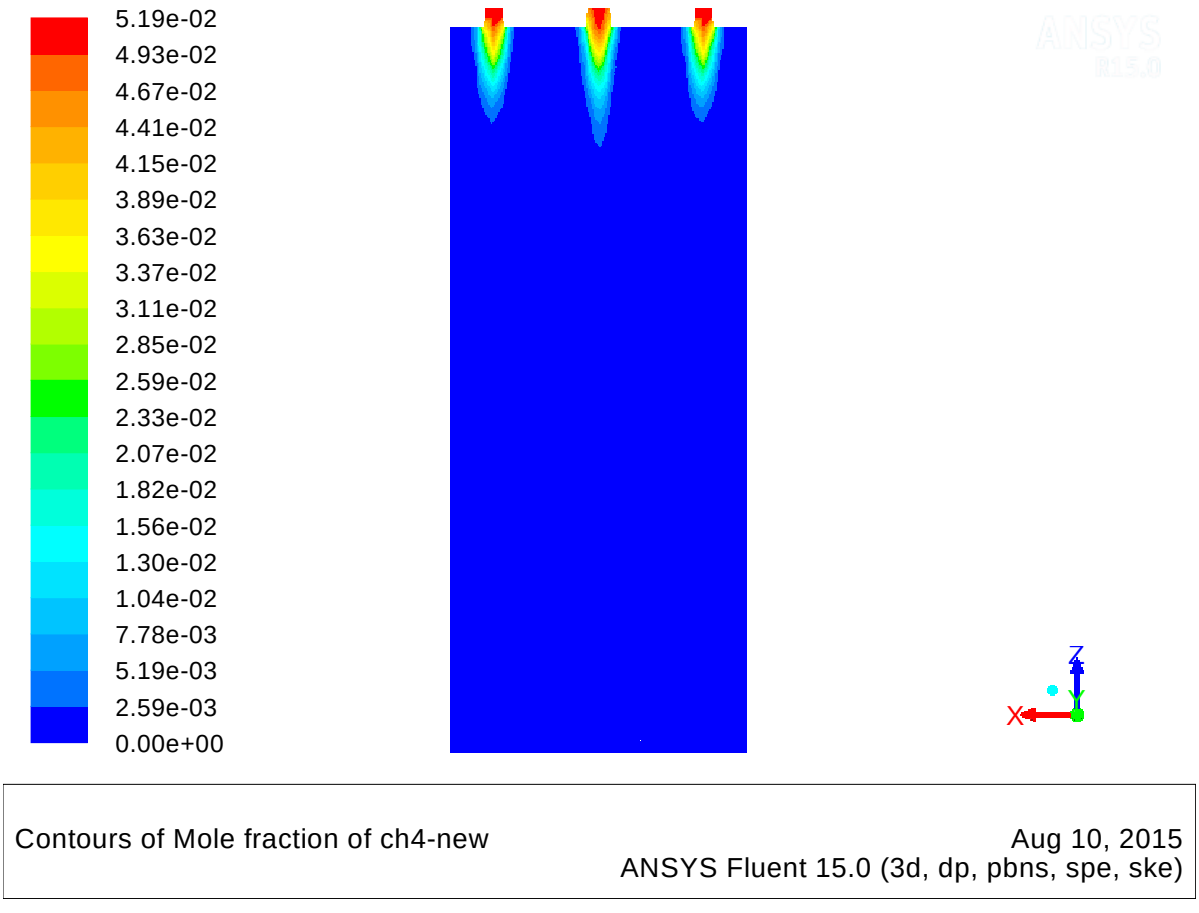

Figure 9.24: CH_4 mole fraction profile (furnace side) of small-scale reformer model.

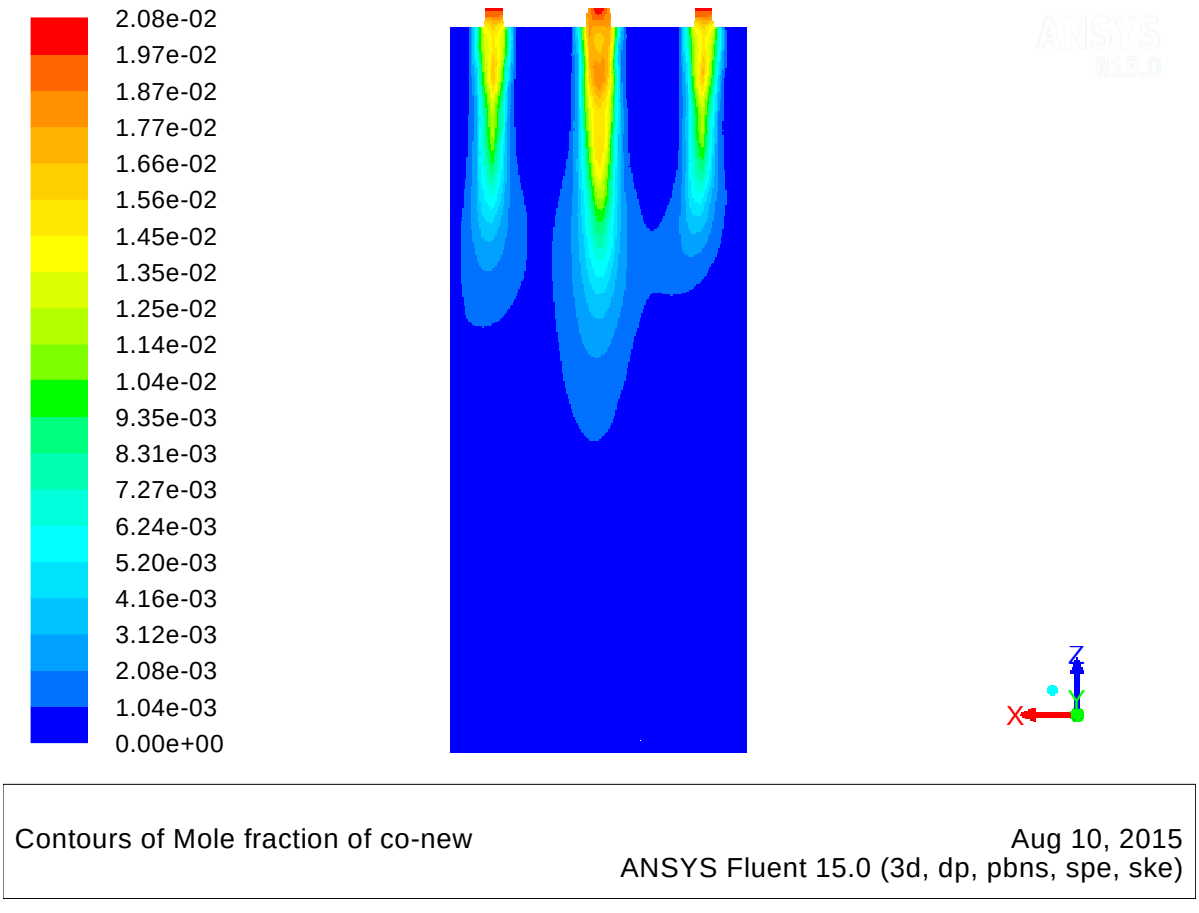

Figure 9.25: *CO* mole fraction profile (furnace side) of small-scale reformer model.

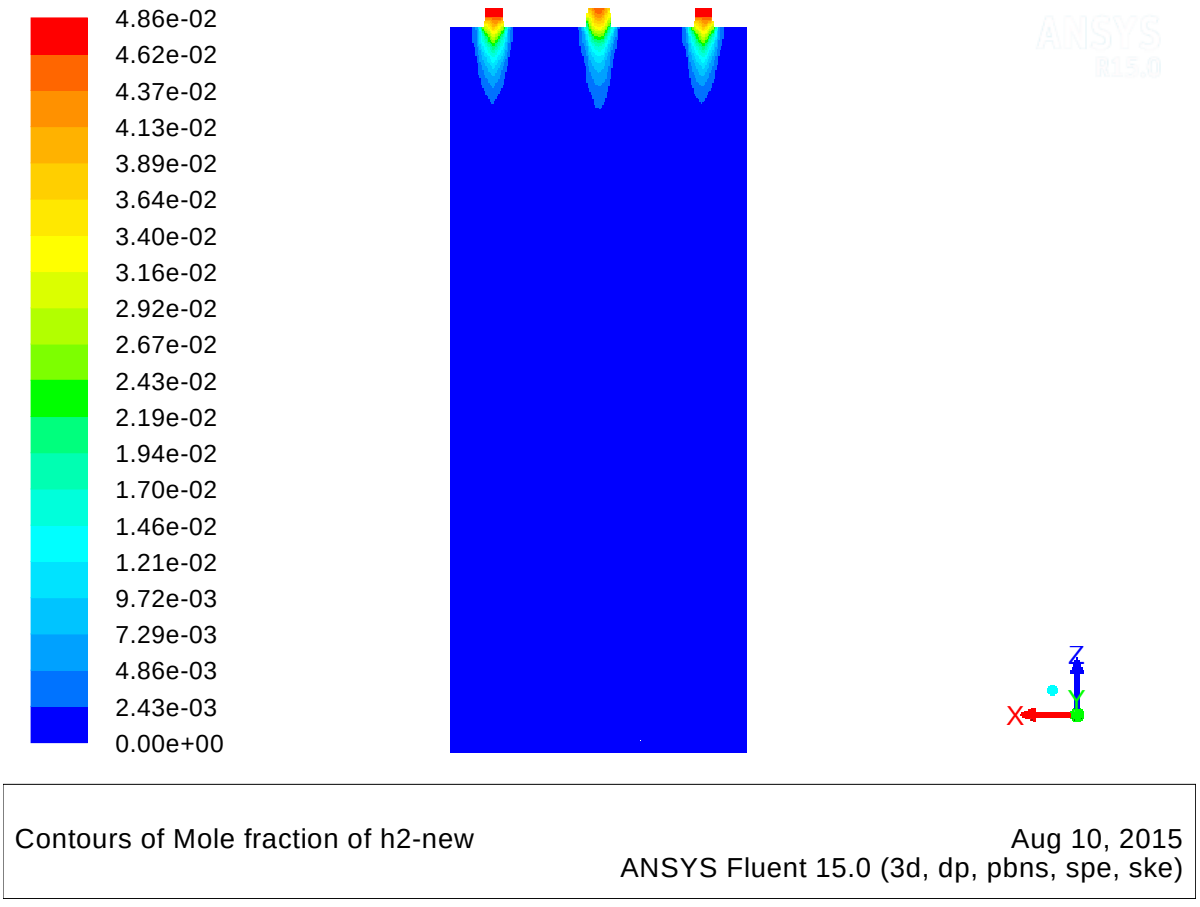

Figure 9.26: H_2 mole fraction profile (furnace side) of small-scale reformer model.

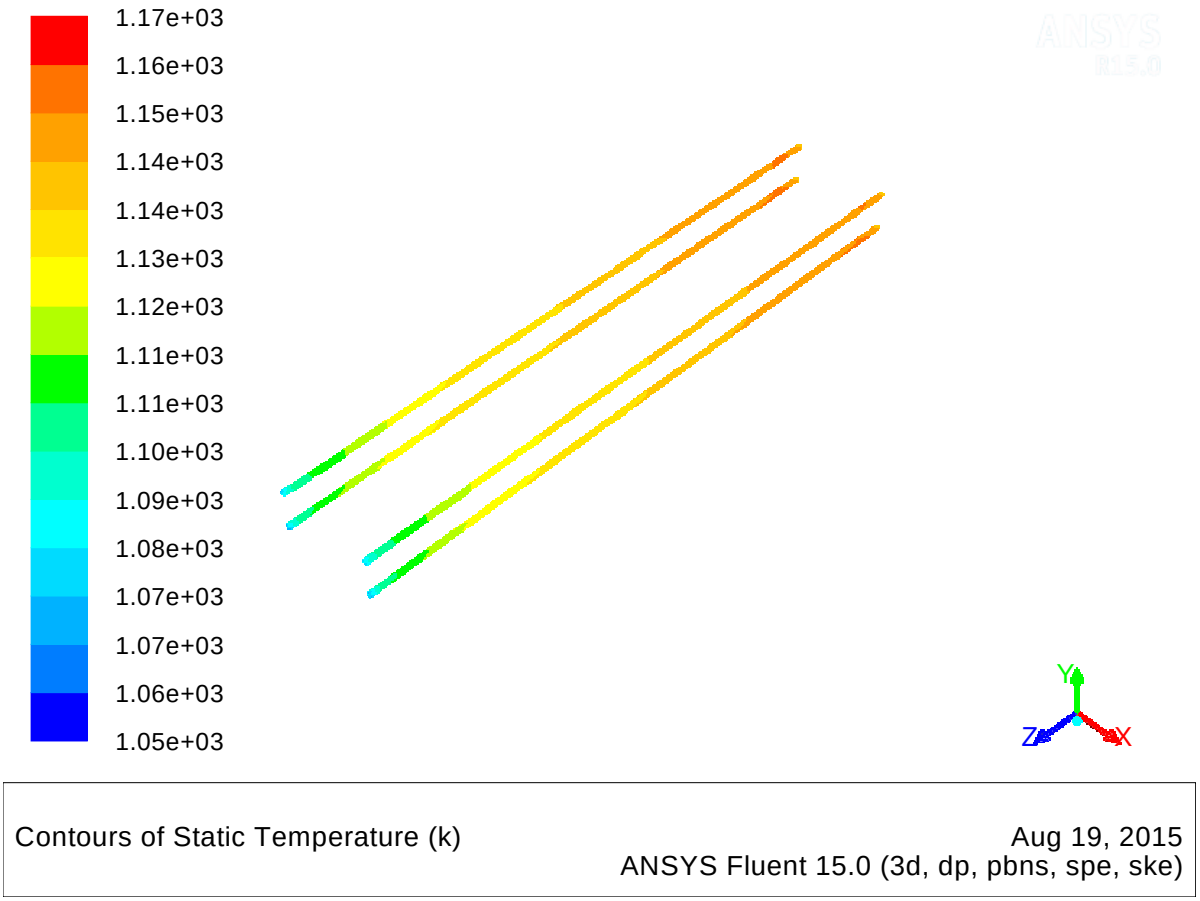

Figure 9.27: Tube wall temperature profile of small-scale reformer model (dashed line).

the heat flux value from the single tube modeling.

Finally, in the process side, the heat transferred from the tube skin provides the energy for the steam methane reforming reactions. The mole fraction profile of H_2 is demonstrated in Fig. 9.29. The average mole fraction of H_2 at the outlets of these four reforming tubes is about 46.9% which is also very close to the plant data. In terms of the pressure drop, the detailed pressure profiles inside these four reforming tubes are shown in Fig. 9.30, and the average pressure drop of these four reforming tubes is 118.4 *kPa*.

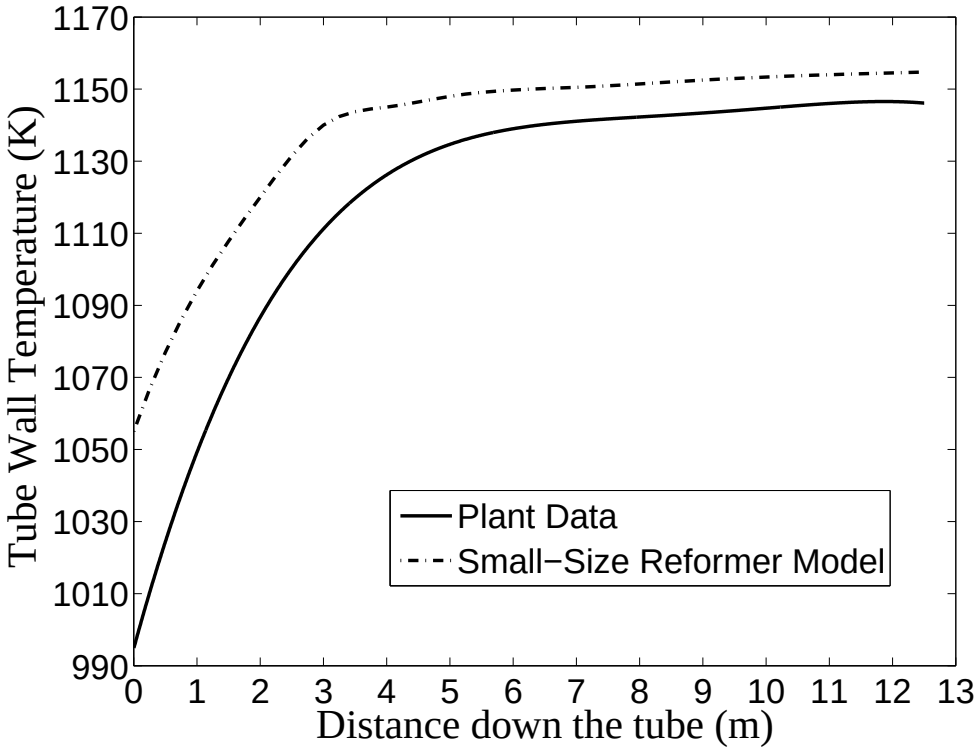

Figure 9.28: Tube wall temperature profile of small-scale reformer model.

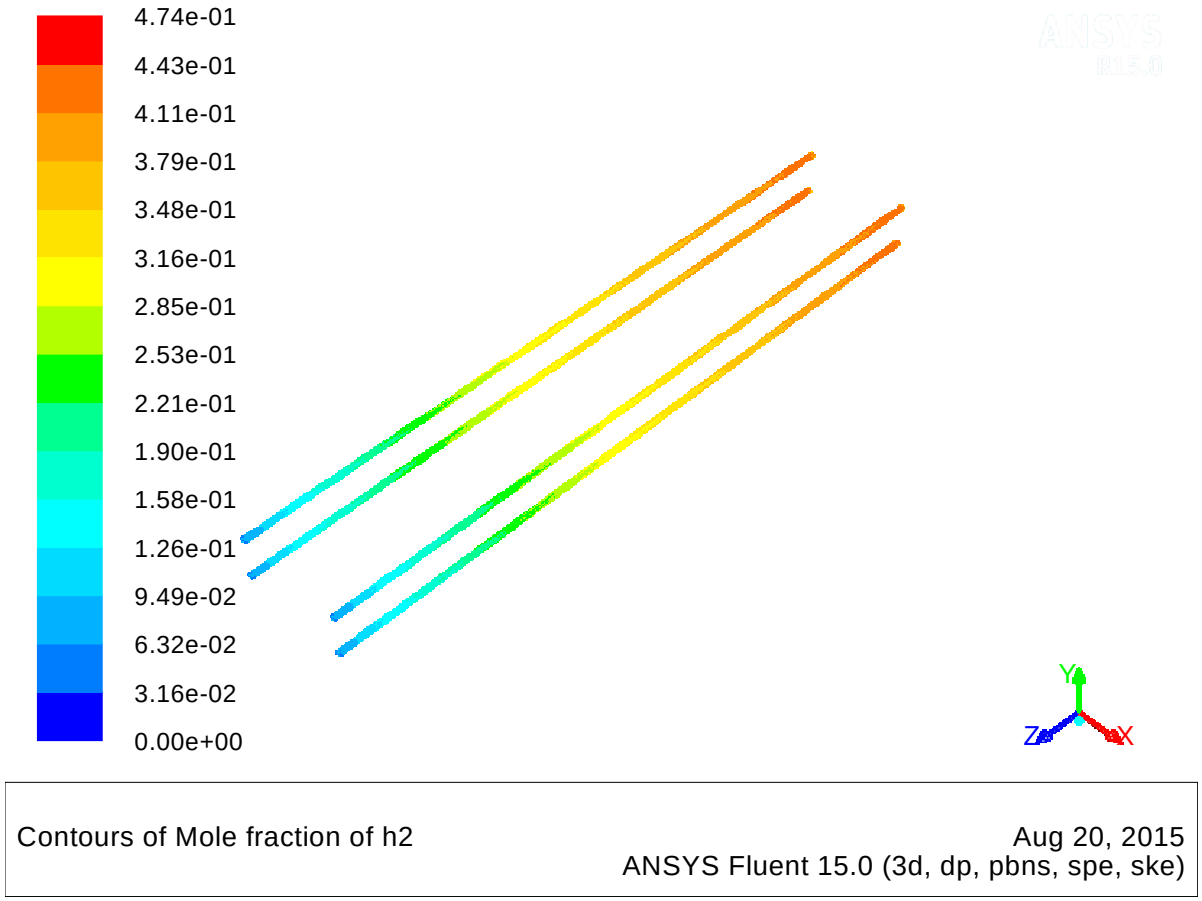

Figure 9.29: H_2 mole fraction profile (process side) of small-scale reformer model.

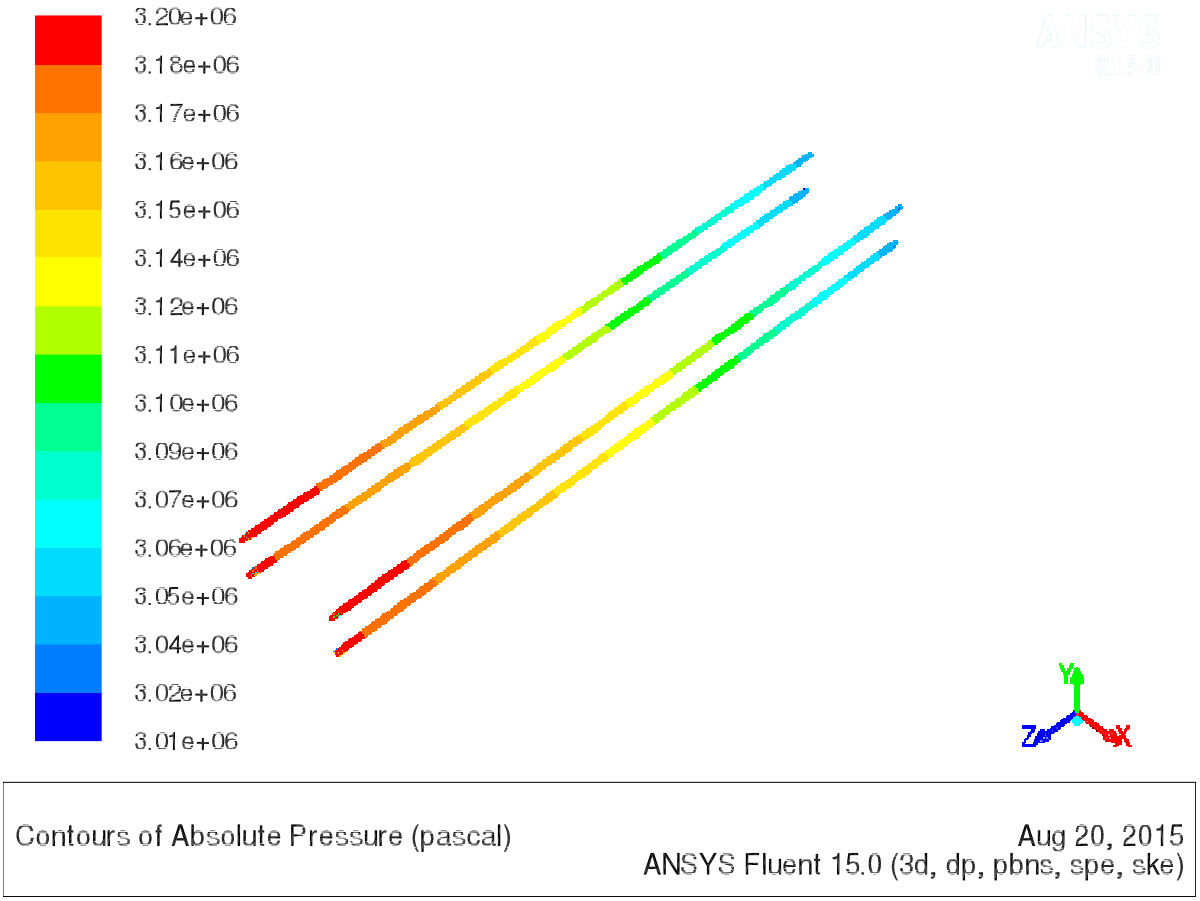

Figure 9.30: Tube interior pressure profile (process side) of small-scale reformer model.

Table 9.8: Mesh quality of full-size reformer mesh.

Angle	Aspect Ratio	Determinant ($3 \times 3 \times 3$)	Distortion	Eriksson Skewness
$25^o - 90^o$	1 - 15	0.398 - 1	0.604 - 1	0.651 - 1

9.5 Full-Size Reformer Model

9.5.1 Mesh Generation

Mesh generation is the most time-consuming part of the CFD modeling of this full-size steam methane reformer. To reduce the computational burden and improve potential convergence performance, a mesh structure of the structured mesh nodes is developed in ICEM-CFD. An overall view of the generated mesh structure is shown in Fig. 9.31. This mesh has about 15 million nodes which consist of almost 14 million hexahedrons and 1 million quadrilaterals. 6 million nodes are designed for the three hundred thirty-six reforming tubes, and the rest 9 million nodes are for the furnace chamber and burners. The detailed mesh structures are shown in Figs. 9.31-9.33. There is no negative volume mesh node, and the main indices of the mesh standard[74] are listed in Table 9.8.

Based on the mesh quality indices shown in Table 9.8 and the detailed mesh structure in Figs. 9.31-9.33, the generated mesh is acceptable for CFD simulation. Also, boundary layer structures are designed for both the inner and outer surfaces of all the reforming tubes as we do for the small-scale model.

9.5.2 Tuning Method

From the simulation of the single reforming tube, it is established that the time scale of reforming reactions is relatively shorter when compared with that which is required to heat up the packed bed from heat radiation of the flue gas. The time scale of the heat

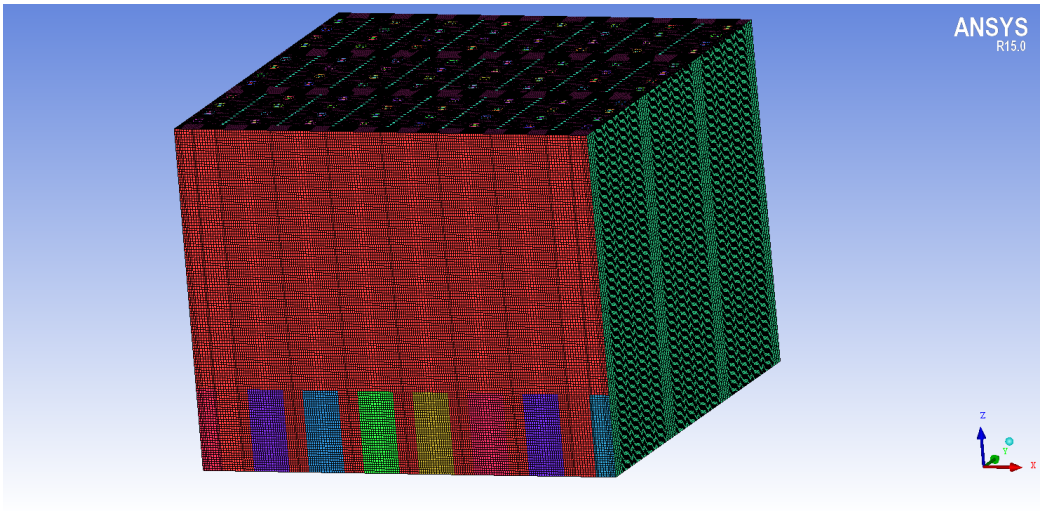

Figure 9.31: Overall view of full-size reformer mesh.

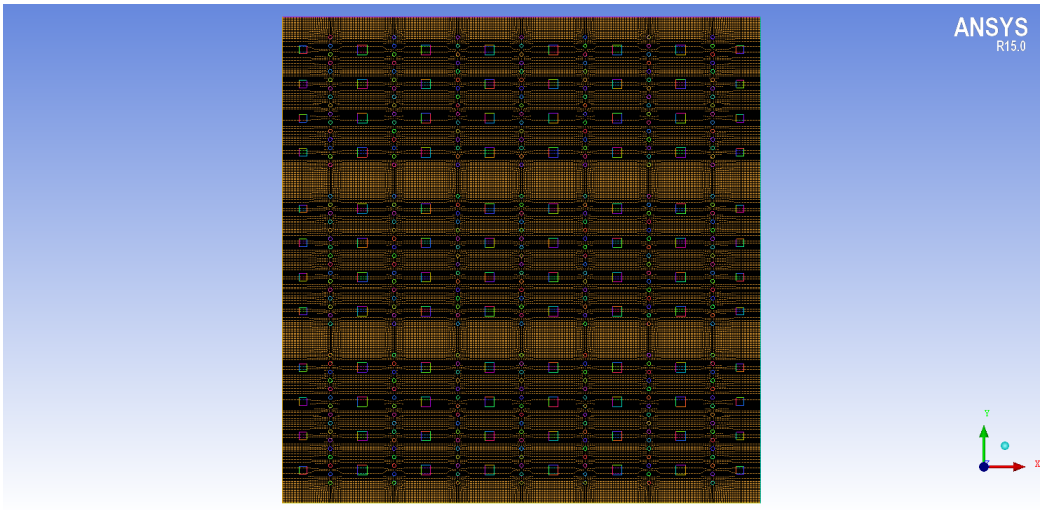

Figure 9.32: Top view of full-size reformer mesh.

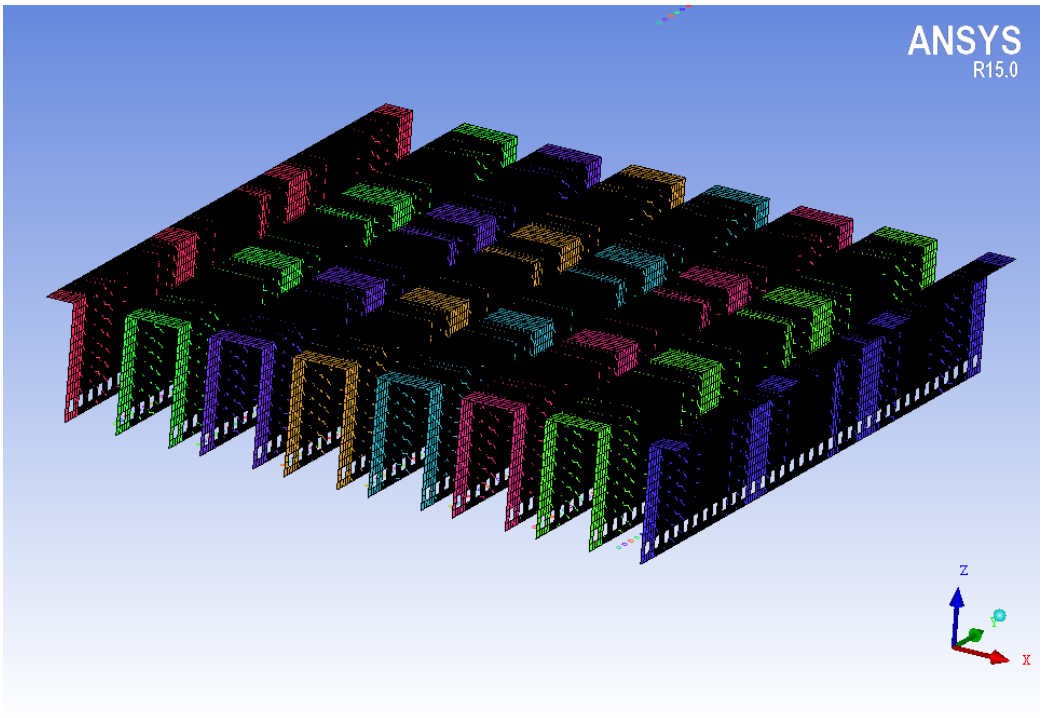

Figure 9.33: Flue gas tunnels of full-size reformer mesh.

radiation process is much larger than that of the fuel combustion process. Considering that the predominant radiative heat transfer determines the speed of heating up the packed bed and providing heat for reforming reactions, then for this model coupling both the process side and the furnace side, the convergence speed is mainly constrained by the radiation process in the furnace chamber. Namely, the heat released by the fast combustion needs a long time to heat up all the reforming tubes and achieve the desired reaction progress. To ensure the computational efficiency and model convergence performance for the whole reformer simulation, an iterative convergence method is developed. In detail, after the FMG initialization, the full-size model is running with the combustion and an approximate finite rate form of the reforming reaction kinetics with steady solver. When the fluid variable profiles are close to the expected results, the UDF of the reforming reaction kinetics[141] is applied to modify the reaction phenomena inside the reforming tubes. Then, from that

point, a transient solver is used to ensure the simulation convergence performance.

9.6 Conclusion

In this work, we developed a CFD model of an industrial level steam methane reformer including both furnace and process sides. A single reforming tube CFD model was first developed with detailed reforming reaction kinetics, porous media and fixed tube wall temperature. The CFD simulation result of this single reforming tube was consistent with the plant data of an industrial reformer. Then, the coupling of the combustion process and the reforming reaction process inside the tubes was demonstrated in a small-scale reformer. A detailed modeling method was proposed for the CFD model of this small-scale model, and reasonable simulation results were achieved. Finally, the developed modeling method of coupling combustion and reforming reaction for the small-scale reformer was applied to the full-size reformer.

Chapter 10

Conclusions

Motivated by the increasing importance of preventive maintenance to the reliability, safety and economic objectives of process operation, this dissertation developed methods for integrating on-line preventive maintenance of actuators and sensors with advanced process control system design. In addition, we developed for the first-time methods for EMPC of transport-reaction processes and proposed a framework for multiscale modeling of an industrial steam methane reforming unit.

Specifically, in Chapter 2, a LEMPC to integrate preventive maintenance of control actuators, process economic performance, and process control was proposed. During a scheduled preventive maintenance task on the j-th control actuator, the actuator is effectively taken off-line. In general, the steady-state with all available control actuators and with actuators taken off-line to perform a scheduled preventive maintenance task may be different (i.e., the former may not even be a steady-state of the latter scenario). To address this point, the proposed LEMPC was designed to ensure that the closed-loop state will be forced from the stability region of the steady-state of all m actuators to the stability region with $m-1$ actuators on-line before the j-th control actuator was taken off-line. Closed-loop stability in the sense of boundedness of the closed-loop state was proved. The

LEMPC capable of handling preventive maintenance was applied to a benzene alkylation process which yielded improved closed-loop economic performance over steady-state operation and demonstrated its ability to handle changing number of on-line actuators.

Subsequently, in Chapter 3, a novel robust moving horizon estimation scheme that accommodates a varying number of sensors to continuously supply accurate state estimates to a LEMPC system was established. It was shown that the proposed RMHE-based LEMPC scheme can maintain process closed-loop stability under standard observability and stabilizability assumptions. Then, the proposed RMHE-based LEMPC was applied to a chemical process; the simulation results exhibited its ability to accomplish control system reconfiguration under a changing number of on-line sensors and to achieve minimal economic performance degradation by operating the process in an economically optimal fashion, while preserving closed-loop stability.

Chapter 4 developed a proactive fault-tolerant Lyapunov-based MPC that can account for a known future fault and work for complete fault rejection. The practical stability of a closed-loop nonlinear system with the proposed proactive fault-tolerant LMPC was proved. The proposed controller was demonstrated through a chemical process consisting of two CSTRs in series followed by a flash separator. The simulated process demonstrated that the proactive fault-tolerant LMPC was able to achieve practical stability of the closed-loop system. However, sensor faults or even process abnormal events which are very often encountered in practice, also have a significant effect on the controller performance. Thus we plan to explore these types of faults in a future work.

Also, considering that EMPC of transport-reaction processes modeled by PDEs is an important theoretical problem of practical importance, this dissertation developed EMPC formulations for transport-reaction processes modeled by either parabolic PDEs or hyperbolic PDEs.

Specifically, in Chapter 5, a low-order and high-order finite-dimensional economic

model predictive (EMPC) systems is developed, through the application of Galerkin's method and involvement of singular perturbation arguments, for transport-reaction processes described by nonlinear systems of parabolic PDE . The formulated EMPC systems were applied to a tubular reactor example described by two nonlinear parabolic PDEs, where the average reaction rate along the length of the reactor was used as the cost function. Closed-loop simulations demonstrated that in the absence of state constraint, the low-order EMPC system is sufficient to meet the constraint on the availability of the reactant material over one operation period, and yields improved closed-loop economic performance compared to when the reactant material is fed uniformly in time to the reactor by requesting a suitable time-varying reactor operation. On the other hand, when a state constraint on the maximum value of the temperature along the length of the reactor is imposed, the use of a high-order (yet computationally efficient) EMPC system allows to account for the process dynamics with sufficient accuracy and meet both the input and state constraints simultaneously while improving the economic cost over uniform in time feeding of the reactant material.

Subsequently, in Chapter 6, two types of EMPC systems for systems of quasi-linear PDEs were presented: (1) an output feedback EMPC system, and (2) an EMPC system formulated with a reduced-order model derived using empirical eigenfunctions as basis functions. The EMPC systems were applied to a tubular reactor of industrial importance. Through time-varying operation, the EMPC systems yielded improved closed-loop economic performance over steady-state operation. Additionally, constructing a reduced-order model (ROM) on the basis of historical data-based empirical eigenfunctions by applying Karhunen-Loève expansion demonstrated computational benefits over using analytical sinusoidal/cosinusoidal eigenfunctions as basis functions.

Chapter 7 developed an EMPC design for a system of parabolic PDEs which integrated the APOD method and a high-order finite-difference method to deal with control system

computational efficiency and state constraint satisfaction. EMPC systems adopting POD, APOD, a high-order spatial discretization by central finite-difference method and the proposed EMPC flow chart were applied to a non-isothermal tubular reactor where a second-order chemical reaction takes place. These EMPC systems were compared with respect to their model accuracy, computational time, APOD update requirements, state constraint satisfaction and closed-loop economic performance of the tubular reactor. The simulation results demonstrated the advantages of APOD on improving computational efficiency of EMPC design, but also demonstrated a potential problem on state constraint violation. To address this issue, an EMPC scheme inheriting the high computational efficiency from APOD and the high state prediction accuracy from high-order finite-difference method is proposed; simulation results demonstrated that this EMPC scheme successfully improves the computational efficiency, while avoiding state constraint violations. Future work will focus on developing an output feedback EMPC scheme based on APOD in which the state measurements will be limited to few discrete points along the spatial domain.

In Chapter 8, both state feedback and output feedback EMPC schemes for a system of two coupled hyperbolic PDEs arising in the modeling of a non-isothermal plug flow reactor were developed. Through extensive simulation studies, key metrics like economic closed-loop performance under EMPC versus steady-state operation, impact of horizon length on computation time and economic performance, effect of number of measurement points on state estimation and closed-loop economic performance were evaluated and discussed. Future work will attempt to develop a theoretic framework of the presented computation algorithms.

Finally, in Chapter 9, a CFD model of an industrial level steam methane reformer including both furnace and process sides was developed. A single reforming tube CFD model was first developed with detailed reforming reaction kinetics, porous media and fixed tube wall temperature. The CFD simulation result of this single reforming tube was consistent

with the plant data of an industrial reformer. Then, the coupling of the combustion process and the reforming reaction process inside the tubes was demonstrated in a small-scale reformer. A detailed modeling method was proposed for the CFD model of this small-scale model, and reasonable simulation results were achieved. Finally, the developed modeling method of coupling combustion and reforming reaction for the small-scale reformer was applied to the full-size reformer.

In summary, this thesis developed novel EMPC schemes that explicitly account for scheduled preventive control actuator/sensor maintenance programs, process economics and feedback control, proposed EMPC schemes that are formulated on the basis of suitable reduced-order models to ensure input and state constraint satisfaction and economics optimization for both parabolic and hyperbolic PDEs, and proposed multiscale, computational fluid dynamics modeling framework for an industrial-level steam methane reforming unit.

Bibliography

[1] National Aeronautics and Space Administration. NASA's viscous grid spacing calculator. *http://geolab.larc.nasa.gov/APPS/YPlus/*.

[2] J. H. Ahrens and H. K. Khalil. High-gain observers in the presence of measurement noise: A switched-gain approach. *Automatica*, 45:936–943, 2009.

[3] I. Aksikas, L. Mohammadi, J. F. Forbes, Y. Belhamadia, and S. Dubljevic. Optimal control of an advection-dominated catalytic fixed-bed reactor with catalyst deactivation. *Journal of Process Control*, 23:1508–1514, 2013.

[4] R. Amrit, J. B. Rawlings, and D. Angeli. Economic optimization using model predictive control with a terminal cost. *Annual Reviews in Control*, 35:178–186, 2011.

[5] D. Angeli, R. Amrit, and J. B. Rawlings. On average performance and stability of economic model predictive control. *IEEE Transactions on Automatic Control*, 57:1615–1626, 2012.

[6] A. Armaou and P. D. Christofides. Dynamic optimization of dissipative PDE systems using nonlinear order reduction. *Chemical Engineering Science*, 57:5083–5114, 2002.

[7] M. Baburić, N. Duić, A. Raulot, and P. J. Coelho. Application of the conservative discrete transfer radiation method to a furnace with complex geometry. *Numerical Heat Transfer, Part A: Applications*, 48:297–313, 2005.

[8] J. Baker and P. D. Christofides. Finite-dimensional approximation and control of non-linear parabolic PDE systems. *International Journal of Control*, 73:439–456, 2000.

[9] M. J. Balas. Feedback control of linear diffusion processes. *International Journal of Control*, 29:523–534, 1979.

[10] S. P. M. Bane, J. L. Ziegler, and J. E. Shepherd. Development of one-step chemistry models for flame and ignition simulations. Technical report, GALCIT Report GALCITFM:2010.002, Mar. 2010.

[11] S. Banerjee, J. V. Cole, and K. F. Jensen. Nonlinear model reduction strategies for rapid thermal processing systems. *IEEE Transactions on Semiconductor Manufacturing*, 11:266–275, 1998.

[12] R. E. Barlow and F. Proschan. *Mathematical Theory of Reliability*. Society for Industrial and Applied Mathematics, Philadelphia, PA, 1996.

[13] N. Behnam, A. G. Dixon, P. M. Wright, M. Nijemeisland, and E. H. Stitt. Comparison of CFD simulations to experiment under methane steam reforming reacting conditions. *Chemical Engineering Journal*, 207-208:690–700, 2012.

[14] F. Beyer, J. Brightling, P. Farnell, and C. Foster. Steam reforming - 50 years of development and the challenges for the next 50 years. In *AIChE 50th Annual Safety in Ammonia Plants and Related Facilities Symposium*, Toronto, Canada, Sept. 2005.

[15] Y. Bindar. *Ph. D. Thesis: Experimental and numerical investigations of a multi-burner furnace operated with various heat transfer boundary conditions*. Queen's University, 1996.

[16] M. Bryner. Smart manufacturing: the next revolution. *Chemical Engineering Progress*, 108:4–12, 2012.

[17] H. Budman and P. L. Silveston. Control of periodically operated reactors. *Chemical Engineering Science*, 63:4942–4954, 2008.

[18] H. P. A. Calis, J. Nijenhuis, B. C. Paikert, F. M. Dautzenberg, and C. M. van den Bleek. CFD modelling and experimental validation of pressure drop and flow profile in a novel structured catalytic reactor packing. *Chemical Engineering Science*, 56:1713–1720, 2001.

[19] C. R. Cassady, R. O. Bowden, L. Liew, and E. A. Pohl. Combining preventive maintenance and statistical process control: a preliminary investigation. *IIE Transactions*, 32:471–478, 2000.

[20] C. R. Cassady and E. Kutanoglu. Integrating preventive maintenance planning and production scheduling for a single machine. *IEEE Transactions on Reliability*, 54:304–309, 2005.

[21] F. Castillo, E. Witrant, C. Prieur, and L. Dugard. Boundary observers for linear and quasi-linear hyperbolic systems with application to flow control. *Automatica*, 49:3180 – 3188, 2013.

[22] S. Chand and J. F. Davis. What is Smart Manufacturing? *Time Magazine Wrapper*, Jul., 2007.

[23] C. C. Chen and H. C. Chang. Accelerated disturbance damping of an unknown distributed system by nonlinear feedback. *AIChE Journal*, 38:1461–1476, 1992.

[24] X. Chen, M. Heidarinejad, J. Liu, and P. D. Christofides. Distributed economic MPC: Application to a nonlinear chemical process network. *Journal of Process Control*, 22:689–699, 2012.

[25] P. D. Christofides. *Nonlinear and Robust Control of PDE Systems: Methods and Applications to Transport-Reaction Processes*. Birkhäuser, Boston, MA, 2001.

[26] P. D. Christofides and P. Daoutidis. Feedback control of hyperbolic PDE systems. *AIChE Journal*, 42:3063–3086, 1996.

[27] P. D. Christofides and P. Daoutidis. Finite-dimensional control of parabolic PDE systems using approximate inertial manifolds. *Journal of Mathematical Analysis and Applications*, 216:398–420, 1997.

[28] P. D. Christofides, J. F. Davis, N. H. El-Farra, D. Clark, K. R. D. Harris, and J. N. Gipson. Smart plant operations: Vision, progress and challenges. *AIChE Journal*, 53:2734–2741, 2007.

[29] P. D. Christofides and N. H. El-Farra. *Control of nonlinear and hybrid process systems: Designs for uncertainty, constraints and time-delays*. Springer-Verlag, Berlin, Germany, 2005.

[30] D. A. Crowl and J. F. Louvar. *Chemical process safety: fundamentals with applications (3rd edition)*. Prentice Hall, Upper Saddle River, NJ, 2011.

[31] R. F. Curtain and A. J. Pritchard. *Infinite Dimensional Linear Systems Theory*. Lecture Notes in Control and Information Sciences. Springer-Verlag, Berlin-Heidelberg, 1978.

[32] J. F. Davis, T. Edgar, J. Porter, J. Bernaden, and M. Sarli. Smart manufacturing, manufacturing intelligence and demand-dynamic performance. *Computers & Chemical Engineering*, 47:145–156, 2012.

[33] J. R. Davis. *Alloy Digest Sourcebook: Stainless Steels (Alloy Digest)*. ASM International, Materials Park, OH, 2000.

[34] M. Diehl, R. Amrit, and J. B. Rawlings. A Lyapunov function for economic optimizing model predictive control. *IEEE Transactions on Automatic Control*, 56:703–707, 2011.

[35] A. G. Dixon. CFD study of effect of inclination angle on transport and reaction in hollow cylinder catalysts. *Chemical Engineering Research and Design*, 92:1279–1295, 2014.

[36] S. Dubljevic. Boundary model predictive control of Kuramoto–Sivashinsky equation with input and state constraints. *Computers & Chemical Engineering*, 34:1655–1661, 2010.

[37] S. Dubljevic and P. D. Christofides. Predictive control of parabolic PDEs with boundary control actuation. *Chemical Engineering Science*, 61:6239–6248, 2006.

[38] S. Dubljevic, N. H. El-Farra, P. Mhaskar, and P. D. Christofides. Predictive control of parabolic PDEs with state and control constraints. *International Journal of Robust and Nonlinear Control*, 16:749–772, 2006.

[39] S. Dubljevic, P. Mhaskar, N. H. El-Farra, and P. D. Christofides. Predictive control of transport-reaction processes. *Computers & Chemical Engineering*, 29:2335–2345, 2005.

[40] P. Dufour, F. Couenne, and Y. Toure. Model predictive control of a catalytic reverse flow reactor. *IEEE Transactions on Control Systems Technology*, 11:705–7074, 2003.

[41] P. Dufour and Y. Touré. Multivariable model predictive control of a catalytic reverse flow reactor. *Computers & Chemical Engineering*, 28:2259–2270, 2004.

[42] P. Dufour, Y. Touré, D. Blanc, and P. Laurent. On nonlinear distributed parameter model predictive control strategy: On-line calculation time reduction and application to an experimental drying process. *Computers & Chemical Engineering*, 27:1533–1542, 2003.

[43] G. W. A. Dummer, R. Winton, and M. Tooley. *An elementary guide to reliability*. Butterworth-Heinemann, 1997.

[44] N. H. El-Farra, A. Armaou, and P. D. Christofides. Analysis and control of parabolic PDE systems with input constraints. *Automatica*, 39:715–725, 2003.

[45] M. Ellis and P. D. Christofides. Economic model predictive control with time-varying objective function for nonlinear process systems. *AIChE Journal*, 60:507–519, 2014.

[46] M. Ellis and P. D. Christofides. On finite-time and infinite-time cost improvement of economic model predictive control for nonlinear systems. *Automatica*, 50:2561–2569, 2014.

[47] M. Ellis and P. D. Christofides. Real-time economic model predictive control of nonlinear process systems. *AIChE Journal*, 61:555–571, 2015.

[48] M. Ellis, H. Durand, and P. D. Christofides. A tutorial review of economic model predictive control methods. *Journal of Process Control*, 24:1156–1178, 2014.

[49] M. Ellis, J. Zhang, J. Liu, and P. D. Christofides. Robust moving horizon estimation-based output feedback economic model predictive control. *Systems & Control Letters*, 68:101–109, 2014.

[50] S. Ergun and A. A. Orning. Fluid flow through randomly packed columns and fluidized beds. *Industrial & Engineering Chemistry*, 41:1179–1184, 1949.

[51] B. A. Finlayson. *The Method of Weighted Residuals and Variational Principles*. Academic Press, New York, 1972.

[52] B. A. Finlayson. *Nonlinear Analysis in Chemical Engineering*. McGraw-Hill Inc., New York, 1980.

[53] C. Foias, M. S. Jolly, I. G. Kevrekidis, G. R. Sell, and E. S. Titi. On the computation of inertial manifolds. *Physics Letters A*, 131:433–436, 1988.

[54] C. Foias, G. R. Sell, and E. S. Titi. Exponential tracking and approximation of inertial manifolds for dissipative nonlinear equations. *Journal of Dynamics and Differential Equations*, 1:199–244, 1989.

[55] Center for Chemical Process Safety (1st edition). *Guidelines for Implementing Process Safety Management Systems*. Wiley-AIChE, 1994.

[56] Center for Chemical Process Safety (1st edition). *Guidelines for Safe Automation of Chemical Processes*. Wiley-AIChE, 1994.

[57] A. M. Fuxman, J. F. Forbes, and R. E. Hayes. Characteristics-based model predictive control of a catalytic flow reversal reactor. *The Canadian Journal of Chemical Engineering*, 85:424–432, 2007.

[58] H. Ganji, J. S. Ahari, A. Farshi, and M. Kakavand. Modelling and simulation of benzene alkylation process reactors for production of ethylbenzene. *Petroleum and Coal*, 46:55–63, 2004.

[59] M. D. Graham and J. B. Rawlings. *Modeling and analysis principles for chemical and biological engineers*. Nob Hill Publishing, Madison, WI, 2013.

[60] L. Grüne. Economic receding horizon control without terminal constraints. *Automatica*, 49:725–734, 2013.

[61] L. Grüne and M. Stieler. Asymptotic stability and transient optimality of economic MPC without terminal conditions. *Journal of Process Control*, 24:1187–1196, 2014.

[62] A. Guardo, M. Coussirat, M. A. Larrayoz, F. Recasens, and E. Egusquiza. CFD flow and heat transfer in nonregular packings for fixed bed equipment design. *Industrial & Engineering Chemistry Research*, 43:7049–7056, 2004.

[63] Y. Han, R. Xiao, and M. Zhang. Combustion and pyrolysis reactions in a naphtha cracking furnace. *Chemical Engineering & Technology*, 30:112–120, 2006.

[64] E. M. Hanczyc and A. Palazoglu. Sliding mode control of nonlinear distributed parameter chemical processes. *Industrial & Engineering Chemistry Research*, 34:557–566, 1995.

[65] M. Heidarinejad, J. Liu, and P. D. Christofides. Economic model predictive control of nonlinear process systems using Lyapunov techniques. *AIChE Journal*, 58:855–870, 2012.

[66] M. Heidarinejad, J. Liu, and P. D. Christofides. State-estimation-based economic model predictive control of nonlinear systems. *Systems & Control Letters*, 61:926–935, 2012.

[67] M. Heidarinejad, J. Liu, and P. D. Christofides. Algorithms for improved fixed-time performance of Lyapunov-based economic model predictive control of nonlinear systems. *Journal of Process Control*, 23:404–414, 2013.

[68] M. Heidarinejad, J. Liu, and P. D. Christofides. Economic model predictive control of switched nonlinear systems. *Systems & Control Letters*, 62:77–84, 2013.

[69] P. Holmes, J. L. Lumley, and G. Berkooz. *Turbulence, Coherent Structures, Dynamical Systems and Symmetry*. Cambridge University Press, New York, New York, 1996.

[70] H. C. Hottel and A. F. Sarofim. *Radiative Transfer*. McGraw-Hill, New York, 1967.

[71] R. Huang, E. Harinath, and L. T. Biegler. Lyapunov stability of economically oriented NMPC for cyclic processes. *Journal of Process Control*, 21:501–509, 2011.

[72] E. A. N. Idris and S. Engell. Economics-based NMPC strategies for the operation and control of a continuous catalytic distillation process. *Journal of Process Control*, 22:1832–1843, 2012.

[73] J. M. Igreja, J. M. Lemos, and R. N. Silva. Controlling distributed hyperbolic plants with adaptive nonlinear model predictive control. In Rolf Findeisen, Frank Allgwer, and LorenzT. Biegler, editors, *Assessment and Future Directions of Nonlinear Model Predictive Control*, volume 358 of *Lecture Notes in Control and Information Sciences*, pages 435–441. Springer Berlin Heidelberg, 2007.

[74] ANSYS Inc. ANSYS Fluent Theory Guide 15.0. Nov., 2013.

[75] ANSYS Inc. ANSYS Fluent User's Guide 15.0. Nov., 2013.

[76] K. Ito and K. Kunisch. Receding horizon optimal control for infinite dimensional systems. *ESAIM: Control, Optimisation and Calculus of Variations*, 8:741–760, 2002.

[77] J. Jäschke, X. Yang, and L. T. Biegler. Fast economic model predictive control based on NLP-sensitivities. *Journal of Process Control*, 24:1260–1272, 2014.

[78] W. P. Jones and B. E. Launder. The prediction of laminarization with a two-equation model of turbulence. *International Journal of Heat and Mass Transfer*, 15:301–314, 1972.

[79] H. K. Khalil. *Nonlinear Systems*. Prentice Hall, 2002.

[80] H. K. Khalil and F. Esfandiari. Semiglobal stabilization of a class of nonlinear systems using output feedback. *IEEE Transactions on Automatic Control*, 38:1412–1415, 1993.

[81] W. Kim, K. Ji, and A. Srivastava. Network-based control with real-time prediction of delayed/lost sensor data. *IEEE Transactions on Control Systems Technology*, 14:182–185, 2006.

[82] P. Kokotović and M. Arcak. Constructive nonlinear control: a historical perspective. *Automatica*, 37:637–662, 2001.

[83] L. Lao, M. Ellis, and P. D. Christofides. Proactive fault-tolerant model predictive control. *AIChE Journal*, 59:2810–2820, 2013.

[84] L. Lao, M. Ellis, and P. D. Christofides. Economic model predictive control of parabolic PDE systems: Addressing state estimation and computational efficiency. *Journal of Process Control*, 24:448–462, 2014.

[85] L. Lao, M. Ellis, and P. D. Christofides. Economic model predictive control of transport-reaction processes. *Industrial & Engineering Chemistry Research*, 53:7382–7396, 2014.

[86] L. Lao, M. Ellis, and P. D. Christofides. Smart manufacturing: Handling preventive actuator maintenance and economics using model predictive control. *AIChE Journal*, 60:2179–2196, 2014.

[87] L. Lao, M. Ellis, and P. D. Christofides. Handling state constraints and economics in feedback control of transport-reaction processes. *Journal of Process Control*, 32:98–108, 2015.

[88] L. Lao, M. Ellis, and P. D. Christofides. Real-time preventive sensor maintenance using robust moving horizon estimation and economic model predictive control. *AIChE Journal*, 2015, in press.

[89] D. Latham. *Masters Thesis: Mathematical Modeling of An Industrial Steam Methane Reformer*. Queen's University, 2008.

[90] B. E. Launder and B. I. Sharma. Application of the energy dissipation model of turbulence to the calculation of flow near a spinning disc. *Letters in Heat and Mass Transfer*, 1:131–138, 1974.

[91] W. J. Lee and G. F. Froment. Ethylbenzene dehydrogenation into styrene: kinetic modeling and reactor simulation. *Industrial & Engineering Chemistry Research*, 47:9183–9194, 2008.

[92] N. G. Leveson and G. Stephanopoulos. A system-theoretic, control-inspired view and approach to process safety. *AIChE Journal*, 60:2–14, 2014.

[93] Y. Lin and E. D. Sontag. A universal formula for stabilization with bounded controls. *Systems & Control Letters*, 16:393–397, 1990.

[94] Y. Lin, E. D. Sontag, and Y. Wang. A smooth converse Lyapunov theorem for robust stability. *SIAM Journal on Control and Optimization*, 34:124–160, 1996.

[95] J. Liu. Moving horizon state estimation for nonlinear systems with bounded uncertainties. *Chemical Engineering Science*, 93:376–386, 2013.

[96] J. Liu, X. Chen, D. Muñoz de la Peña, and P. D. Christofides. Sequential and iterative architectures for distributed model predictive control of nonlinear process systems. *AIChE Journal*, 56:2137–2149, 2010.

[97] J. L. Massera. Contributions to stability theory. *The Annals of Mathematics*, 64:182–206, 1956.

[98] Johnson Matthey. Johnson Matthey Catalysts - Delivering world-class hydrogen plant performance. *http://www.jmcatalysts.cn/en/pdf/HydrogenTechBrochFeb2007.pdf*.

[99] C. McGreavy and M. W. Newmann. Development of a mathematical model of a steam methane reformer. In *Institution of Electrical Engineering, Conference on the Industrial Applications of Dynamic Modelling*, Durham, NC, Sept. 1969.

[100] P. Mhaskar, N. H. El-Farra, and P. D. Christofides. Stabilization of nonlinear systems with state and control constraints using Lyapunov-based predictive control. *Systems & Control Letters*, 55:650–659, 2006.

[101] P. Mhaskar, A. Gani, C. McFall, P. D. Christofides, and J. F. Davis. Fault-tolerant control of nonlinear process systems subject to sensor faults. *AIChE Journal*, 53:654–668, 2007.

[102] P. Mhaskar, J. Liu, and P. D. Christofides. *Fault-tolerant process control: Methods and applications*. Springer-Verlag, London, England, 2012.

[103] A. A. Moghadam, I. Aksikas, S. Dubljevic, and J. F. Forbes. Boundary optimal LQ control of coupled hyperbolic PDEs and ODEs. *Automatica*, 49:526 – 533, 2013.

[104] B. S. Mordukhovich and J. P. Raymond. Dirichlet boundary control of hyperbolic equations in the presence of state constraints. *Applied Mathematics and Optimization*, 49:145–157, 2004.

[105] D. Muñoz de la Peña and P. D. Christofides. Lyapunov-based model predictive control of nonlinear systems subject to data losses. *IEEE Transactions on Automatic Control*, 53:2076–2089, 2008.

[106] M. A. Müller, D. Angeli, and F. Allgöwer. Economic model predictive control with self-tuning terminal cost. *European Journal of Control*, 19:408–416, 2013.

[107] M. A. Müller, D. Angeli, and F. Allgöwer. On the performance of economic model predictive control with self-tuning terminal cost. *Journal of Process Control*, 24:1179–1186, 2014.

[108] D. G. Nicol. *Ph. D. Thesis: A Chemical Kinetic and Numerical Study of NOx and Pollutant Formation in Low-emission Combustion*. University of Washington, 1995.

[109] M. M. Noor, P. W. Andrew, and T. Yusaf. Detail guide for CFD on the simulation of biogas combustion in bluff-body mild burner. In *International Conference on Mechanical Engineering Research*, Kuantan, Malaysia, Jul. 2013.

[110] K. Othmer. *Kirk-Othmer Encyclopedia of Chemical Technology*. John Wiley and Sons Inc.

[111] A. Pariyani, W. D. Seider, U. G. Oktem, and M. Soroush. Incidents investigation and dynamic analysis of large alarm databases in chemical plants: A fluidized-catalytic-cracking unit case study. *Industrial & Engineering Chemistry Research*, 49:8062–8079, 2010.

[112] C. Perego and P. Ingallina. Combining alkylation and transalkylation for alkylaromatic production. *Green Chemistry*, 6:274–279, 2004.

[113] S. Pitchaiah and A. Armaou. Output feedback control of distributed parameter systems using adaptive proper orthogonal decomposition. *Industrial & Engineering Chemistry Research*, 49:10496–10509, 2010.

[114] S. Pitchaiah and A. Armaou. Output feedback control of dissipative PDE systems with partial sensor information based on adaptive model reduction. *AIChE Journal*, 59:747–760, 2013.

[115] D. B. Pourkargar and A. Armaou. Modification to adaptive model reduction for regulation of distributed parameter systems with fast transients. *AIChE Journal*, 59:4595–4611, 2013.

[116] S. S. Ravindran. Adaptive reduced-order controllers for a thermal flow system using proper orthogonal decomposition. *SIAM Journal on Scientific Computing*, 23:1924–1942, 2002.

[117] J. B. Rawlings and R. Amrit. *Optimizing process economic performance using model predictive control*. Springer-Heidelberg, Berlin, Germany, 2009.

[118] J. B. Rawlings, D. Angeli, and C. N. Bates. Fundamentals of economic model predictive control. In *The 51st IEEE Annual Conference on Decision and Control (CDC)*, pages 3851–3861, Maui, Hawaii, Dec. 2012.

[119] W. H. Ray. *Advanced Process Control*. McGraw-Hill, New York, New York, 1981.

[120] G. V. Reklaitis. A systems engineering approach to reliability, availability, and maintenance. In *the First International Conference on Foundations of Computer Aided Process Operations*, pages 221–252, Park City, UT, Jul. 1987.

[121] L. Schenato. Optimal estimation in networked control systems subject to random delay and packet drop. *IEEE Transactions on Automatic Control*, 53:1311–1317, 2008.

[122] P. O. M. Scokaert and J. B. Rawlings. Feasibility issues in linear model predictive control. *AIChE Journal*, 45:1649–1659, 1999.

[123] H. Shang, F. Forbes, and M. Guay. Model predictive control for quasilinear hyperbolic distributed parameter systems. *Physics Letters A*, 43:2140–2149, 2004.

[124] J. J. Siirola and T. F. Edgar. Process energy systems: Control, economic, and sustainability objectives. *Computers & Chemical Engineering*, 47:134–144, 2012.

[125] P. L. Silveston and R. R. Hudgins. *Periodic Operation of Reactors*. Elsevier, Oxford, England, 2013.

[126] M. A. Singer and W. H. Green. Using adaptive proper orthogonal decomposition to solve the reaction-diffusion equation. *Applied Numerical Mathematics*, 59:272–279, 2009.

[127] L. Sirovich. Turbulence and the dynamics of coherent structures. I - Coherent structures. II - Symmetries and transformations. III - Dynamics and scaling. *Quarterly of Applied Mathematics*, 45:561–590, 1987.

[128] J. Smoller. *Shock Waves and Reaction-Diffusion Equations*. Springer-Verlag, Berlin-Heidelberg, 1983.

[129] E. D. Sontag. A 'universal' construction of Artstein's theorem on nonlinear stabilization. *Systems & Control Letters*, 13:117–123, 1989.

[130] U.S. Energy Information Administration EIA Independent Statistics and Analysis. Electricity storage can take advantage of daily price variations. *http://www.eia.gov/todayinenergy/detail.cfm?id=6350*, May 21, 2012.

[131] G. D. Stefanidis, B. Merci, G. J. Heynderickx, and G. B. Marin. CFD simulations of steam cracking furnaces using detailed combustion mechanisms. *Computers & Chemical Engineering*, 30:635–649, 2006.

[132] J. S. Tan and M. A. Kramer. A general framework for preventive maintenance optimization in chemical process operations. *Computers & Chemical Engineering*, 21:1451–1469, 1997.

[133] R. Temam. *Infinite-Dimensonal Dynamical Systems in Mechanics and Physics*. Applied Mathematical Sciences. Springer-Verlag, New York, New York, 1988.

[134] A. Theodoropoulou, R. A. Adomaitis, and E. Zafiriou. Model reduction for optimization of rapid thermal chemical vapor deposition systems. *IEEE Transactions on Semiconductor Manufacturing*, 11:85–98, 1998.

[135] I. Uriz. Computational fluid dynamics as a tool for designing hydrogen energy technologies. In L. M. Gandía, G. Arzamendi, and P. M. Diéguez, editors, *Renewable Hydrogen Technologies: Production, Purification, Storage, Applications and Safety*, pages 401–435. Elsevier, Oxford, UK, 2013.

[136] A. Varshney, S. Pitchaiah, and A. Armaou. Feedback control of dissipative PDE systems using adaptive model reduction. *AIChE Journal*, 55:906–918, 2009.

[137] C. G. Vassiliadis and E. N. Pistikopoulos. Maintenance scheduling and process optimization under uncertainty. *Computers & Chemical Engineering*, 25:217–236, 2001.

[138] D. H. von Seggern. *CRC Standard Curves and Surfaces with Mathematica*. Chapman & Hall/CRC Applied Mathematics & Nonlinear Science. Taylor & Francis, 2006.

[139] A. Wächter and L. T. Biegler. On the implementation of an interior-point filter line-search algorithm for large-scale nonlinear programming. *Mathematical Programming*, 106:25–57, 2006.

[140] M. H. Wesenberg and H. F. Svendsen. Mass and heat transfer limitations in a heterogeneous model of a gas-heated steam reformer. *Industrial & Engineering Chemistry Research*, 46:667–676, 2007.

[141] J. Xu and G. F. Froment. Methane steam reforming, methanation and water-gas shift: I. intrinsic kinetics. *AIChE Journal*, 35:88–96, 1989.

[142] H. You, W. Long, and Y. Pan. The mechanism and kinetics for the alkylation of benzene with ethylene. *Petroleum Science and Technology*, 24:1079–1088, 2006.

[143] J. Zhang and J. Liu, S.and Liu. Economic model predictive control with triggered evaluations: State and ouptut feedback. *Journal of Process Control*, 24:1197–1206, 2014.